An investigation into the feasibility of Fused Deposition Modelling for 3D printing oral pharmaceuticals

Jehad Nasereddin

Thesis submitted in fulfilment of the requirements for the degree of Doctor of Philosophy, University of East Anglia. Norwich, United Kingdom

Acknowledgements

I dedicate this work to the memory of my grandfather, Jehad Hasan Nasereddin, who passed on the morning on January 3rd, 2018. I'm sorry you didn't get to see it through, but I trust that as you look down on me, you feel pride in who you left behind. And thank you for the name you passed on to me. I will wear it proudly till the last of my days. May your memory live forever.

I would like to thank my supervisors. Dr. Sheng Qi, Prof. Peter Belton and my adoptive supervisor, Dr. Muqdad Alhijjaj. You have been the most patient of souls. Through your help and guidance, I could see myself grow into my own both as a researcher and a person. To that, I extend the warmest gratitude.

I also would like to take a moment to thank my brothers in arms, Dr. Janine Wilkinson, Zuzana Hlaskova, (hopefully, by the time of this writing Dr.) Salman Rahman, Randa Ziqlam, Chak Tam, and Sherif Ismail. In the words of Kurt Cobain, our little group has always been and always will until the end.

My family, my greatest gift. Mom, Dad, Sara, Amer, Lara. I love you all, and thank you for your endless love and support. I would've never made it this far without you.

And to those who extended a hand of friendship and guidance throughout this journey, I thank you all. Dr. Laszlo Fabian, Dr. Klaus Wellner, Prof. Yaroslav Khimyak, Alex, Veronica, Noelia, Muhammad, Sara, the lovely team at PCE Automation, thank you!

Abstract

Fused Deposition Modelling (FDM) is a variant of 3D Printing (3DP) that relies on the melt extrusion of thermoplastic polymers for the fabrication of objects. Using FDM, objects with customised geometries, mass, shapes, and dimensions can be printed on-demand. This customisability makes FDM a robust method for creating patient-tailored, personalised dosage forms. Therefore, the past few years have seen an increase in research demonstrating the use of FDM to produce solid dosage forms. Various research efforts have demonstrated the capacity of FDM to create dosage forms with customised geometries, tailored release profiles, and polypills containing multiple drugs. However, there remains no commercially available products are produced by FDM. This may be due to reported works describing the use of FDM as a pharmaceutical manufacturing process often employ a trial-and-error approach to arrive at a formulation, with little work demonstrating a thorough understanding of the FDM process and the involved parameter interactions as a whole. The work presented herein describes an investigation into the parameters involved in FDM, and their impact on the perceived quality parameters of 3D printed solid dosage forms, which should help to guide towards a more rational approach towards FDM printable dosage forms.

The work conducted herein investigated material properties, and FDM printing speed, printing temperature, and infill density, and their impact on perceived quality attributes of the printed dosage forms. Optimising the mechanical properties of the filament was found to be the rate limiting in creating a printable formulation. Chapter 3 describes a method developed to predetermine the mechanical suitability of a filament for FDM. Chapter 4 describes an investigation into the critical quality parameters of FDM, in which printing speed was found to have greater impact on the quality of printed dosage forms than printing temperature. Furthermore, a distortion effect related to material melt flow was observed and described, which is dubbed the *First Layer Effect.* Chapter 5 demonstrated how the use of the infill process parameter can be used to manipulate the drug release rate from a 3D printed dosage form and tune the formulation to a range of release characteristics ranging from an immediate release formulation to a sustained release and even a delayed release formulation without the need to alter the constituents of the printed dosage form.

Table of Contents

List of Publications

1) Nasereddin, J. M., Wellner, N., Alhijjaj, M., Belton, P., & Qi, S. (2018). Development of a Simple Mechanical Screening Method for Predicting the Feedability of a Pharmaceutical FDM 3D Printing Filament. Pharmaceutical Research, 35(8), 151.

2) Alhijjaj, M., Nasereddin, J., Belton, P., & Qi, S. (2019). Impact of Processing Parameters on the Quality of Pharmaceutical Solid Dosage Forms Produced by Fused Deposition Modeling (FDM). Pharmaceutics 2019, Vol. 11, Page 633, 11(12).

3) Qi, S., Nasereddin, J., & Alqahtani, F. (2018). Personalized Polypills Produced by Fused Deposition Modeling 3D Printing. In M. Maniruzzaman (Ed.), 3D and 4D Printing in Biomedical Applications: Process Engineering and Additive Manufacturing (First Edit, pp. 273–295). Wiley-VCH Verlag GmbH & Co. KGaA.

List of Figures

List of Tables

Chapter 1
Introduction

1.1. 3D printing for oral solid dosage forms, the solution to Personalised Medicine?

1.1.1. The personalised medicine challenge:

In recent years, it has been observed that an increasing number of marketed drugs, drugs under development, and New Chemical Entities (NCEs) being screened for pharmacological activity are more likely to be hydrophobic molecules, possessing poor aqueous solubility (Figure 1-1). This increase in the number of poorly water-soluble drug substances is believed to be correlated with a trend in pharmacotherapy to favour molecules that exhibit higher potency. Potency which is mediated, at least in part, by hydrophobic interactions between the molecule and the corresponding receptors in the body (1). This creates a problem for formulation scientists; most NCEs and drugs under development are likely to be formulated as oral solid dosage forms, which dictate that the drug substance must possess at least a minimum threshold of aqueous solubility for the formulation to be adequately bioavailable (2,3).

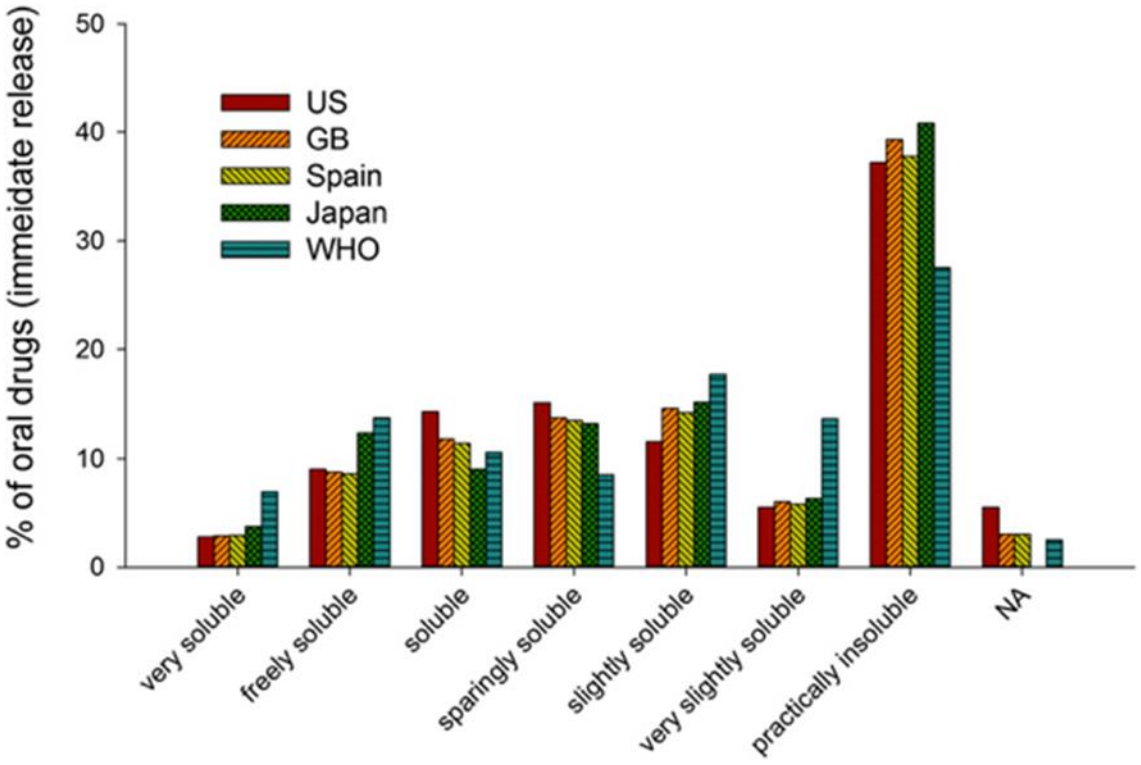

Figure 1-1: comparison of the distribution of the solubility of the top 200 oral drugs around the world. Figure obtained from Williams et al. (1).

Furthermore, the advent of therapeutic regimens involving potent pharmacotherapeutic drugs led to an increased understanding of the individualised needs of different patients. The “one-size-fits-all” approach to pharmacotherapy has proven to be less than suitable

for therapy monitoring and prognosis assessment. Which in turn led to the birth of the field of personalised medicine, which is the premise that different patients will always have genetic differences (and by extension, metabolic differences) that require different doses of the same drug substance to achieve an equivalent therapeutic effect. This, in turn, bottlenecks formulation development; most pharmaceutical manufacturing techniques have been adapted and optimized for quick and consistent production of large quantities of static doses of drug substances. Therefore, formulating potent drug substances while allowing for dosing personalization requires revamping of techniques and manufacturing processes used in the pharmaceutical industry (4,5).

Yet another issue that needs to be addressed when discussing personalised medicine is the increasing number of polypharmacy patients (6). A polypharmacy patient is defined as a patient undergoing a therapeutic regimen requiring 5+ tablets to be administered daily, a phenomenon that is becoming increasingly prevalent, particularly in geriatric patients (7–9). Being on a polypharmacy regimen is a known cause of poor patient compliance with the therapeutic regimen, which negatively affects disease prognosis and could lead to life-threatening complications (6).

There have been a few efforts aimed at developing dosage forms that allow for dosing flexibility and personalisation, such techniques include the formulation of drugs into liquid dosage forms (in which the volume corresponding to the desired dose is measured and administered to the patient) (10), fragmented solid dosage forms (like granules, pellets, or mini-tablets), in which a single unit (i.e. a single granule) contains a fraction of the dose, with the desired dose being achieved by counting or weighing the number of units required to achieve the prescribed dose. Scored tablets (which can be broken or cut to achieve fractions of the larger dose contained within an entire tablet) have also been investigated as a method to allow dose personalisation (4). Fixed-dose combination formulations have been conceived and are marketed as a method to circumvent the inconvenient number of tablets a polypharmacy patient has to take daily, but as the name suggests, they are “fixed dose” combinations and allow very little in terms of dosing personalisation (11). Therefore, it comes as no surprise that those techniques have, however, proven mostly inadequate, particularly in therapeutic regimens involving very potent drugs, due to either human error (patients on therapeutic drug regimens involving potent drugs are more likely to be geriatric patients (7,9,12) who are less capable of

accurately measuring the required dose), or instrument error due to unstandardized measurement apparatus (i.e. a tablespoon, a teaspoon, half a tablet) (4,10).

One dosing personalisation technique that has generated considerable interest in the past few years is 3D printing (3DP) (13). 3DP was pioneered in the late 20th century as a rapid prototyping, high-throughput fabrication method for engineering applications. However, the past few years have seen a rise in the number of affordable "desktop" 3D printers aimed at the general public. With the technique becoming less specialised for niche applications, and more suitable (both in terms of cost and complexity) for hobbyists. Which led to the technique being explored for applications in a number of different industries (14). The technique has since found applications in the healthcare industry, being used as means to fabricate medical devices, artificial limbs, pharmaceutical dosage forms, and even live human tissue (13,15–17). The use of 3DP as a method for the manufacture of pharmaceutical dosage forms is discussed in section 1.2 below.

1.2 Pharmaceutical 3D printing: current advancements and trends

3DP has generated a lot of research interest within the pharmaceutical industry, mainly due to it seemingly holding the key to solving the challenge the industry is facing in terms of personalised medicine (15,18,19). It has been postulated numerous times that, due to the sequence of events through which 3DP fabricates an object, it is possible to manufacture dosage forms consisting of multiple drugs in hybrid dosings, adapted to the needs of a particular patient, by embedding different drugs in different layers of the same unit dosage form (20). The prospects promised by 3DP were further cemented in 2015 when the United States Food and Drug Administration (US FDA) approved for commercialisation the first 3D printed pharmaceutical product, Spritam®, manufactured by pharmaceutical company Aprecia Pharmaceuticals (21). Although Spritam® is manufactured via 3DP, it does not utilise the full capabilities made possible by 3DP. Spirtam® is a mass-manufactured dosage form that is produced only as a single, 1000 mg dose of a single drug, levitracetam, and does not utilise the capabilities offered by 3DP for dose personalisation. However, the FDA authorisation of this 3D printed drug does show prospects in the possibility of general acceptance of marketing dosage forms manufactured by 3DP.

The term "3DP" does not refer to a particular technology. It is rather an umbrella term that is used to refer to a number of different techniques that fabricate objects by additive manufacturing (AM). AM is a fabrication process in which the object is built up sequentially by the superimposition of layers of material atop one another (Figure 1-2). The main difference between the different variants of 3DP is the materials they utilise, and their material deposition mechanism (5,13). Variants of 3DP include Powder-Based Printing (PBP), Stereolithography (STL), Semi-Solid Extrusion (SSE), Selective Laser Sintering (SLS), and Fused Deposition Modelling (FDM) (22–26). Of all the variants of 3DP, PBP has been the most pharmaceutically successful, being, to date, the only variant of the technology to successfully bring a product to the market, with the product Spritam® (1000 mg levitracetam) becoming the first 3D printed drug to gain FDA approval (21). The different 3DP techniques are discussed in the upcoming sections.

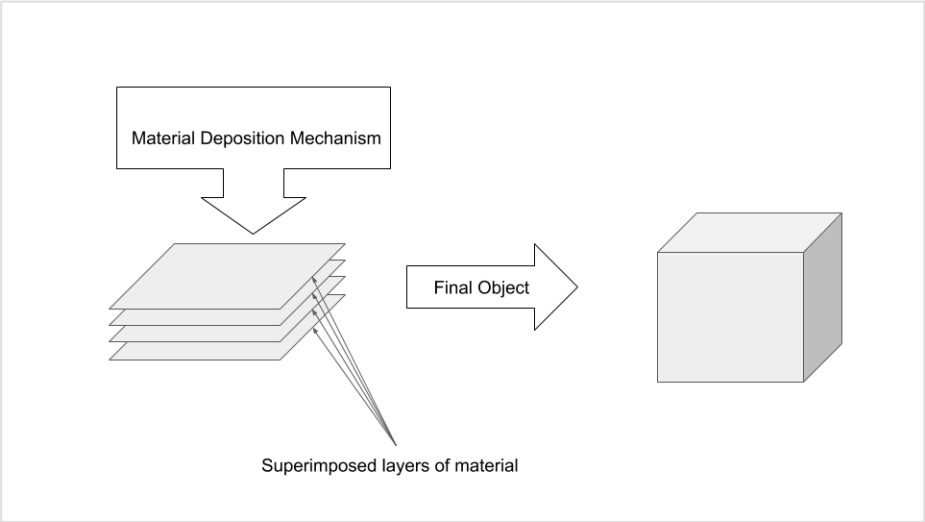

Figure 1-2: Layer superimposition to form the 3D object during 3DP

1.2.1. Powder-bed 3D printing:

PBP is a variant of 3DP technology that utilizes the controlled distribution of thin layers of powders. During a PBP printing run, a layer of powder is spread on the build plate, the layer is then glued together by the action of droplets of binder solution that are sprayed on it, followed by addition of a second layer of powder and so on. The process is continued layer-by-layer until completion of the build (13,27).

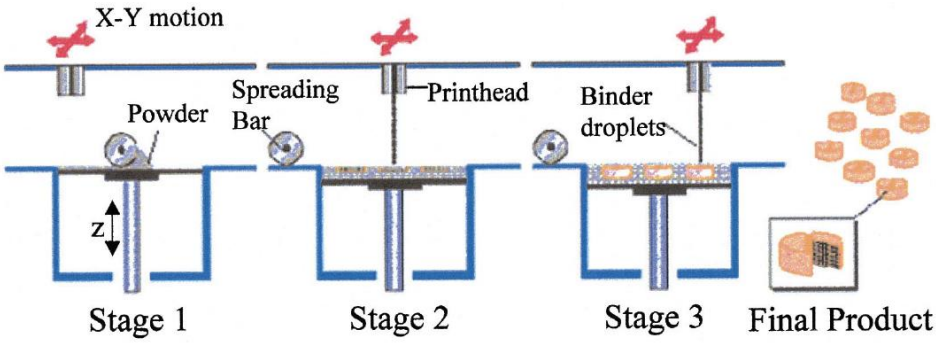

Figure 1-3: Powder bed 3DP. Figure obtained from Alhnan et al. (13).

The use of PBP for the fabrication of pharmaceutical dosage forms has been widely described, with the technique being investigated to fabricate tablets with modified release profiles (15). Yu et al. used PBP to fabricate fast-disintegrating tablets of paracetamol (28), Pryce-Lewis et al. was awarded a patent for his design of powder-bed printed, cylindrical drug delivery systems (29). And, as previously mentioned, Spritam®, an immediate-release formulation of levitracetam, became the first 3D printed drug to gain US FDA approval in August 2015 (21). Spritam® is manufactured via PBP, it employs a

technology that manufacturer Aprecia Pharmaceuticals has dubbed *ZipDose*® technology (30). The technology is claimed to provide very rapid disintegration, coupled with high drug loading whilst providing efficient taste masking (31).

The main drawbacks associated with PBP are the friability and high porosity of the finished products, as well as the low printing resolution, and the post-printing processing required to achieve the finalized product (13).

Despite the fact that PBP is generally considered a variant of 3DP, it is worth noting that, from a materials perspective, PBP offers little variation from wet granulation techniques commonly used in the pharmaceutical industry; in wet granulation, powders are blended and formed into granules by the addition of a binder solution and are then compressed to form a tablet (32). In PBP, the same "powder held by a binder solution" logic is used, albeit with a different processing route. Which suggests that the technique may suffer from similar challenges to those faced by traditional, punch-pressed tablets; such as loss of mechanical strength over the shelf life of the product, tendency to friability, and need for coating to manipulate drug release.

1.2.2. Stereolithographic 3D printing:

STL is a variant of 3DP technology. Fabrication is done via controlled exposure of photopolymeric resins to UV radiation, causing curing of the resins to form the solid object. In STL, lens-focused UV radiation is deflected by a rotating mirror onto the top-most layer of the photosensitive resin which rests on a build plate. The UV radiation causes curing and hardening of the material, the build plate is then lowered along the Z-axis by a set amount to allow the addition of a second layer on top of it (Figure 1-4), with the movement of the mirror and the plate controlled by computer software (23). Polymers which have been investigated for use in STL include low molecular weight methacrylates, as well as mono- and macro- polymeric epoxy resins. Those polymers often form rigid, brittle, glassy materials (13).

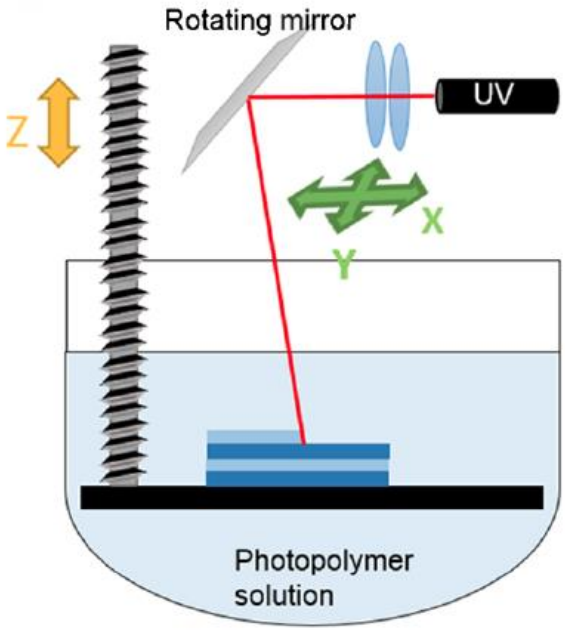

Figure 1-4: Printing mechanism used in STL. Figure obtained from Alhnan et al. (13)

There have been attempts to utilise STL as a method for manufacturing pharmaceutical solid dosage forms. Robles-Martinez et al. used STL to fabricate six-layered, stratified polypills, with each layer hosting a drug (prednisolone, chloramphenicol, caffeine, paracetamol, aspirin, and naproxen) (33). The printing was conducted using a stop-start method in which the printer needs to be paused after each drug layer was printed, to swap the resin in the printer for one containing the next drug. Healey et al. used STL 3DP to produce caplets containing either paracetamol or aspirin (34).

Despite its high printing resolution (layer thickness $\approx$ 0.2 μm), STL is generally considered to be a poor candidate for pharmaceutical adaptation due to its several disadvantages; most photo-curable resins suitable for STL are carcinogenic, their photosensitivity suggests that they are most likely to be unstable and susceptible to photo-degradation, and the use of UV radiation during manufacturing can degrade some of the drugs being printed (13). Products fabricated via STL often require additional curing following printing which makes it a less time-efficient process in comparison to some of its counterparts (23). Furthermore, because the tablet being printed is submerged in the resin from which it is cured. Drug migration to and from the resin may be a concern. This phenomenon was particularly notable in the experiment Robles-Martinez et al. mentioned prior (33), in which almost every layer in the printed tablets was contaminated with at

least one drug which was meant to reside in a different layer within the matrix of the tablet.

1.2.3. Selective Laser Sintering:

SLS can be considered the ambient variant of PBP. SLS printing uses a powder bed as raw materials for the build, the powder is fused via the use of a high-intensity laser which serves to liquefy and fuse the powder particles, resulting in the fusion of the powder into a solid layer (13).

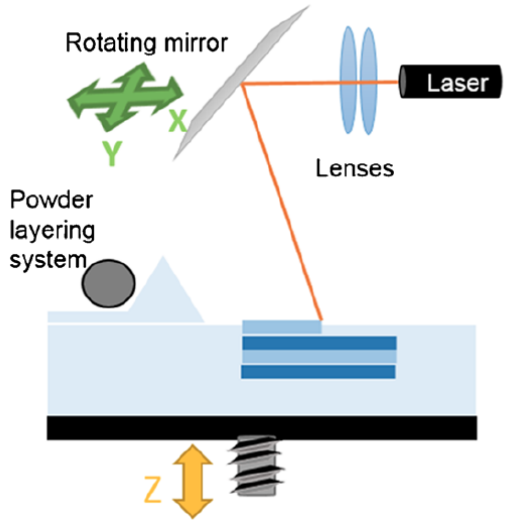

Figure 1-5: Selective laser sintering. Figure obtained from Alhnan et. al (13).

The use of SLS for the fabrication of pharmaceutical dosage forms has not been explored, which could be attributable to either the high-intensity laser used in the process, which has the potential to degrade most drugs or to the fact that materials that are laser-curable are often carcinogenic and are suitable for drug delivery applications (13).

1.2.4. Semi-solid Extrusion:

SSE printing involves the layer-wise extrusion of semi-solid pastes through a syringe (13). The pastes used in said formulations are often mixtures of drug/polymer/solvent systems whose viscosity was optimised to be extrudable through the printer syringe (24).

Khaled et al. used SSE to fabricate a 5-in-1, hybrid release profiles polypill, consisting of an immediate-release compartment housing aspirin and hydrochlorothiazide, and a sustained release compartment housing pravastatin, ramipril and atenolol (35). Khaled et al. also used SSE to produce guaifenesin-loaded HPMC bi-layer tablets (24). Kyobula et al. used SSE to print fenofibrate-loaded beeswax tablets (36)

The main drawback of SSE lies in semi-solid nature of the starting materials, which shrink upon drying, compromising the geometrical integrity of the fabricated tablet. Furthermore, the fabricated structures are very likely to collapse if a layer did not harden sufficiently before the addition of the next (13). There have been attempts to circumvent this drawback, by using an SSE – STL hybrid printing technique in which the semi-solid gels printed are made from curable resins, which are cured by UV light immediately upon printing (37).

1.2.5. Fused Deposition Modelling:

FDM is perhaps the most commercially available variant of 3DP (5). The availability of low-cost, FDM-based desktop 3D printers has caused a boost in the interest of using utilizing FDM (16). For Pharmaceutical 3D Printing (P3P), FDM is especially more attractive than other AM techniques. FDM is, in the most abstracted form, a melt extrusion technique, which makes it readily utilisable for polymeric drug delivery applications, namely amorphous solid dispersions (ASDs) (2,38).

In a typical FDM printing run, a thermoplastic polymer (which had previously been shaped into a thin strand called a *filament*), is fed into the printer by the action of two counter-rotating rollers. The feeding rollers carry the filament to a heating zone where the filament heated to a temperature beyond its melting point to form a melt, which is then deposited as a layer on the build plate through a nozzle. For the type of printer used herein, the maximum operational temperature the print head may be used at is 250 °C (39). The mechanical assembly consisting of the feeding rollers, heating zone, and the nozzle are collectively referred to as the printing head. After the melt exits the printing head, it is deposited onto the build plate to form a layer, this is then followed by the previously described downwards movement of the build plate to allow for a second layer to be deposited atop the first (40–42).

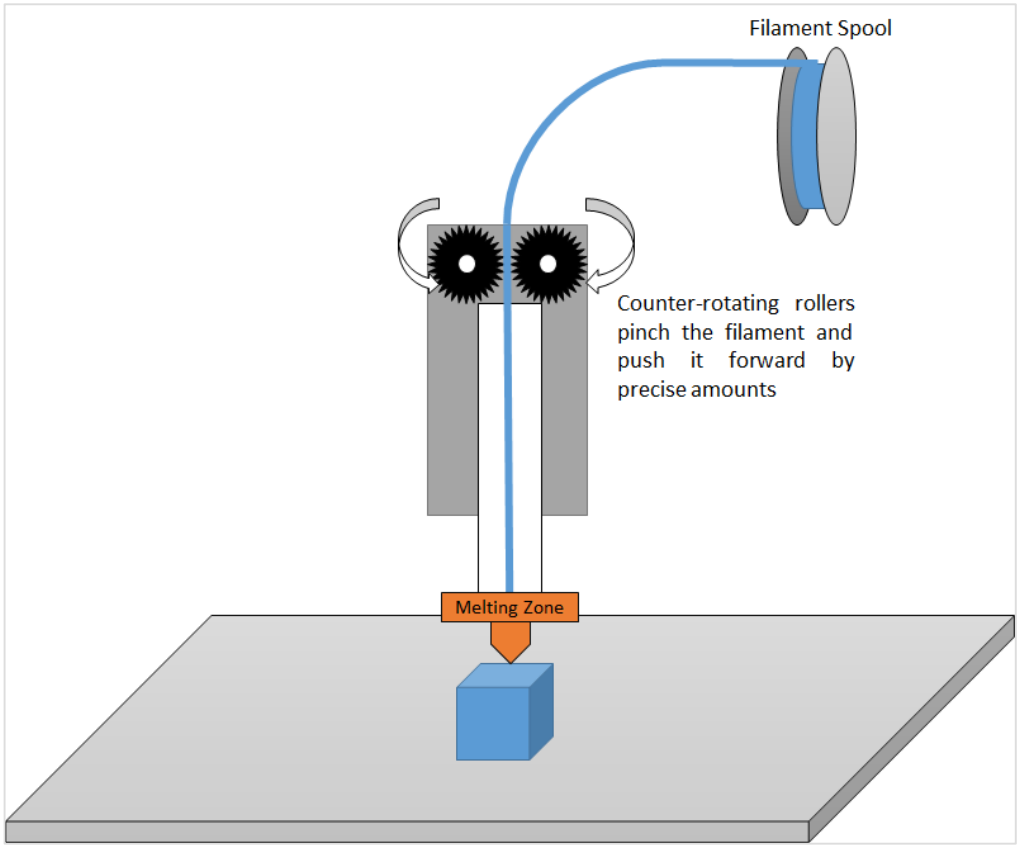

Figure 1-6: An illustration of FDM.

Out of all the variants of 3DP described in prior sections, FDM is seemingly the most attractive for pharmaceutical applications, with various research efforts demonstrating its feasibility; Goyanes et al. used commercial PVA filaments loaded with fluorescein as a model drug to demonstrate the feasibility of the technique for printing tablets (16), Goyanes also used FDM to print commercial PVA filaments loaded with 4-, and 5-aminosalicylate (4-ASA and 5-ASA respectively) (26), Skowyra et al. used FDM to print prednisolone-loaded, commercial PVA filaments (18). This loading of commercial filaments is achieved by incubation of the filament in an organic solution of the drug substance. A method that, although feasible, is noted for its inability to achieve sufficiently high drug loading percentages (Table 1-1). (9).

Table 1-1: the poor loading percentages of printed dosage forms prepared by incubation of commercial filaments

Drug	Polymer	Loading percentage	Reference
4-ASA	PVA	0.236% w/w	(26)
5-ASA	PVA	0.063% w/w	(28)
Fluorescein	PVA	0.29% w/w	(16)
Prednisolone	PVA	1.9% w/w	(18)

Pietrzak et al. used Hot-Melt Extrusion (HME) to prepare filaments of solid dispersions of theophylline, loaded in hydroxypropyl cellulose (HPC), Eudragit® RS PO, Eudragit® RL PO, and Eudragit® EPO, demonstrating that, when used in conjunction with HME, FDM has the potential to produce formulations possessing adequate drug loading, and greatly expanding the number of materials that may be used for P3P applications (44).

Alhijjaj et al. described the fabrication of a 5-component matrix containing either Eudragit® EPO, Soluplus®, or PVA, plasticised with polysorbate (Tween®) 80, polyethylene oxide (PEO) N10, and polyethylene glycol (PEG) 4000 with felodipine as a model drug and the fifth component of the matrix. Alhijjaj noted that the unavailability of pharmaceutically relevant materials suitable for P3P applications is the primary challenge against the development of commercially scaled FDM printing processes in the pharmaceutical industry (43).

A second challenge that stands in the way of successful commercialisation of P3P lies in the barrier posed by regulatory bodies (20). Regulatory bodies, such as the FDA and the Medicines and Healthcare Products Regulatory Agency (MHRA) require the demonstration consistency and reliability during manufacturing; the tried-and-tested methods that have been employed in the pharmaceutical industry for decades are considered to be more trusted, and by extension, safer than a newcomer technology like 3DP (45). However, the introduction of process exploratory paradigms such as pharmaceutical Quality Risk Management (QRM) and Quality by Design (QbD) by the US FDA provided pharmaceutical manufacturers with a margin of freedom to explore innovative approaches to drug formulation and development, provided that they demonstrated satisfactory understanding of the Critical Process Parameters (CPPs) that govern a particular industrial process (46).

Huang et al. grouped the CPPs relating to FDM into either one of three categories: machine-specific parameters, operation-specific parameters, and material-specific parameters (47). The parameters, as identified by Huang, can be found in Table 1-2.

Table 1-2: Critical Process Parameters relating to FDM as reported by Huang et al. Table recreated from Huang et al. (47).

Parameter category	Process parameter
Machine-Specific	Nozzle Diameter
	Filament Diameter
	Roller Speed
	Filament Feed Rate
	Flow Rate
Operation-Specific	Layer Thickness
	Road width
	Head Speed
	Fill Pattern
	Part Orientation
	Extrusion Temperature
	Environment Temperature
Material-Specific	Viscosity
	Stiffness
	Flexibility
	Thermal Conductivity

While the CPPs outlined by Huang et al. are limited to physical parameters, some literature suggests that slicing algorithms play a significant role in the overall quality of the printed object (48,49). Slicing is the process by which the computer-generated 3D model is translated into movement instructions for the printer motors. It should be noted, however, that the classification is described from the perspective of FDM as an engineering tool, and does not account for special requirements that are undoubtedly necessary for robust pharmaceutical adaptations. When characterising the FDM printed objects, the non-pharmaceutical literature is largely concerned with the surface roughness and tensile strength of the fabricated objects (40,50–53). In pharmaceutical applications, where the FDM printed objects are intended to be used as solid dosage forms, achieving precise and highly reproducible dimensions and weight is critical. Thusly, the CPPs for P3P may be outlined as shown in Figure 1-7.

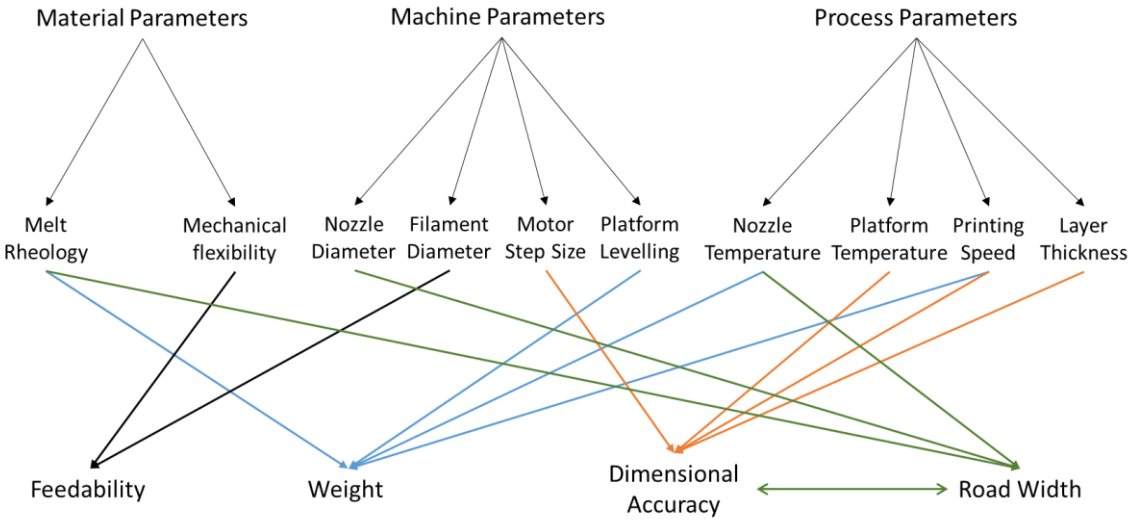

Figure 1-7: Summary of the interactions between the materials properties and the machine and process parameters in an FDM 3D printing process.

To date, FDM has been constrained to being explored only by repurposing commercial, hobbyist application 3D (16,18,26,43,44,54–57). Such commercial application printers do not allow the user to control some of the machine parameters described prior; parameters such as nozzle diameter, filament diameter, roller speed, feeding rate, flow rate, road width, head speed, infill pattern, and part orientation are pre-installed into the hardware and/or firmware of the printer, preventing the user from controlling said parameters freely, and at best offering the user the choice between a number of pre-programmed presets relating to the aforementioned parameters (39).

The main disadvantage of FDM lies in the fact that it is liable to induce thermal degradation of the pharmaceutical product due to the process requiring elevated processing temperatures. However, it is worth noting that thermal processing techniques like HME have been extensively used in the context of pharmaceutical manufacturing, and the relevant literature contains a wealth of information regarding the mitigation against the risks of thermal degradation (58–61). Furthermore, simple methods like Thermogravimetric Analysis (TGA) are capable of providing detailed information about the thermal stability of APIs and excipients being processed, and can be used to gain an understanding of the degradation temperature and residence time that a drug/excipient may be exposed before becoming liable to thermally decompose (62,63).

In the present work, FDM was used in conjunction with HME to fabricate drug-loaded filaments for 3DP.

1.2.6. 3D printing terminology:

As previously mentioned, 3DP is an umbrella term describing the mechanism by which the objects are fabricated. In the object-oriented engineering applications for which 3DP was conceived, this may be appropriate as the technology is used to produce parts that provide mechanical and geometrical functionality, regardless of the materials from which they are constructed (51,52,64), with some manufacturers offering the different variants of 3DP as alternative means to produce the same object (65). In the material-centric pharmaceutical applications, this equivalency is not applicable. The use of different materials to fabricate the same geometrical object will yield dosage forms that perform differently and are specialised to particular applications depending on the formulation constituents (i.e. different polymers produce different, pH-dependent drug release profiles (66)). For example, PBP utilizes powders and binder solutions, making it almost identical in formulation constituents to traditional tabletting techniques, and unrelated (from a materials perspective) to the continuous polymeric matrices used in FDM. Due to those differences, it is in the view of this writing that grouping all the different types of AM techniques under the umbrella term of "3DP" may lead to some ambiguity. FDM is therefore regarded as the orphan 3DP technique in this writing.

1.3. Phases of the solid state: crystalline and amorphous solids, and amorphous solid dispersions

FDM, as previously mentioned, necessarily requires a polymeric matrix to be the primary formative material for the fabricated object (13,43,54,64,67). When preparing filaments for FDM, formulating the filament as an ASD, in which the drug is dispersed in the polymeric matrix, is often desirable to create sufficiently bioavailable dosage forms. The upcoming sections discuss some of the underlying theory regarding ASDs and their ability to increase the bioavailability of poorly soluble drugs.

The use of polymeric matrices as vehicles for drug delivery applications is a well-established method for improving the bioavailability of poorly water-soluble drugs (38,54,59,60,63,68–80). This is often achieved by molecularly dispersing the API to be formulated within the matrix of the chosen carrier polymer to form an amorphous solid dispersion (2,59,81,82).

1.3.1. Crystalline versus amorphous: short, and long-range molecular order and its impact on dissolution properties:

Solid materials exist as either crystalline, semi-crystalline, or completely amorphous materials. The terms “crystalline” and “amorphous” are two terms used to describe the organisation of the packing of molecules within the solid lattice. The main difference between the two lies in their molecular packing; crystalline solids tend to have precisely packed molecules based on a regularly shaped repeating unit, forming a continuous, long-range order of molecules, while amorphous solids generally have short-range, discontinuous domains (Figure 1-8), with no regularly repeating patterns (38,83). Furthermore, crystalline materials are known to exhibit polymorphism (83–86), a phenomenon that arises when molecules of the same material can arrange themselves in different arrangements (Figure 1-9), yielding chemically identical, yet physically distinguishable crystalline forms. The existence of what is known as “polyamorphous” solids is a debated idea (38). However, the pharmaceutical relevance of polyamorphous phases is yet to be described (38)

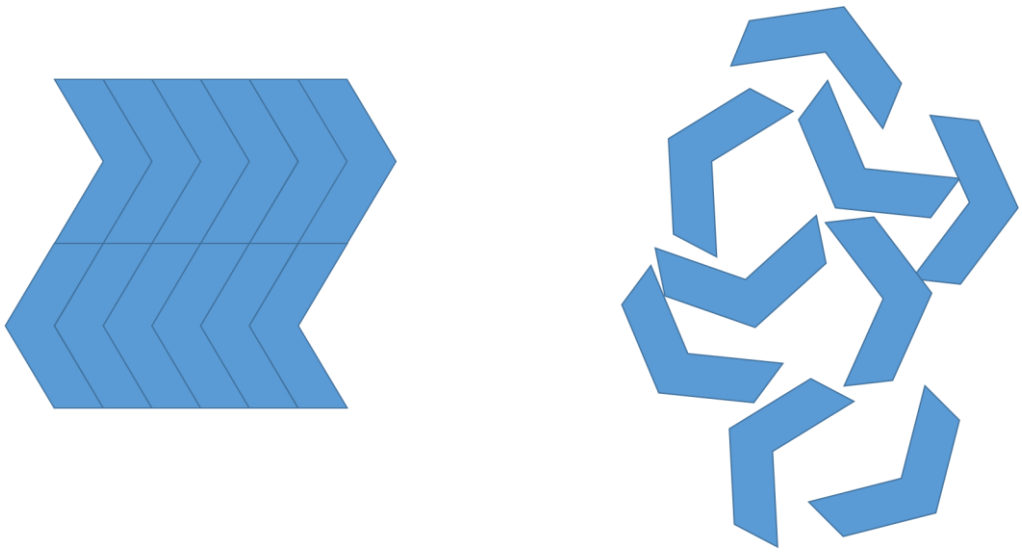

Figure 1-8: A representation of the molecular packing of an amorphous solid structure (right) vs. a crystalline solid structure (left).

The physical phenomenon of melting, otherwise known as fusion, is the endothermic destruction of the crystal lattice of a solid, resulting in the thermodynamic event that is the phase transition from solid to liquid. The melting temperature (T_m) of a crystal is a defining physical characteristic of that particular crystal (83,87). Amorphous materials, on the other hand, do not exhibit melting in the strict definition; on exposure to heat, amorphous materials will exhibit either an increase or a decrease in heat capacity (relative to the direction of the heat gradient) once the applied temperature crosses the threshold of the glass transition (T_g). This transition is a kinetic event that may be shifted or even bypassed by varying the rate of change in the heating gradient (38,88).

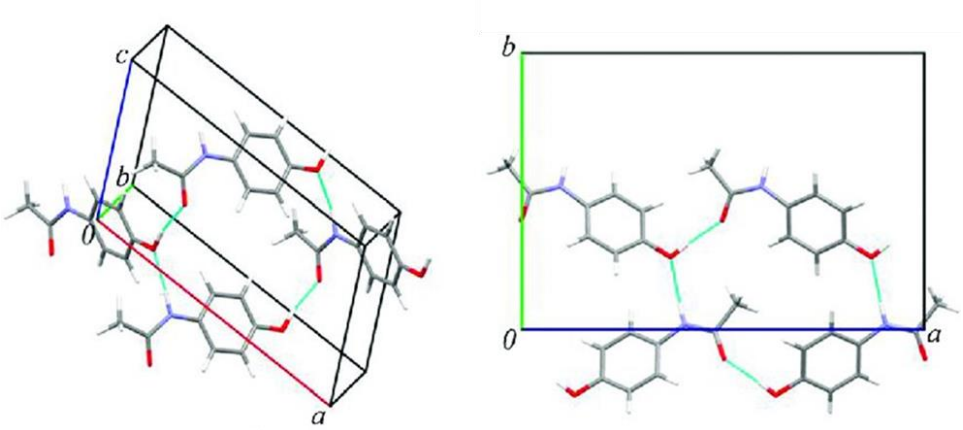

Figure 1-9: Polymorphs of paracetamol. Left: monoclinic (Form I) form. Right: Orthorhombic (Form II) form. (89)

Amorphous solids are particularly of interest in the pharmaceutical industry due to their ability to enhance the dissolution of poorly water-soluble drugs (80). It has been postulated that receptor affinity (and by extension, the efficacy) of pharmacologically active molecules is directly correlated with their capacity to exhibit lipophilic interactions with the target receptors (3), which could be the reason why most drugs fall into class II in the biopharmaceutical classification system (BCS) (Figure 1-10) (1). Enhancing the aqueous solubility of BCS class II drugs is often regarded as the deterministic factor in their successful formulation (90).

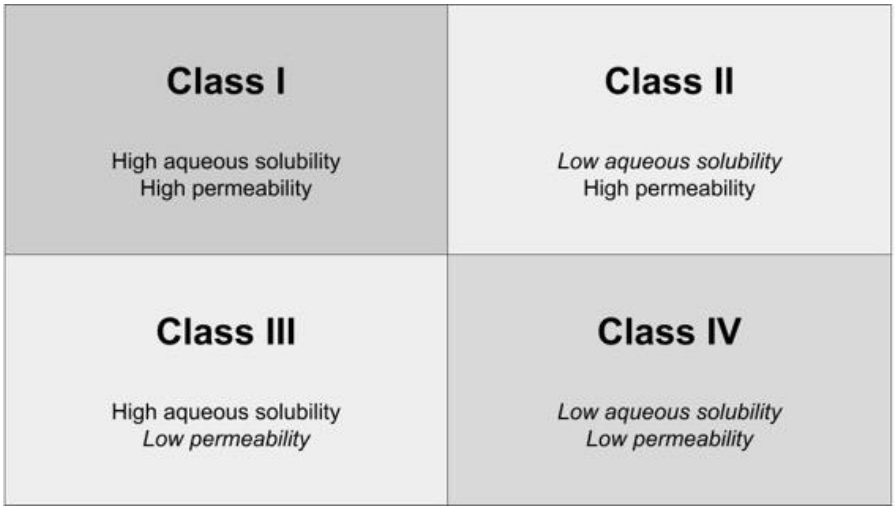

Figure 1-10: Biopharmaceutical classification system classes. Figure recreated from Wu & Benet (3).

The preparation of amorphous solids is generally carried out by suddenly and very rapidly forcing the material into the solid state, which does not allow enough time for the molecules to arrange themselves and establish the more thermodynamically stable long-range ordered domains, resulting in solid whose molecules are arranged in discontinuous, short-range domains possessing higher free energy than its crystalline counterpart (38,91,92). Systems possessing higher free energy spontaneously tend towards relaxation, whether by recrystallisation or via dissolution. A common metaphor for amorphous solids is the compressed spring; a compressed spring has a large amount of stored potential energy that, once the opportunity allows for the spring to relax, it will spontaneously jump back into the uncompressed state. Similarly, when provided with the opportunity to escape the strained, thermodynamically unstable amorphous conformation (i.e. when placed in an aqueous medium, allowing it to dissolve), an amorphous solid will spontaneously jump to the more thermodynamically favourable dissolved state (56). In

lay terms, a molecule would prefer "escaping" to the dissolved state than remaining in the high-strain amorphous state.

This phenomenon may be more formally described by the change in Solution Free Energy (ΔG_s) equation:

$$\Delta G_s = G_P + G_C + G_{Sol} \qquad \textit{(Equation 1-1)}$$

where G_P is the Packing Free Energy; the net free energy on the disruption of the packing of the lattice of the solute to liberate a single molecule. G_C is the Captivation Free Energy, the net free energy change when solvent molecules expand to create a cavity which can accommodate the liberated solute molecule, and G_{Sol} is the Solvation Free Energy; the net free energy change due to the spontaneous formation of solvent-solute interactions. For dissolution to occur, $\Delta G_s < 0$. Which implies that the $G_{Sol} < (G_P + G_C)$. In other words, dissolution is thermodynamically favoured when the energy released due to the formation of solvent-solute interactions (G_{Sol}) is larger than the energy consumed disrupting the solvent (change in G_S) and solute (change in G_P) molecules to accommodate dissolution.

Since crystalline solids are, by definition, highly stable conformations due to the organised packing of molecules within the crystal lattice, their G_P often tends to be much larger than the net sum of G_C and G_{Sol}. Making dissolution less thermodynamically favoured than maintaining the stable conformation of the crystalline phase. On the other hand, amorphous conformations are thermodynamically unstable, and therefore highly strained structures (38) and possess more stored potential energy, and thus have a lower G_P figure and are less thermodynamically stable. Due to their decreased thermodynamic stability, amorphous solids spontaneously favour the dissolved state over their strained amorphous conformation.

The main challenge in the formulation of amorphous solids lies in their physical instability; they are very likely to recrystallise throughout the shelf life of the drug due to the formation of nuclei which serve as the basis for the formation of crystals (83). However, incorporation of amorphous solids into polymeric matrices to form solid dispersions has been demonstrated to inhibit nucleation and improve the physical stability of amorphous solids (2,72,93).

1.3.2. Solid Dispersions:

In its simplest definition, a solid dispersion is a binary system in which one material is molecularly dispersed within the matrix of another (1,59,92). Systems consisting of a drug (regardless of solid state) with a matrix consisting of either a sugar, emulsifier, small molecule, or a polymer (regardless of whether a glass or an eutectic mixture was formed) have all been traditionally described as solid dispersions (92,94). In recent years, the convention in the pharmaceutical literature has become to use the term *solid dispersion* to describe a system in which an API is molecularly dispersed within the matrix of a polymer (59,74,92). Such systems are also often dubbed *solid solutions* (69), this term is likely arising from the common solute/solvent metaphor used to describe the dispersed API and the polymeric matrix respectively. This metaphor extends past terminology, as the use of theoretical solubility models has been reported as a method to approximate drug-polymer compatibility (70,78,95,96).

As previously discussed, the rationale behind formulating a pharmaceutical product as a solid dispersion stems from the need to enhance its oral bioavailability by increasing the apparent aqueous solubility of the drug (1,59). For solid dispersions to successfully improve the bioavailability of BCS-Class II drugs, the drug should remain molecularly dispersed and not crystallise out of the polymeric matrix throughout the entire shelf-life of the dosage form (1,70,97). Those stability requirements require that the drug be miscible with the polymer during production, and must remain thermodynamically stable (or possibly kinetically stable, if the rate of the recrystallisation process is sufficiently slow) throughout the shelf-life of the product (38,71,74,97–103).

Miscibility of two components in a thermodynamically closed system, when expressed as a function of the net energy change induced by their interactions during mixing, can be expressed in terms of the change in the Gibbs Free Energy of the system (96,104,105):

$$\Delta G_{mix} = \Delta H_{mix} - T * \Delta S_{mix} \qquad \textit{(Equation 1-2)}$$

Where ΔG_{mix} is the change Gibbs Free Energy of the system, while ΔH_{mix} and ΔS_{mix} are the change in enthalpy of mixing (net energy liberated or absorbed during mixing) and change in entropy (disorder) at temperature T, respectively. Two components are said to be miscible if ΔG_{mix} is negative ($\Delta H_{mix} < T\Delta S_{mix}$). In other words, miscibility is favoured

at temperature T when the degree of disorder of the system is greater than the net energy change brought about by mixing the two components of the system.

The present worked used HME to prepare ASDs of paracetamol dispersed in HPMCAS (Chapter 3, Chapter 5), and three different formulations of acetylsalicylic acid dispersed in PCL (Chapter 4). HME is a commonly used method for preparing ASDs (72,93,103,106,107). During the HME process, the drug and polymer are heated to the molten state. At that elevated temperature, the drug becomes more readily miscible with the polymer. The increased polymer chain mobility and the elevated temperature increase the degree of disorder in the system ($T\Delta S_{mix}$), if the increase in the entropy of mixing is sufficient to exceed ΔH_{mix}, the drug and polymer become miscible inside the extruder, forming a homogenous melt.

Once retrieved and allowed to cool back to a solid, the drug-polymer mixture must remain sufficiently stable and homogenous. Instability of solid dispersions manifests as recrystallisation of the drug, causing it to phase-separate from the matrix, and is attributed to inadequate drug-polymer interactions (81,92,99). A number of theoretical methods for predicting drug-polymer miscibility exist (78). Experimentally, observing the formation of drug-polymer interactions can be done by detecting the formation of hydrogen bonds or dipole-dipole interactions between the polymer and drug (69–71,77,101,108–112). One may consider this practical approach an extension of Hansen's theory of solubility, what is known as the "like dissolves like" principle; the principle that a solvent may dissolve a solute if the solvent-solute molecules interact in a manner similar to how the molecules of each interact with themselves. ASDs that remain stable in the absence of any distinct drug-polymer interactions are said to be kinetically stable (78,113,114).

In the present work, the paracetamol ASDs were found to be stable, as no crystals of paracetamol were observed in the finished formulation. However, two of the acetylsalicylic acid formulations were found to be unstable, with phase separate drug crystals being detectable in both formulations. When characterised by infrared spectroscopy, the paracetamol-HPMCAS ASD was observed to be kinetically stable, as no distinct HPMCAS-paracetamol interactions were observed (Section 3.3.1.). Of the three acetylsalicylic acid formulations, the formation of hydrogen bonds was observed between the drug and the polymer only in the one formulation found to maintain a stable ASD.

1.4. Aims and objectives

As previously discussed in section 1.2.5., the CPPs governing P3P are still not very well understood. Furthermore, the absence of regulation means that there is no agreed upon standard 3D printer. Variations between different brands of 3D printers will inadvertently introduce brand-specific oddities, making consistent reproduction of 3D printed dosage forms more challenging, thus adding another barrier towards commercialization.

Despite this lack of standardization, Hsiao et al. noted that the Makerbot® Replicator 3D Printer has "*spearheaded"* the P3P movement (56). Observing the convention in the literature, it indeed appears as though the Makerbot® Replicator 2 has become a de facto standard of P3P (16,18,26,43,44,54,55,57). A particular brand being conventionally popular for P3P applications does not automatically indicate its suitability for such applications; the Makerbot® Replicator 2 was not designed to be a Good Manufacturing Practices (GMP) compliant machine. However, its popularity among pharmaceutical scientists means that it can serve as a metaphorical "yardstick", by which we can investigate the capabilities and limitations of P3P, and possibly describe some of the design requirements of a GMP-compliant 3D printer by observing the shortcomings of the current "de facto standard" printer.

The work presented herein attempted to serve as an investigation of the capabilities and limitations of the current form of P3P via a systematic investigation of some of the accessible CPPs outlined in Figure 1-7. The parameters investigated were:

- Mechanical properties of filaments and their impact on the feedability of a filament.
- Process parameters (printing speed and printing temperature) and their impact on the weight and dimensions of the 3D printed objects, and the reproducibility of printing at different process conditions.
- The impact of infill density on the drug release rate from a 3D printed dosage form.

Chapter 2
Materials and Methods

2.1. Materials

2.1.1. Acrylonitrile Butadiene Styrene and High-Impact Polystyrene:

Acrylonitrile Butadiene Styrene (ABS) and High-Impact Polystyrene (HIPS) are amorphous, thermoplastic polymers (115) that are synthesised via the incorporation of butadiene rubbers into either styrene-acrylonitrile (in the case of ABS) or polystyrene (in the case of HIPS) (116,117). ABS and HIPS possess various attractive properties which makes them a staple of the plastic industry; both polymers are readily mouldable, possesses high chemical resistance, and high impact strength (12, 13, 14). ABS and HIPS are commonly used in various manufacturing industries including toys, automotive, protective gear, electronics, and piping (116–118). In recent years, the two polymers have been used to produce filaments for FDM 3DP. ABS is regarded as the "de facto standard" FDM printing filament (14), with various 3D printer manufacturers offering ABS filaments as the standard filament for FDM printing. HIPS is commonly used in FDM as a support material due to its ability to be selectively dissolved by limonene without affecting the ABS (119).

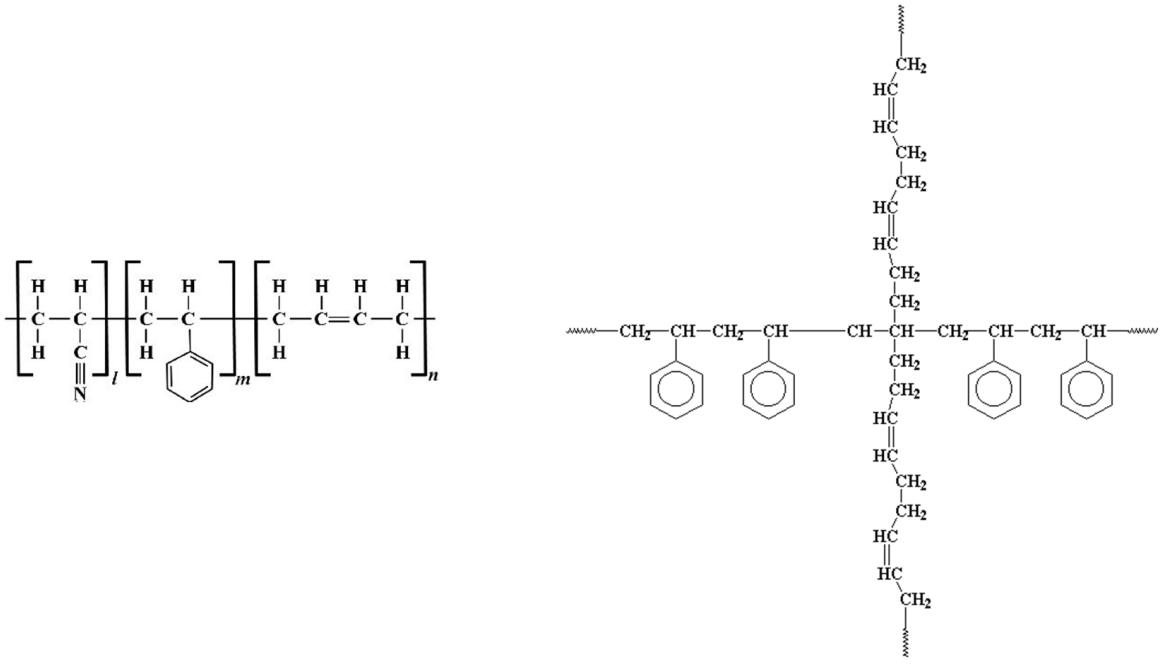

Figure 2-1: Chemical structure of ABS (left) and HIPS (right). Figures retrieved from Okada et al. (120) *and Polymer Science Learning Center* (121) *respectively.*

ABS and HIPS were used in this work as reference materials for mechanical properties after which in-house made filaments were modelled. ABS was also used as a purge material to clean the 3D printer nozzle. ABS, and HIPS (MakerBot® Dissolvable Filament) used in this study was purchased as pre-extruded filaments from MakerBot®

Industries (Makerbot Industries LLC., New York, United States). Both materials were of an undeclared grade.

2.1.2. Polyvinyl alcohol:

Polyvinyl alcohol (PVA) is a synthetic, semi-crystalline, water-soluble polymer. PVA is available in different grades, from partially hydrolysed to completely hydrolysed grade. With a T_m ranging between 180 °C – 228 °C depending on the degree of hydrolysis (63,122,123). PVA is commonly used to manufacture resins, lacquers, and textiles. It is also commonly used as a pharmaceutical coating material, a matrix former for the fabrication of solid dispersions, and as a food additive (54,63,74,76). PVA is also widely available in the form of commercial filaments for 3DP applications. Being one of very few pharmaceutically-relevant, 3DP-suitable polymers, commercially available filaments of PVA are very commonly used for P3P, with the drug being loaded either by impregnation or by re-extruding the pelletized filament with the drug (16,18,26,43,54,109,121–125).

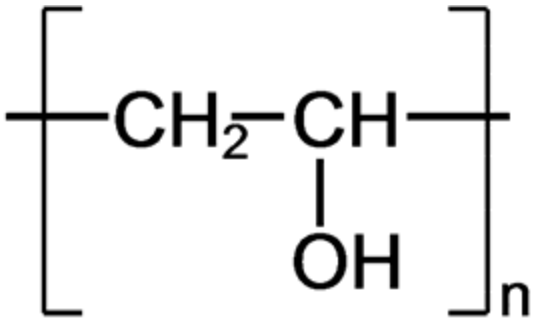

Figure 2-2: Chemical structure of a PVA monomer. Figure recreated from The Handbook of Pharmaceutical Excipients (123)

PVA used in this work was purchased as either pre-extruded commercial filaments from XYZprinting.com (XYZprinting Inc., California, United States) or as Mowiflex® C-17 pellets, which are melt-extrudable pellets that yield filaments possessing suitable mechanical properties for 3DP (129). Mowiflex® pellets are pre-formulated pellets containing PVA and an undeclared plasticiser. Mowiflex® pellets used in this study were obtained as gratis from Kurary (Kurary GmbH, Frankfurt, Germany.

2.1.3. Polycaprolactone:

Polycaprolactone (PCL) is a semi-crystalline, hydrophobic, and biocompatible polyester. The T_m of PCL is ~60 °C, and its T_g is -65 °C (Figure 4-3).

PCL is commonly used in parenteral formulations (123), and for fabricating implantable biomaterials and scaffolds (25,130,131). In recent years, PCL has also found use as a filament for 3DP applications (132).

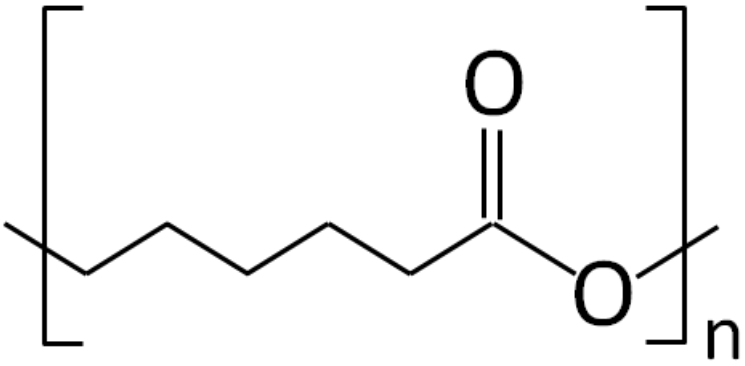

Figure 2-3: Structure of a PCL monomer. Figure retrieved from Deshmukh et al. (133)

Two variants of PCL were used in this work; PCL commercial filaments were purchased from MakerBot® Industries (Makerbot Industries LLC., New York, United States). PCL pure powder (CAPA™, Lot #: 130115) was purchased from Perstorp Chemicals (Perstorp Chemicals GmbH, Arnsberg, Germany).

2.1.4. Polyethylene Glycol/Polyethylene Oxide:

Polyethylene glycol (PEG), or polyethylene oxide (PEO) are two terms used to refer to the synthetic, semi-crystalline polyether of ethylene oxide (134). While the terms PEG and PEO describe a polymer comprising of the same repeating ethylene oxide subunit, they cannot be used interchangeably; the term PEG is used to refer to poly-[ethylene oxide] polymers whose molecular weight does not exceed 100,000, with the term PEO being reserved for poly-[ethylene oxide] polymers whose molecular weight exceeds 100,000 (135). PEO and PEG typically possess a T_m of 60 °C (Figure 3-4) and a T_g of -55 °C (43,63).

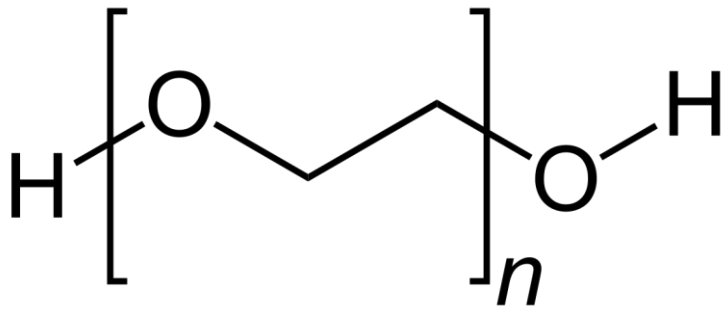

Figure 2-4: Chemical structure of a PEG/PEO monomer. Figure obtained from the Handbook of Pharmaceutical Excipients (123)

PEG/PEO is very widely used in the pharmaceutical industry in topical, injectable, and oral dosage forms (123), and as a plasticiser for HME (19). Grades of PEG possessing a molecular weight between 3350 and 6000 are used clinically as a laxative, in which case they are commonly referred to by the international non-proprietary name (INN) macrogol (136). PEO grades of the polyether have been used to produce filaments for 3DP (54), making it one of the few pharmaceutically relevant polymers which are suitable for 3DP. PEG (molecular weight: 4000. Lot #: BCBP6905V) was obtained from Sigma Aldrich, (Sigma Aldrich, Salisbury, United Kingdom) and was used as a plasticiser for preparing filaments by HME. PEO (molecular weight: 100,000. Lot #: DT367148) used in this study was obtained as gratis from Colorcon (Colorcon Ltd., Dartford, United Kingdom) and was used both as a plasticiser for HME, and to create a reference filament for the mechanical properties screening.

2.1.5. Polysorbate 80:

Polysorbate (Tween) 80 is a fatty acid ester of a sorbitol-ethylene oxide copolymer. Tween 80 is a hydrophilic, non-ionic surfactant and is commonly used as an emulsifier, and as a solubilising agent in topical, oral, and parenteral pharmaceutical preparations (123). Tween 80 has also been used as a plasticiser in HME (43,137). Tween 80 used in this study was purchased from Acros Organics (Acros Organics, Geel, Belgium. Lot #: BCBQ4189V).

2.1.6. Hypromellose acetate succinate:

Hypromellose acetate succinate (HPMCAS) is an amorphous, semi-synthetic cellulose derivative. The T_g of HPMCAS is 120 °C (Figure 3-4), depending on the grade. Its solubility is pH-dependant, with the three available grades all dissolving above pH 5.5 (138).

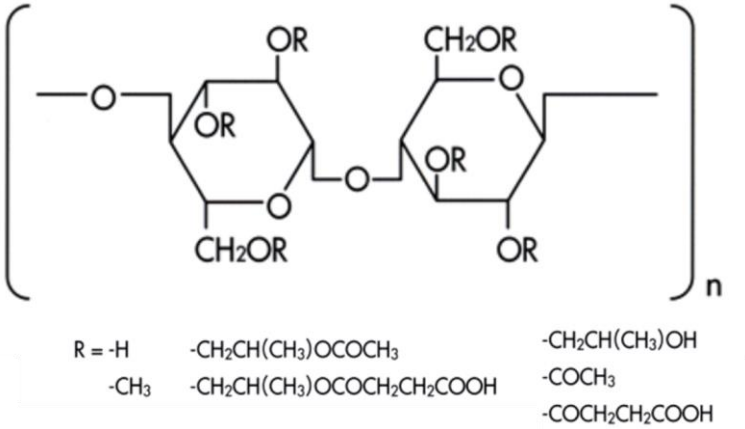

Figure 2-5: Chemical structure of HPMCAS. Figure adapted from Shin Etsu (138).

Due to its film forming properties and its pH-dependant solubility, HPMCAS was traditionally used as an enteric coating material to infer either pH-dependant or sustained release properties onto a tablet. HPMCAS since been employed in the manufacture of solid dispersions, both by HME and by spray drying (1,69,77,82,92,111).

HPMCAS (Low-Fine grade: LF. Lot #: 60410001) used in this work was obtained as gratis from Shin Etsu (Shin Etsu Inc., Tokyo, Japan).

2.1.7. Eudragit® EPO:

Eudragit EPO is an amorphous, synthetic polymethacrylate copolymer that is commonly used as a film coating material in the pharmaceutical industry. It has a T_g of 45 °C (Figure 3-3) (43,112). Eudragit EPO is soluble below pH 5 and swells to form a permeable matrix above pH 5 (123,139). Eudragit EPO has also been used to prepare nanoparticles (140), and as a matrix former in the formulation of solid dispersions (32,43,79,103,112).

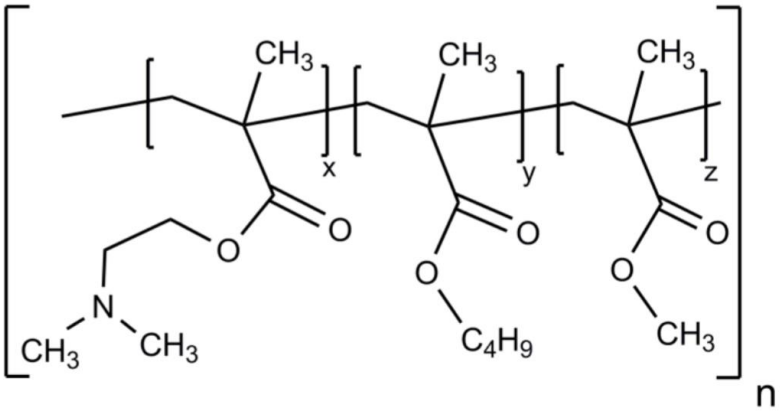

Figure 2-6: Chemical structure of Eudragit EPO. Figure obtained from Evonik Industries (139).

Eudragit EPO used in this work was obtained as gratis from Evonik Industries (Evonik, Darmstadt, Germany. Lot #: G170331544).

2.1.8. Soluplus®:

Soluplus is a polyethylene-glycol–polyvinyl caprolactam–polyvinyl acetate graft copolymer that was purposely designed by BASF® for HME applications (141). It is a self-plasticised amphiphilic polymer possessing a relatively low T_g of $\approx$70 ^{o}C (Figure 3-3), making it ideal for HME applications (95), and is commonly used to prepare solid dispersions by HME (1,43,63,69,70,74,77,99).

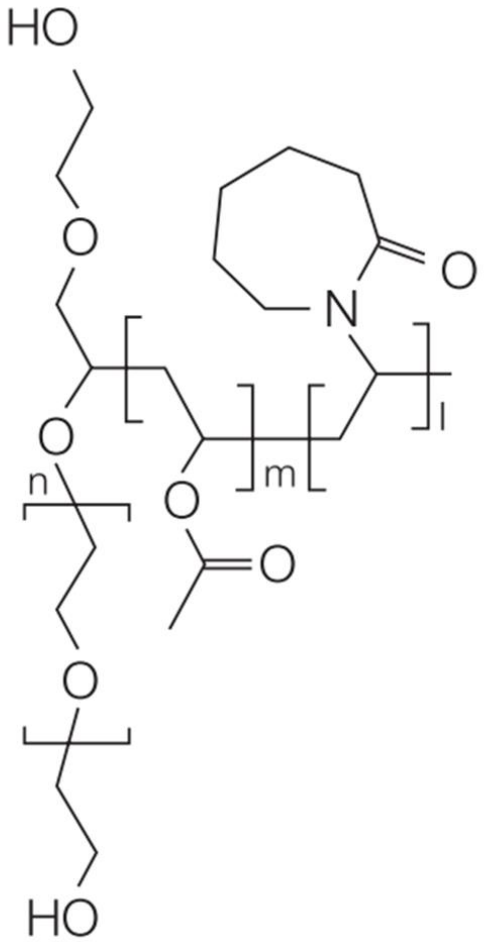

Figure 2-7: Chemical structure of Soluplus. Figure obtained from BASF Inc (141).

Soluplus used in this study was obtained as gratis from BASF® (BASF inc., Ludwigshafen, Germany. Lot #: 84414368E0).

2.1.9. Copovidone®:

Copovidone, also known as polyvinylpyrrolidone-vinyl acetate (PVPVA), is an amorphous, synthetic copolymer that is commonly used in the pharmaceutical industry. It has a T_g of $\approx$110 ^{o}C (111). Copovidone is commonly used as a binder for wet granulation, and as a coating material for controlled release tablet coating (123). It has also found use as a matrix former in the formulation of amorphous solid dispersions (1,59,73,92,97). Copovidone (grade 64) used in this study was obtained as gratis from BASF® (BASF inc., Ludwigshafen, Germany. Lot #: 23408975L0).

2.1.10. Hydroxypropyl cellulose:

Hydroxypropyl cellulose (HPC) is a semi-synthetic, poly(hydroxypropyl) ether of cellulose. HPC is commonly used in the pharmaceutical industry as a coating material,

tablet binder, viscosity-adjusting agent, and as a matrix former in the formulation of amorphous solid dispersions. HPC also use in 3DP due to its mechanically suitable properties for printing (44,54,123,142).

HPC used in this work was Klucel® EF grade and was obtained as gratis from Ashland (Ashland Industries Europe GmbH, Schaffhausen, Switzerland. Lot #: 53013).

2.1.11. Paracetamol:

Paracetamol (also known as acetaminophen), is an active pharmaceutical ingredient (API) that is commonly used as an analgesic and antipyretic (143). It is polymorphic, with the stable form (monoclinic form) having a melting point of 169 °C (144). It is very slightly soluble in cold water (1 to 5 mg/mL at 22 °C) but soluble in hot water (145).

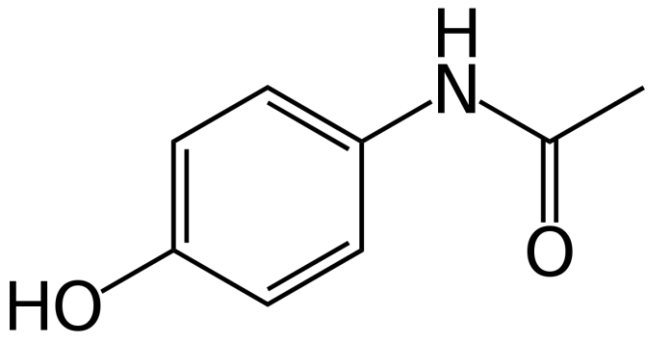

Figure 2-8: Chemical Structure of paracetamol. Figure adapted from Ivanova (146)

Pharmaceutical grade paracetamol (>99.0% pure) was used in this study was purchased from Sigma Aldrich (Sigma Aldrich Ltd., Dorset, United Kingdom. Lot #: SLBC6391V) and was used as a model drug.

2.1.12. Acetylsalicylic acid:

Acetylsalicylic acid (also known as aspirin) is an API that is commonly used as an analgesic, antipyretic, anti-inflammatory, and antiplatelet (147,148). Acetylsalicylic acid is polymorphic (149) with the stable form possessing a melting point of 135 °C. Aspirin is very slightly soluble in water (less than 1 mg/mL at 22 °C) (150).

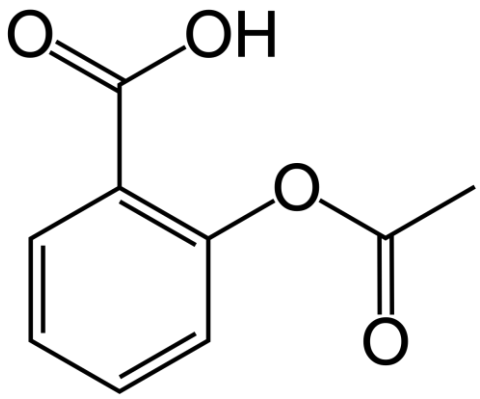

Figure 2-9: Chemical structure of acetylsalicylic acid. Figure recreated from Varughese et al. (149)

Pharmaceutical grade aspirin (>99.0% pure) used in this study was purchased from Sigma Aldrich (Sigma Aldrich Ltd., Dorset, United Kingdom. Lot #:081M0194V) and was used as a model drug.

2.1.13. Sodium bicarbonate:

Sodium bicarbonate ($NaHCO_3$) is a commonly used excipient pharmaceutical formulations. Under acidic conditions, $NaHCO_3$ reacts vigorously with water, producing carbon dioxide. Due to its vigorous reaction with water in which carbon dioxide is evolved (123), $NaHCO_3$ is used as a disintegrant in effervescent pharmaceutical formulations.

2.2. Methods

2.2.1. Hot-Melt Extrusion:

Hot-Melt Extrusion (HME) is a process by which materials (in the molten state) are forced through a barrel by the action of conveyer screws into a die cavity to obtain a final product comprising a matrix of uniform shape and density. During the process, a polymer and the API are fed into the extruder by a gravimetric hopper, the materials are then received by two, co-rotating screws which serve to convey the materials into the various regions within the extruder. They are first carried into the melting zone where they are melted by the action of the heat conduction of the barrel and the mechanical shear from the screws, the molten materials are then carried by the screws to the mixing region where mixing elements homogenise the molten drug and polymer together to create a uniform dispersion, the mixture is then pumped through a die where the melt is cooled and collected for further processing (103,151).

The technique was originally pioneered for the plastic industry, but it has been ported into the pharmaceutical industry, having demonstrated its robustness as a technique to manufacture solid dispersions (1,2,82), and more recently as a method to prepare drug-loaded filaments for FDM (43,44,54).

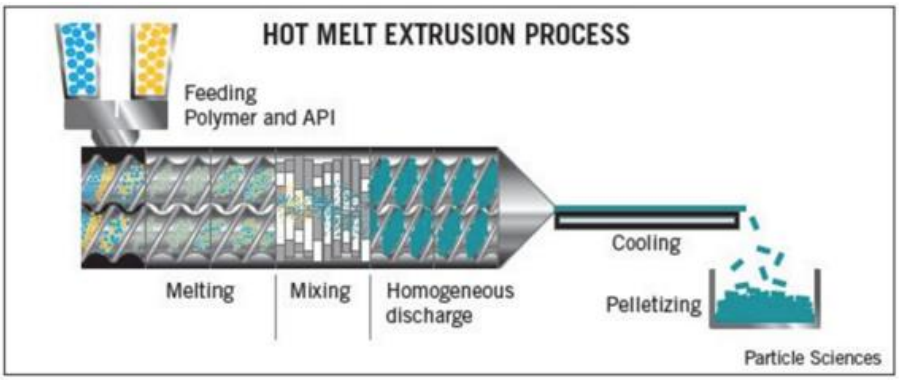

Figure 2-10: Basic anatomy of a hot melt extruder, Figure obtained from Particle Sciences (106).

It should be noted that depending on certain parameters (such as temperature, screw configuration, and the physicochemical properties of the processed materials) during the extrusion process, the produced extrudates can be in a range of different physical states, from amorphous to semi-crystalline and crystalline. However, the greatest utilization of HME has been for the fabrication of amorphous solid dispersions. In the manufacture of

ASDs, HME offers several advantages over other commonly used methods; other methods used to prepare ASDs like spray drying, and freeze drying mandate that both the drug and polymer be soluble in a common solvent (2,38,75). HME, on the other hand, is an ambient process, requiring no solvent use, which makes HME a more robust process that allows for greater flexibility in making solid dispersions as it cuts down on the time needed to identify and prepare a solvent (or solvent mixture) and prepare the drug/polymer solution (59,125,151,152). Furthermore, HME is a continuous manufacturing process, which makes it a more readily scalable process than both spray drying and freeze drying, which allows for easier incorporation of online Process Analytical Technologies into the production pipeline (60,77,153).

All formulations produced in this study were produced using a Haake Minilab II benchtop melt extruder (Thermo Fisher Scientific, Karlsruhe, Germany) equipped with a 1.75mm circular die.

2.2.2. Material Characterisation Methods:

2.2.2.1. Differential Scanning Calorimetry

Differential Scanning Calorimetry (DSC) is a thermal materials characterisation technique. DSC is regarded as a quintessential thermal characterisation technique in the pharmaceutical industry, due to its ability to provide highly detailed information about the physicothermal properties of a material whilst consuming minute amounts of material (up to a few milligrams) per scan (113).

Two variants of DSC exist, heat flux DSC, and power-compensated DSC. In heat-flux DSC, two pans (one containing the sample to be tested and the other a blank reference pan) are placed in the same furnace. The furnace is heated as per the user-submitted heating sequence. The temperature difference between the sample pan and the reference pan is measured and converted to energy. In power compensated DSC, the two pans (sample and reference) are placed in separate furnaces, with the machine measuring the energy required to maintain the two pans at the same temperature (154). This study used a heat flux DSC exclusively.

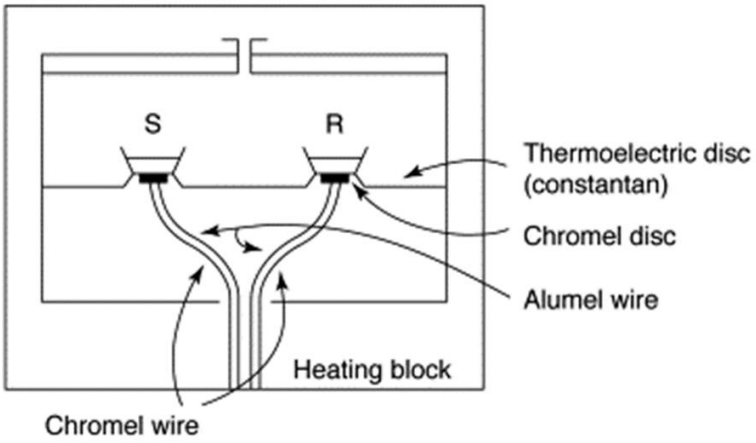

Figure 2-11: A graphical representation of a heat flux DSC. S: sample pan, R: reference pan. Figure adapted from Clas et al. (113)

DSC is used to detect changes in material properties with respect to temperature change. Thermal transitions visible by DSC include melting (fusion), recrystallisation, solvent evaporation, β-transitions, glass relaxations, and glass transitions (63,113,154).

As previously discussed in section 1.3.1., observing the nature of thermal transitions is a common method to distinguish between crystalline and amorphous solids. Crystalline solids exhibit sharp and precise melting points (T_m), amorphous solids, however, do not melt on heating, but rather exhibit an increase in their molecular mobility after crossing a particular temperature threshold called the glass transition temperature (T_g). This characteristic difference between the thermal behaviours of the two solid phases allows for them to be easily distinguished via DSC. Furthermore, since the general goal of formulating pharmaceutical substances into solid dispersions is to remove the crystallinity of the drug substance, DSC is very commonly used in characterising solid dispersions; the presence of peaks corresponding to the melting of the drug indicates failure to formulate a stable solid dispersion, while the absence of a peak corresponding to the T_m of the drug is indicative of the formation of a solid dispersion (38,69,76–78,82,137,155).

This study used both a Q20 DSC and a 2500 Discovery DSC, both of which were manufactured by TA Instruments (TA Instruments, Newcastle, USA). All pans used in this study were standard aluminium pans (TA Instruments, Newcastle, USA).

2.2.2.2. Thermogravimetric Analysis

Thermogravimetric analysis (TGA) is a thermal characterisation technique. TGA is used to measure changes in the mass of a sample relative to the change in temperature. Temperature-dependent events which result in a change in the mass of the sample such as solvent loss or degradation can be easily observed and quantified using TGA (154).

A TGA machine consists of a hook that is used to gravimetrically suspend the sample pan in an environmentally isolated furnace. Inside the furnace, the sample may be exposed to a temperature ramp, or held isothermally at a set temperature, with the machine recording the change in mass relative to temperature or time (154).

The TGA used in this study was a TA Instruments 5500 Discovery TGA (TA Instruments, Newcastle, USA).

2.2.2.3. Attenuated Total Reflectance – Fourier Transform Infrared Spectroscopy

Infrared spectroscopy is a vibrational spectroscopic technique used to detect vibrations of bonds (i.e. bending or stretching of a bond) within a molecule. The base principle of infrared spectroscopy relies on the fact that if the wavelength of a particular infrared beam (i.e. 5714 nm/1750 cm^{-1}) matches the frequency of a particular oscillation of a bond (i.e. the stretching oscillation of the C=O bond), the infrared beam will be absorbed by that particular bond. Infrared spectroscopy is conventionally used to refer to IR spectroscopy conducted in the mid-infrared region (2500 nm – 25000 nm. Equivalent to 4000 cm^{-1} – 400 cm^{-1}), with modern spectrometers applying a Fourier transform to yield an FTIR spectrum (63,105).

Attenuated total reflectance (ATR) is an infrared sampling technique developed by Fahrenfort (156). ATR-FTIR spectroscopy offers many advantages over conventional, transmittance infrared spectroscopy; ATR-FTIR is quick and requires little to no sample preparation, and does not carry with it the risk of altering the properties of the sample which may happen during milling or pressing the sample as is the case with conventional, transmittance infrared spectroscopy (156).

At the heart of an ATR accessory is a crystal of high reflective index and no infrared absorption (i.e. diamond). The spectrum that is obtained from ATR-FTIR is a result of

measuring the change in an infrared beam that is totally reflected inside the crystal when it comes in contact with the sample, penetrating it not more than a few micrometres (157).

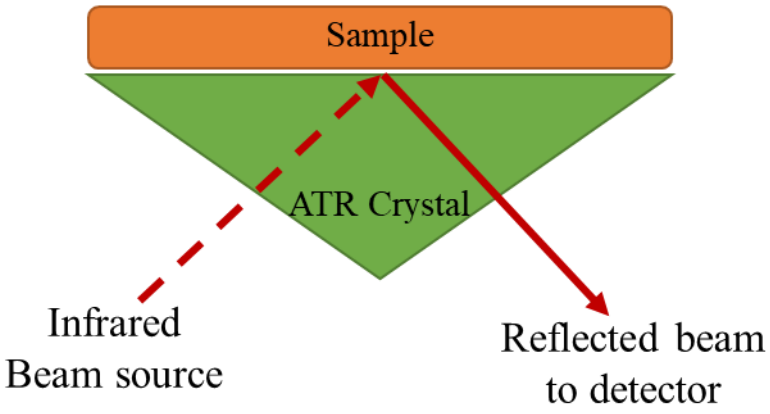

Figure 2-12: schematic representation of total internal reflectance in an ATR crystal. Figure recreated from Lee et al. (158)

ATR-FTIR is commonly used in the pharmaceutical industry as a rapid method for material identification (159), solid state characterisation (84,85), and for determining the mechanism of drug-polymer interactions in solid dispersions (1,19,59,77,160).

ATR-FTIR spectra presented in this work were measured using a Vertex 70 infrared spectrometer (Bruker Optics Ltd., Coventry, United Kingdom), equipped with Golden Gate ATR accessory (Specac Ltd., Orpington, United Kingdom) fitted with a diamond internal reflection element.

2.2.2.4. Powder X-Ray Diffraction

Powder X-Ray Diffraction (PXRD) is a structural characterisation technique. PXRD can be used to deduce information about solid state, polymorphism, crystal orientation, and degree of crystallinity within a sample (161).

The working principle of PXRD relies on the fact that crystalline materials act as diffraction gratings for x-ray beams whose wavelengths match the spacing of the planes within a crystalline lattice. Lawrence Bragg defined the working principle of PXRD when he described the X-Ray scattering phenomenon in what is now known as Bragg's law: supposing a crystalline lattice comprised of parallel planes of a constant parameter *d,* an incident X-Ray beam produces a Bragg peak if its reflections off the various planes interfere constructively (161,162).

PXRD is a particularly powerful tool for determining the solid state of a material (101,163). As previously discussed in section 1.3.1., amorphous materials lack the long-range order that is characteristic of a crystal lattice. Therefore, no Bragg peak is produced when an amorphous material is exposed to PXRD, as the lack of long range order indicates the absence of parallel planes within the lattice, and therefore no constructive interference of the X-Ray (161).

The X-Ray diffraction patterns of crystalline materials are often sharp precise peaks, while amorphous materials typically exhibit broad features often dubbed the "amorphous halo" (Figure 2-13) (82). Deconvolution of the broad features of the amorphous halo is not a simple process and is often needed to determine whether the features observed are due to the presence of an amorphous material or due to micro- or nanocrystalline materials, as PXRD is well-documented to be affected by the granule size of the materials being tested (164).

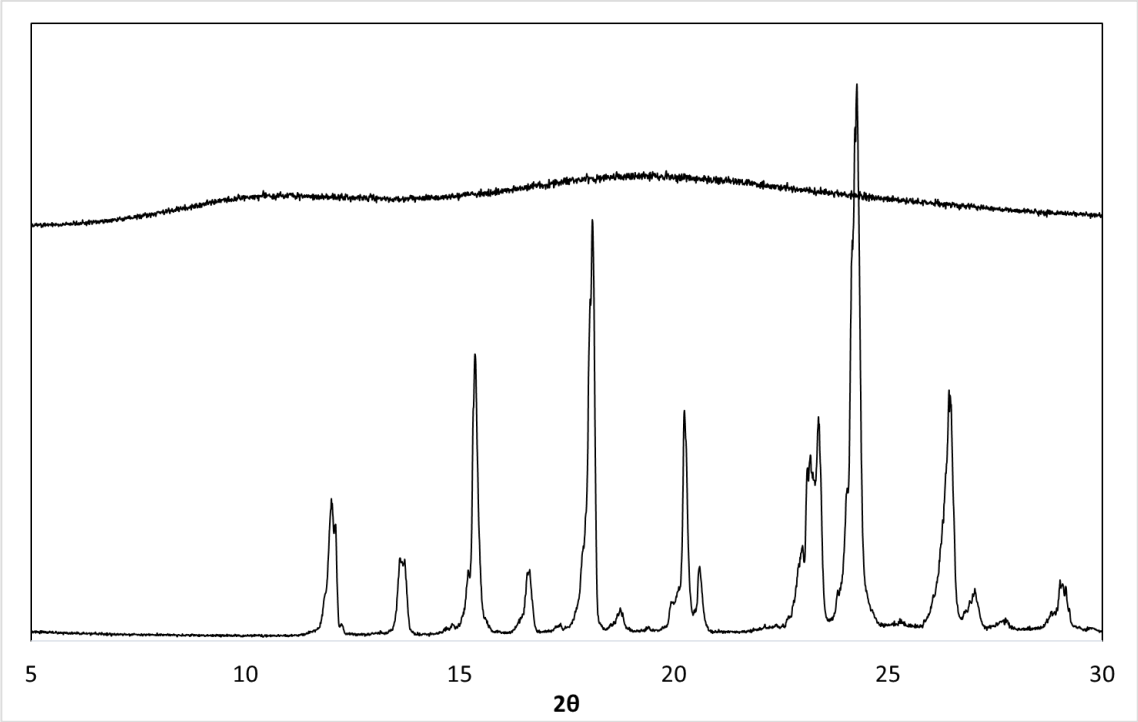

Figure 2-13: A crystalline material (paracetamol form I; bottom) and an amorphous material (HPMCAS; top) as they appear under PXRD

This study used a Thermo ARL Xtra X-ray diffractometer (Thermo Scientific, Switzerland) equipped with a copper X-ray Tube (k = 1.540562 Å) as a solid state characterisation tool. No baseline correction was applied to the diffraction patterns, as the

same machine was used to scan all samples and compare differences in the diffraction patterns.

2.2.2.5. Scanning Electron Microscopy:

Scanning electron microscopy (SEM) is a high-resolution microscopic characterisation technique commonly used to examine surfaces and microstructures of materials. During SEM imaging, an electron beam is used to scan the material. The electron beam is fired from the electron gun, which is then focused and demagnetised by a series of focusing lenses. The beam is then demagnetised and focused onto the sample being investigated (63).

The SEM used in this study was a JSM 5900LV Field Emission Scanning Electron Microscope (Jeol Ltd, Japan) equipped with a tungsten hairpin electron gun.

2.2.3. Texture Analysis:

Texture analysis (TA) is a technique commonly used for studying the mechanical properties of materials (165). The technique is very commonly used in the food industry to extract information about the texture and mechanical properties of food (166–168). The technique has also found use in the pharmaceutical industry, particularly to quantitatively measure the mechanical properties of hard gelatin capsules (169).

A texture analyser consists of a mechanical moving arm that is equipped with a load cell. The arm is used to deform the sample to be tested. The load cell records the force response exerted by the sample as resistance to the deformation. The output result is a curve showing the force (resistance exerted by the sample) against either time, or distance travelled by the mechanical arm. The produced force graph can be used to extract information about brittleness, compressibility, and yield strength (165).

The work presented herein used a Stable Micro Systems TA.XT 2 Plus Texture Analyser (Stable Micro Systems, Godalming, United Kingdom).

The operational parameters for all the methods described in this section are detailed in their respective section in the relevant chapters.

2.2.4. Principal Component Analysis:

Principal Component Analysis (PCA) is a multivariate statistical analysis technique that is commonly used as a method to reduce the dimensionality of multivariate data (158,170). PCA is used to extract the most important information from a data set and project it on a set of new uncorrelated, orthogonal variables called Principal Components (PCs), retaining maximum variability of the data set (171). In a data set consisting of two variables Y_1 and Y_2, the first PC is extracted by plotting Y_1 vs. Y_2, discarding the axes, while retaining the data points relative to each other. The best fit axis maintaining maximum data variance is then calculated, resulting in the first PC. Subsequent PCs are then plotted with each subsequent PC perpendicular to the last, provided that maximum possible data variance is maintained. Finally, the data matrix is rotated such that the newly extracted first PC becomes the X-axis of the PC matrix (172). The rotated data matrix is described by its eigen-decomposition values (eigenvector and eigenvalue). The eigenvector is the vector in the matrix that maintains its direction following the matrix rotation, with the eigenvalue denoting the magnitude said eigenvector was multiplied by during the matrix rotation (172). The eigen-decomposition values of a covariance matrix of a data set is its PCA rotation (171). PCA is a popular data analysis technique that is commonly used across multiple disciplines to facilitate the analysis of multivariate data, it is also a cornerstone of chemometric data analysis (172–174).

Chapter 3
Investigating the mechanical properties of melt-extruded filaments and their suitability for 3D printing

3.1. Introduction

The filament-based feeding mechanism employed by FDM printers utilises mechanical gearing arrangements to push the filament into the heating zone (Figure 3-1) (41). For the filament movement to be accurately controlled, it has to be held tightly (pinched) between the two rollers (175), leaving the filament effectively under pressure between the rollers and the nozzle during the feeding. In situations where the filament is brittle, this is likely to cause the filament to fracture, stopping the forward propulsion of the filament, causing a blockage in the printing head, as illustrated in Figure 3-1. Blockages in the printing head are very problematic; broken pieces of filaments inside the printing head can contaminate the machine, compromising the purity of any dosage forms one wishes to fabricate. Blockages in the printing head are also difficult to clean, often requiring disassembly of the entire printing head to be cleared. Therefore, there is a need for screening the mechanical suitability of the filament before attempting to feed the filament into a printer.

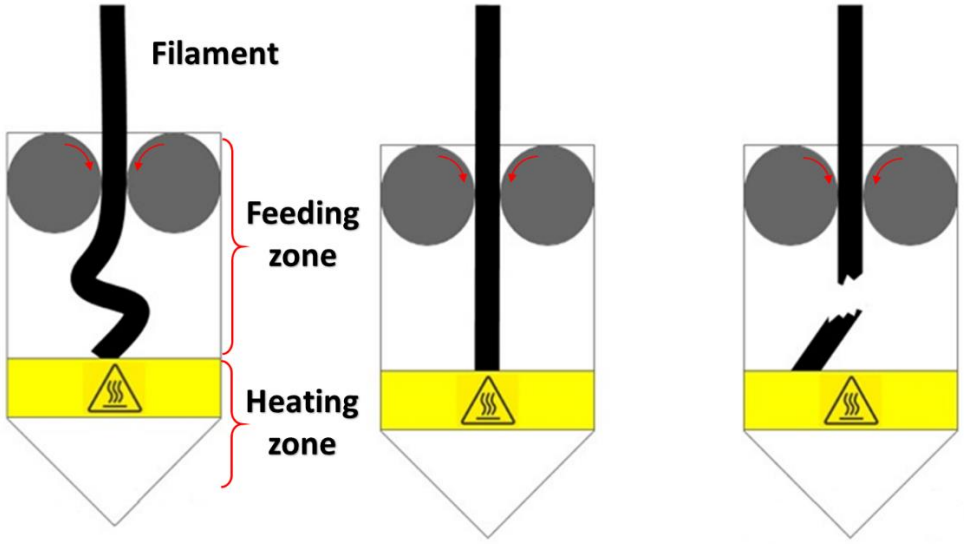

Figure 3-1: Illustration of the different behaviour of filaments during feeding. Left: a filament that is too flexible to be fed. Centre: an ideal filament. Right: a filament that is too brittle to be fed

Zhang et al. described a characterisation method utilising the 3-point bend test to determine the mechanical suitability of filaments prepared by HME for FDM (176). Zhang identified two parameters, filament stiffness (breaking strain) and filament brittleness (breaking distance) as the deterministic parameters in determining the mechanical suitability of the filaments for 3DP. While the method determined which filaments were too brittle to be printed, there was no clear correlation in the mechanical properties of the filaments which were deemed mechanically adequate for printing was

observed. Furthermore, Zhang required that a filament must coil inside the printing head over six times to be deemed too flexible to be printed. More recently, applying the 3-point bend test to the filament has been conducted solely to determine the brittleness of the filament to avoid fracture inside the print head (137,177,178). Ponsar et al. investigated whether Young's Modulus may be used to extrapolate information about the feedability of filaments, but reported that differences in Young's Modulus were *"of little practical relevance"* (177). Similarly, data reported by Borujeni et al. showed no correlation between Young's Modulus and the feedability of the filaments (179).

This study describes the development of a screening method for predicting the feedability of melt-extruded filaments for FDM. Unlike the 3-point bend test, the method presented herein uses a texture analyser to compress the filament parallel to the direction of feeding. Unlike the attempts utilising Young's Modulus as a method to determine feedability, the entire compression force vs. probe travel distance curve was used. Since its publication (180), successful use of this method to determine feedability of filaments was reported by Gültekin et al., (181), as well as in another section presented in this work (Appendix 1).

In this study, a number of binary and ternary polymer blends were prepared as filaments via HME. Furthermore, a complex, quaternary formulation that has been reported by Alhijjaj et al. (43) to be feedable was also used studied as a higher complexity system. Filaments were prepared and attempted to be fed into an unmodified Makerbot® Replicator 2 3D printer to determine their feedability. A custom-made Texture Analyser rig (Figure 3-2) was used to test the filament response in a compress-and-release cycle, yielding a plot of force (exerted by the filament as resistance to deformation) vs. distance compressed. Such data was used to quantify the mechanical properties of the filaments and to determine whether it is possible to predict the feedability of a filament without having to compromise the printing head.

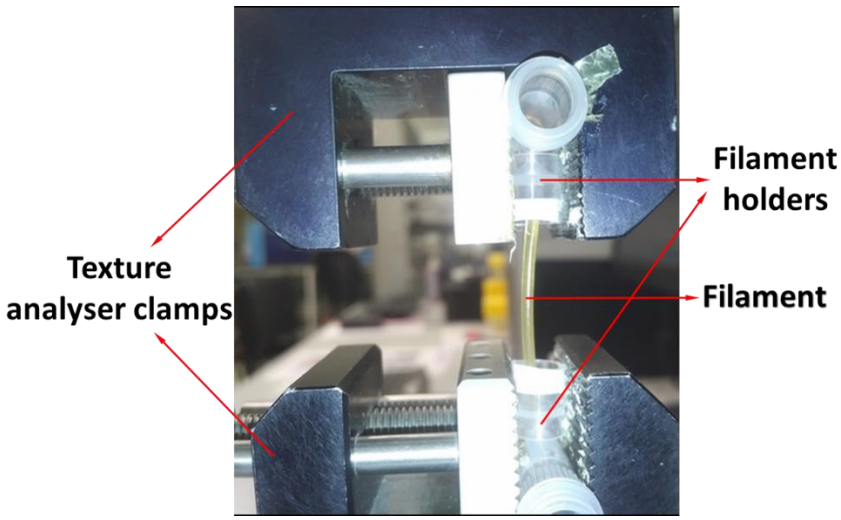

Figure 3-2: The Texture Analysis rig used in this study

Using the force/distance plots (hereinafter referred to as the *flexibility profile*) produced by commercial filaments as a control, correlation analysis and principal component analysis (PCA) were used to determine whether there exists a statistically significant correlation between the flexibility profiles of different filaments and their feedability and subsequently printability. This allows one to predetermine whether or not a produced filament is feedable, therefore printable. The relationship between the formulation composition and the feedability of the filament investigated in this study can bring new insights into the development of principles in the rationalisation of FDM printable formulation design.

3.2. Materials and Methods

3.2.1. Materials:

The materials used in this study were ABS, HIPS, PVA (both as a commercial filament, and as Mowiflex pellets), HPMCAS, Tween 80, PEO, Eudragit EPO, Soluplus, Copovidone, PEG, and paracetamol. The three commercial filaments (ABS, HIPS, and PVA) were used as purchased. Detailed descriptions of the materials and their sourcing can be found in Section 2.1.

3.2.2. Preparation of in-house filaments:

In-house filaments were prepared by HME and extruded through a 1.75 mm circular die. A list of prepared formulations and their key extrusion parameters can be found in Table 3-1. All multi-component formulations were cycled in the extruder for 5 minutes at a screw speed of 100 RPM to ensure homogenous mixing (43). Following extrusion, the filaments with diameters of 1.75 mm ± 0.05 mm were collected for further testing.

Table 3-1: Compositions and extrusion temperature of the studied filaments.

Formulation	Constituents	Temperature
Mowiflex	Mowiflex® (contains PVA and an undeclared plasticizer at an undeclared concentration	170 ºC
HPMCAS	HPMCAS (100% w/w)	170 ºC
PEO	PEO (100% w/w)	75 ºC
Copovidone	PVP/VA 64 (100% w/w)	140 ºC
Soluplus	Soluplus® (100% w/w)	120 ºC
Eudragit EPO	Eudragit® EPO (100% w/w)	120 ºC
EUD	Eudragit EPO (55.5% w/w) + 11.1% w/w, 16.7% w/w, and 16.7% Tween 80, PEG, and PEO, respectively (43)	100 ºC
HD	HPMCAS (90% w/w) and paracetamol (10% w/w)	150 ºC
HP10	HPMCAS (90% w/w) and PEO (10% w/w)	150 ºC
HP10D	HPMCAS (81% w/w), PEO (9% w/w) and paracetamol (10% w/w)	140 ºC
HP20	HPMCAS (80% w/w) and PEO (20% w/w)	150 ºC

Formulation	Constituents	Temperature
HP20D	HPMCAS (72% w/w), PEO (18% w/w) and paracetamol (10% w/w)	130 ºC
HP30	HPMCAS (70% w/w) and PEO (30% w/w)	140 ºC
HP30D	HPMCAS (63% w/w), PEO (27% w/w)and paracetamol (10% w/w)	120 ºC
HP40	HPMCAS (60% w/w) and PEO (40% w/w)	130 ºC
HP70	HPMCAS (30% w/w) and PEO (70% w/w)	100 ºC
HP90	HPMCAS (10% w/w) and PEO (90% w/w)	85 ºC
SP	Soluplus® (90% w/w) and PEG (10% w/w)	110 ºC
ST	Soluplus® (80% w/w) and Tween® 80 (20% w/w)	100 ºC

3.2.3. Filament Characterisation:

3.2.3.1. Differential Scanning Calorimetry

DSC was conducted using a Q20 differential scanning calorimeter. All in-house prepared filaments were tested using a heat-cool-reheat cycle with a temperature range of 20 ºC to 185 ºC at 10 ºC/min. Physical mixes were scanned using a heat-cool-reheat program along the aforementioned temperature range. All samples were tested as fresh samples (where applicable) immediately after extrusion. All tests were done in triplicates.

3.2.3.2. Attenuated Total Reflectance – Fourier Transform Infrared Spectroscopy

FTIR spectroscopy was conducted using a resolution of 4 cm^{-1}, 32 scans for each sample, within the range of wavenumbers from 4000–550 cm^{-1}. Spectra analysis was conducted using OPUS version 7.8 (Bruker Optics Ltd., United Kingdom). All measurements were done in triplicate.

3.2.3.3. Powder X-Ray Diffraction

A scanning range of $3^{o} < 2\theta < 30^{o}$, using a step scan mode with a step width of 0.01^{o} and a scan speed of 1 s/step was used to conduct all measurements.

3.2.4. FDM feedability testing:

Feedability of the extruded filaments was tested by feeding into the printing head of using the aforementioned Makerbot® Replicator 2. Successful extrusion of the polymer through the nozzle tip was regarded as successful feeding, making the filament *feedable*. It should be highlighted that the printing quality was not assessed and is out of the scope of this study. All filaments were fed at the printer's default feeding temperature of 230 ºC.

3.2.5. Texture analysis:

Texture analysis was conducted using a compression method; the filaments were compressed axially with a 3.15 mm/sec compression speed, corresponding to the roller movement speed of a Makerbot® Replicator 2X (determined by feeding an accurately cut 10 cm filament into the printer head and measuring the time needed for the filament to pass through the printing head). 5 cm long filament pieces were held standing in conical end caps to allow bending and to avoid fracturing them with the clamps (Figure 3-2). The compression distance was set to 15 mm with a trigger force of 0.05N and data was collected during both compression and release. TA tests were done in triplicate for all tested filaments.

3.2.6. Data manipulation and statistical analysis:

For the compression tests, the varying hardness of the materials dictated that the scaling of the flexibility profile (force (N) vs. distance (mm)) plots was not directly comparable without data range normalisation. Therefore, data range normalisation was performed using the equation:

$$Y^{n}_{Normalized} = \frac{Y^{n}}{\Sigma Y} \qquad \textit{(Equation 3-1)}$$

Where Y^n is the n^{th} point on the Y-axis (force). Correlation analysis of the flexibility profiles of the pharmaceutical filaments with the data of the commercial filaments was conducted using Microsoft® Excel 2016 expanded with the Data Analysis add-on. PCA was conducted using IBM® SPSS Statistical Analysis Suite (version 25), with the Varimax rotation method, extracting components possessing an eigenvalue $\geqslant 1$, as per the Kaiser rule (n=3) (171).

3.3. Results

3.3.1. Materials characterisation:

Figure 3-3 shows the thermograms of Copovidone, Soluplus, Eudragit EPO, ST, and SP. All of which were found to have inadequate mechanical properties to be fed into the 3D printer (all were found to be too brittle, except formulation ST, which was found to be too flexible). The T_g of Copovidone was seen at 107 °C. The T_g of Soluplus was seen at 71 °C. The T_g of Eudragit EPO was seen at 45 °C. The T_g of SP was seen at $\approx 40^\circ$ C. The T_g of formulation ST was not detected.

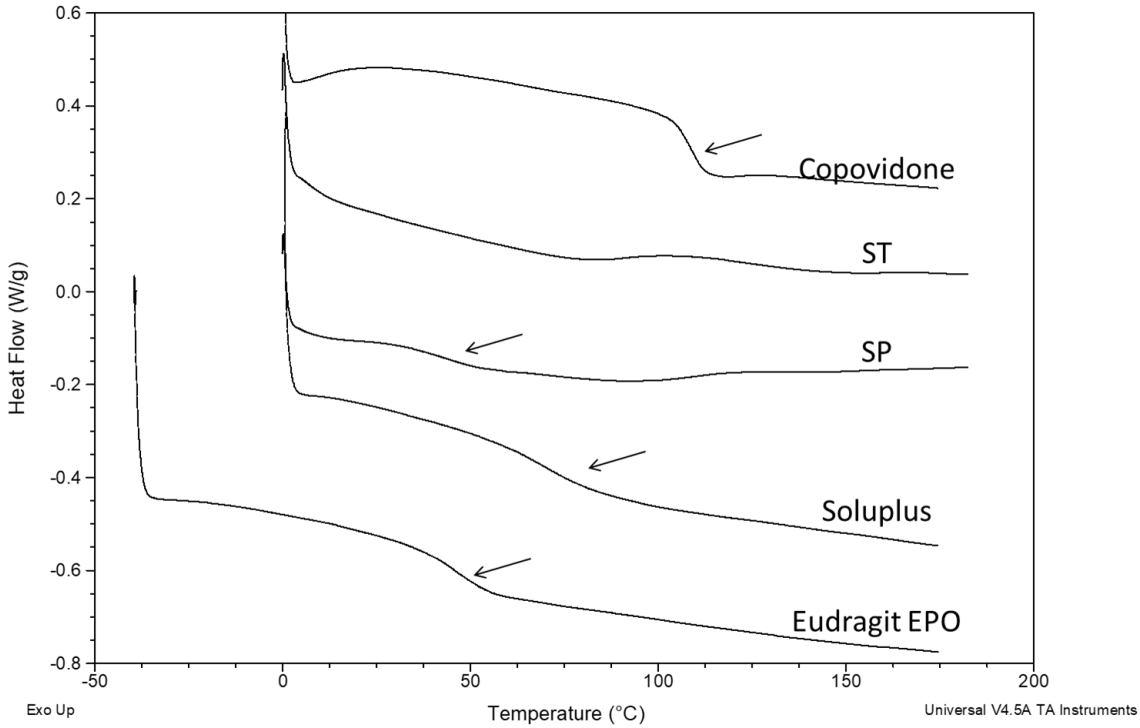

Figure 3-3: DSC thermograms of non-feedable filaments

Figure 3-4 shows the DSC thermograms of the raw materials used in the HPMCAS-based formulations. The T_g of HPMCAS was seen at ~120 °C. An endothermic event corresponding to the T_m of PEO was seen at ~60 °C, and another endothermic event corresponding to the T_m of paracetamol form I (monoclinic form) (130) was seen at ~169 °C.

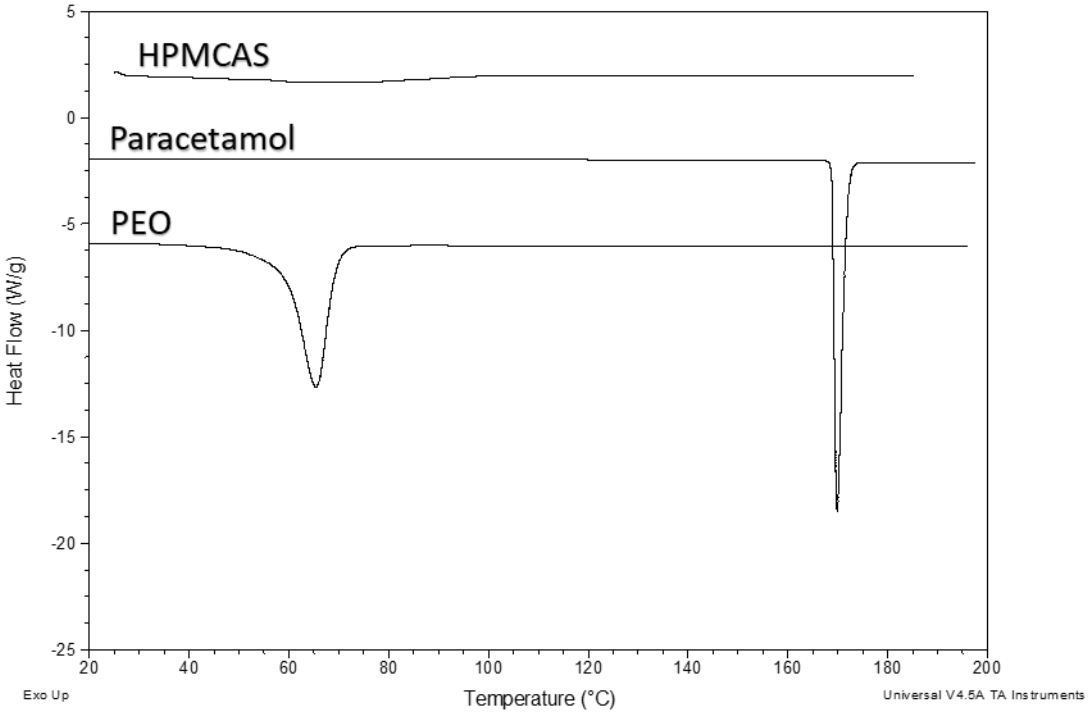

Figure 3-4: DSC thermograms of raw materials.

Figure 3-4 shows the DSC thermograms of the physical mixes (2nd heating cycle) and extruded filaments of HPMCAS based filaments HP10, HP20, and HP30. For the physical mixes, the decreased enthalpy of the T_m of PEO, and a decrease in the T_g of HPMCAS were observed in the 2nd heating cycle and are summarised in Table 3-2 below:

Table 3-2: Enthalpy of the melting of PEO, and the shifted T_g in the physical mixes of formulations HP10, HP20, and HP30.

Formulation	Enthalpy of T_m of PEO	T_g
HP10	4.01 J/g ± 0.04 J/g	110 °C ± 1.53 °C
HP20	5.20 J/g ± 0.11 J/g	86 °C ± 2.50 °C
HP30	9.50 J/g ± 0.18 J/g	Not seen

In the extruded filaments, the melting of PEO is absent in formulations HP10, HP20, and HP30. This result indicates that with 10-30% PEO loading, HPMCAS mixed well with PEO after extrusion and the amount of HPMCAS present was sufficient to prevent PEO from recrystallization.

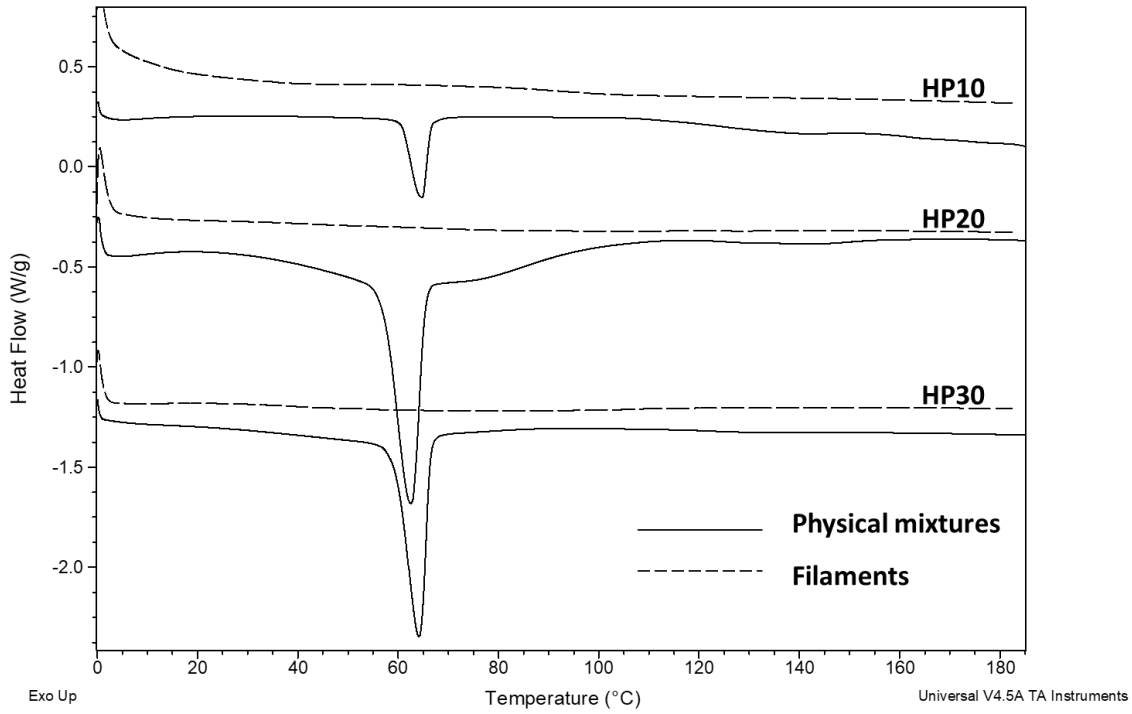

Figure 3-5: DSC thermograms of the HPMCAS based filaments HP10, HP20, and HP30

When increasing the PEO content to above 30%, clear melting of phase-separated crystalline PEO can be identified (Figure 3-6). Using the melting enthalpy values of the PEO melting in the HP filaments and the enthalpy value of the pure PEO (obtained from the DSC results of pure PEO), it is possible to estimate the degree of crystallinity of PEO in the filaments. HP90 and HP70 have 56.3% and 51.5% crystallinity, respectively, which is much higher than the 30.8% for HP40. This indicates that in high PEO content filaments (HP70 and HP90) the continuous phase is the semi-crystalline PEO. This contrasts with low PEO content filaments (HP10-HP30) that has the HPMCAS as the continuous phase. For HP40, as the contents of HPMCAS and PEO are close, it is reasonable to expect that there is no clear a continuous phase which would contribute the significant mechanical property difference observed later in the texture analysis tests.

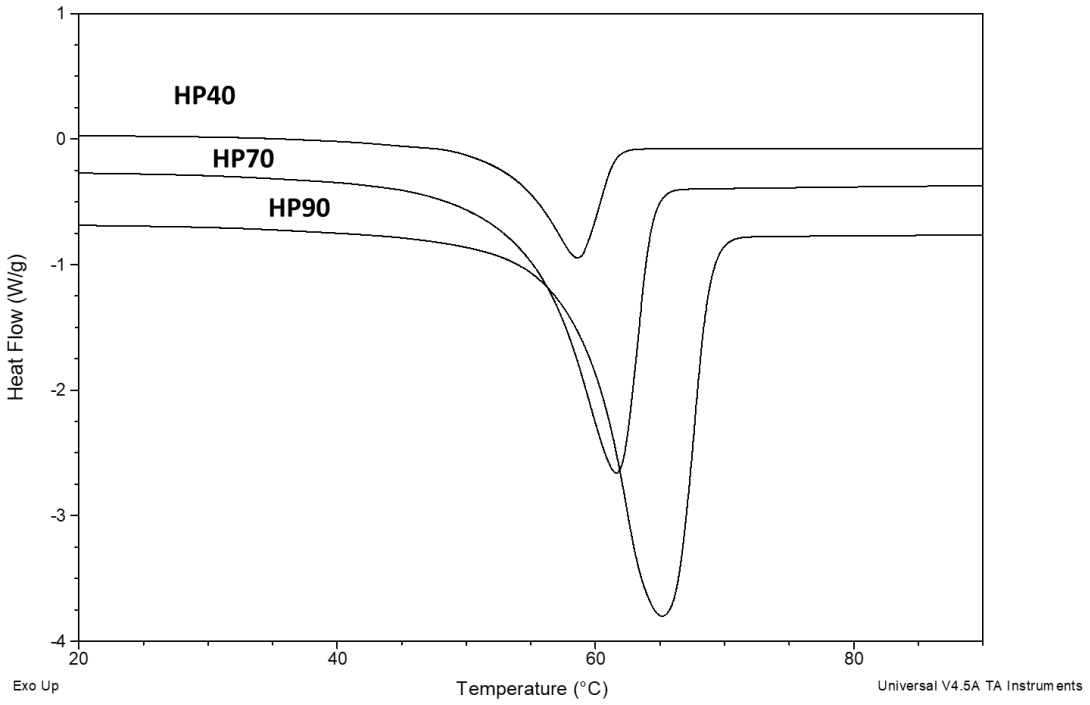

Figure 3-6: DSC thermograms of formulations HP40, HP70, and HP90

For the drug loaded physical mixes, a small melting endotherm at ~169 ºC can be seen corresponding to the melting of paracetamol. A small melting endotherm of PEO was detected in the thermogram of the HP30D filament, suggesting the existence of some phase separate, semi-crystalline PEO in this drug-loaded filament. The T_m of paracetamol was not seen in any of the drug-loaded filaments, suggesting the formation of an amorphous solid dispersion of paracetamol. The T_g values of the drug-loaded filaments could not be identified. The DSC thermograms of the drug-loaded formulations can be seen in Figure 3-7.

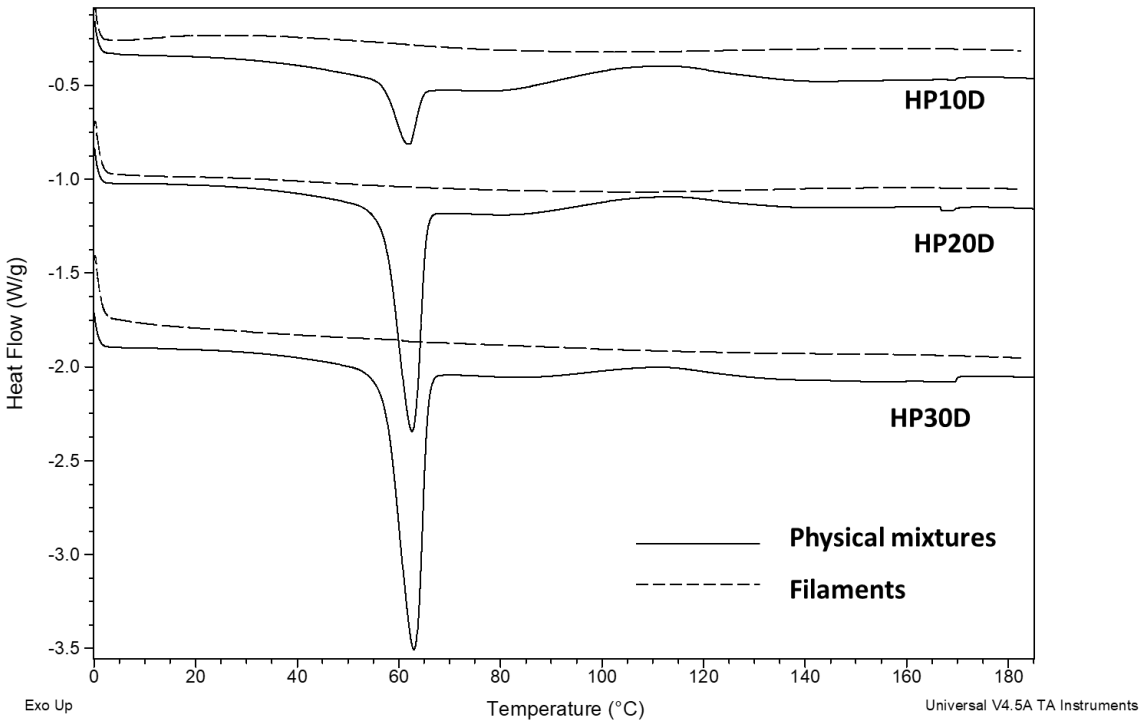

Figure 3-7: DSC thermograms of drug loaded filaments and their physical mixes

ATR-FTIR and PXRD were carried out to further confirm the amorphous nature of the filaments and investigate any possible molecular interactions between the polymers and additives. Figure 3-8 and shows the ATR-FTIR spectra of paracetamol, PEO, and HPMCAS, as well as the filaments.

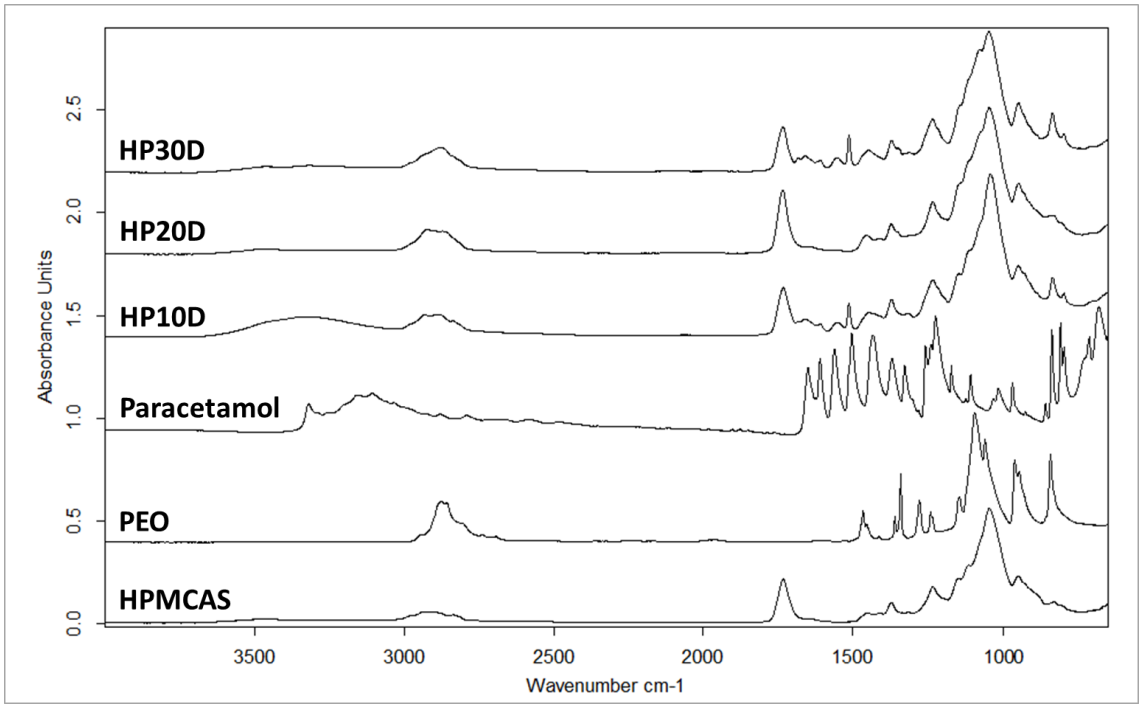

Figure 3-8: ATR-FTIR spectra of the drug-loaded filaments and their constituents.

Across the whole FTIR spectrum, the sharp bands of crystalline paracetamol are absent and a broad peak at 3321 cm^{-1} which corresponds to the N-H stretching of paracetamol in its amorphous state can be seen in all drug-loaded filaments. Furthermore, the paracetamol peak at 808 cm^{-1}, corresponding to the out-of-plane bending of a para-substituted aromatic ring, documented to be particularly indicative of the crystal packing of the monoclinic form of paracetamol (111,146), was notably absent in the spectra of the filament. The drug-loaded filaments showed no observable change in the carbonyl peak of HPMCAS indicating that there is neither hydrogen bonding nor dipole-dipole interactions between the polymer and drug. This absence of hydrogen and dipole-dipole interactions suggests that the mechanism of stabilisation of this solid dispersion is kinetic stabilisation (78).

The PXRD patterns of the milled filaments shown in Figure 3-9 confirm the fully amorphous nature of all drug-loaded filaments, as no peaks corresponding to neither PEO nor paracetamol are visible in the PXRD diffraction patterns of HP10D, HP20D, and HP30D filaments.

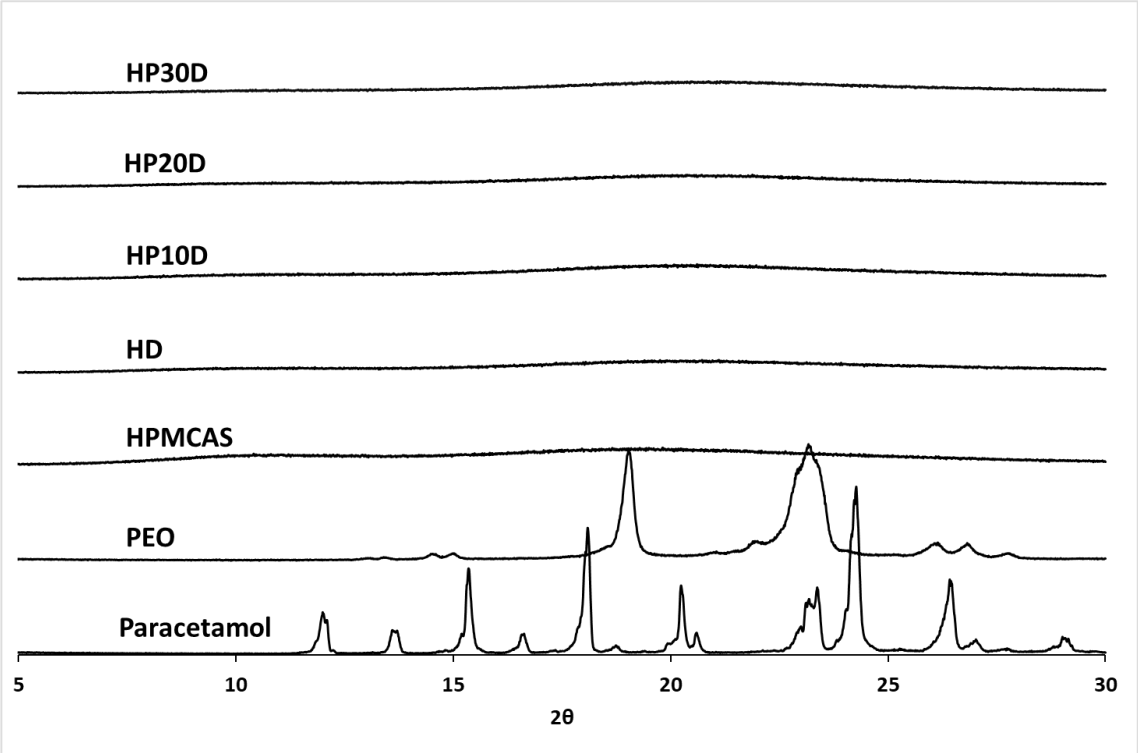

Figure 3-9: PXRD of the drug-loaded formulations and their constituents

3.3.2. Filament feedability tests:

Pure polymer filaments Eudragit EPO, HPMCAS, copovidone, and Soluplus were found to be too brittle and would fracture inside the printing head whenever feeding was attempted. Formulations ST, SP, and HD (plasticised with Tween 80, PEG, and paracetamol, respectively) were also found to not be feedable. SP and HD were found too brittle to be fed, while ST was too flexible and would coil inside the print head. Increasing the contents of the plasticizers (20% of Tween 80 for ST and 40% of PEO for HP40) led to over-plasticization. The ST and HP40 filaments were found to be overly flexible and would coil up inside the feeding zone and would not thread through into the melting zone of the printing head. The rest of the pharmaceutical filaments were successfully fed through the FDM printer. The feedability test results are summarized in Table 3-3.

Table 3-3: Feedability of the tested filaments

Filament	Feedability
HPMCAS	N
Mowiflex	Y
PEO	Y
PVPVA64	N
Soluplus	N
Eudragit EPO	N
EUD	Y
HD	N
HP10	Y
HP10D	Y
HP20	Y
HP20D	Y
HP30	Y
HP30D	Y
HP40	N
HP70	Y
HP90	Y
SP	N
ST	N

3.3.3. Texture Analysis screening tests:

TA tests were used to obtain the force-distance curves of the filaments under axial compression. The force curves were normalised as shown in Equation 3-1 to obtain a comparable scaling of the flexibility profiles. Normalised Force vs. Distance curves were then plotted to compare the behaviours of different filaments.

Figure 3-10 shows the TA plot of the non-feedable filaments. All the tested filaments were found to fracture during the test, which appears in the flexibility profile as a sudden drop of Force down to 0. As can be seen in Figure 3-10, Copovidone was the most brittle of the materials, fracturing immediately without bending. Soluplus and Eudragit EPO were slightly more malleable; neither filament fractured at peak axial force but rather bent slightly before fracturing. Plasticised filaments HD and SP, and the pure HPMCAS filament were yet more malleable and bent considerably before fracturing. However, all filaments shared a characteristic fracture pattern, with the aforementioned bending being negligible in comparison to the feedable filaments.

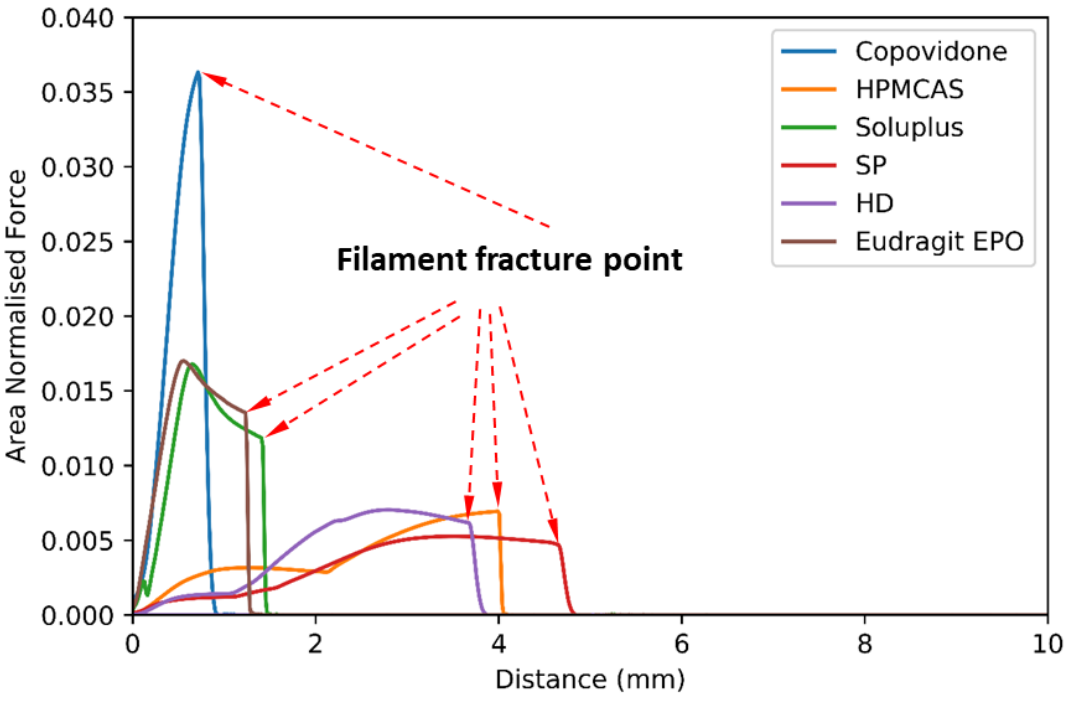

Figure 3-10: Flexibility profile plots of non-feedable filaments

Of all the non-feedable filaments, filaments ST and HP40 could not be tested using TA as both filaments were too floppy and would collapse under their own weights rather than

stand up straight between the two holsters attached to the texture analyser probe (Figure 3-11).

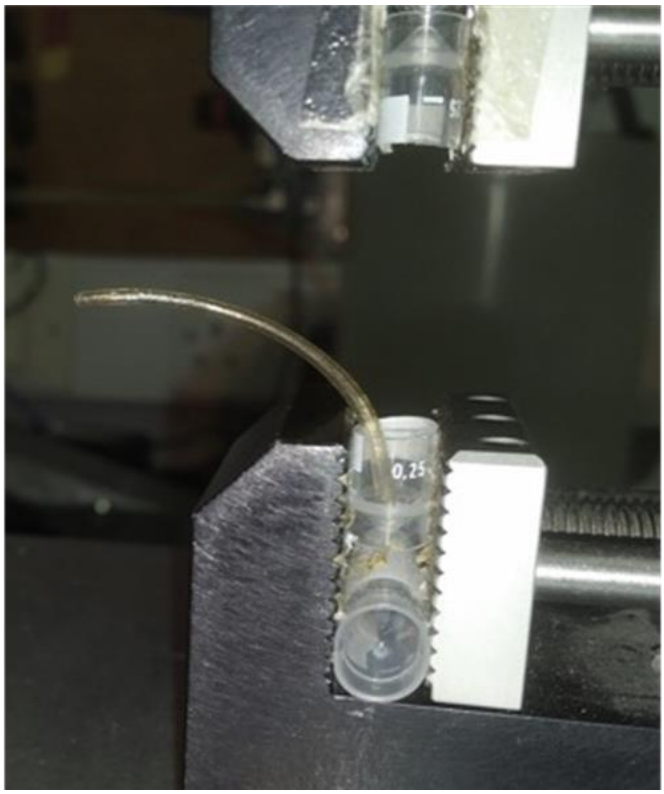

Figure 3-11: non-testable filament. Shown: filament HP40.

Figure 3-12 shows the flexibility profiles of the commercial filaments ABS, HIPS and PVA commercial filaments. Notably, none of the three commercial filaments fractured during the TA test, with all three filaments only bending.

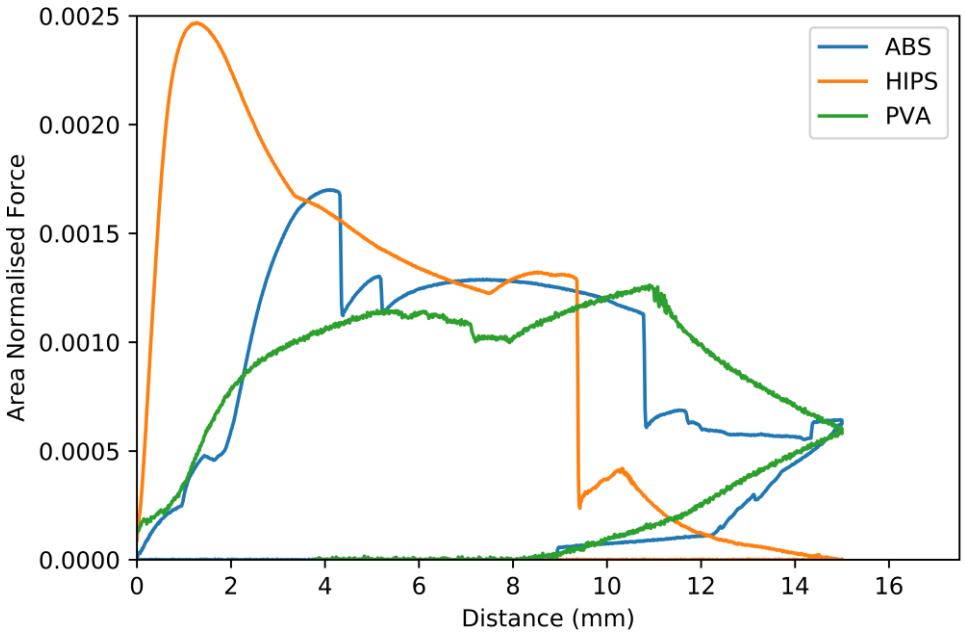

Figure 3-12: Flexibility profile plots of commercial filaments.

Figure 3-13 shows the flexibility profiles of the in-house extruded feedable filaments. Similar to the commercial filaments, none of the in-house extruded filaments that were found to be feedable fractured during the TA tests, with all filaments only bending.

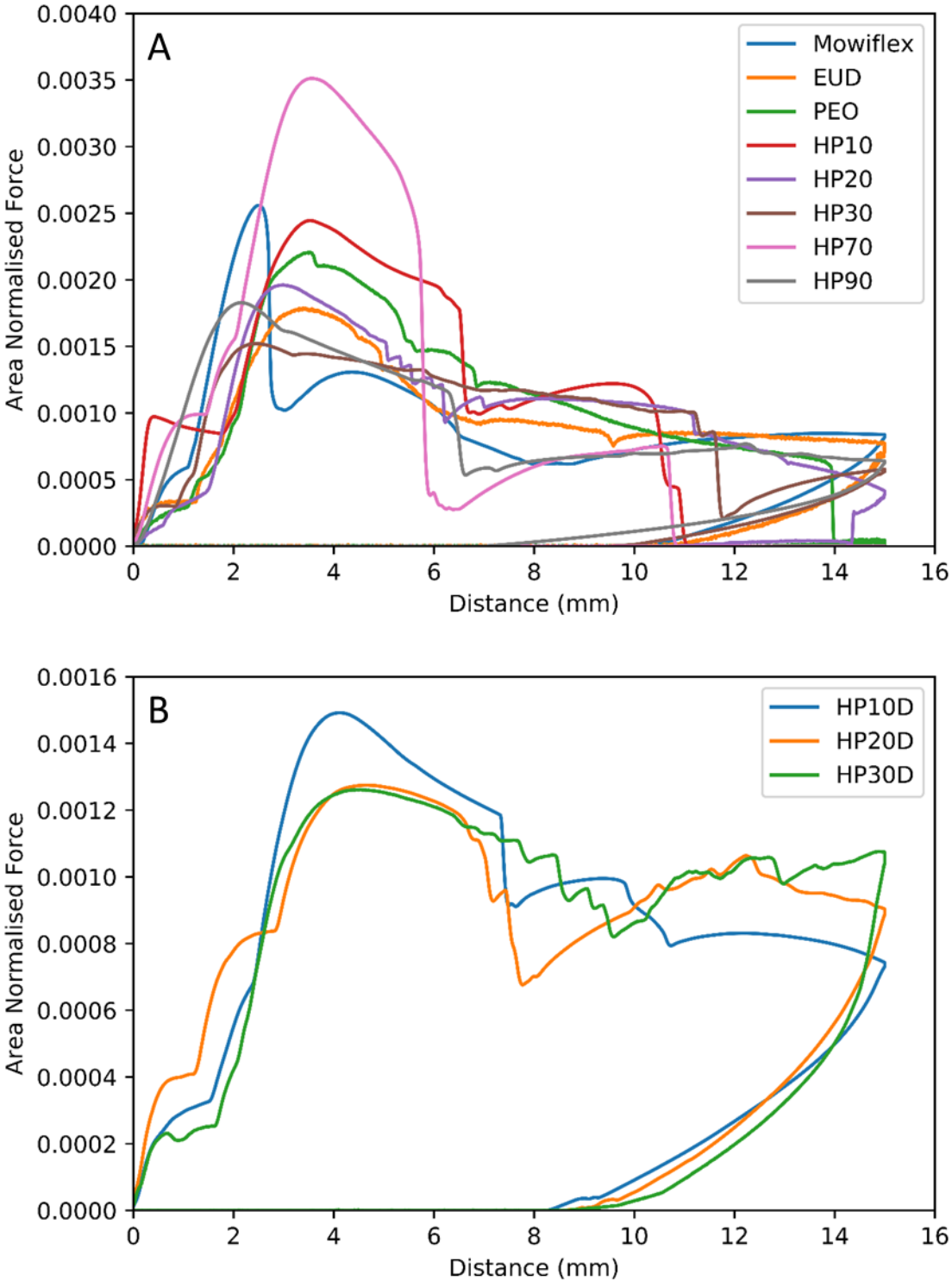

Figure 3-13: Flexibility profiles of in-house melt-extruded filaments. A: placebo filaments, B: drug-loaded filaments.

Using this data, it is possible to group filament behaviour in order to examine the correlation between the flexibility profile and the feedability of the filaments tested directly using the FDM printer. The ST and HP40 filaments were too flexible to be placed in the TA rig (as illustrated in Figure 3-11). The rest of the non-feedable filaments all

shared a characteristic brittle fracture pattern, with sudden discontinuation of force on the filament after reaching a peak fracture force. These filaments fractured immediately at the maximum force, showing no bending, plastic, or elastic deformation to accommodate the increased strain. Within the non-feedable filaments, Eudragit EPO, PVPVA64 and Soluplus exhibited much sharper fracture and lower strain-bearing ability than HPMCAS, HD and SP. This is evident by the longer travel distance of the probe before the fracture of the HPMCAS, HD and SP filament.

Despite seeming random at first glance, the flexibility profiles of the feedable filaments all share a characteristic bending deformation after the maximum strain bearing point is reached. When the TA probe was returning to the start position, the filaments were able to partially recover and straighten within the rig even though they had lost some of their stiffness. Of the feedable filaments, filament HP10 was notably the only filament to fracture during TA. However, filament HP10 did exhibit substantial bending after reaching peak tension force and only fractured after being bent considerably by the texture analyser probe. Therefore, its recorded fracture pattern was found to considerably differ from the sharp brittle fracture patterns exhibited by non-feedable filaments.

3.3.4. Correlation Analysis:

The correlations between the flexibility profiles (the normalised area under the force-distance curves) of each in-house filaments and each of the three commercial FDM printable filaments, ABS, dissolvable filament and PLA, were generated and listed in Table 3-4. This correlation can be treated as the quantification of the level of similarity between the flexibility profile of the in-house pharmaceutical filaments and the commercial printable filaments. The higher the correlation score, the more similar were the tested filament to the commercial filament.

As seen in Table 3-4, for most of the filaments, the correlation scores to the three commercial filaments vary. This is not surprising as the correlation scores of the flexible profiles of the three commercial filaments also vary indicating there are some differences in their flexible profiles. The correlation data were further analysed by taking the mean of the three correlation scores per filament using the equation:

$$\frac{C_{ABS}+C_{Dissolvable\ Filament}+C_{PVA}}{3} \quad \textit{(Equation 3-2)}$$

where C_x is the correlation score with commercial filament x. Overall, all the in-house filaments that passed the feedability test had a mean correlation score above 0.5; whereas the filaments that failed the feedability test all had a mean correlation score below 0.5. Furthermore, the correlation scores of plasticised filaments were higher than those of non-plasticized filaments indicating that plasticisation improves the flexibility of the filaments.

Table 3-4: Correlation analysis of the flexibility profiles of in-house extruded filaments against commercial filaments

Filament	ABS	HIPS	PLA	Mean	Rounded mean score
HPMCAS	0.38	0.64	0.18	0.40	0
Mowiflex	0.76	0.69	0.74	0.73	1
PEO	0.92	0.71	0.82	0.82	1
PVPVA64	-0.08	0.22	-0.12	0.01	0
Soluplus	-0.56	0.40	-0.75	-0.30	0
Eudragit EPO	-0.70	0.30	-0.79	-0.40	0
EUD	0.94	0.65	0.88	0.82	1
HD	0.32	0.60	0.18	0.37	0
HP10	0.85	0.82	0.67	0.78	1
HP10D	0.96	0.53	0.94	0.81	1
HP20	0.94	0.70	0.87	0.84	1
HP20D	0.90	0.48	0.95	0.78	1
HP30	0.95	0.77	0.89	0.87	1
HP30D	0.91	0.40	0.94	0.75	1
HP70	0.70	0.73	0.51	0.65	1
HP90	0.81	0.81	0.74	0.79	1
SP	0.49	0.63	0.28	0.47	0

3.3.5. Principal Component Analysis:

PCA is a multivariate statistical technique that, from a data table containing observations describing a multitude of inter-related variables, can extract key information which is represented as functions of "Principal Components". Similarities between the observations can be represented by plotting the variables on a map referred to as a *space plot* (171). PCA was performed to further explore the relationship between the flexibility profiles of the filaments and their feedability. As the correlation scores of the Dissolvable

filament with the other commercial filaments are low, the dissolvable filament was treated as an outlier and was not included in the PCA. For the PCA, the normalised full force-distance curves were used the analysis. Principal Component 1 shows an eigenvalue of 10.13, Principal Component 2 shows an eigenvalue of 3.57, Principal Component 3 shows an eigenvalue of 1.51, while all other principal components show an eigenvalue < 1. By applying the Kaiser Rule, the first three principal components were extracted.

Figure 3-14 shows the loadings plot of Principal Components 1, 2, and 3. The filaments aggregated on the plot into five clusters. The feedable filaments aggregated into three clusters, the first containing ABS, PVA, HP10D, HP20D, and HP30D. The second contains filaments HP10, HP20, HP30, EUD, and PEO. The third cluster contains filaments Mowiflex, HP70, and HP90. The three clusters are closely aggregated together and can be looked at as a single macro-cluster.

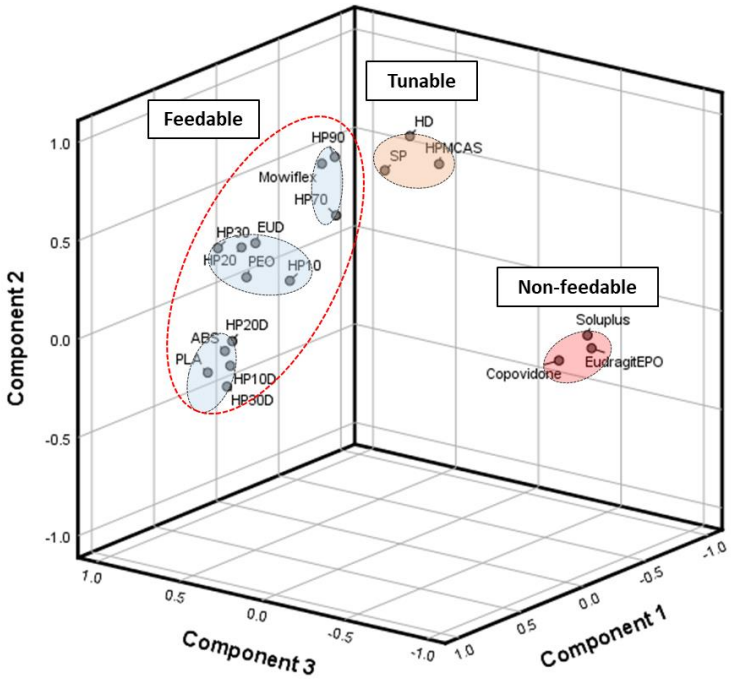

Figure 3-14: Loadings plot of the PCA conducted on the flexibility profiles of all tested filaments.

The fourth cluster contained filaments SP, HD, and HPMCAS, which are the filaments that showed some strain-bearing ability in the TA tests but still fractured as the result of compression (Figure 3-10). This cluster of slightly deformable brittle filaments is closely positioned to the macro-aggregated cluster of feedable filaments. Although the filaments

in this cluster are not feedable, they exhibited some potential and with formulations modification such as adding plasticisers they can be feedable. HPMCAS is an example. The fifth cluster contains the highly brittle and non-feedable filaments of Eudragit® EPO, Copovidone, and Soluplus.

3.4. Discussion

3.4.1. Intrepretation of the Texture Analysis Flexibility Profile:

The data presented in Section 3.3.3. suggests that examining the whole of the TA flexibility profile may be necessary to extrapolate information about the feedability of the filament. As discussed in Section 3.3.3., the characteristic attribute of non-feedable filaments was the brittle fracture pattern exhibited by all the tested filaments (Figure 3-10). Feedable filaments, on the other hand, were notable for their capacity to recover post-deformation.

Figure 3-15 shows an example of a flexibility profile combined with photographs of the filament at critical points in the profile. At the beginning of a TA test, the straight filament received the compression forces, with the continuous movement of the TA probes towards each other, the forces born by the filament continuously increase. At a critical point in the applied force, the filament reaches the Euler point at which an infinitesimal lateral force will cause bending. This is the bending point highlighted in Figure 3-13. After this, the applied force acts to both compress the filament and to further bend the filament at the weakened bend point which leads to the complex TA profile pattern of this stage of the test as seen in the flexibility profiles of the feedable filaments (Figures 3-11 and 3-12). Nevertheless, the common feature of the ability to bend was observed in all feedable filaments.

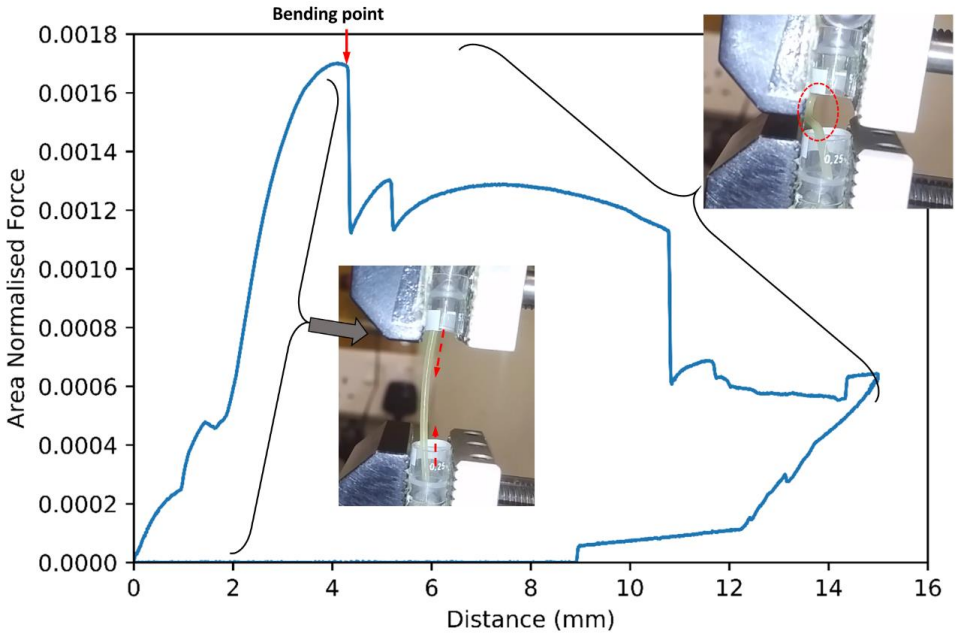

Figure 3-15: Flexibility profile of a feedable filament, annotated with images of every region of the curve.

Despite the previous argument, fracturing of a feedable filament was observed in filament HP10. The fracturing behaviour of said filament was notably different to that of the brittle fracture patterns exhibited by the non-feedable filaments, seeing as its Flexibility Profile exhibited more of the characteristics of a feedable filament, rather than a non-feedable filament, as shown in Figure 3-16, which highlights the key characteristics of the Flexibility Profiles of a non-feedable filament, a fracturable feedable filament, and a non-fracturable feedable filament.

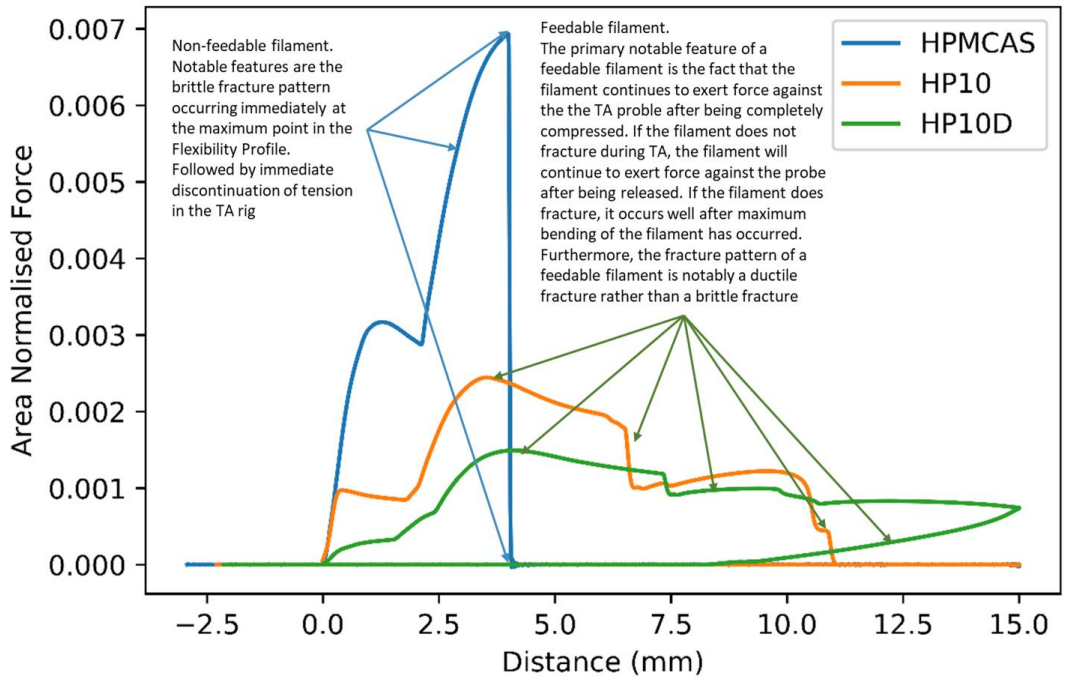

Figure 3-16: highlighting the main features of the Flexibility Profile of a non-feedable filament (HPMCAS). A feedable filament that can fracture (HP10), and a feedable filament that does not fracture (HP10D)

A more detailed discussion of the fracturing pattern of filament HP10 and how it is different from the non-feedable filaments is presented in the upcoming section 3.4.2.

An important factor one must consider when interpreting the Flexibility Profile is the fact that it is of a qualitative nature. The absolute amount of force a filament can bear before bending or fracturing does not appear to correlate with its feedability. Figure 3-17 shows the untreated Texture Analysis curve of a feedable filament (ABS), against a non-feedable filament (Eudragit), as well as the filament that showed the highest strain-bearing force prior to bending (Mowiflex). Both ABS and Mowiflex showed a maximum strain-bearing force of < 20 N, despite the fact that ABS is a commercial, feedable filament, while

Eudragit EPO is a non-feedable, brittle filament. Conversely, Mowiflex, a feedable filament, showed strain-bearing bearing forces higher than all of its non-feedable counterparts, with a strain-bearing force up to 100 N. Even without area normalisation, the patterns outlined in Figure 3-16 can still be clearly observed for all three filaments (bending and recovery for Mowiflex and ABS vs. the brittle fracture pattern exhibited by Eudragit EPO) regardless of the absolute force exerted. Further indicating that the "pattern" exhibited by the filament during TA provides more information about the feedability of the filament, with absolute quantitative values such as maximum force offer little to no help in terms of predicting feedability. This conclusion aligns with what has been previously reported in the literature by Ponsar et al. (177) and Borujeni et al. (179), in which Young's Modulus was found to be of little relevance towards predicting the feedability of filaments, further suggesting that this phenomenon is of qualitative nature.

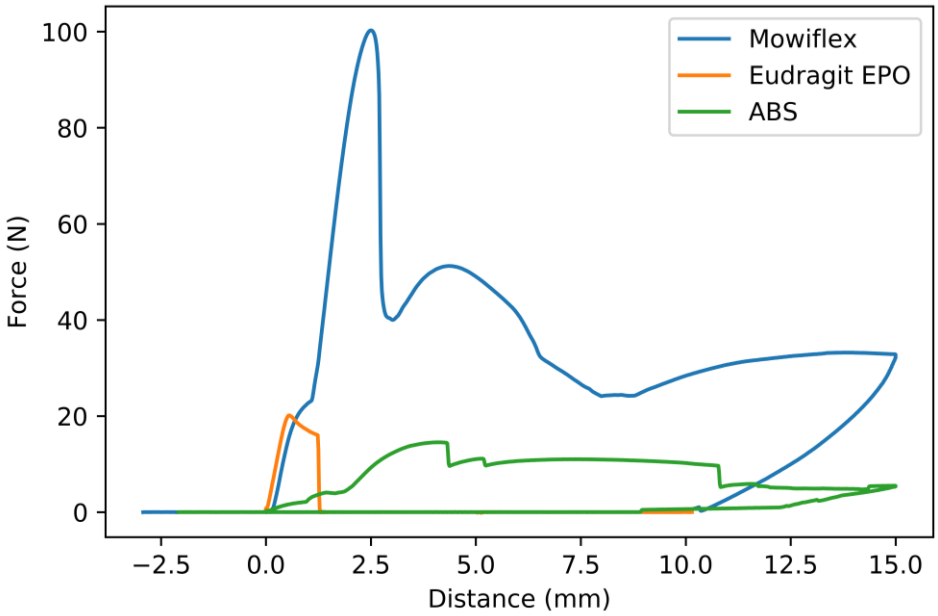

Figure 3-17: Flexibility profiles of Mowiflex, Eudragit EPO, and ABS. Showing absolute force rather than Area Normalised Force

3.4.2. Correlation between mechanical properties and feedability:

This study is aimed to develop a screening method to speed up the formulation development of FDM printable solid formulations. To achieve good printability, the FDM filaments first need to exhibit good feedability to allow the smooth and continuous delivery of the filaments to the heating zone of the printing head. As previously discussed, the feeding mechanism employed by FDM printers involves mechanical pushing of a filament held between two counter-rotating gears. In situations where the filament being fed is too brittle to bear the mechanical strain generated from the compression and

pushing, this is likely to cause the filament to fracture, discontinuing the force that is propelling the filament forward, causing a block in the printing head. If it is too ductile it will deform when being passed forward and again block the head.

When HME is used in the fabrication of traditional solid dosage forms (i.e. tablets), the extrudates produced often undergo particle size reduction, to produce powders or granules with a suitable particle size for pharmaceutical processing (i.e. compression) (103). Unsurprisingly, brittle extrudates are more suitable in that regard, as brittle materials require less time and energy to be milled or granulated as opposed to ductile/flexible materials (182). Therefore, most pharmaceutically relevant polymers that are suitable for HME often yield brittle extrudates that readily fracture, and while this makes such polymers suitable for traditional pharmaceutical applications of HME, it renders those polymers unsuitable for FDM implementation.

From the TA test, it is clear that there are two groups of non-feedable polymers, both exhibiting brittle fractures, but differ in whether they show any strain bearing ability. The addition of plasticisers allows for an increase in the strain bearing ability of the filaments. As an example, pure Soluplus filament exhibited no strain bearing capacity in the TA test, whereas the addition of 10% PEO (SP) shifted the flexibility profile to the group exhibiting some strain bearing capacity, which is attributable to the plasticisation effect of PEG. Plasticisers used in the formulation of pharmaceutical blends for FDM printing include triethyl citrate, triacetin, various grades of polyethylenes (PEG and PEO), Tween 80, and glycerol (16,18,43,44,54). Over-plasticisation of filaments was observed to also cause a feeding defect; filaments HP40 and ST were found to coil inside the printing head when feeding was attempted. Those filaments possess little-to-no rigidity and would readily deform when any force is applied, with their texture being more similar to a fabric than to thermoplastic polymers. This indicates that the appropriate level of plasticisation is vitally important. The non-feedability of the over-plasticised filaments is because they readily deform inside the printing head making them unable to thread through the melting zone for deposition. This lack of rigidity sits in stark contrast to feedable filaments which are pliable enough to bend and deform on handling, but retain their original shape when force is released.

HPMCAS was selected as the platform polymer for drug loading and plasticization screening because, although the filament itself was not feedable, its flexibility profile

displayed some strain-bearing properties comparable to those of plasticised Soluplus (SP). The addition of 10% PEO was found to readily transform the filament into a feedable one. Furthermore, the addition of 10% paracetamol to the filament significantly changed its fracture pattern from a brittle fracture to a slightly more ductile fracture (Figure 3-16). This can be attributed to the plasticisation effect of the drug on the polymer. This is also supported by the fact that although HP10 did fracture (but was still feedable), filament HP10D did not, suggesting that the addition of 10% paracetamol further increased the strain-bearing ability of the filament.

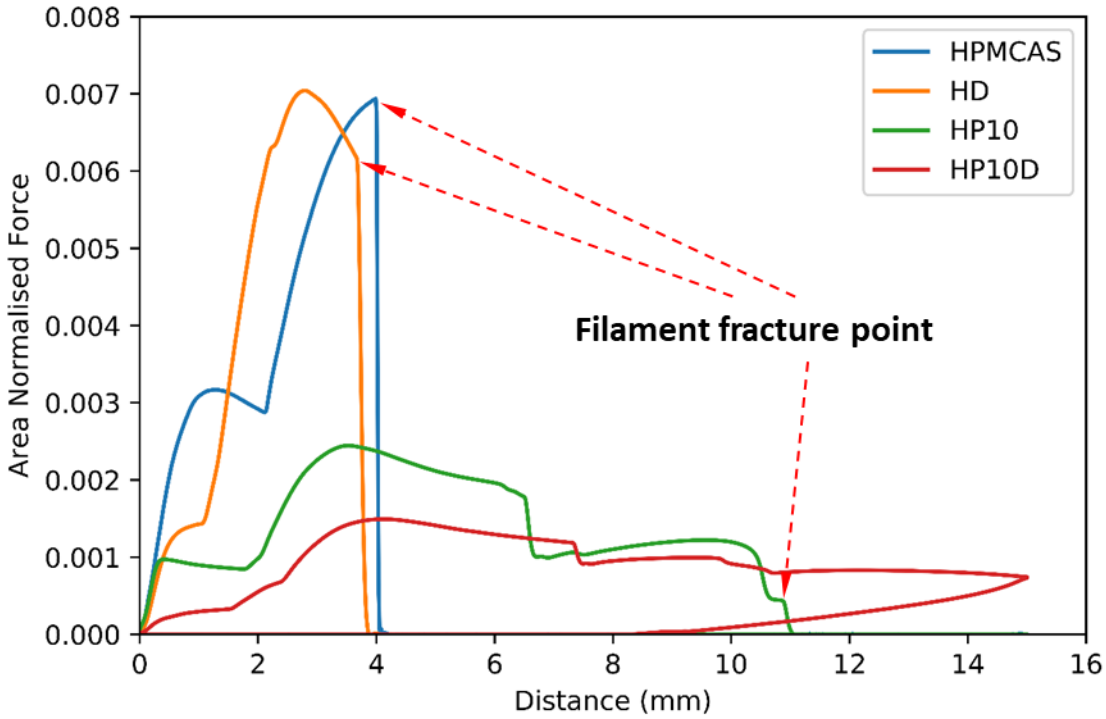

Figure 3-18: Impact of plasticisation on the flexibility profiles of HPMCAS-based formulations.

Filaments HP10, HP20, HP30, HP20D, and HP30D were all found to be feedable, suggesting that, at least for HPMCAS, there is a wide margin available for plasticiser loading without unduly influencing the mechanical properties. Increasing the PEO loading to 40% rendered the filament unfeedable (HP40), which most likely is due to the significant phase separation of HPMCAS and PEO as indicated by DSC (Figure 3-6). Inversely, filaments HP70 and HP90 were found to be feedable. The high PEO loading in comparison to HP10, HP20, and HP30 means that the filaments are most likely PEO-based with the HPMCAS being the second material in the matrix. This is further supported by the colour difference; HP10, HP20, and HP30 all had the characteristic pale yellow colour of hot-melt extruded HPMCAS (163), while filaments HP70 and HP90

were coloured identically to a PEO filament. Based on these results, it is reasonable to hypotheise that in the case of HPMCAS-PEO blends, the existence of a continuous phase (either HPMCAS or PEO) as the matrix is important to maintain the mechanical strength of the filaments.

3.4.3. Using flexibility profile towards screening

In terms of screening, the TA test was designed to simulate the conditions inside the printing head as closely as possible, the speed of compression was set to 3.15 mm/sec, which matches the speed of feeding inside the printer. Tested filaments were found to exist in either one of three categories; brittle filaments, string-like filaments, and pliable filaments. Brittle filaments are filaments that fracture during the analysis. String-like filaments are filaments could not be tested due to them being too flexible to maintain a vertically suspended straight beam shape and would collapse under their weight. Pliable filaments are filaments that would deform due to compression by the texture analyser, but recover when the force is removed.

It should be noted that the aforementioned categories do not have clearly defined boundaries, but are rather like a spectrum. Filaments SP, HD, and HPMCAS, despite being brittle filaments, did exhibit some pliability before fracturing. Inversely, filament HP10 did fracture during TA, but the predominating mechanical property it exhibited was pliability.

A high correlation between the feedable in-house filaments and the commercial filaments was observed. All feedable filaments displayed correlation scores > 0.50 with the commercial filaments, indicating the significance of the relationship between the flexibility profiles of the filaments and their feedability. However, no observations were made that indicate feedability existing as a spectrum property of the filaments (i.e. no filaments were found to be “more feedable than others”). Feedability of the filaments is a Boolean value, being either true or false. The TA data is a curve which is then normalised and sorted into categories by statistical analysis. The normalisation procedure used in the analysis removes differences in the absolute values of force applied. Mowiflex is feedable but notably much stiffer than all other tested materials, with the minimum required force for deforming Mowiflex being 120 N. The higher stiffness of Mowiflex filaments does not affect feedability and suggests that provided the shape of the overall flexibility profile follows the acceptable trend, the filament will be feedable regardless of the absolute

mechanical properties. To further simplify the analysis, rounding the mean correlation scores of each filament to the nearest integer (values < 0.5 are rounded down to 0, while values > 0.5 are rounded to 1) produces a method (Table 3-4) that simply sorts the filaments into feedable with a score of 1 (True) and non-feedable filaments with a score of 0 (False).

PCA was used as a qualitative statistical method to sort the different filaments using their flexibility profiles into feedable and non-feedable filaments. As seen in Figure 3-14, three clusters were observed in the rotated space plot of the filament flexibility profiles. The feedable and non-feedable filaments are well separated. Interestingly a cluster containing filaments that can be easily tuned to be feedable (referred in the Figure 3-14 as 'tunable' filament) is also isolated. Using HPMCAS as an example, as demonstrated in Figure 3-18, with the addition of a plasticiser, the non-feedable polymers and polymer blends (HPMCAS and HD) in this cluster can be transferred into feedable filaments (HP10 and HP10D). This data demonstrates that the flexible profile obtained from the TA test can be correlated to the feedability and used to predict the potential of the FDM printability of the targeted materials.

3.4. Conclusion

Mechanical properties of the HME filaments are an important property determining the processibility for FDM 3DP. By measuring the flexibility, one of the most directly relevant mechanical properties of the HME filaments, this study described the development of a simple method for screening the feedability and subsequent printability of HME filament for FDM printing. A wide range of filaments prepared using pharmaceutical polymers and excipients were tested to validate the method. The method described was able to accurately and reproducibly separate feedable and non-feedable filaments. Furthermore, coupled with PCA, more insights were gained in the aspects of how plasticisation and phase separation could influence the feedability of the pharmaceutical filaments.

Chapter 4
Investigating the impact of printing temperature and printing speed on pharmaceutically-relevant quality attributes

4.1. Introduction:

When characterising FDM printed objects, the non-pharmaceutical literature is largely concerned with the surface roughness and tensile strength of the fabricated objects (40,50–53). In pharmaceutical applications, when the FDM printed objects are intended to be used as dosage forms, achieving precise and highly reproducible dimensions and weight is critical. However, to date, there is no debate on whether the fundamental design of these prototype-building FDM printers is suitable for pharmaceutical manufacturing.

In the FDM printing process, the quality of the printed object is the result of a complex interplay between the properties of the printing material and the settings of the machine (both adjustable and non-adjustable), as shown in Figure 1-7. For the printer used in this work, the machine adjustable parameters are print speed; extrusion temperature; build plate temperature, and layer thickness. These represent the main variables in the FDM printing process. Temperature will affect the material properties, in particular, its rheological properties (183). These, in turn, will determine the flow out of the printing head, often known as melt flow, which is one of the factors investigated in this study, and the spread on the build plate which may then affect the reproducibility and dimensional precision of the printed object. Under some circumstances, high temperature may increase the fluidity of the printing material and cause unstable layer deposition (in the work presented herein, temperatures high enough to cause this phenomenon were temperatures greater than 120 °C). At the other extreme, low temperatures may cause reduced flow in the print head, resulting in a blockage or a flow rate too small to print adequately at some printing speeds (in the work presented herein, 70 °C was the only temperature low enough to cause insufficient polymer flow). Obviously, the range of temperatures at which a polymer can be printed without suffering from unstable layer deposition or insufficient polymer flow depends on the thermal and rheological properties of that particular polymer. Rheology also affects flow after deposition on the build plate. In this chapter, the interaction of the machine adjustable parameters and the print material rheological properties (as indicated by the melt flow index), and their effect on the reproducibility and adherence to design specification of the printed object are investigated. We note that some research suggests that computational factors such as slicing (the process by which the computer-generated 3D model is translated into movement instructions for the printer motors) algorithms could play a significant role in the overall quality of the printed object (48,49). However, computational parameters are outside the scope of this work, which is restricted to exploring the relevant physical parameters.

Furthermore, the ‘levelling’ of the printer build plate, a calibration process carried out to ensure that the distance between the printing head and the build plate is constant across the printing area should be performed to ensure the reproducible quality of the printed objects. It has been reported (54) that, for a machine of the same make and model as the one used herein, the outcome of this process could be operator dependent, indicating that the printing outcome may be irreproducible between operators. We report below on our examination of this problem.

Polycaprolactone (PCL) is one of the very few polymers approved for pharmaceutical use that are suitable for FDM without further plasticisation (43,180). PCL was used as the model polymer to investigate the effect of material and process parameters on the quality of printing. In the course of the work, it was noted that the first deposited layer tended to have different morphology to the layers above. A phenomenon which we have dubbed *The First Layer Effect* (FLE). Apart from the variables discussed above, the surface properties of the build plate may affect the first layer so the printing behaviour on different surfaces was also investigated. This is expected to have great importance for selecting the best build plate lining that allows the most suitable adherence of the printing material to the build plate during the building process and provides the easy peel-off of the object after the complete production of the printed dosage forms.

The work presented in this study summarises an investigation on the impact of FDM process parameters (printing speed and printing temperature) and how they affect the perceived quality attributes of a 3D printed dosage form (weight, weight uniformity, dimensional authenticity, road width, and reproducibility).

4.2. Materials and methods

4.2.1. Materials:

Materials used in this study were PCL (both as commercial filaments, and as a powder for HME), and acetylsalicylic acid (ASA).

4.2.2. Preparation of drug loaded filaments by HME:

Three drug loaded PCL filaments containing 5%, 10%, and 15% (w/w) ASA were prepared using HME. For each batch of the filament, the powder mixes were accurately weighed then thoroughly mixed using a mortar and pestle before extrusion. Extrusion was performed at 100 °C with a screw rotation speed of 100 RPM. All formulations were cycled in the extruder for 5 minutes to ensure homogeneous mixing of ASA and PCL before being flushed out.

4.2.3. FDM 3D printing of commercial filaments and drug-loaded filaments:

The solid dosage form used in this study was a film with the 25 mm in width, 25 mm in length, and 0.6 mm in thickness. The film is made up of 3 layers with a layer thickness of 0.2 mm. The film is comprised of 31 identical rods (rod dimensions: 0.4 mm wide, 0.2 mm thick, and 25 mm long). The design of the film is shown in Figure 4-1. The Film was designed using Blender software and was then exported as an STL file. The STL file was printed using MakerBot® MakerWare™.

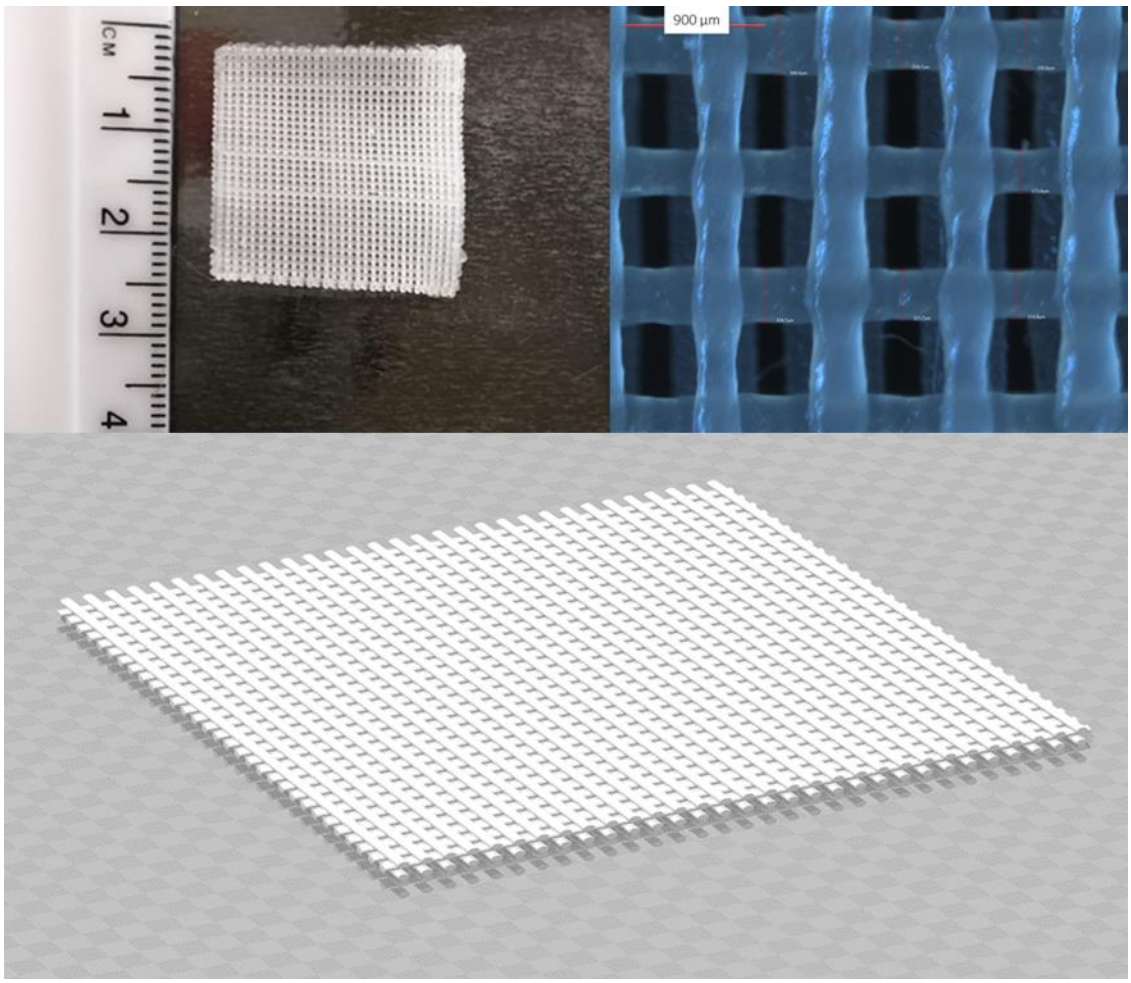

Figure 4-1: Macroscopic (left), light microscopy image (right), and the computer-generated image of the STL file (bottom) design of the 3D printed film.

Twelve sets of different printing experiments were conducted, each varying either one of three factors (nozzle temperature, build plate temperature, and printing speed), as seen in Table 4-1. Five films were printed using each set of printing parameters. Each printed film was weighed and the dimensions of the films were then accurately measured using a digital calliper. Printing of the drug-loaded filaments was performed using a nozzle temperature of 100 °C, an unheated build plate and using a printing speed of 90 mm/sec.

Table 4-1: Experimental parameters used for printing the selected 3D object using MakerBot® Flexible filament

Nozzle Temperature (°C)	Platform Temperature (°C)	Printing Speed (mm/sec)
100	30	30
100	30	90
100	30	160
110	30	30
110	30	90
110	30	160
120	30	30
120	30	90
120	30	160
100	45	30
100	45	90
100	45	160

4.2.4. Melt Flow Index measurements:

The melt flow index (MFI) of the filaments was measured using an adaptation of the ISO 1133-1 standard method (184). The printing head of the MakerBot® Replicator 2X was detached from its roller feeding zone and used to melt the filaments. A piston attached to a metal weight of 80 g was used to propel 2 cm slices of the filament through the nozzle (Figure 4-2). The filament melt flowing from the nozzle was collected at specified time intervals and weighed. The mass of the polymer (in milligrams) extruded per second was regarded as the MFI of the polymer. Using this adapted method maintains the gravimetric flow of the polymer melt that is characteristic of standard MFI measurements, but over the relevant capillary diameter of the printing nozzle. The MFI measurements for PCL were performed using a temperature range of 70 ºC to 130 ºC.

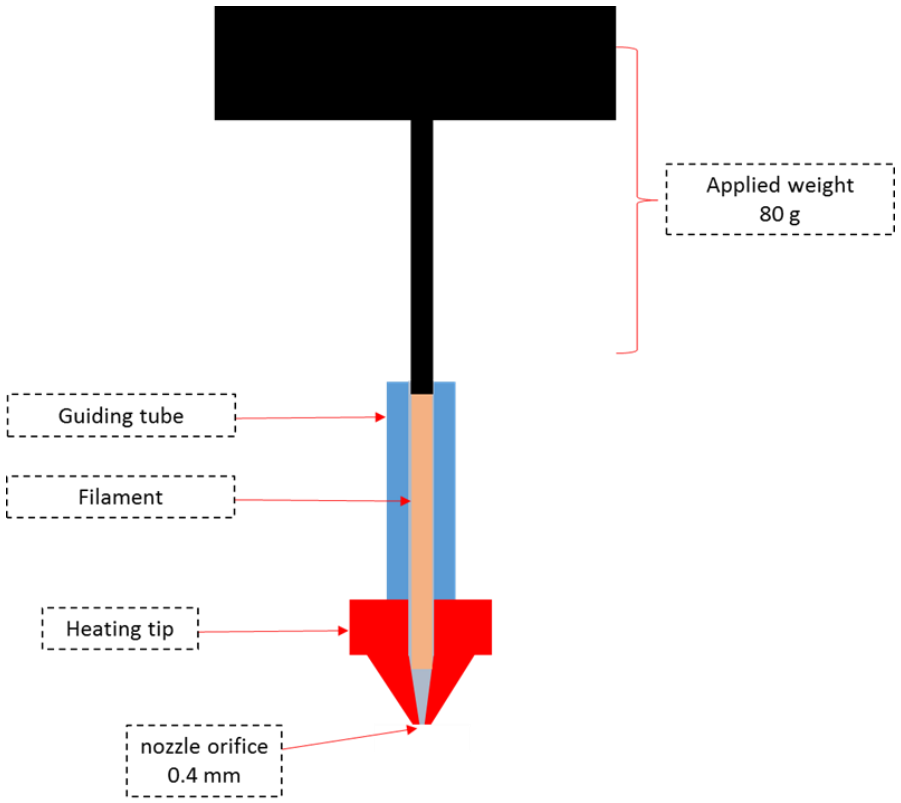

Figure 4-2: Illustration for the method adapted for measuring the melt flow index for different materials

The quantity (in milligrams) of material deposited per second during an actual FDM printing process is defined in this study as the FDM-MFI. The FDM-MFI values of the PCL filaments were measured at three different printing speeds (30 mm/sec, 90 mm/sec, and 160 mm/sec) over a range of processing temperatures (70-130 °C). For both MFI and FDM-MFI measurements, the rate of deposition of the objects was then expressed as weight deposited per unit time (mg/min).

4.2.5. Levelling of the build plate of the printer:

Two investigations of the platform levelling were performed. Inter-person calibration: the platform was levelled by two operators, then six square films were printed and their weights and dimensions quantified. Same person inter-day calibration: the platform was levelled by the same operator on two different days; then, a set of six squares were printed and their weights and dimensions were quantified. The object used for calibration was a simple square design with an edge length of 10 mm and a thickness of 1 mm printed using standard printer settings at 100 ºC. The printed squares were accurately weighed and measured with a digital calliper. The measured values were compared via an Independent

Sample T-Test, the null hypothesis being there is no significant difference in the weight and dimensions of the films when different operators levelled the printer.

Levelling was conducted as per the standard printer levelling procedure outlined in the user manual of the printer (39). The card supplied with the instrument was placed between the nozzle and the build plate at various positions around the build plate and the levelling screws were adjusted until the card can just slide between the build plate and the nozzle.

4.2.6. Printing on different surfaces

The FLE was further investigated by printing the PCL films on three different surfaces, Kapton® (polyimide) Tape, aluminium, and glass. Aluminium and glass were secured to the build plate using double-sided adhesive tape, to ensure that there was no movement of the test surface during printing. All of these printing experiments were conducted using a nozzle temperature of 100 °C and a printing speed of 90 mm/sec. The build plate was levelled following the protocol described in section 4.2.5. before each printing attempt.

4.2.7. Characterization of printed solid dosage forms

Microscopic images were acquired using a Linkam Imaging Station, equipped with a Linkam MDS600 heating/cooling stage (Linkam Scientific Instruments, Tadworth, United Kingdom). Image analysis (dimensions measurements) was conducted using LINK software version 1.0.5.9 (Linkam Scientific Instruments, Tadworth, United Kingdom) to measure the road widths of the 3D printed objects.

ATR-FTIR spectroscopy and DSC were used to characterise all materials used in this study. ATR-FTIR was conducted using a scanning range of 4000 cm^{-1} – 600 cm^{-1}. DSC was used to characterize the pure materials (PCL commercial filament, PCL powder, and ASA powder), the physical mixes, and extruded filaments. PCL powder was characterised using a heat-cool-reheat method with a range from 20 ºC to 120 ºC, followed by cooling to -90 ºC, then reheating to 120 ºC. ASA powder and physical mixes of all three formulations were scanned using a heat-cool-reheat method; samples were tested over a range of 20 ºC to 150 ºC, then cooled to -90 ºC, and then reheated to 150 ºC. All extruded filaments were characterized using a heat-cool-reheat method using a temperature range of -90 ºC to 150 ºC. A heating/cooling rate of 10 ºC/min was used for all experiments. All samples were equilibrated for 3 minutes at either 20 ºC or -90 ºC at the start of each experiment. All characterization experiments were carried out in triplicates.

4.2.8. Statistical Analysis

Independent sample T-tests were conducted using Microsoft Excel (version 2016) expanded with the statistical data analysis add-on.

Summed Standard Deviation (SSD) was calculated as follows: For each value of temperature (T) and speed (S), the normalised standard deviations ($P^{'}$) of the measured parameters weight (M), length (L), width (W), thickness (D), and road width (R), were calculated using the equation.

$$\boldsymbol{P_i^{'}} = (\frac{\sigma_i^p}{P_i})_{T,S} \qquad \textit{(Equation 4-1)}$$

Where $\boldsymbol{P_i}$ is the value of the measured parameter at a fixed value of S and T and σ_i^p is its standard deviation. These were summed as shown in equation 2.

$$\boldsymbol{SSD} = \sum_{\substack{S=0 \\ T=0}}^{\substack{S=n \\ T=n}} [\boldsymbol{P^{'}_M + P^{'}_L + P^{'}_W + P^{'}_D + P^{'}_R}]_{T,S} \qquad \textit{(Equation 4-2)}$$

Principal Component Analysis (PCA) was conducted on all the measured responses using IBM® SPSS statistics (version 25). Following the Kaiser rule, only principal components with an eigenvalue $\geqslant$ 1 were extracted (n = 2), yielding a total explained variance of 82.15% (Principal Component 1: 57.77%. Principal Component 2: 24.38%). The unrotated components matrix showed no factor that could be explained solely by either principal component (coefficient < 0.4), therefore, Varimax rotation was conducted such that each factor is solely described by a single principal component. The loadings plot was used to extract variable scores for each of the two factors (printing temperature, and printing speed), the scores were imported into Microsoft Excel and used to generate a biplot (171,172).

4.3. Results

4.3.1. Material characterisation:

4.3.1.1. Differential Scanning Calorimetry

Drug incorporation can often cause changes to the printability of polymeric filaments, in most cases due to the plasticisation effect of the drug when a molecular dispersion is formed between the drug and the polymer. Three levels of drug loading were used to create filaments that were either true molecular dispersions or supersaturated with the crystalline drug in the filaments. DSC and ATR-FTIR spectroscopy were used to characterise the physical state of the ASA in the filaments prepared by HME.

Figure 4-3 shows the DSC thermograms of PCL (both powder and commercial filaments) and pure ASA powder. The T_g of PCL was seen at approximately -64 °C in both the powder and commercial filaments. T_m onset was seen at approximately 53 °C, with the peak midpoint at 59 °C for the commercial filament, and 57 °C for the powder. T_m of ASA was seen at 141 °C.

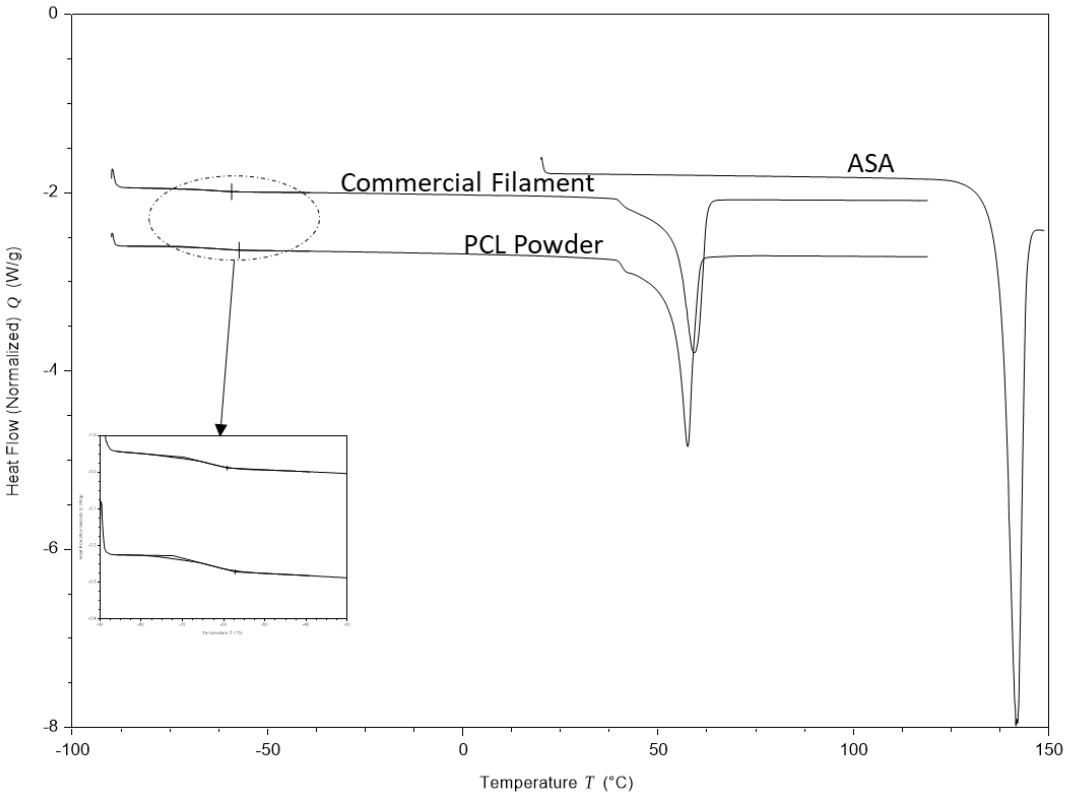

Figure 4-3: DSC thermograms of ASA, PCL commercial filament, and PCL powder

For the powder mixtures (Figure 4-4), the T_m of ASA was not seen during the first heating cycle in neither the 5% nor the 10% ASA-to-PCL ratios. In the 15% ratio, an endothermic

event occurring at approximately 135 °C was seen. During the second heating cycle of the powder mixtures, significant changes in the glass transitions were observed; the T_g of the 5% was seen at -70.74 °C, the T_g of the 10% mixture was seen at -63 °C, and the T_g of the 15% mixture was seen at -55 °C. A depression in the T_m of PCL was also seen in the second heating cycle of the powder mixtures. The magnitude of this T_m depression is notably inversely proportional to the %ASA within the mixture.

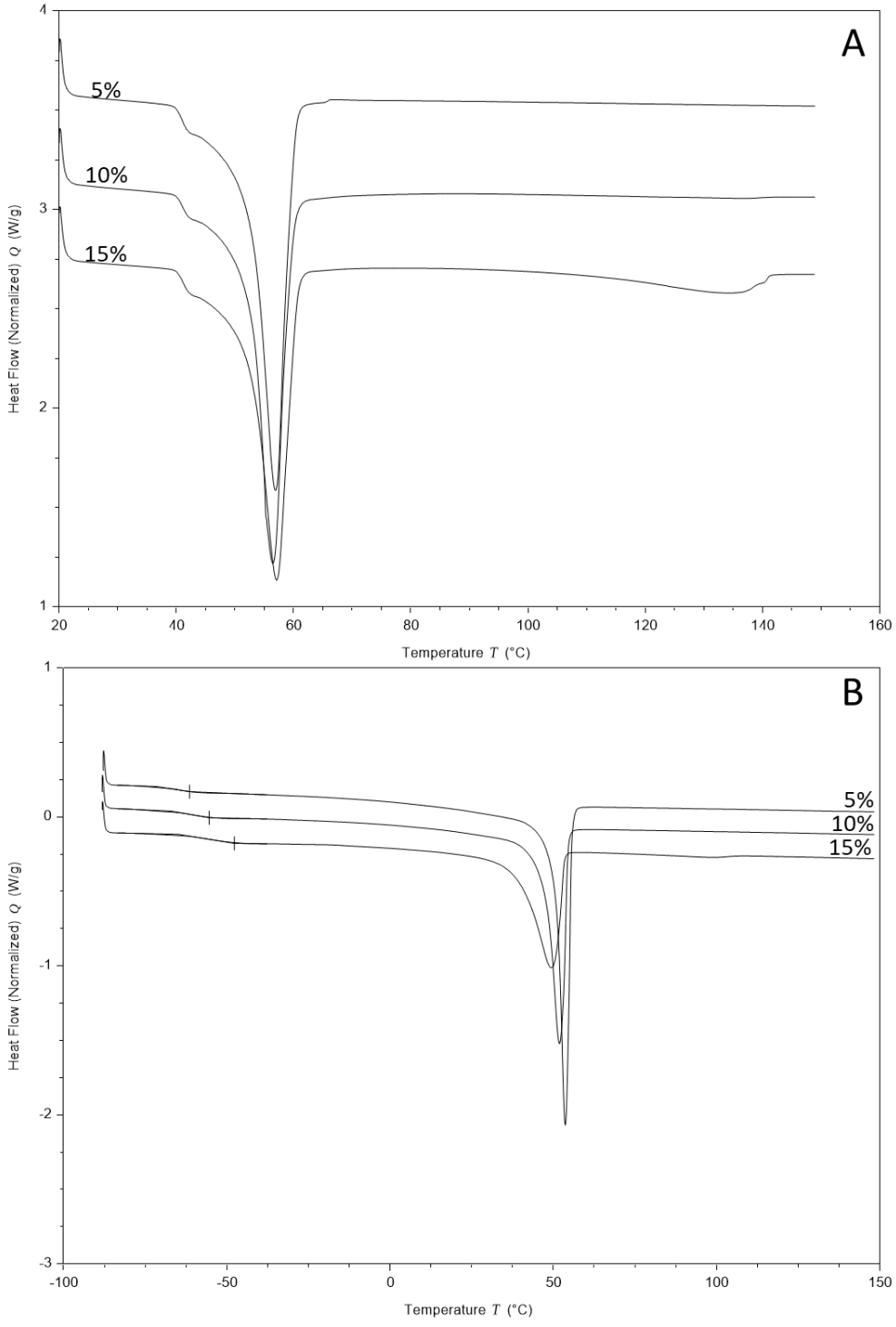

Figure 4-4: DSC thermograms of the PCL-ASA powder mixtures. A: first heating cycle. B: second heating cycle

Figure 4-5 shows the DSC thermograms of the ASA-PCL melt-extruded filaments. In the 5% melt-extruded filament, the T_g of PCL was seen at -64 °C. The T_g of PCL was seen at -61 °C in both the 10% and 15%. Notably, an endothermic event was seen in the DSC of the 15% filament at approximately 80 °C.

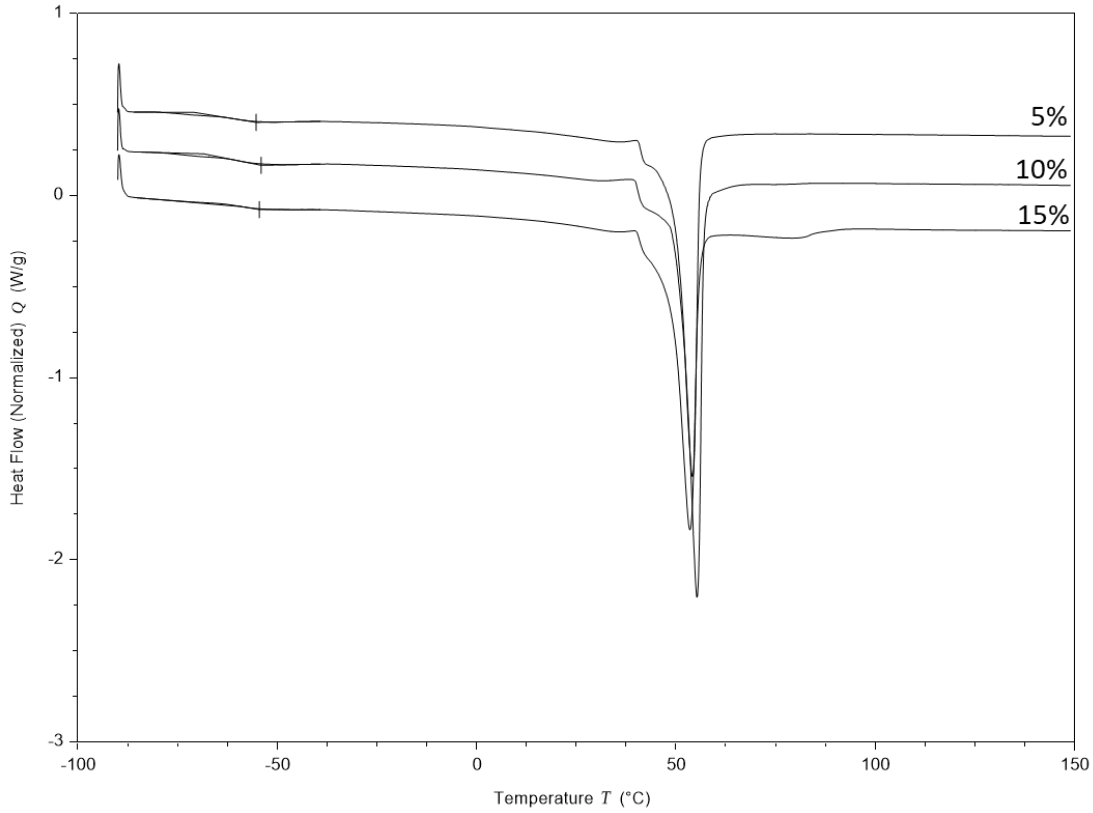

Figure 4-5: DSC thermograms of melt-extruded PCL-ASA filaments.

4.3.1.2. Attenuated Total Reflectance – Fourier Transform Infrared Spectroscopy

Figure 4-6 shows the ATR-FTIR spectra of PCL, and ASA (both as a crystalline powder and a melt), and the ASA-PCL formulations. Absorption bands characteristic of PCL include the C=O stretching at 1725 cm^{-1}, C-O stretching at 1293 cm^{-1}, and the C-OH stretching at 1163 cm^{-1}.

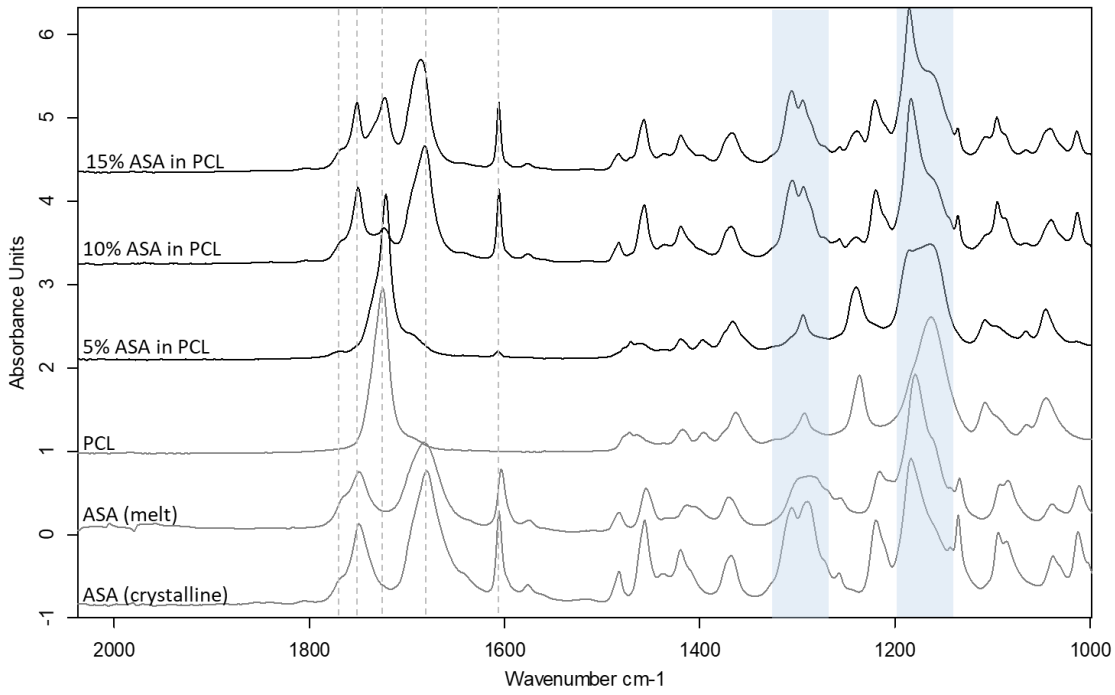

Figure 4-6: ATR-FTIR spectra of the melt-extruded filaments and their raw materials.

Bands characteristic to crystalline ASA are the C=O stretching peaks at 1749 cm^{-1} and 1679 cm^{-1}, corresponding to the carboxyl groups in the acetate and salicylate moieties comprising the structure of ASA, aromatic C=C stretching at 1606 cm^{-1}, and a strong doublet peaking at 1306 cm^{-1} and 1294 cm^{-1}, likely corresponding to C-O stretching of the acetate moiety, and a strong peak at 1184 cm^{-1} corresponding to the C-OH stretching of the salicylate moiety. In the ASA melt, the carboxyl band at 1679 cm^{-1} was shifted to 1683 cm^{-1}, the C=C benzene stretch was shifted to 1603 cm^{-1}, the doublet at 1306 cm^{-1}/1294 cm^{-1} morphed into a broad singlet peak centred around 1288 cm^{-1}. The C-OH peak was shifted to 1179 cm^{-1}.

The spectrum of the 5% formulation was dominated by PCL bands. The C=O stretching band of PCL was seen, albeit shifted to 1722 cm^{-1}. The C=C stretching of the benzene ring in ASA and the C-O stretching of PCL are also visible, without any shifts. A broad C-OH peak was seen, centred around 1165 cm^{-1}, the shape and the significant broadening of this peak suggests that it consists of the merged C-OH peaks of PCL and ASA.

In the 10% formulation, ASA bands are more prominent. The carboxyl stretching peaks of ASA can both be seen, without any shifts from those seen in crystalline ASA. The C=C stretching peak at 1606 cm^{-1} is more prominent. The C-O doublet which was absent in

the 5% is now clearly visible, with the peak at 1290 cm^{-1} being shifted to 1294 cm^{-1}. Furthermore, the C-OH peak of ASA is now clearly visible, having shifted to 1182 cm^{-1}, this peak also notably has a shoulder, which is absent from the peak in crystalline ASA but is present in the spectrum of the ASA melt.

The spectrum of the 15% showed all the characteristic peaks of both ASA and PCL very clearly. The C=O stretching peaks of both ASA and PCL are very prominent, the two C=O stretching bands of ASA can be seen at 1686 cm^{-1} and 1751 cm^{-1}. The C=O stretching of PCL can be seen at 1723 cm^{-1}. Similar to the 10% formulation, the C-O doublet is visible at 1306 cm^{-1}, with the peak previously seen at 1290 cm^{-1} having shifted to 1294 cm^{-1}. The C-OH stretch of ASA was seen at 1185 cm^{-1}, albeit with much broader and clearly defined shoulder, likely caused by merging with the C-OH peak of PCL.

The results indicate the formation of a molecular dispersion of ASA in PCL at 5% drug loading, whereas both the 10% and 15% formulation contain a crystalline fraction of ASA. The shifted peaks of the C-O and C-OH groups indicate the molecular interaction of ASA and PCL via hydrogen bonding at the carboxyl groups, as seen in Figure 4-6.

4.3.2. Impacts of build plate levelling:

It has been previously reported in the literature that the levelling of the build plate of MakerBot® printers causes a significant difference in the weights of the 3D printed objects when conducted by different operators (54). In an attempt to prevent this discrepancy from misattributing other findings of this work, two investigations of the platform levelling were performed. Inter-person calibration: the platform was levelled by two operators, then six square films were printed and their weights and dimensions quantified. The results of the inter-person calibration are shown in Table 4-2.

Table 4-2: Effect of levelling by different operators on the weight and dimensions of the printed objects. RSD: Relative standard deviation ($(Standard\ deviation\ /\ Mean) \times 100$).

Operator I				
n	**Thickness (mm)**	**Length (mm)**	**Width (mm)**	**Weight (mg)**
1	1.09	9.92	10.01	110.6
2	1.04	10.03	10.10	114.6
3	1.07	10.00	10.16	113.4
4	1.05	10.00	10.09	111.0
5	1.10	9.91	10.02	109.8
6	1.05	9.99	10.20	111.0
RSD	2.25%	0.48%	0.74%	1.65%
Operator II				
n	**Thickness (mm)**	**Length (mm)**	**Width (mm)**	**Weight (mg)**
1	1.03	10.05	10.16	107.7
2	1.08	10.05	10.23	112.6
3	1.04	10.06	10.13	111.1
4	1.06	10.05	10.20	112.5
5	1.04	9.96	10.18	108.7
6	1.06	9.94	10.10	110.1
RSD	1.71%	0.53%	0.46%	1.8%
Independent Sample *T*-Test				
P-Value (Length)		*P*-Value (Width)	*P*-Value (Thickness)	*P*-Value (Weight)
0.223		0.101	0.127	0.137

For the same person inter-day calibration, the platform was levelled by the same operator on two different days; then, a set of six squares were printed and their weights and dimensions were quantified. The object used for calibration was a simple square design with an edge length of 10 mm and a thickness of 1 mm printed using standard printer settings at 100 ºC. The results are shown in Table 4-3.

Table 4-3: Inter-day variation in levelling on the weight and dimensions of the printed objects. RSD: Relative standard deviation ((Standard deviation/Mean)×100).

Day 1				
n	**Thickness (mm)**	**Length (mm)**	**Width (mm)**	**Weight (mg)**
1	1.09	9.92	10.01	110.6
2	1.04	10.03	10.10	114.6
3	1.07	10.00	10.16	113.4
4	1.05	10.00	10.09	111.0
5	1.10	9.91	10.02	109.8
6	1.05	9.99	10.20	111.0
RSD	2.25%	0.48%	0.74%	1.65%
Day 2				
n	**Thickness (mm)**	**Length (mm)**	**Width (mm)**	**Weight (mg)**
1	1.02	10.08	10.11	108.7
2	1.04	10.09	10.12	108.4
3	1.07	10.03	10.14	105.2
4	1.03	10.06	10.11	107.9
5	1.02	10.03	10.08	104.5
6	1.04	10.06	10.14	109.7
RSD	1.83%	0.25%	0.23%	1.93%
Independent Sample *T*-Test				
P-Value (Length)		*P*-Value (Width)	*P*-Value (Thickness)	*P*-Value (Weight)
0.004		0.213	0.04	0.006

4.3.3. Impacts of melt flow of the printed materials:

The Melt Flow Index (MFI), is defined by the ISO standard 1133-1 as *"the mass of the molten polymer, in grams, that flows through a capillary of a specific diameter in 10 minutes"* (184). The MFI of a filament is often cited as one of the key factors defining the success of an FDM printing process (43,180,185). The MFI is highly associated with the thermal viscosity of the filament materials at a certain printing temperature (183). Therefore, MFI measurements (which describe the amount of PCL deposited due to its melt flow) were compared to the amount deposited during FDM printing. The results are presented below in Figure 4-7.

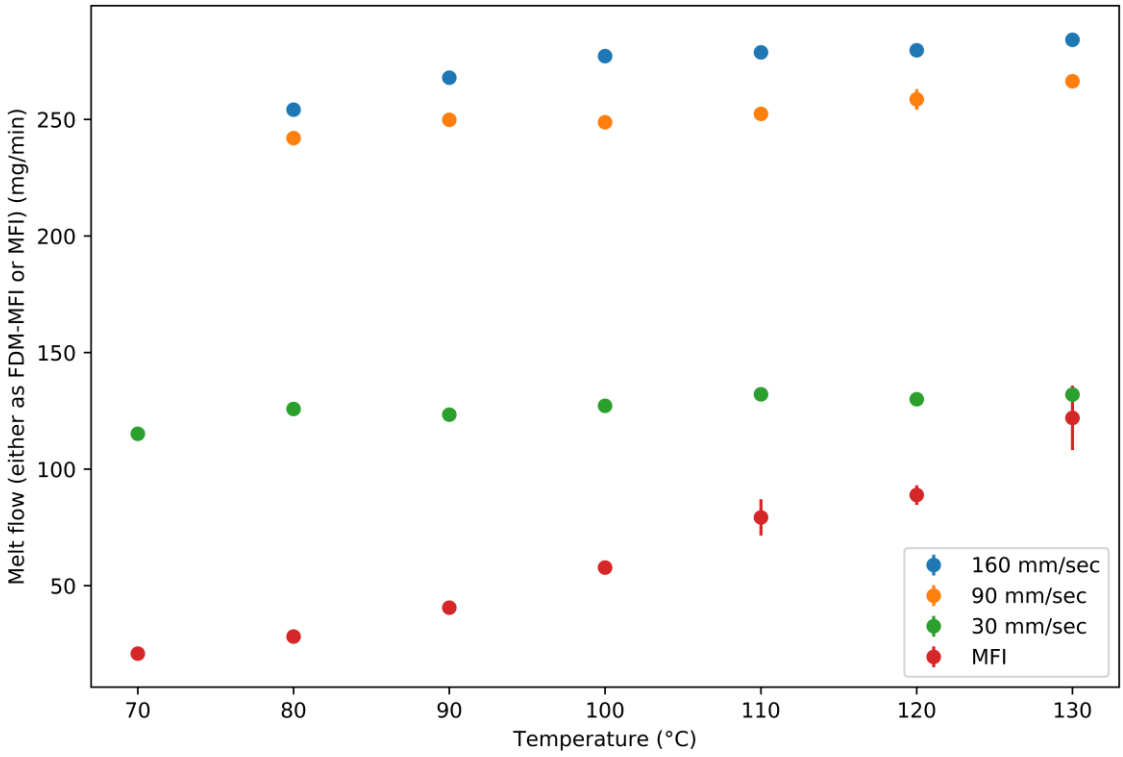

Figure 4-7: FDM-MFI and MFI (secondary axis) measurements of PCL commercial filament

MFI measurements showed that PCL has a measurable MFI at a temperature of 70 ºC; however, the printing of PCL was only possible at this temperature at the lowest speed of 30 mm/sec. Objects printed at 80 ºC and either 90 mm/sec or 160 mm/sec were distorted, with very poor printing quality and erratic melt deposition. Therefore, samples printed at 70 ºC and 80 ºC were disregarded. This suggests that there is a lower limit to the melt flow index below which good quality printing is not possible.

Despite the temperature dependence of rheology seen in the MFI experiments, there was a very weak temperature dependence of deposition rates when printed using FDM. This implies that over the range of relevant printing temperatures, the change in the melt flow of the filament is not too great to significantly impact the amount of material being deposited by the print head. The only effect was seen at 70 ºC where printing was only possible at a printing speed of 30 mm/s. This leads to the hypothesis that, provided that the operating speed is sufficient to overcome the viscosity of the polymer melt, the contribution of operating temperature to the printability of the material is not of prime importance.

4.3.4. Impact of processing conditions on weight uniformity:

Figure 4-8 shows the weights of the printed films at different processing conditions. At a fixed printing speed, increasing the printing temperature caused an increase in the weights of the printed grids. The standard deviations of weights does not seem to follow any trends either with temperature or printing speed. The largest recorded standard deviation was ±3.2 mg at 90 mm/sec and 120 ºC. The second largest being ±3.0 mg at 30 mm/sec and 70 ºC, and the third-largest being ±2.4 mg at 30 mm/sec and 110 ºC. Notably, fixing the printing speed at 160 mm/sec yields the narrowest standard deviations, with the smallest standard deviation at that speed being ±0.1 mg at 100 ºC, and the largest being ±0.9 mg, seen at both 120 ºC and 130 ºC. Even though all the reported standard deviations fall well within acceptable limits for weight uniformity specified in the pharmacopoeias, it is worth noting that changing the printing conditions was seen to substantially impact weights of the printed objects, by as much as 31.3 mg. The lightest printed object weighed 169.1 mg (±0.5 mg, printed at 70 ºC, and 160 mm/sec), and the heaviest printed object weighing 200.3 mg (±1.5 mg, printed at 130 ºC, and 30 mm/sec).

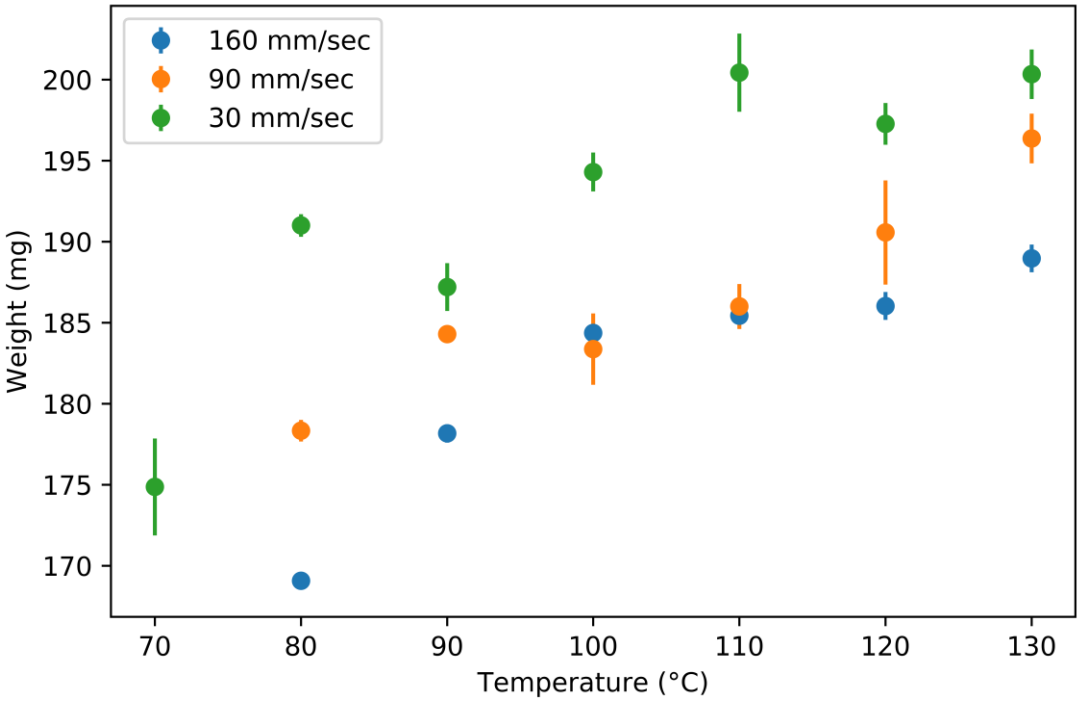

Figure 4-8: weights of the 3D printed films

On average, the impact of the printing temperature on melt deposition rate was not as significant as printing speed. It appears that it may impact the reproducibility of the weights of the printed objects.

4.3.5. Impact of processing conditions on dimensional authenticity:

Figure 4-9 shows the impact that different printing conditions had on the lengths and widths of the 3D printed films. Printing at 90 mm/sec and 160 mm/sec yielded objects that possessed greater length and lower width than the target (average dimensions being 25.29 mm ± 0.06 mm x 24.95 mm ± 0.04 mm for 90 mm/sec, and 25.29 mm ± 0.11 mm x 24.93 mm ± 0.04 mm for 160 mm/sec), showing no significant difference in dimensions between the two conditions. However, printing at 30 mm/sec yielded objects that were smaller than the target geometry of 25 mm x 25 mm (with the films being, on average, 24.68 mm ± 0.06 mm x 24.33 mm ± 0.11 mm). At this speed, no changes in length and width relative to changing the temperature were observed. In terms of reproducibility of lengths and widths, none of the three printing speeds showed remarkably different results, with no significant differences between the standard deviations of dimensions between the three printed conditions.

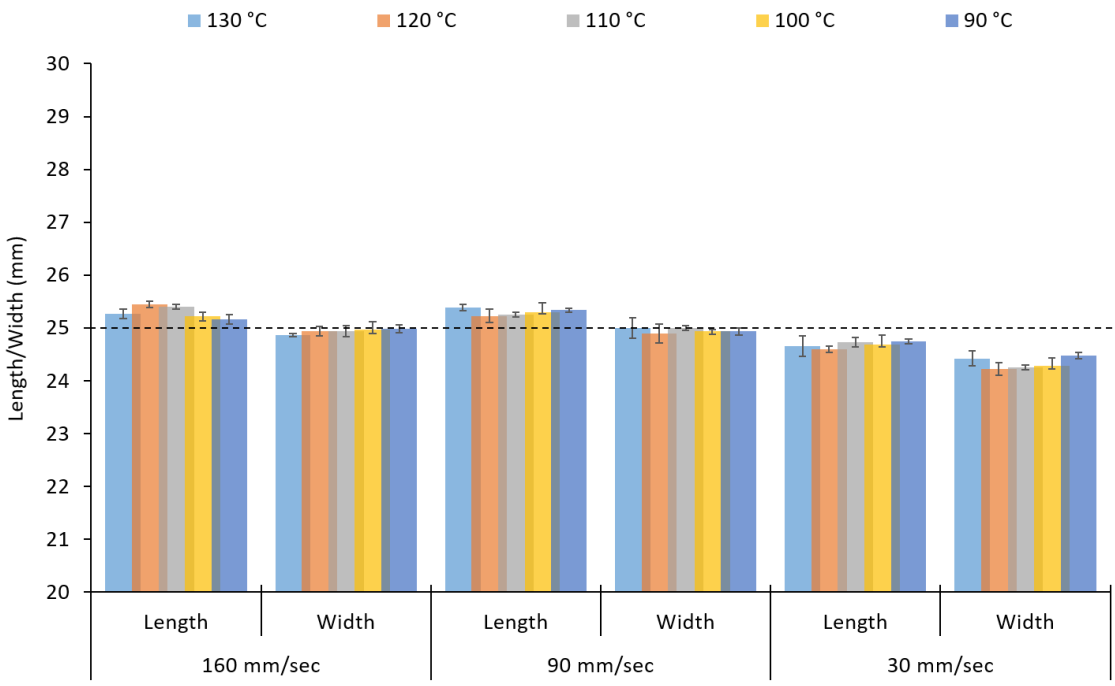

Figure 4-9: Impact of processing conditions on the lengths and widths of the 3D printed films

Figure 4-10 shows the impact of printing conditions on object thickness. The thickness of the 3D printed objects tended to decrease with increasing temperature for both 160 mm/sec and 30 mm/sec, going from 0.65 mm ± 0.00 mm at 90 ºC to 0.61 mm ± 0.01 mm at 130 ºC when printed at 30 mm/sec, and from 0.65 mm ± 0.02 mm to 0.59 ± 0.01 mm when printing at 160 mm/sec. Objects printed at 90 mm/sec had, on average, consistent

thickness, independent of printing temperature. Furthermore, printing at 90 mm/sec appears to have the most reproducible object thicknesses, with the narrowest recorded standard deviation at said speed being ± 0.00 mm, and the widest being ± 0.01 mm (within the limits of detection of the digital calliper used).

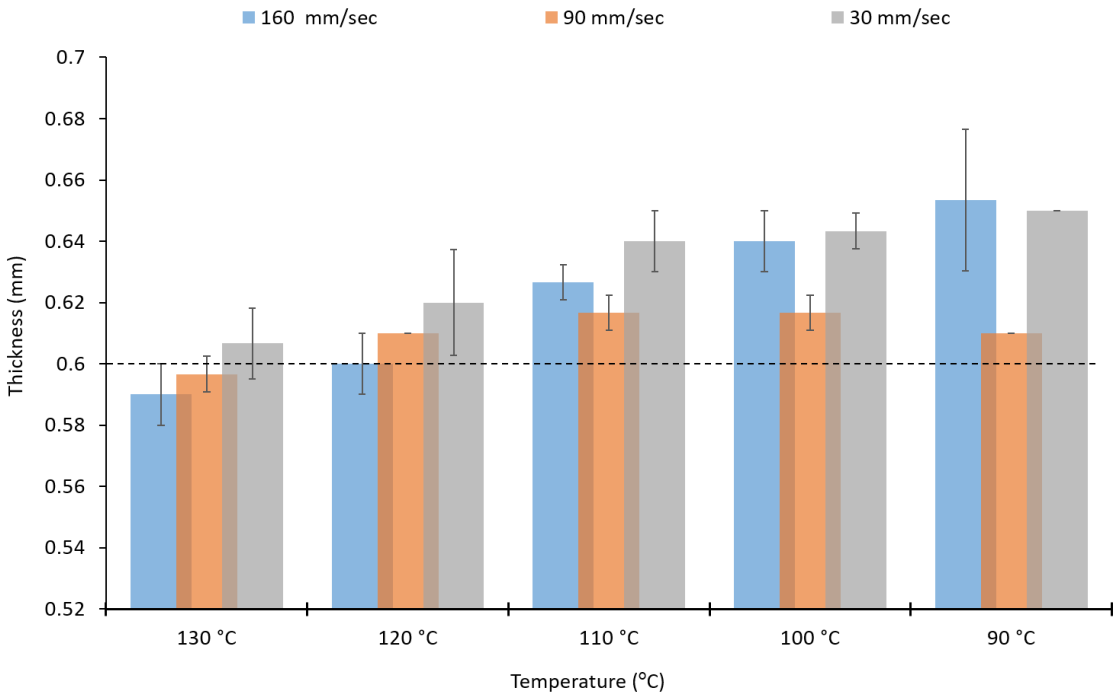

Figure 4-10: Impact of processing conditions on the thickness of 3D printed films

Microscopic imaging of the printed films revealed that the road width of the first layer is much larger than that of the subsequent layers, and the width of the first layer appears to be correlated to the nozzle temperature. This correlation between first layer road width and the reduction of object thickness with increasing temperature suggests that when the first layer is deposited on the build plate, the fluid melt spreads sideways, increasing in width and decreasing in thickness, resulting in the observed effect.

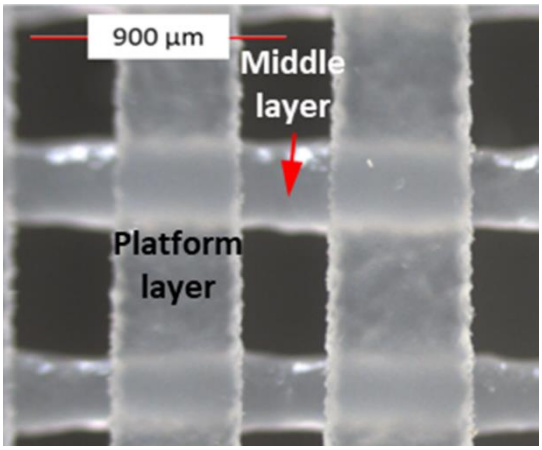

Figure 4-11: The First Layer Effect.

For the commercial printers, the pre-set (target) object parameters are dimensions instead of weight. Therefore, it is important to understand the effect of the process parameters by comparing the measured printed object dimensions to the target values pre-set by the STL file. Despite the source STL file being designed as a square in this study, all the objects printed displayed a difference between length and width. To avoid ambiguity, length was defined as the dimension parallel to the roads of the first layer, and width as the dimension perpendicular to the roads of the first layer. The impact of the printing temperature on the dimensions (width, length, and thickness) of the objects are illustrated in Figures 4-9 and 4-10. For each printing condition, the length of the objects was found to be larger than the width of the objects. The printing temperature showed no significant effect on the reproducibility of the length and width of the printed films at a fixed printing speed.

4.3.6. Impact of processing conditions on the road width:

Figure 4-12 shows the average road width of each layer under different printing conditions. The top layer is the closest to the nozzle. The platform layer is the bottommost layer resting on the build plate of the printer.

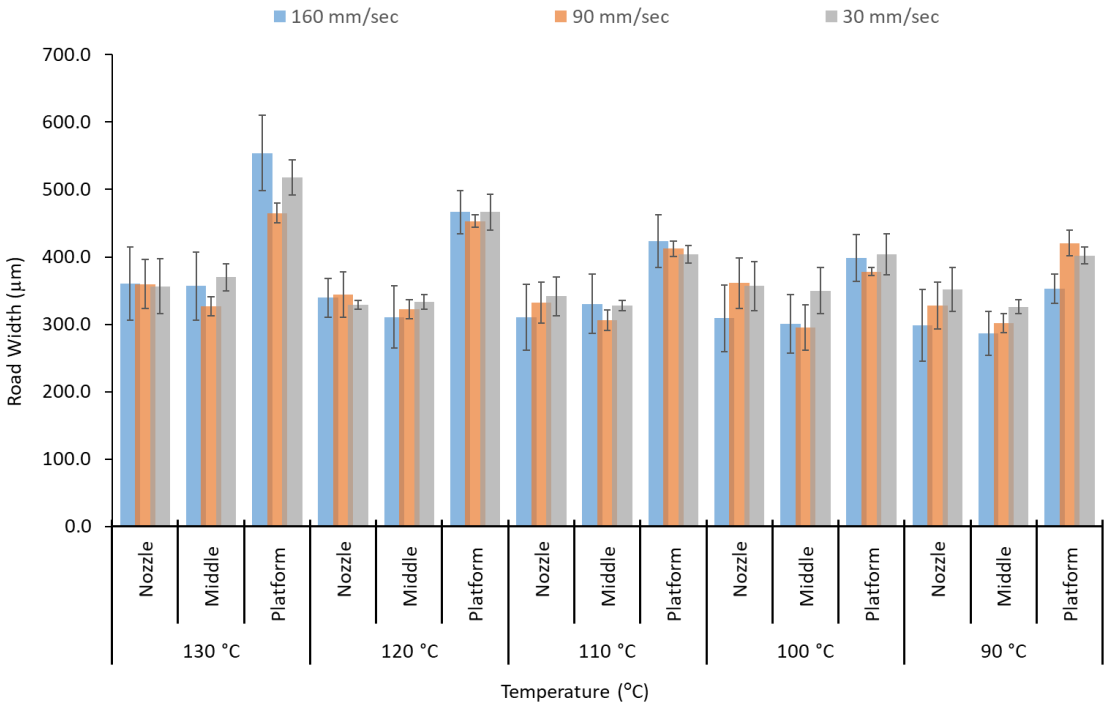

Figure 4-12: Impact of processing conditions on the road widths of the printed films

No significant difference was seen between the top and middle layers of the objects, regardless of printing conditions. The average road width for the top layer was 347.0 µm ± 12.00 µm at 30 mm/sec, 345.0 µm ± 15.37 µm at 90 mm/sec, and 323.5 µm ± 25.62 µm at 160 mm/sec. The average road width for the middle layer was 341.3 µm ± 18.46 µm at 30 mm/sec, 310.4 µm ± 13.56 µm at 90 mm/sec, 316.8 µm ± 27.45 µm at 160 mm/sec. The platform layer displayed a larger road width than the corresponding top and middle layers at every printing condition, with the average road width of the platform layer being 438.8 µm ± 51.79 µm at 30 mm/sec, 425.8 µm ± 34.56 µm at 90 mm/sec 436.1 µm ± 68.63 µm at 160 mm/sec.

The road width of the platform layer was also observed to vary proportionally to printing temperature. There was a notable decrease in the average road width of the first layer at different printing temperatures; at 30 mm/sec, the road width increased from 402.1 µm ± 12.9 µm at 90 ºC to 517.5 µm ± 26.0 µm at 130 ºC. At 90 mm/sec, the road width increased from 420.5 µm ± 19.1 µm at 90 ºC to 465.2 µm ± 14.9 µm. At 160 mm/sec, the road width increased from 422.0 µm ± 35.7 µm at 90 ºC to 554.0 µm ± 55.9 µm at 130 ºC. Due to the platform layer being the first layer constructed during the fabrication of the object, this phenomenon has been dubbed *The First Layer Effect* (FLE). This spreading effect is

assumed to be caused by the nature of the interaction of PCL with the surface of the Kapton® tape. Therefore, printing was attempted on different surfaces.

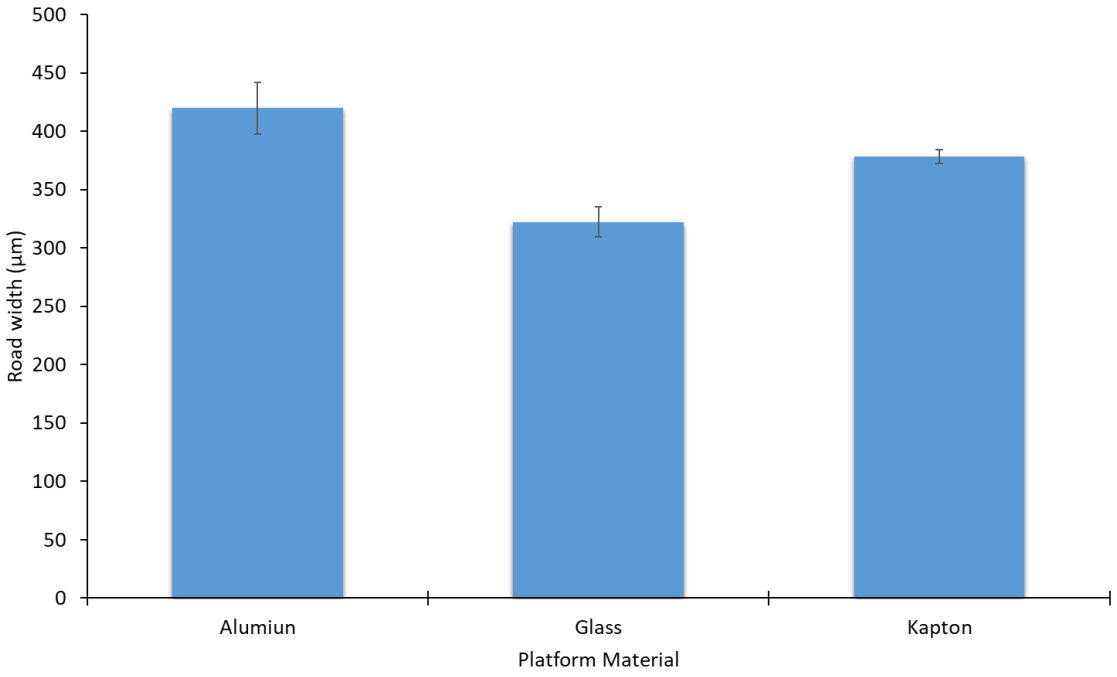

Figure 4-13: Road widths of the first layer when printing on different platform surfaces.

Printing on different surfaces yielded different spreading amounts (Figure 4-13). Building on glass was found to yield the narrowest average road width (322.3 µm ± 13.03 µm). Building on aluminium was found to yield the widest road width (419.8 µm ± 22.00 µm). The increased spreading with temperature when printing on Kapton® is likely due to decreased viscosity of PCL at higher temperatures allowing it to flow more prior to solidifying.

When printed at higher temperatures (> 110 °C) PCL was found to bind strongly to the Kapton® tape. When printed at lower temperatures (i.e. 80 °C – 100 °C), the PCL films were easily removed. However, no sticking to aluminium or glass was observed. This is most probably caused by weak interactions between PCL and Kapton® at higher temperatures.

4.3.7. Impact of drug incorporation

It would be expected that a drug-polymer molten solution would exhibit different spreading behaviour when printed on the surface since the incorporation of the drug would be expected to alter the physical properties of the mix (99). This was investigated

by printing ASA-loaded PCL filaments at a median condition of 100 °C and 90 mm/sec. The results can be seen in Figure 4-14 against a placebo filament printed at the same conditions.

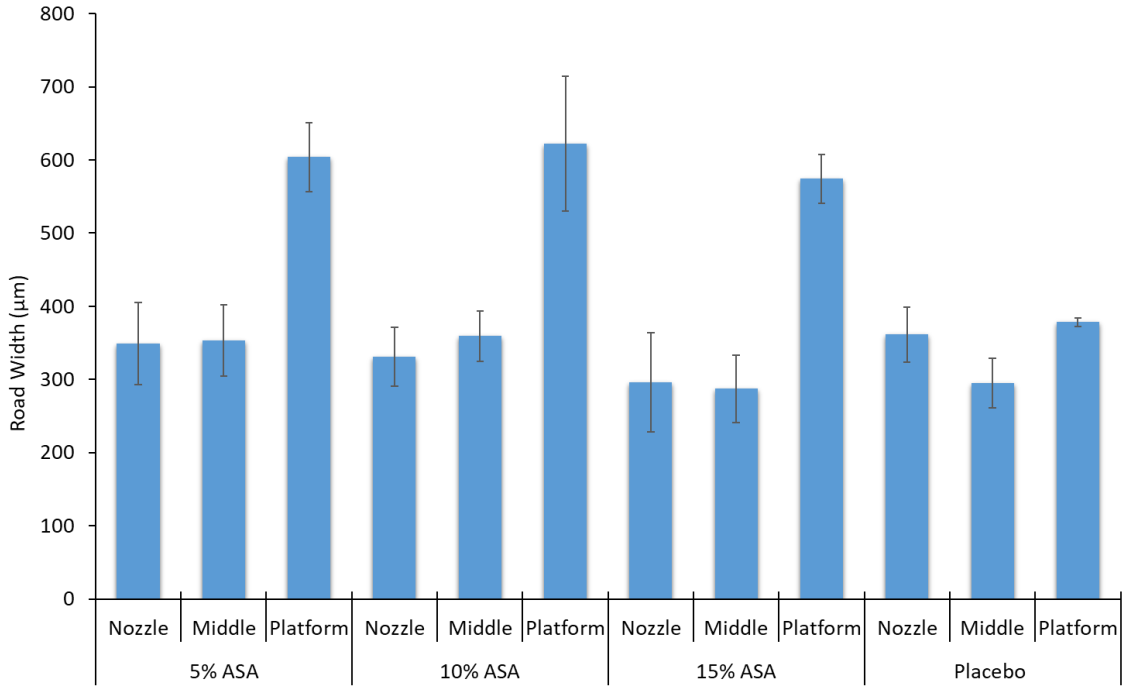

Figure 4-14: First layer road width of drug loaded and placebo filaments printed at 90 mm/sec and 100 °C

No significant difference was seen in the nozzle and middle layer between the three drug-loaded filaments and the placebo filament. However, there is a significant increase in the average road width of the first layer that was brought about by incorporation of ASA in PCL; printing at 90 mm/sec and 100 ° C showed an increase in the first layer road width from ≈ 390 µm to > 600 µm. This is likely due to the presence of ASA in the PCL matrix decreasing the viscosity of the melt, allowing for a greater extent of spreading before the road completely solidifies. No significant difference was seen between the three drug-loaded formulations, this could be attributed to the ASA-PCL melt reaching the maximum possible wettability it can achieve on Kapton® before it solidifies, regardless of drug loading. Notably, the drug-loaded objects exhibited greater sticking to the platform than their placebo counterparts, requiring very careful peeling off the platform with a razor blade to avoid severely deforming the object printed.

4.3.8. Statistical Analysis

The SSD scores for all printing conditions can be seen in Figure 4-15. The processing parameters 120 °C and 90 mm/sec yielded the lowest SSD while 130 °C and 160 mm/sec yielded the highest SSD. Objects printed at 90 mm/sec notably had lower SSD scores for every single temperature than their counterparts printed at 30 mm/sec and 160 mm/sec. The SSD scores represent a figure of merit which can be used to select a set of printing conditions which will give minimal overall variability.

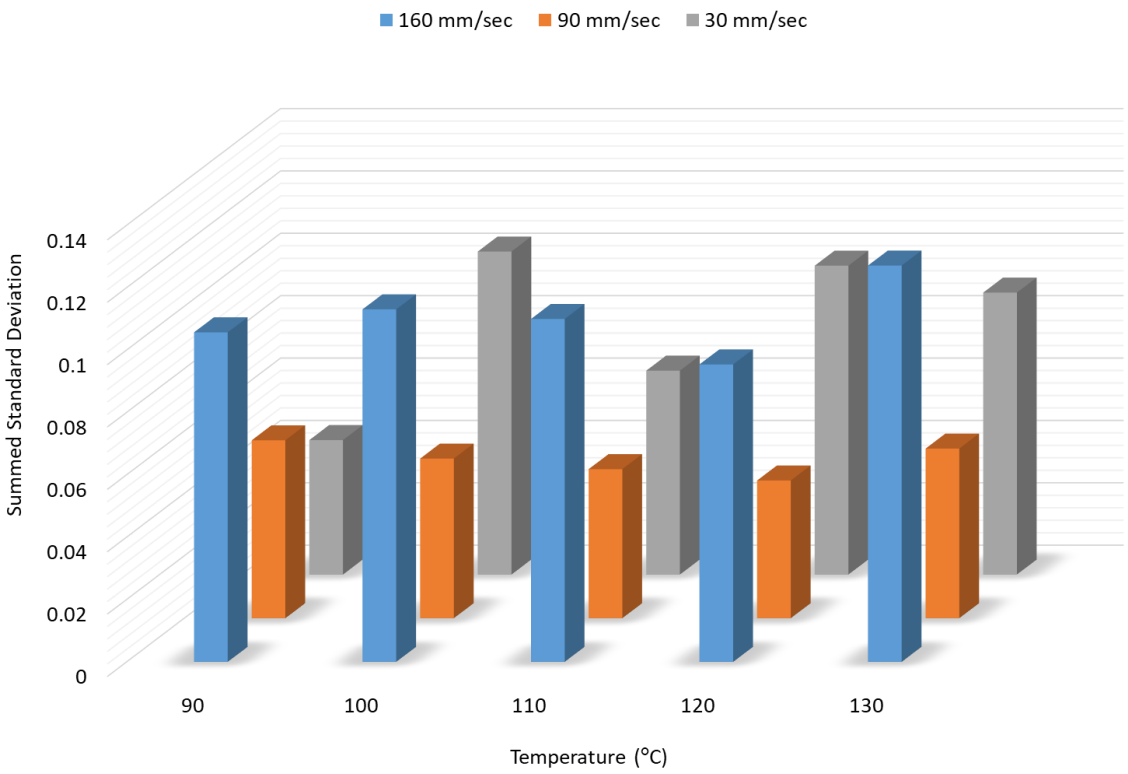

Figure 4-15: *SSD scores of printability of all tested conditions.*

Figure 4-16 shows the loadings plot of the measured responses in rotated space. Principal Component 1 (PC1) was found to describe object mass, road width, length, width, and the printer deposition index, corresponding to 57.77% of the total variance. Principal Component 2 (PC2) was found to describe object thickness, and first layer width, corresponding to 24.38% of the total variance. Object thickness and the first layer effect were found to correlate more strongly with printing temperature than with printing speed. Object mass, length and width, and the FDM-MFI were found to vary more significantly in response to change in printing speed rather than printing temperature. Therefore, one may extrapolate that PC1 may be redubbed the speed axis, as it describes variance introduced due to change in printing speed. Similarly, PC2 may be named the temperature

axis as the variables it describes are those that alter more significantly in response to changes in printing temperature.

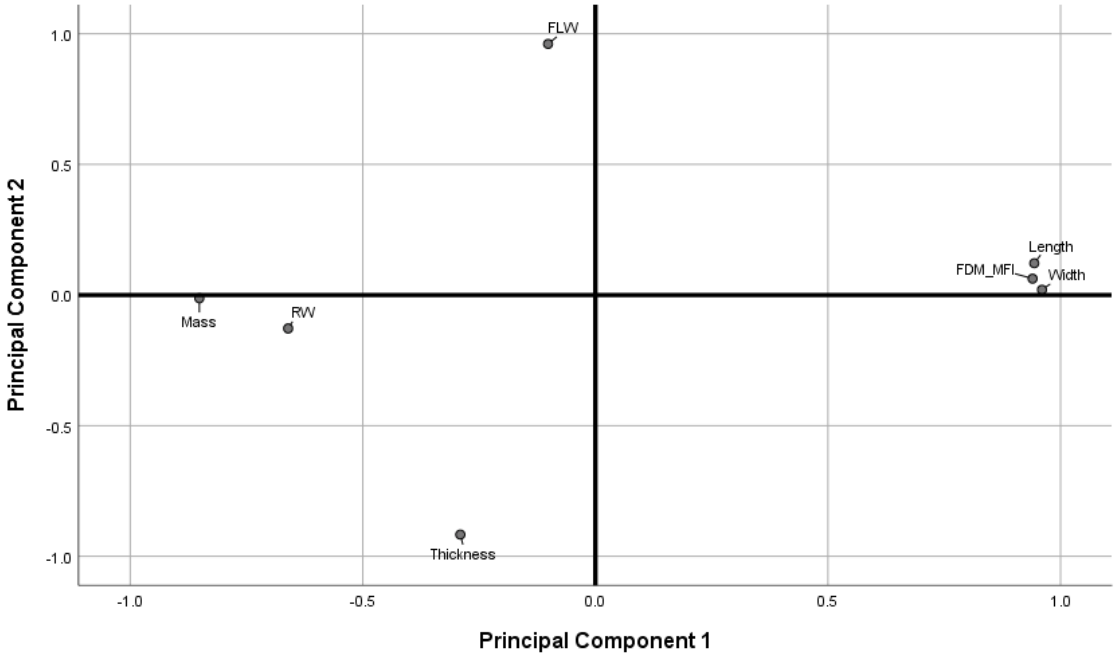

Figure 4-16: Loadings plot in rotated space. (FLW: first layer width. RW: road width).

Length, width, mass, FDM-MFI, and road width were all described by the speed axis. Length, width, and FDM-MFI being anti-correlated to mass and road width, with the former three loading positively, and the latter negatively, indicating that length, width, and the FDM-MFI are directly correlated to printing speed, while mass and road width are inversely correlated.

Figure 4-17 shows the biplot obtained when case scores were projected onto the loadings plot shown in Figure 4-16. The X-axis, denoting the scores of the cases against PC1, unsurprisingly separates the cases into three clusters relative to printing speed, with three clusters showing clear separation between the 30 mm/sec set, followed by 90 mm/sec, and followed by 160 mm/sec.

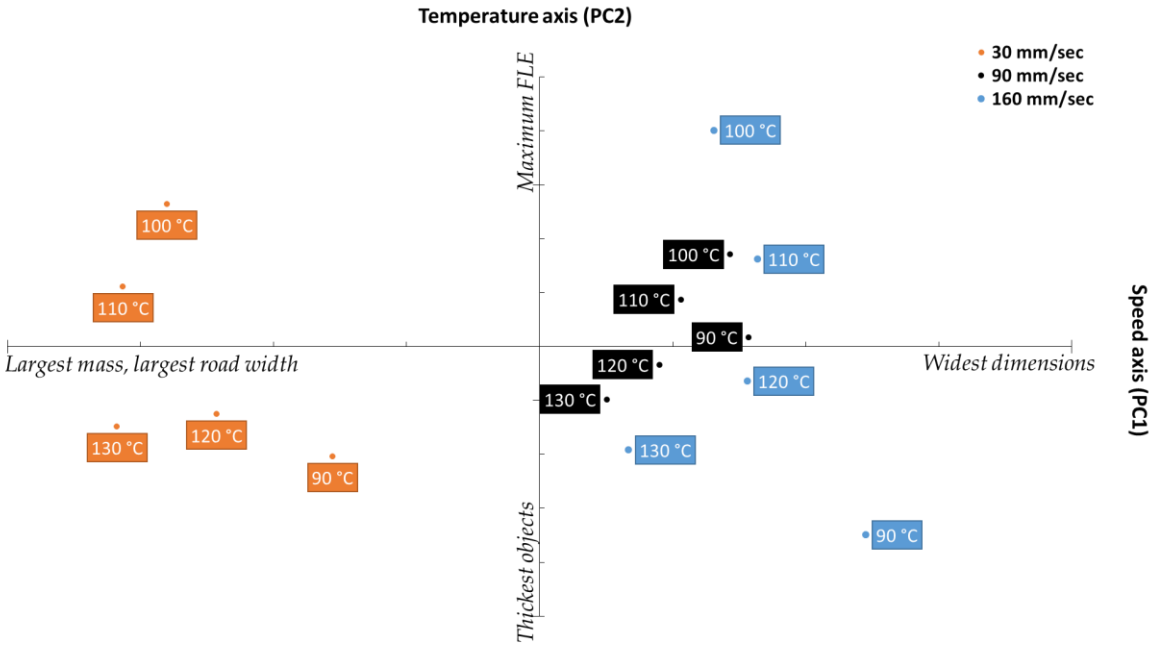

Figure 4-17: Biplot projecting the scores of the studied cases onto the response loadings.

The Y-axis, which shows the scores loadings relative to PC2 (the temperature axis) describes quality parameters which are influenced by printing temperature (object thickness, and the FLE). While the clusters do not appear to offer any meaningful metric towards either parameter at first glance, closer observation reveals that both object thickness and FLE are not described within each cluster, but rather between the clusters. With respect to object thickness, looking at objects printed at the same temperature (i.e. 90 ºC), the one printed at 160 mm/sec was the thickest, followed by the object printed at 30 mm/sec, with 90 mm/sec coming in third. Similarly, with respect to FLE, of the objects printed at 100 ºC, the one printed at 160 mm/sec had the largest FLE, followed by the one printed at 30 mm/sec, followed by the one printed at 90 mm/sec. This inter-cluster pattern was found to apply to all the observed cases. Furthermore, the 90 mm/sec cluster was the most centred cluster with respect to the four quadrants of the biplot, indicating that 90 mm/sec offers the best compromise between the opposing quality parameters.

4.4. Discussion

4.4.1. Material characterisation:

The DSC thermograms of the ASA-PCL physical mixtures suggest that the mechanism by which ASA is incorporated into PCL is via thermal dissolution. This is evidenced by the absence of the melting of ASA in both the 5% and 10% physical mixtures during the first heating cycle, but the existence of a significant difference in both the T_g and the T_m of PCL between the formulations in the second cycle. The depressed T_m of ASA was seen in the 15% physical mix at approximately 135 °C but was not seen in the second cycle. ASA appears to have an antiplasticisation effect on PCL, as evidenced by the increase in the T_g of PCL per ASA concentration in the physical mix. The T_g of ASA was presumably seen at -33 °C during the second heating cycle. However, it should be noted that, due to ASA rapidly degrading beyond its melting point, it is difficult to ascertain whether the detected transition belongs to ASA or to a related compound to which ASA degrades.

The thermogram of the 5% formulation showed no signs of crystalline ASA within the matrix. Furthermore, the ATR-FTIR spectrum of the 5% filament showed a clear shift in the C=O stretching band of PCL from 1725 cm^{-1} to 1722 cm^{-1}, and the C-OH peak shifted from 1163 cm^{-1} to 1165 cm^{-1}. Furthermore, the C-O stretch at 1293 cm^{-1} was notably a weak singlet peak, unlike the strong doublet seen in crystalline ASA. The absence of peaks characteristic to crystalline ASA in the ATR-FTIR spectrum, coupled with the absence of the T_m of ASA in the thermogram strongly suggests ASA is molecularly dispersed in the PCL matrix. The shift in the C=O and C-OH peaks of PCL point towards hydrogen bonding at the carboxyl groups as the main ASA-PCL interaction maintaining the solid dispersion.

The endothermic event seen at 80 °C in the thermogram of the 15% filament likely corresponds to the depressed melting endotherm of ASA. The absence of any significant difference in the glass transition and melting endotherm of PCL in the 10% and the 15% formulations further supports that the continuous phases of the two formulations are similar, indicating that the thermal event seen at 80 °C is crystallised ASA. The ATR-FTIR spectra of the 10% and 15% filaments both display the C-O doublet previously seen in the spectrum of crystalline ASA. However, the peak at 1290 cm^{-1} has shifted to 1295 cm^{-1} in the 10% filament, and to 1294 cm^{-1} in the 15% formulation. The C-OH peak seen in crystalline ASA at 1184 cm^{-1} was seen in the 10% peak at 1182 cm^{-1}. This indicates that both the 10% and 15% formulation contain a crystalline fraction of ASA, which was

not seen in the 10% thermogram possibly due to detection limits of the DSC. The shifted peaks of the C-O and C-OH groups still indicate that the molecularly dispersed fraction of ASA is maintained by hydrogen bonding at the carboxyl groups. The saturation solubility of ASA in PCL is likely somewhere between 5% and 10%.

4.4.2. Validation of build plate levelling:

An article published by Melocchi et al. previously reported the existence of significant variation on the weights and dimensional accuracy of FDM printed objects when the printer platform was levelled by different individuals, and even by the same individual on different occasions (54). Therefore, minor validations of platform levelling operation were conducted (Tables 4-2 and 4-3). This was coupled with the use of an independent sample T-Test to compare the weights and dimensions yielded when the printer is levelled by different operators. As can be seen in Table 4-2, the levelling of the printer by different operators had no significant impact on the weight uniformity, nor the dimensional consistency of the 3D printed objects. However, as shown in Table 4-3, a significant difference was observed (most importantly in weights of the printed objects) when the printer was levelled by the same operator on two different days.

Both our findings and what was reported by Melocchi et al. serve to highlight the operator dependence of the calibration of this model of printer which can be a potential problem in this design of the printer if it is used for printing pharmaceutical standard products. The current method employed by the printer to level the build plate is very subjective; The instructions for levelling the platform of a MakerBot® Replicator 2 used in both studies read *"tighten the three knobs under the build plate until a thin piece of paper can just slide between the nozzle and the platform with some friction"* (39). Relying on the operator's judgment as 'suitable friction' between the nozzle tip and levelling card. While this may be adequate for printing large commercial prototype objects, it is unlikely to be a suitable 'calibration' method for pharmaceutical printing of oral solid dosage forms where high printing precision is required. Therefore, we conclude that the contradictions between what was previously reported by Melocchi et al., and what is presented herein actually serve to highlight a major flaw of the current engineering of FDM 3D printers.

4.4.3. Impact of processing conditions on the perceived quality attributes of 3D printed objects.

Optimisation of printing temperature, and by extension the melt rheology of the polymers, is regarded as a key significant factor to optimize for FDM formulation design (43,185). Initially, MFI studies (Figure 4-7) were conducted to attempt to determine the rationale behind manufacturer-recommended printing temperatures from a melt-flow perspective. The commercial PCL filament tested unsurprisingly exhibited pseudoplastic melt flow that is characteristic of thermoplastic, polymeric materials (183). However, no noteworthy change in FDM-MFI was observed at, or near the manufacturer recommended printing temperature.

As can be seen in Figure 4-7, plotting the MFI of PCL commercial filament against its FDM-MFI at different speeds shows the fundamentally different behaviour exhibited by random melt flow in comparison to printing. The FDM-MFI, being an adaptation of ISO MFI standard, yields a largely exponential curve with temperature. The MFI standard method, as well as the adapted version described herein, rely on a weight being pulled by the influence of gravity to propel the polymer melt through the orifice. Which dictates that the object will always be accelerating downwards by a factor of 9.8 m/sec^2 minus the resistance to flow exerted by the polymer melt. However, FDM printers propel the filament through the use of a stepper motor at a constant rate. Furthermore, as can be seen in Figure 4-8, weights of the 3D printed films were not found to correlate with printing temperature. And, as seen in Figure 4-7, FDM-MFI was not found to be influenced by temperature, but rather by printing speed, leading to the conclusion that, provided the selected printing temperature allows for the flow of the polymer melt, printing temperature does not significantly impact the properties of objects printed via FDM. This is further supported by considering the engineering of the FDM printer. The printing head utilises a stepper motor to drive the filament forward. As can be seen in Equation 4-3 below, the torque of a stepper motor is a function of the current flowing through the motor multiplied by its intrinsic torque constant (186).

$$Torque = KT * i \qquad \textit{(Equation 4-3)}$$

Where KT is the torque constant of the motor, and i is the current. In other words, the torque is independent of the weight/resistance to motion of the material the motor is attempting to push. The load on the stepper motor in the 3D printer is the temperature-

dependent resistance to flow exerted by the polymer melt. Which explains the temperature-independence of the FDM-MFI observed in this study.

An engraving on the back of the stepper motor driving the 3D printer used in this study identified its make and model to be a Moons' MS17HD4P6038 (Moons' Electric Co. Ltd., Shanghai, China). The datasheet of the motor was retrieved from the website of the manufacturer (187), from which Figure 4-18, the torque-speed curve of the motor, was obtained. As can be seen in Figure 4-18, operating the motor at higher speeds yields lower torque values. The magnitude of this decrease tends to a plateau at higher operating speeds (hereinafter referred to as the steady torque region). Notably, the increase in the FDM-MFI from 30 mm/sec to 90 mm/sec was much larger than the increase in FDM-MFI from 90 mm/sec to 160 mm/sec. Which is likely due to the high operating speeds (90 mm/sec and 160 mm/sec) occurring near or on the steady torque region of the motor. Furthermore, attempted printing at 70 °C was notably only successful at 30 mm/sec, this is likely due to it being the only speed at which the motor possesses sufficient torque to overcome the viscosity of the PCL melt at that temperature.

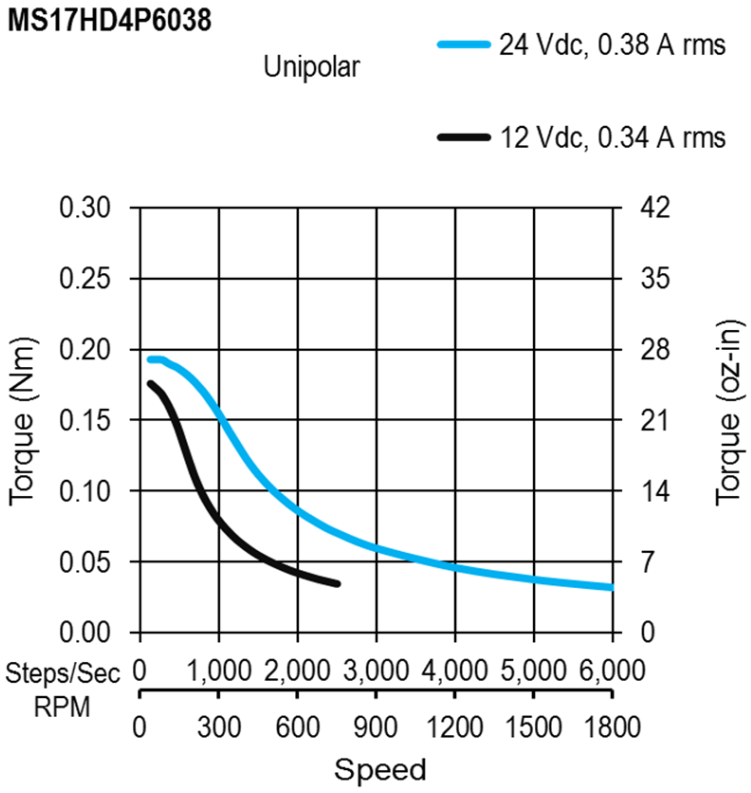

Figure 4-18: Torque vs. speed curve of the Moons' MS17HD4P6038 stepper motor used by the Makerbot® Replicator 2

Per every printing condition, the printer was found to yield highly reproducible weights (Figure 4-8). With the largest recorded standard deviation being 3.2 mg for objects printed at 120 °C and 90 mm/sec. While this falls well within general pharmacopoeial standards, simply modifying the printing speed caused the printed film to increase in weight by nearly 20 mg in some cases. If FDM is to be utilised in personalised medicine, careful screening of the printing parameters, and choosing the appropriate conditions to match the target dose is of utmost importance (4).

As shown in Figures 4-9 and 4-10, none of the objects printed in this study matched the theoretical dimensions dictated by the STL file. While none of the objects created in this study matched the theoretical dimensions, no significant difference was seen in printing at 90 mm/sec and 160 mm/sec, printing at 30 mm/sec, however, yielded objects that were significantly different from the other two printing speeds.

4.4.4. The First Layer Effect

A significant difference in road width was seen between the platform layer and the two subsequent layers. This effect was found to be temperature-dependent, with the road width of the platform layer being directly correlated with the printing temperature. Notably, no significant difference was seen between the middle layer and the top layer regardless of printing temperature, nor printing speed.

This spreading effect is assumed to be caused by the surface wettability of the Kapton® tape. Printing on different surfaces yielded different spreading amounts, as can be seen in Figure 4-13. However, there was a notable difference in the stickiness of the PCL printed films to the different surfaces; PCL was found to bind strongly to the Kapton® tape and was very difficult to remove, particularly when printed at higher temperatures (> 110 °C). When printed at lower temperatures (i.e. 80 °C – 100 °C), the PCL films were easily retrieved off the platform. However, almost no sticking to aluminium nor glass was observed. This points towards the existence of two factors influencing this behaviour. The first being the wettability of the surface. The temperature-dependent spreading and the sticking of the objects to the Kapton® tape at elevated temperatures are probably due to the formation of PCL-polyimide interactions at elevated temperatures, yielding greater wetting and adhesion to the surface.

4.4.5. Statistical Analysis

The data above demonstrated the quality of the printed dosage form is a result of the complex interplay between different processing and materials factors. These factors also often interact such that varying the level of factors concurrently has a greater impact over a perceived measure of goodness than varying either parameter individually. Furthermore, while one can measure particular properties of the 3D printed object (such as weight, dimensions, road width, etc.) to be utilised as measures of goodness for parameter selection, this remains a non-straightforward process. Mainly because processing conditions that appear to produce a more favoured object when observing one measure of goodness fail when another measure of goodness is considered (i.e. weight v.s. dimensional authenticity). Therefore, it is clear that there exists a need for an overarching method for selecting the optimum printing conditions which will produce the objects with the greatest overall quality. For this purpose, a measure of goodness to determine the printing conditions which will produce objects with the highest overall printing reproducibility was conceived. Said conditions are those that will yield the minimum Summed Standard Deviation (SSD) score. This proposed SSD can be calculated by first normalising, then summing the standard deviations of each measured value at each condition. As previously mentioned, objects printed at 90 mm/sec had lower SSD scores for every single temperature than their counterparts printed at 30 mm/sec and 160 mm/sec. Suggesting that 90 mm/sec is the optimum printing speed for this filament.

While the SSD provides a quick method to determine the optimum printing conditions for a given filament, further statistical analysis techniques can be used to extract more information about the process parameters and how they interact to influence the process. Therefore, PCA was conducted as an exploratory data analysis tool to investigate the interplay between the different perceived quality parameters.

Observing the measured variables as described by the loadings plot (Figure 4-16) allows for a more overarching look at how printing speed and temperature both influence perceived quality attributes, as well as how the quality attributes relate to one another. Object thickness and first layer width load opposite to each other on the temperature axis, suggesting the two are anti-correlated. This suggests that the spreading of the first layer not only increases its road width but also decreases road height in the Z-axis. Furthermore, first layer width loads positively, while thickness loads negatively on the axis, indicating that wider road widths are brought about by higher temperatures while greater object

thickness is a result of lower printing temperature. Therefore, a conclusion can be drawn that printing at higher temperatures leads to a more drastic FLE, while printing at lower temperatures leads to thicker objects.

The length/width vs. road width correlation is an interesting one as it gives insight into the operation of the feeding motors, as well as printer accuracy; the anti-correlation between road width and printing speed suggests that at higher printing speeds, the printer is not feeding sufficient material to keep up with the demands of the higher printing speed, leading to the deposited road to be tugged as the print head is moving, stretching it thinner (leading to a decrease in road width) and longer (leading to an increase in length/width). This argument relating printing speed and feeding speed suggests that, at higher print speeds, the printer is not providing enough material feed to faithfully replicate a print at lower speeds. Therefore, objects printed at higher speeds should have less mass than their lower speed counterparts. This was found to be true as mass loaded negatively on the speed axis, and was found to be anti-correlated to length, width, and FDM-MFI. The latter, which was found to increase relative to speed (Figure 4-7) was unsurprisingly found to load positively on the speed axis. This inverse correlation between printing speed and object mass further supports the argument presented in section 4.4.3. regarding the printing motor torque-speed relationship. The clustering pattern seen in the biplot in Figure 4-17 further supports the argument presented prior relating printing speed to object mass and dimensions, as the leftmost cluster, falling on the “largest mass” quadrant of the biplot belonged to the 30 mm/sec, then 90 mm/sec, which was then followed by 160 mm/sec, the “widest dimensions” set. Notably, there is less separation between the latter two sets than between 30 mm/sec and 90 mm/sec, which strongly mirrors the FDM-MFI results displayed in Figure 4-7.

Of the three clusters, the 90 mm/sec group appears to show the least variance relative to the change in printing temperature. Indicating that that printing speed further minimizes the significance of printing temperature. This sits in agreement with the result obtained from the SSD displayed in Figure 4-15, in which printing at a speed of 90 mm/sec yielded the lowest SSD, regardless of printing temperature, indicating that higher reproducibility is achieved when printing at 90 mm/sec. Therefore, one may extrapolate that, for the PCL filament used herein, printing at 90 mm/sec offers the most predictable and reproducible results, making it the optimum printing speed for this filament.

4.5. Conclusion

The results of this study demonstrated the significant impacts of the processing parameters on the weights and dimensions of the 3D printed dosage forms. For the printer used in the study, the printing speed exhibited more profound effects than the printing temperature on the weight uniformity and dimension authenticity of the printed dosage forms. Printing temperature and the build plate surfaces contribute significantly to the *FLE*. For pharmaceutical applications, the control of such impacts should be thoroughly understood as it can impact the performance of the printed formulation. These results brought to the conclusion of that careful engineering for a pharmaceutically-suitable FDM 3D printer should be treated as a priority for making the shift of FDM 3D printing from proof-of-concept to industrial application. The use of summed standard deviations enables the calculation of a figure of merit indicating the most reproducible set of printing conditions.

Chapter 5

Infill density and its impact on drug release kinetics from oral solid dosage forms prepared by Fused Deposition Modelling

5.1. Introduction

Infill density is a manipulable parameter in FDM 3D printing (26,68,125,128). The term defines the ratio of the volume of free space to the volume of deposited roads within the 3D printed object. Traditionally, even if the infill is set to 0%, the printed object appears to be a completely solid composite (26). This is due to the roof and floor layers, which are printed at 100% infill regardless of the user input, presumably to maintain an attractive surface finish. The roof and the floor serve to provide a more aesthetically attractive surface finish to the object, as well as provide structural support to strengthen the object. For the make of printer used herein, the default roof and floor thickness are 0.8 mm each. When printing with default settings, any fabricated object will always possess a roof and a floor, each having a thickness of 0.8 mm and an infill density of 100%, regardless of what infill the user has instructed the printer to use (39). An example of this would be the article presented by Goyanes et al., in which they 3D printed 4-aminosalicylic acid (4-ASA) and 5-aminosalicylic acid (5-ASA) loaded polyvinyl alcohol (PVA) tablets at three infill densities (90%, 50%, and 10%). However, the photographs presented in their article show tablets that all share the same, completely filled, external geometry (26) (Figure 5-1).

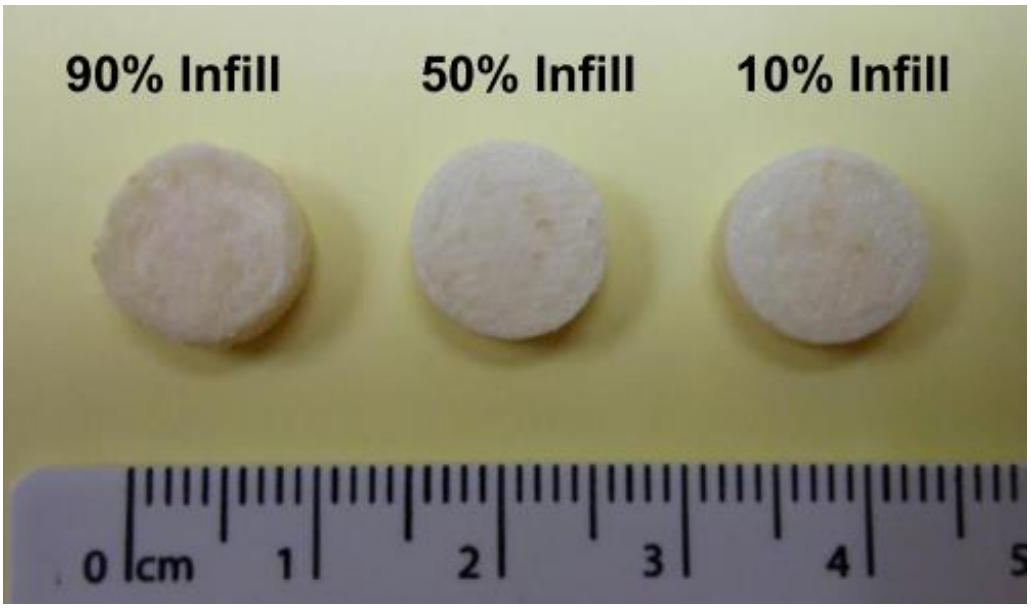

Figure 5-1: 3D lower infill 5-ASA tablets with intact floors and roofs, showing no differences in external geometries. Figure retrieved from Goyanes et al. (26)

Although the infill density of the roof and the floor cannot be changed, the thickness of the roof and floor are customisable, and may even be set to 0 mm, thus allowing the entire

object to be fabricated to the infill density which the user has instructed the printer, and exposing the internal microstructures of infill region of the printed dosage form.

Some previous articles have briefly investigated the effect that manipulation of infill density has on drug release properties, albeit not exhaustively. In the aforementioned article by Goyanes et al. (26), Goyanes reported no significant difference in release rates of the three 5-ASA formulations. However, the 10% infill formulation of 4-ASA showed some enhanced release over its 50% and 90% counterparts. However, no significant difference was seen between 50% and 90%. Goyanes concluded that the use of infill density may be a useful parameter to consider when aiming to modulate the drug release rate from a 3D printed dosage form.

Ibrahim et al. printed metformin-loaded PVA filaments at 10% infill, the tablets were then perforated with either one or two piercings along the diameter to “increase their surface area”. Drug release studies were then conducted to compare the performance of the perforated tablets against tablets left without perforation. Release studies showed no significant difference between the three designs (128).

Clark et al. printed small, thin-layered carvedilol-systems by photo-initiated 3D inkjet printing (37), of which two variants (the mesh and the ring geometries) can be considered infill variants (only those two objects had the same external diameter). No significant difference was seen in the drug release rate of the two infill variants. Clark reported that the dosage forms swelled during drug release studies.

Kyobula et al. used thermal inkjet printing to print fenofibrate-loaded beeswax tablets with honeycomb-pattern infill at different infill densities (36). Of the six infills investigated, the four lower density infill formulations showed no significant differences in drug release between one another but were significantly faster than a higher infill formulation, and the 100% infill formulation. Kyobula reported observing no swelling nor erosion from the system, making the release mechanism entirely diffusion-based.

Lamichhane et al. printed both closed (with roof and floor) tablets at 25%, 50%, and 75% infill, and open tablets (at 25% and 50% infill) of HPMC-loaded pregabalin (188). Closed systems showed no significant difference in drug release rate between any of the three formulations, while open systems showed a significantly faster release rate for the 25%

infill tablet. The open system tablet (25% infill) was tested against a commercially available product (Lyrica™), no significant difference in release rate was observed between the printed tablet and the marketed product, likely because the characterisation results presented showed the drug to be at least partially phase-separated as crystals in the matrix. Due to both the 3D printed formulation and the punch-pressed commercial tablets containing crystalline pregabalin, the rate of drug release is going to be limited by the dissolution rate of the drug crystals present in both, rendering the dissolution rates similar between the 3D printed formulation and the commercially available product.

As outlined prior, there appears to be conflicting evidence about the feasibility of using infill density as means to manipulate drug release. While it is clear that the infill – release rate relationship is only applicable in open systems (i.e. tablets printed without floors and roof), due to the exposed internal structure increasing the available surface area. Investigations into the effect of infill density on the drug release rate show what is seemingly conflicting reports on the effect of infill density on drug release rate. The previously mentioned article by Kyobula et al. (36) showed no effect of infill between four different infills, yet displayed a significant effect between a low infill tablet, a high infill tablet, and a 100% infill tablet. Yet, the aforementioned findings reported by Clark et al. (37) showed no significant difference between the two tablets which can be considered to be infill variants. This suggests that there appears to be a maximum threshold that the infill density may be reduced to, that, once crossed, induces little to no effect on the drug release rate. One factor which has not been accounted for is the distortion of the 3D printed tablets during dissolution, due to matrix-media interactions (swelling, erosion, relaxation, etc), which may alter the shape of the tablet, altering the impact of infill density.

This study investigated the impact of infill on drug release properties of a 3D printed object under swelling, and erosion conditions (by varying pH of the dissolution media), and under a combination of both conditions in which the tablets were placed for two hours in pH 1.2 media, then transferred to pH 6.8 buffer media for six hours.

5.2. Materials and methods:

5.2.1. Materials:

The filament used in this investigation is filament HP10D whose constituents have been previously outlined in section 3.3.2., containing 81% of HPMCAS w/w, 9% PEO w/w, and paracetamol at 10% w/w.

5.2.2. Methods:

5.2.2.1. Preparation of filaments by Hot-Melt Extrusion (HME)

Extrusion was conducted at a screw speed of 100 RPM and a temperature of 155 °C. Materials were cycled in the extruder for 5 minutes before flushing to ensure homogeneity along the filament. The melt was flushed at a screw speed of 35 RPM onto a conveyer belt. The diameter of the extruded filaments was measured using a digital calliper, sections of the filament falling outside the range of 1.6 mm ± 1 mm were discarded.

5.2.2.2. Printing of tablets

Tablets were printed in the shape of a cylinder (dimensions: 10 mm diameter, 2 mm thickness) at a layer thickness of 0.2 mm, corresponding to 10 layers per tablet. Roof and Floor Thickness were set to 0 mm to allow for the exposure of the internal structure of the 3D printed objects. The cylinder shape was designed using Microsoft 3D Builder software (version 16.1) and was then exported as an STL file. The STL file was printed using MakerBot® MakerWare (version 3.8.0).

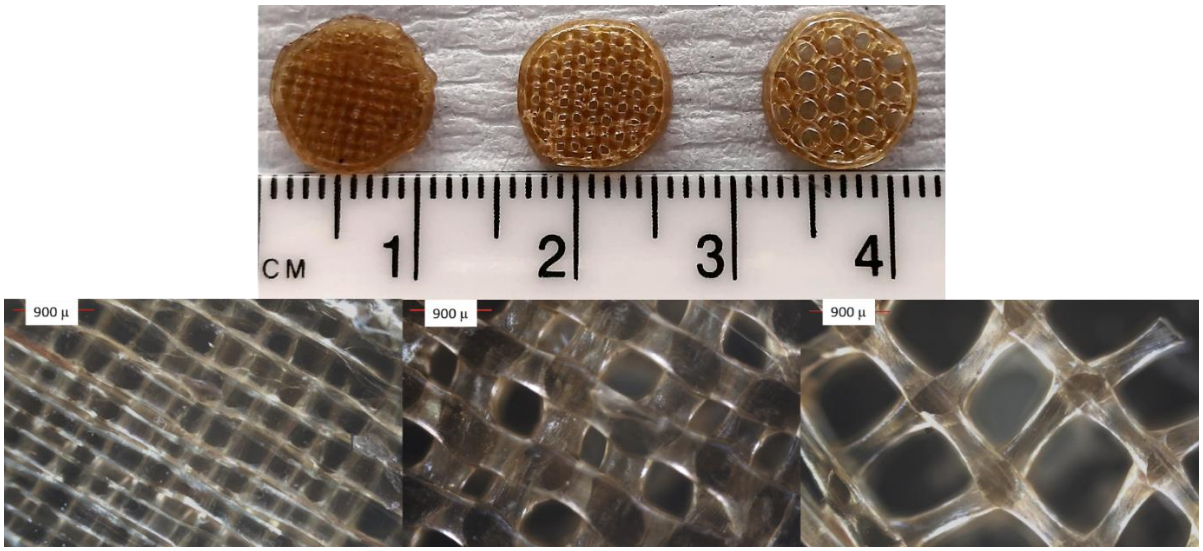

Figure 5-2: Photographic (Top) and microscopic (bottom) images of the 3D printed tablets. Left to right: 100% infill, 75% infill, and 50% infill.

Three batches of tablets were printed, at three different infills: 100% infill, 75% infill, and 50% infill (Figure 5-2), using the default hexagonal infill pattern. All batches were printed using a nozzle temperature of 175 °C onto an unheated build plate.

The microscopic images shown in Figure 5-2 belong to the same samples shown in the photographic images in that figure. However, the reflective light microscope used to obtain the photographic images could only clearly capture the topmost layer. Therefore, some macroscopic distortions visible in the photographs may not be apparent in the microscopic images.

5.2.2.3. Material Characterisation

The materials used were characterised by DSC, ATR-FTIR, and PXRD as described in sections 3.2.3.1., 3.2.3.2., and 3.2.3.3., respectively.

5.2.2.4. Drug content uniformity in the filament

Filament content uniformity measurements were conducted by taking three samples every 5 cm of weights 8 – 15 mg each along the relevant length of the filament, which were then dissolved in pH 6.8 Phosphate Buffer Saline (PBS) overnight. Drug content was analysed by UV–Visible Spectroscopy (Perkin-Elmer lambda 35, USA) at a wavelength of 242 nm. Homogeneity testing was conducted in triplicates.

5.2.2.5. In vitro drug release studies

In vitro drug release testing was conducted using a standard Caleva 8ST dissolution apparatus (Caleva Ltd., Dorset, United Kingdom). Table 5-1 outlines the conducted dissolution experiments. The temperature of the dissolution bath was maintained at 37 ºC ± 0.5 ºC. For all experiments, 5 mL were withdrawn from the dissolution media at predetermined time points and were then promptly replenished with fresh dissolution media. Drug content was analysed using a UV–Visible spectrophotometer (Perkin-Elmer lambda 35, USA) at a wavelength of 242 nm (55). All dissolution tests were conducted with a rotation speed of 50 RPM. All reported measurements were conducted in triplicates.

For the drug release experiments conducted at pH 1.2, the volume of the dissolution media was limited to 750 mL to maintain the same hydrodynamic environment as the drug release experiment conducted under pharmacopoeial conditions (2 hours in 750 mL of pH 1.2 media, followed by 6 hours in pH 6.8 PBS, which is a pharmacopoeial standard

method for delayed-release/gastro-resistant formulations such as the one presented herein (189)).

Table 5-1: List of performed dissolution experiments

Apparatus	Dissolution Media
Paddle	900 mL of pH 6.8 phosphate buffer saline (PBS)
Basket	900 mL of pH 6.8 phosphate buffer saline (PBS)
Basket	750 mL pH 1.2 acidic media
Basket	750 mL of pH 1.2 media for two hours, tablets were then transferred to 900 mL of pH 6.8 PBS

5.2.2.6. Swelling experiments

Measuring swelling rate using weight change on water intake was not possible due to water being entrapped between the pores of the 3D printed objects, particularly the 75% infill formulation. Attempting to release the entrapped water by tapping the tablets on a tissue caused the destruction of the tablets. Therefore, swelling experiments were performed on a two-layer mesh 3D printed using the same formulation. The mesh was designed using Microsoft 3D builder to be a perfect square of length size 15 mm, and a pore size of 400 µm. The printed meshes possessed an average mass of 4.5 mg ± 0.16 mg. Printing of the meshes was conducted using the same conditions used for printing the tablets, as outlined in section 5.2.2.2.

The swelling rate measurements were conducted by placing the meshes in a Petri dish, submerged in 100 ml of pH 1.2 media in a shaking incubator rotating at a speed of 50 RPM. The Petri dish was retrieved at predetermined intervals and the mesh was imaged using a Linkam Imaging Station (Linkam Scientific Instruments, Tadworth, United Kingdom), as shown in Figure 5-3.

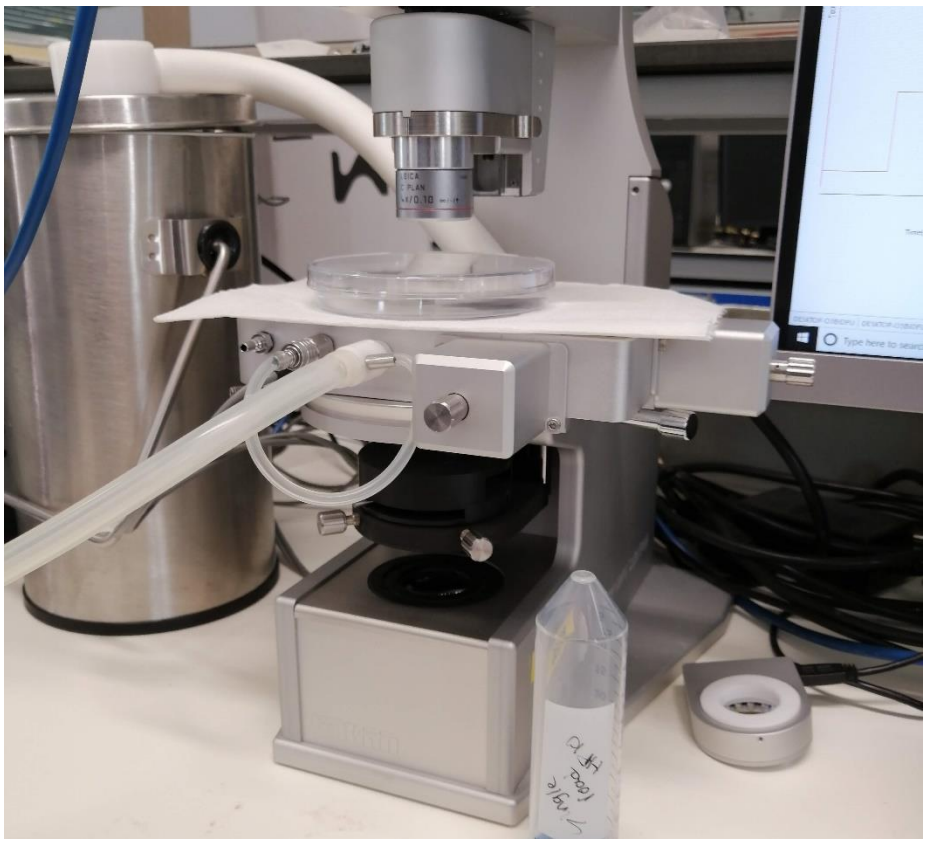

Figure 5-3: the apparatus used for measuring the swelling of the polymer matrix.

The swelling rate was approximated by measuring the decrease in the pore area of the mesh as a function of time. Pore area was measured using the GNU Image Manipulation Program (GIMP) version 2.10.6. Drug release rates from the 3D printed meshes was also measured on a further set of three meshes. At each time point, 5 mL were retrieved from the dissolution media and promptly replaced with 5 mL of fresh dissolution media to maintain sink condition.

All reported measurements were done in triplicates

5.2.2.7. Dissolution kinetics model fitting:

In an attempt to gain an understanding of the underlying drug release mechanism, all the obtained drug release profiles were fitted to the Korsmeyer – Peppas power law. The Korsmeyer – Peppas power law is shown below in Equation 5-1:

$$M_t / M_\infty = kt^n \qquad \textit{(Equation 5-1)}$$

Where M_t/M_∞ is the fraction of drug released at time t, k is the release rate constant, and n is the Peppas coefficient, an exponent whose value describes the underpinning drug release mechanism (190,191). A notable constraint of this model is that the fitting is valid for cases where $M_t/M_\infty \leqslant 0.6$, exclusively. In this study, the limits of n used were the ones for cylindrical systems, as described by Ritger and Peppas (190), and are summarised below in Table 5-2.

Table 5-2: Values of the Peppas Coefficient (n) and the corresponding implied drug release mechanism. Table adapted from Korsmeyer et al., (192)*, and Ritger & Peppas* (190)

n-value	***Drug release mechanism***
0.45	Fickian diffusion
$0.45 < n < 1.00$	Anomalous transport
1.00	Zero-order release
$n > 1.00$	Super Case II transport

The drug release mechanism was also investigated using the first-order model (193):

$$M_t = M_\infty * (1 - e^{-kt}) \qquad \textit{(Equation 5-2)}$$

Where M_t is the amount of drug released at time t, M_∞ is the amount of drug released as t approaches infinity. Unlike the Korsmeyer – Peppas model, which restricts the fitting to the first 60% of the drug release curve, fitting to the first-order model can be conducted to the entire drug release curve.

Curve fitting was conducted using QTiPlot (version 1.0.0 – rc3).

5.3. Results:

5.3.1. Characterisation of the 3D printed tablets:

The average drug content in the filament was found to be 9.3 mg ± 0.24 mg, with no significant differences in drug content along the length of the extruded filament (Figure 5-4).

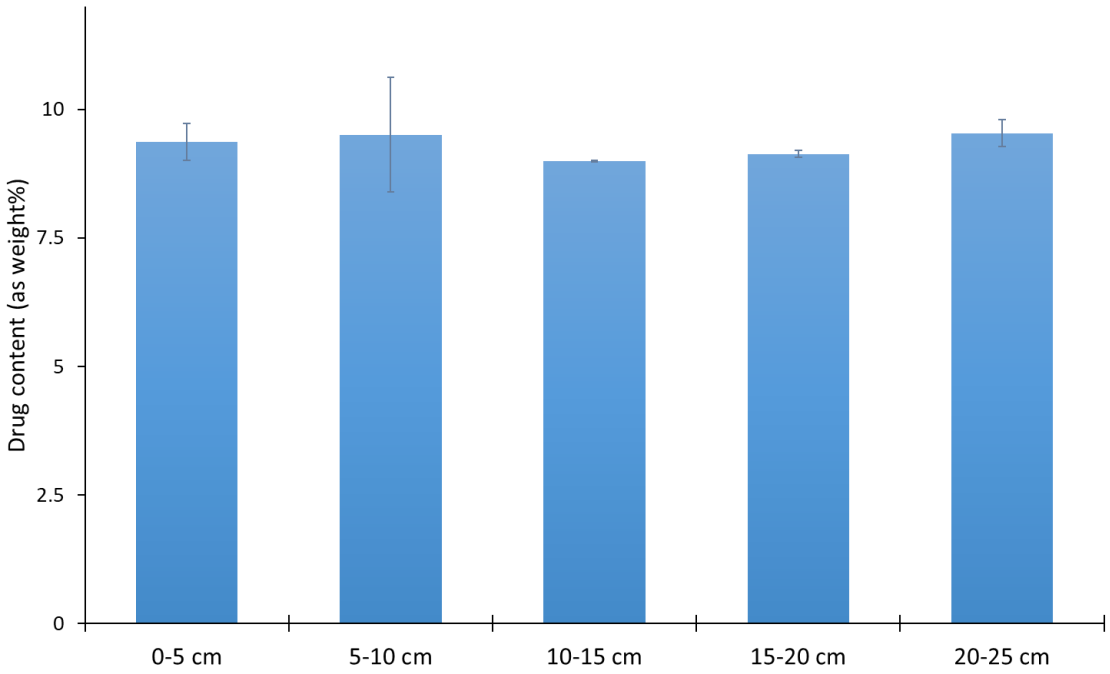

Figure 5-4: Drug content uniformity along the length of the filament.

Mass of the 100% infill tablets was 123.73 mg ± 2.35 mg. Mass of the 75% infill tablets was 76.77 ± 9.76 mg. Mass of the 50% infill batch was 64.03 mg ± 3.95 mg. The 75% infill tablets weighed, on average, 62.0% of the 100% infill tablets. The 50% infill tablets weighed, on average, 51.7% of the 100% infill tablets.

5.3.2. *In vitro* drug release studies:

5.3.2.1. Drug release testing in pH 1.2

Figure 5-5 shows the drug release rate of the three different infill batches in pH 1.2 acidic media. The 50% infill batch possessed the fastest release rate under acidic conditions (~ 47% in 8 hours), followed by the 75% infill batch (~ 30% in 8 hours). The 100% infill formulation was the slowest with ~ 19% drug release in 8 hours.

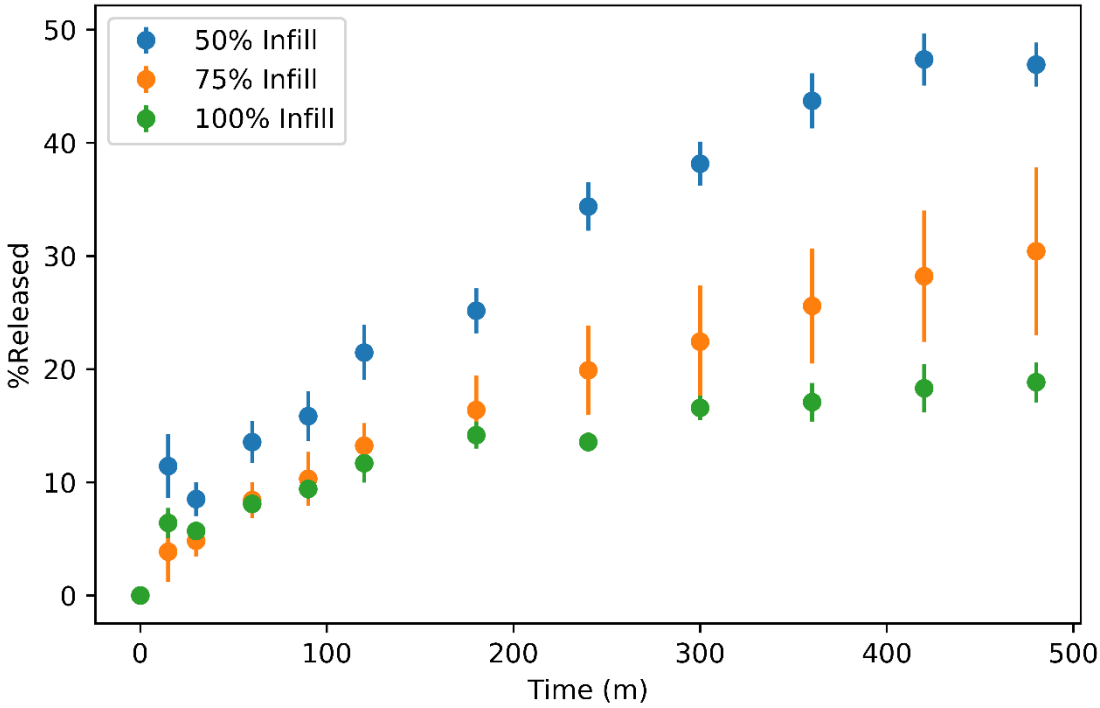

Figure 5-5: Release profile of the three infill batches at pH 1.2.

The tablets remained intact for the duration of the experiment, microscopic imaging of the tablets at the end of the experiment showed that the roads comprising the tablets had swelled significantly during the experiment (Figure 5-6). The swelling behaviour of the formulation is further discussed in Section 5.3.3. and Section 5.4.2.2.

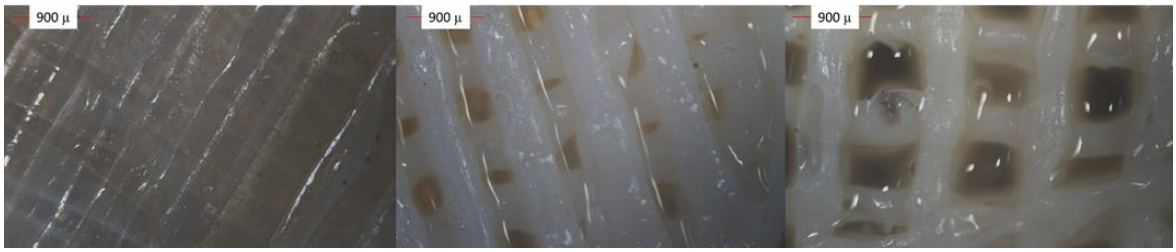

Figure 5-6: Microscopic images of the 3D printed tablets after 8 hours in pH 1.2 media. Left to right: 100% infill, 75% infill, 50% infill

5.3.2.2. Drug release testing in pH 6.8:

Drug release in buffer media (pH 6.8 PBS) was conducted as per USP apparatus II (paddle) (188). However, the 50% infill and the 75% infill tablets were observed to float during the experiment. So the dissolution profiles were reacquired using the basket apparatus to ensure that the tablets are completely submerged.

Figure 5-7 shows the drug release rates of the three infill batches in pH 6.8 PBS using the paddle apparatus, the 50% infill batch possessed the fastest release rate, reaching 100% release in 90 minutes, followed by the 75% infill batch, which reached 100% release in 120 minutes, with the 100% infill batch being the slowest releasing, reaching ~ 100% release in 240 minutes. In all three batches, the tablets were visually observed to erode during dissolution.

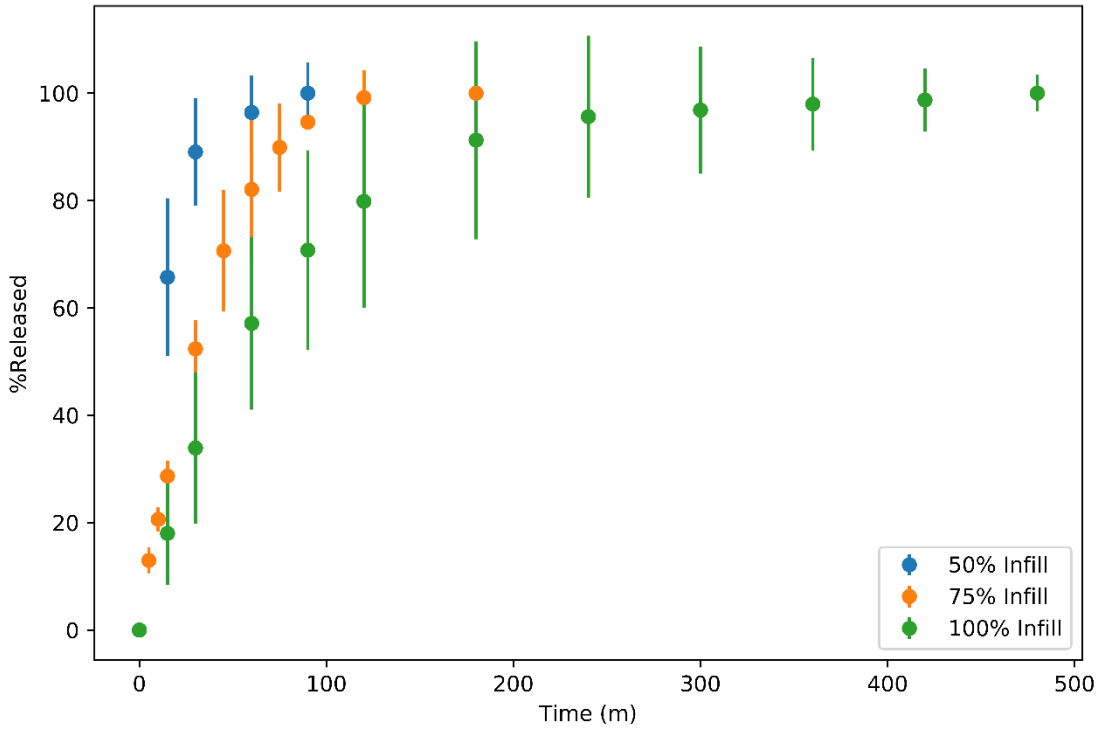

Figure 5-7: Release profile of the three infill batches in pH 6.8 PBS using the paddle apparatus

Figure 5-8 shows the drug release rates of the three infill tablets in pH 6.8 PBS using the basket apparatus. The release rate was found to be considerably slower than what was observed using the paddle method, with the 50% infill and 75% infill formulation requiring 240 minutes to reach 100% drug release. The release rate of the 100% infill formulation was found to not vary significantly between the paddle and the basket apparatus.

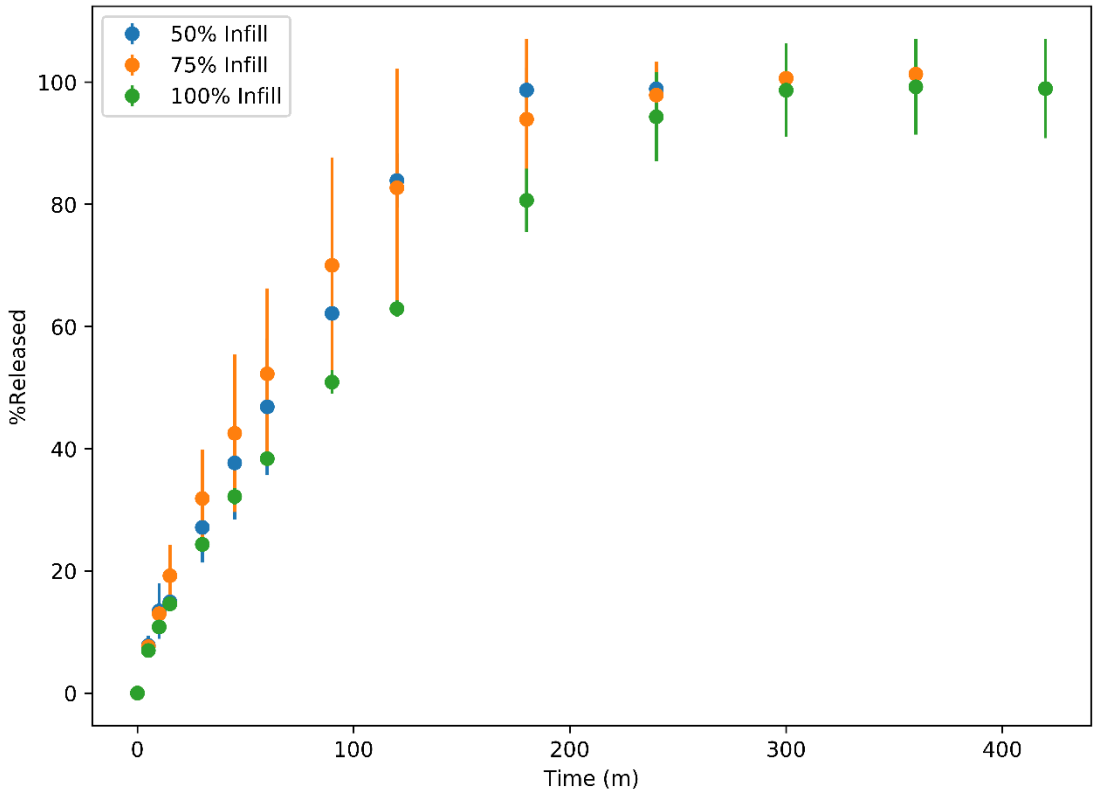

Figure 5-8: Release profile of the three infill batches in pH 6.8 PBS using the basket apparatus

5.3.2.3. Drug release testing under buffer change conditions:

Testing the dissolution rate of the 3D printed tablets under buffer change conditions was conducted as per the United States pharmacopoeial specifications for the testing of enteric release formulations (189); tablets were placed in 750 mL of pH 1.2 media for two hours, then transferred to 900 mL of pH 6.8 PBS for 6 hours (Figure 5-9).

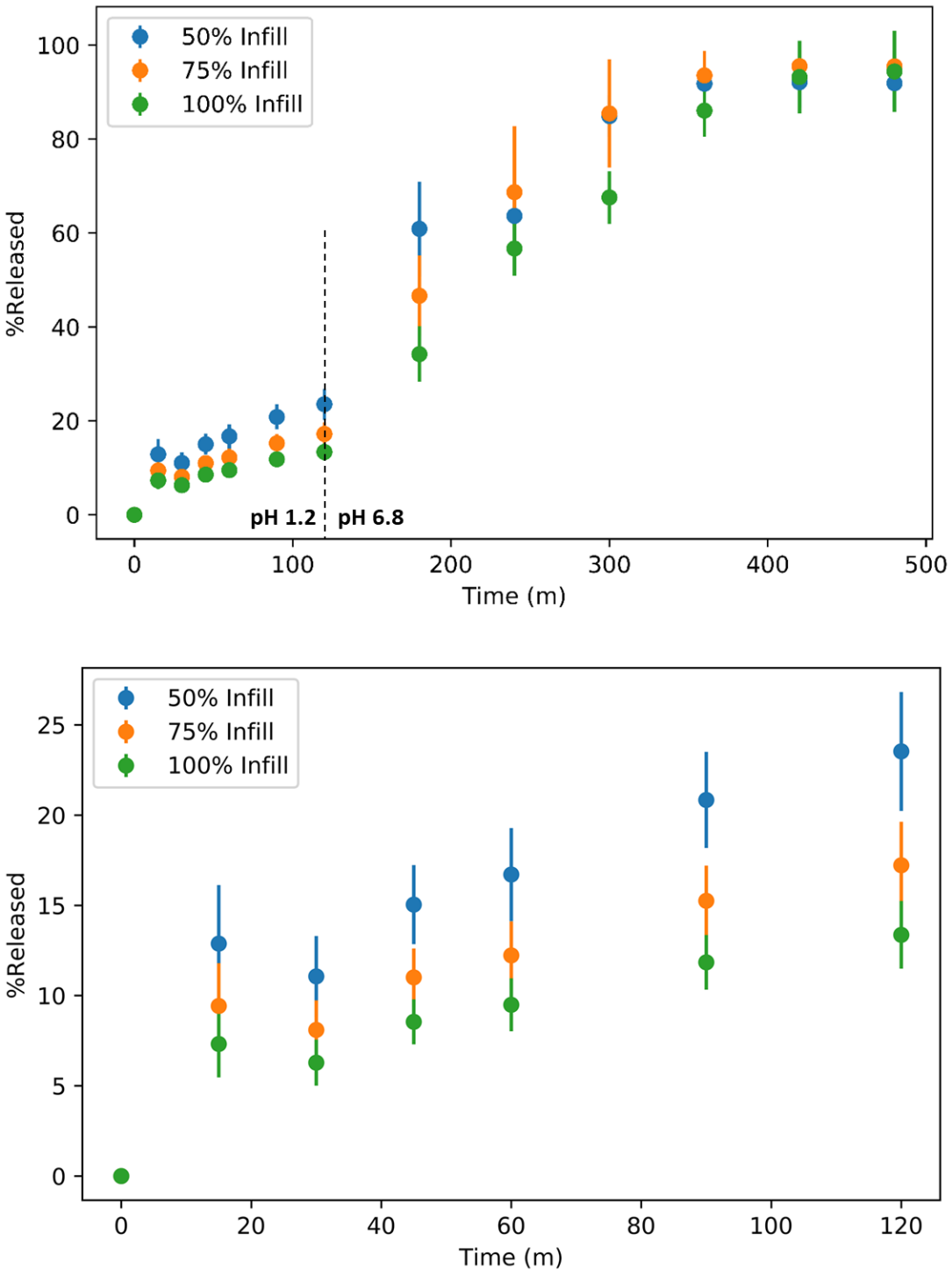

Figure 5-9: Release profile of the three infill batches under buffer change conditions conducted using the basket apparatus (top), with the first 120 minutes magnified to a separate graph (bottom).

As can be seen in Figure 5-9, the portion of the drug release study conducted in pH 1.2 followed the same trend as what was presented prior in Figure 5-5. The portion of the curve observed following the media change was significantly different from what was previously observed under similar conditions (basket method at pH 6.8 PBS). Both the

50% and 75% infill formulations required ~ 360 minutes to achieve 100% release. The 100% infill formulation required 420 minutes to achieve 100% release.

An additional set of three tablets of each infill were placed in 750 mL of pH 1.2 acidic media, then retrieved after two hours and imaged using a light microscope (Figure 5-10).

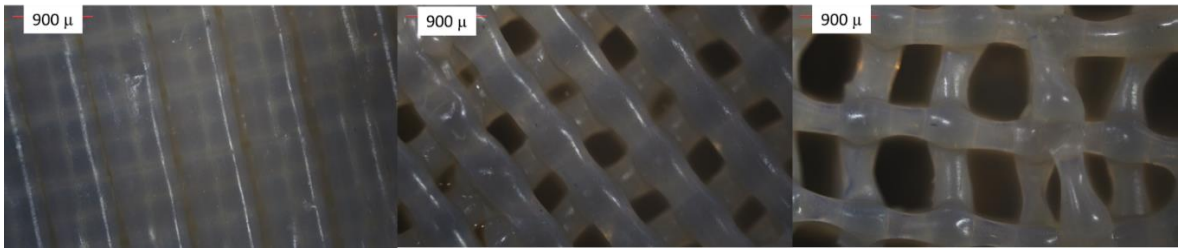

Figure 5-10: Microscopic images of the 3D printed tablets after 2 hours in pH 1.2 media. Left to right: 100% infill, 75% infill, 50% infill

5.3.2.4. Dissolution kinetics model fitting:

The significant differences observed in the behaviour of the 3D printed tablets at different pH (exclusively swelling with no observed erosion at pH 1.2, vs. complete erosion at pH 6.8) strongly suggest a change in mechanism on changing the dissolution media. Therefore, dissolution kinetics modelling was conducted in an attempt to categorise the drug release mechanisms involved at different pH. The Korsmeyer – Peppas model was conceived as a model to describe diffusion mechanisms from non-swellable polymers (190). It is, nonetheless, commonly used to describe drug release from erosion-mediated, and swellable systems (24,194,195). While it is a useful semi-empirical metric, it has notable limitations which may lead to misattribution. Therefore, it is important to explore fitting to other models as well. As mentioned previously, the present work used the Korsmeyer – Peppas model and the first-order release model. A discussion of the release kinetics model fitting, as well as the aforementioned limitations of the Korsmeyer – Peppas model are presented in section 5.4.3.

Table 5-3 shows the results of the curve fitting of the drug release rates of the 3D printed tablets at different release conditions.

*Table 5-3: Results of fitting the drug release curves obtained from the 3D printed tablets to the Korsmeyer – Peppas model and the first-order model. *: dosage form released > 60% drug content in under 15 minutes; fitting was not possible.*

		50% infill	75% infill	100% infill
Basket Apparatus – pH 6.8				
First-order model	R^2	0.991	0.999	0.996
	Rate constant (k s^{-1})	0.0093 ± 0.001	0.0125 ± 0.0003	0.0079 ± 0.0004
Korsmeyer-Peppas Model	R^2	0.997	0.999	1.000
	Rate constant (k s^{-n})	2.128 ± 0.228	2.544 ± 0.136	2.305 ± 0.074
	Peppas Coefficient (n)	0.742 ± 0.028	0.738 ± 0.015	0.688 ± 0.008
pH 6.8 using the paddle apparatus				
First-order model	R^2	0.999	0.997	0.999
	Rate constant (k s^{-1})	0.073 ± 0.003	0.025 ± 0.001	0.014 ± 0.002
Korsmeyer-Peppas Model	R^2		0.998	0.998
	Rate constant (s^{-n})	*	3.14	2.15
	Peppas Coefficient (n)		0.83 ± 0.026	0.80 ± 0.033
Basket Apparatus – pH 1.2				
First-order model	R^2	0.989	0.989	0.969
	Rate constant (k s^{-1})	0.0037 ± 0.0004	0.0037 ± 0.001	0.0085 ± 0.001
Korsmeyer-Peppas Model	R^2	0.989	0.999	0.987
	Rate constant (k s^{-n})	1.039 ± 0.195	0.630 ± 0.034	1.591 ± 0.216
	Peppas Coefficient (n)	0.628 ± 0.033	0.628 ± 0.009	0.404 ± 0.024
fitting the first 120 minutes of the buffer change release experiments				
First-order model	R^2	0.997	0.997	0.993
	Rate constant (k s^{-1})	0.018 ± 0.001	0.017 ± 0.001	0.018 ± 0.001

		50% infill	75% infill	100% infill
Korsmeyer-Peppas Model	R^2	0.996	0.996	0.996
	Rate constant (s^{-n})	2.048 ± 0.247	1.499 ± 0.181	1.164 ± 0.140
	Peppas Coefficient (n)	0.513 ± 0.028	0.513 ± 0.030	0.513 ± 0.028
Post buffer change				
First-order model	R^2	0.857	0.877	0.926
	Rate constant (k s^{-1})	0.0045 ± 0.001	0.0030 ± 0.001	0.0008 ± 0.0001

As previously discussed, the drug release profiles experiments in pH 6.8 were conducted using both the basket and the paddle apparatus. For the drug release profiles acquired using the basket apparatus, good fits were achieved with both the Korsmeyer – Peppas power law and the first-order release model. The *n*-value for all three formulations was in the range of $0.45 < n < 0.89$, which is usually associated with the release mechanisms dubbed anomalous transport. Plots of the curve fit models can be seen in Figures 5-11 and 5-12

For the drug release experiments conducted using the paddle apparatus, Figures 5-13 and 5-14 show the curve fit plots. Curve fitting of the 50% infill formulation to the Korsmeyer – Peppas model was not possible because the tablet had released > 60% of its drug content in under 15 minutes. Therefore, the number of available sampling points was insufficient to allow for a good fit to be achieved, and the aforementioned $M_t/M_\infty \leqslant 0.6$ constraint does not allow for extending the region of the curve used. Similar to what was observed with the basket apparatus, good fits were achieved with both the Korsmeyer – Peppas power law and the first-order release model. The *n*-value for all three formulations was in the range of $0.45 < n < 0.89$.

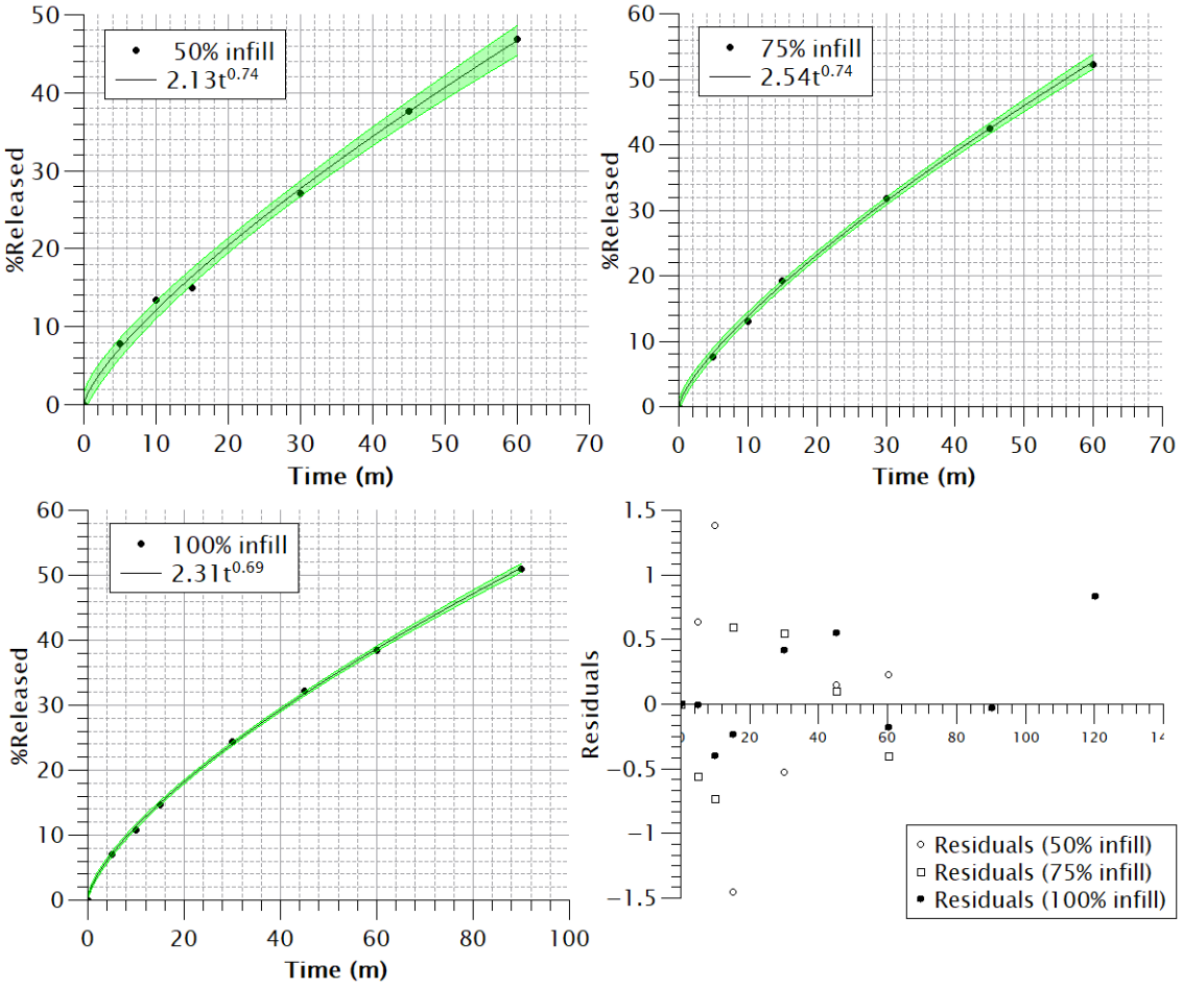

Figure 5-11: fitting the release rates (at pH 6.8, basket apparatus) of the 3D printed formulations to the Korsmeyer-Peppas power law. 95% confidence interval marked.

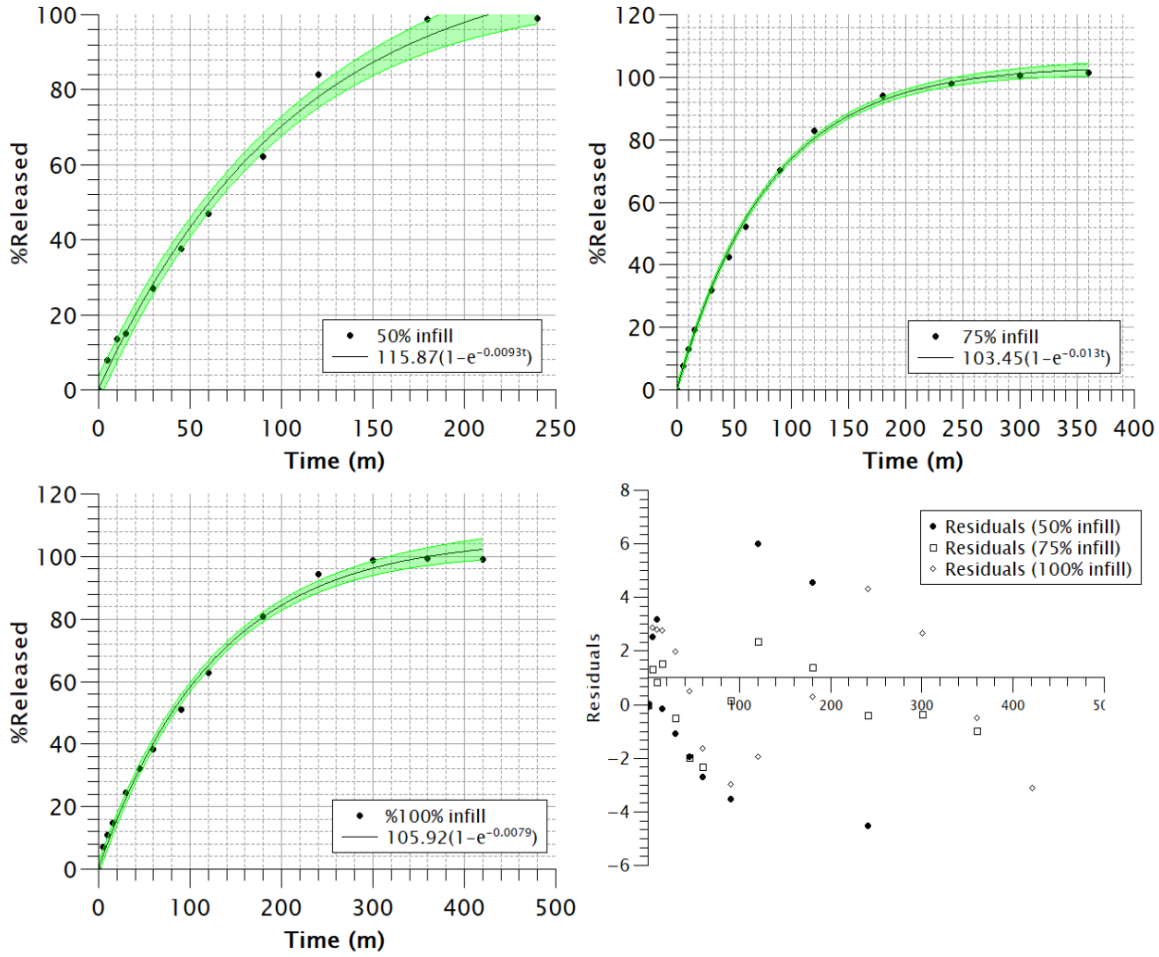

Figure 5-12: fitting the release rates (at pH 6.8, basket apparatus) of the 3D printed formulations to the first-order release model. 95% confidence interval marked.

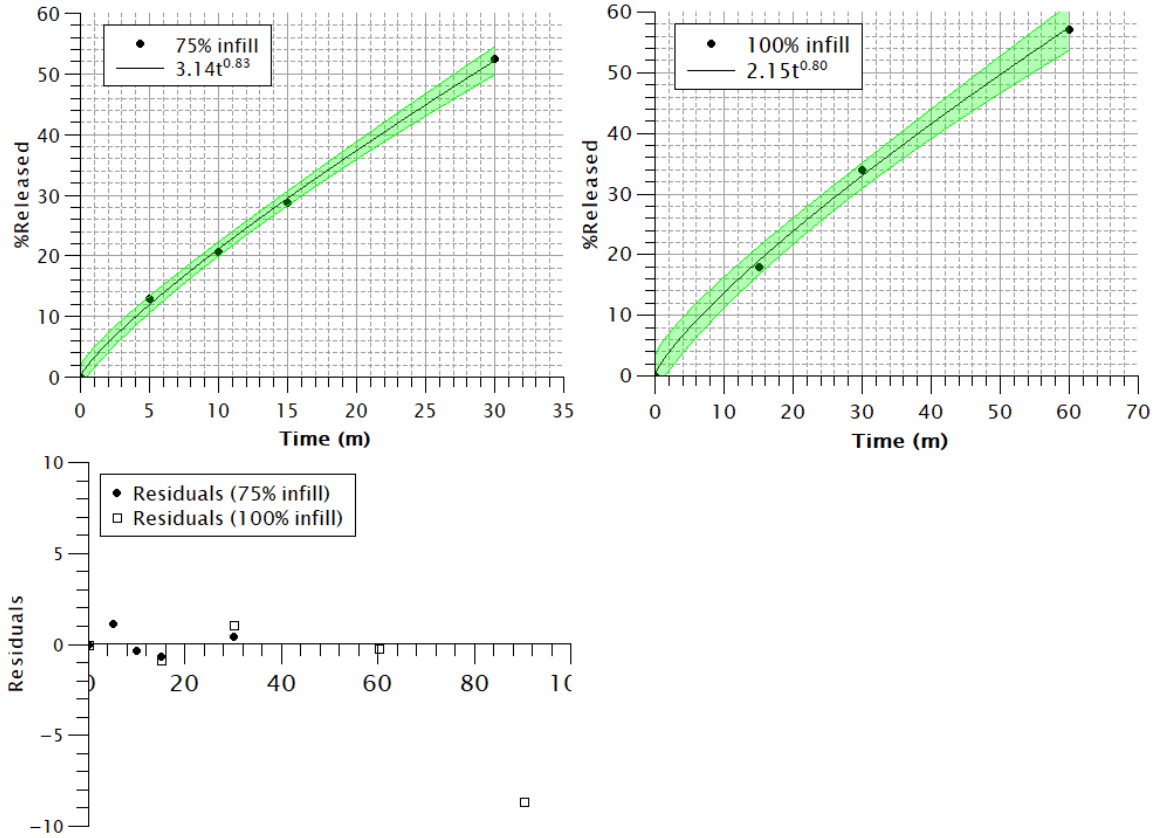

Figure 5-13: fitting the release rates (at pH 6.8, paddle apparatus) of the 3D printed formulations to the Korsmeyer-Peppas power law. 95% confidence interval marked.

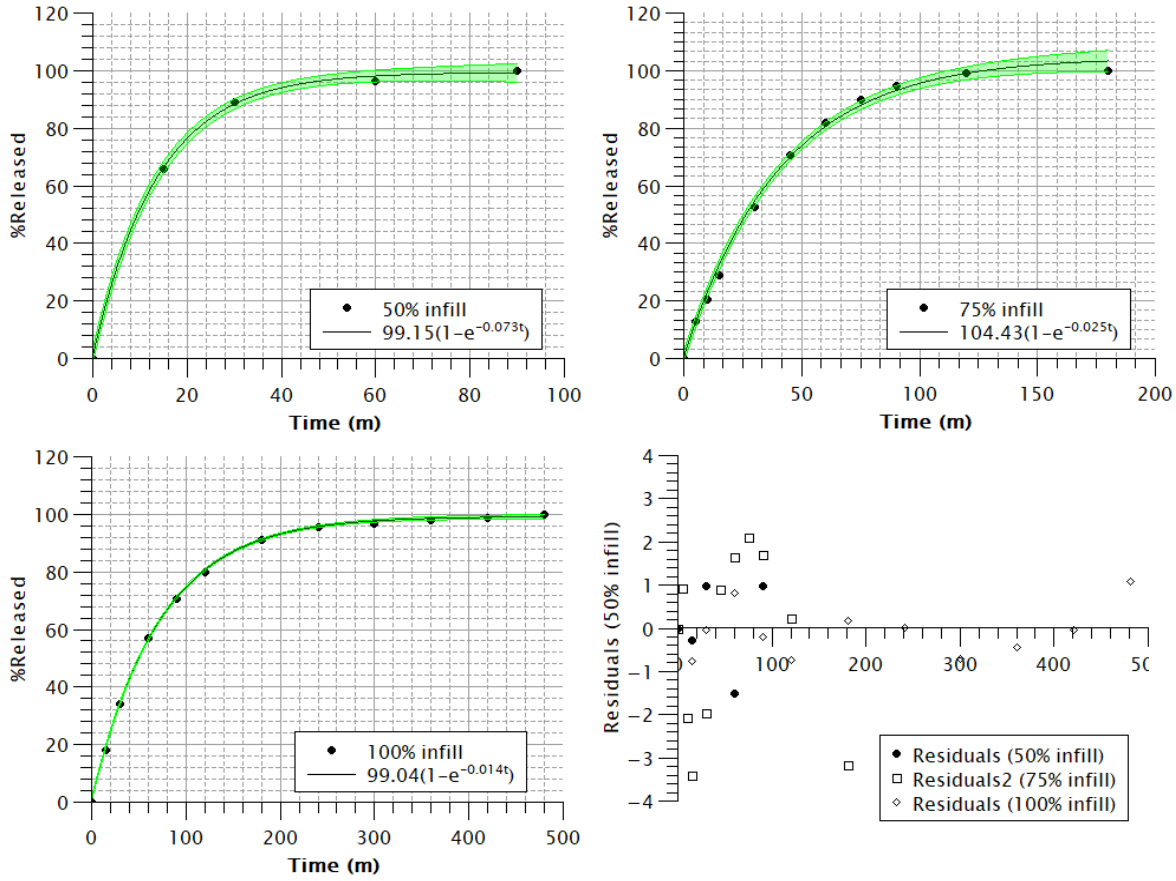

Figure 5-14: fitting the release rates (at pH 6.8, paddle apparatus) of the 3D printed formulations to the first-order release model. 95% confidence interval marked.

The 50% infill formulation had a first-order release rate constant of 0.0093 sec^{-1} under basket conditions, and a first-order release rate constant of 0.073 sec^{-1} under paddle conditions, corresponding to an 87% decrease of the release-constant when using the basket apparatus compared to the paddle apparatus. The 75% infill formulation had a first-order constant of 0.0125 sec^{-1} with the basket apparatus, and 0.025 in the paddle apparatus, corresponding to a 50% decrease in release rate when using the basket apparatus. No differences were observed between the 100% infill formulations at either apparatus.

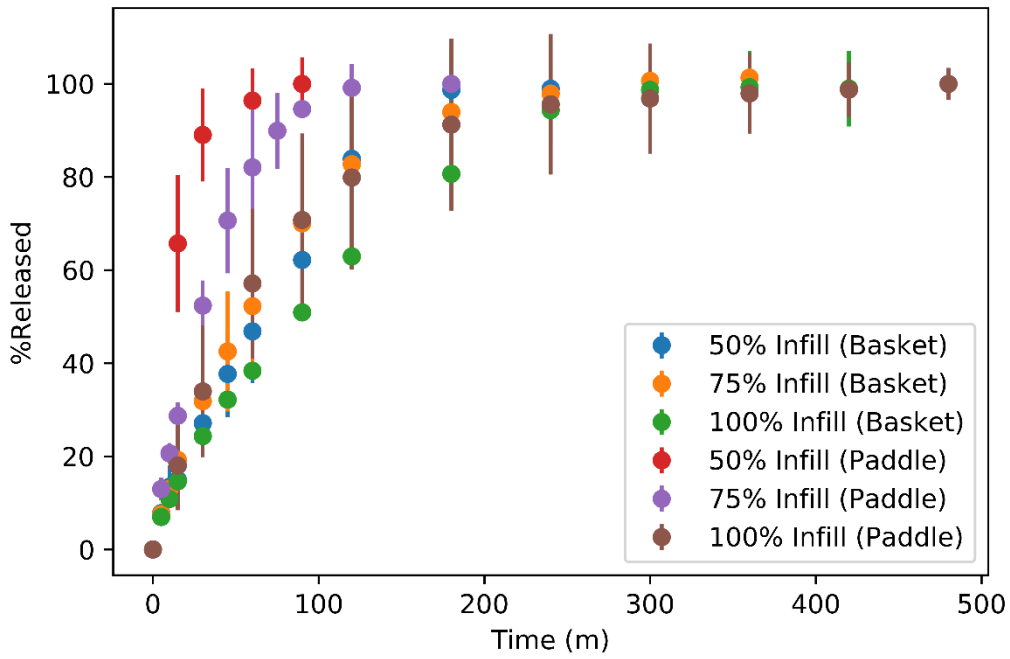

Figure 5-15: Drug release rates from the 3D printed tablets in pH 6.8, showing the release rate difference between experiments conducted with the paddle apparatus vs. the basket apparatus.

A noteworthy observation is, for the case of the 50% infill and the 75% infill tablets, there was a significant decrease in the drug release when the release experiments were conducted using the basket apparatus instead of the paddle apparatus. As can be seen in Figure 5-15, both the 50% infill and 75% infill formulations had a faster drug release rate with the paddle apparatus than their counterparts studied using the basket apparatus. This difference in release rate is also visible in the release rate constants achieved with the model fitting.

Similar to the release profiles obtained in pH 6.8, the drug release profiles obtained in pH 1.2 media were fitted to both the Korsmeyer – Peppas model and the first-order model. Table 5-5 summarises the obtained results. The 50% and 75% infill formulations had an n-value = $0.45 < n < 0.89$. The 100% infill formulation had an n-value of 0.404 ± 0.024. Figures 5-16 and 5-17 show the curve fits for Korsmeyer – Peppas and the first-order model respectively.

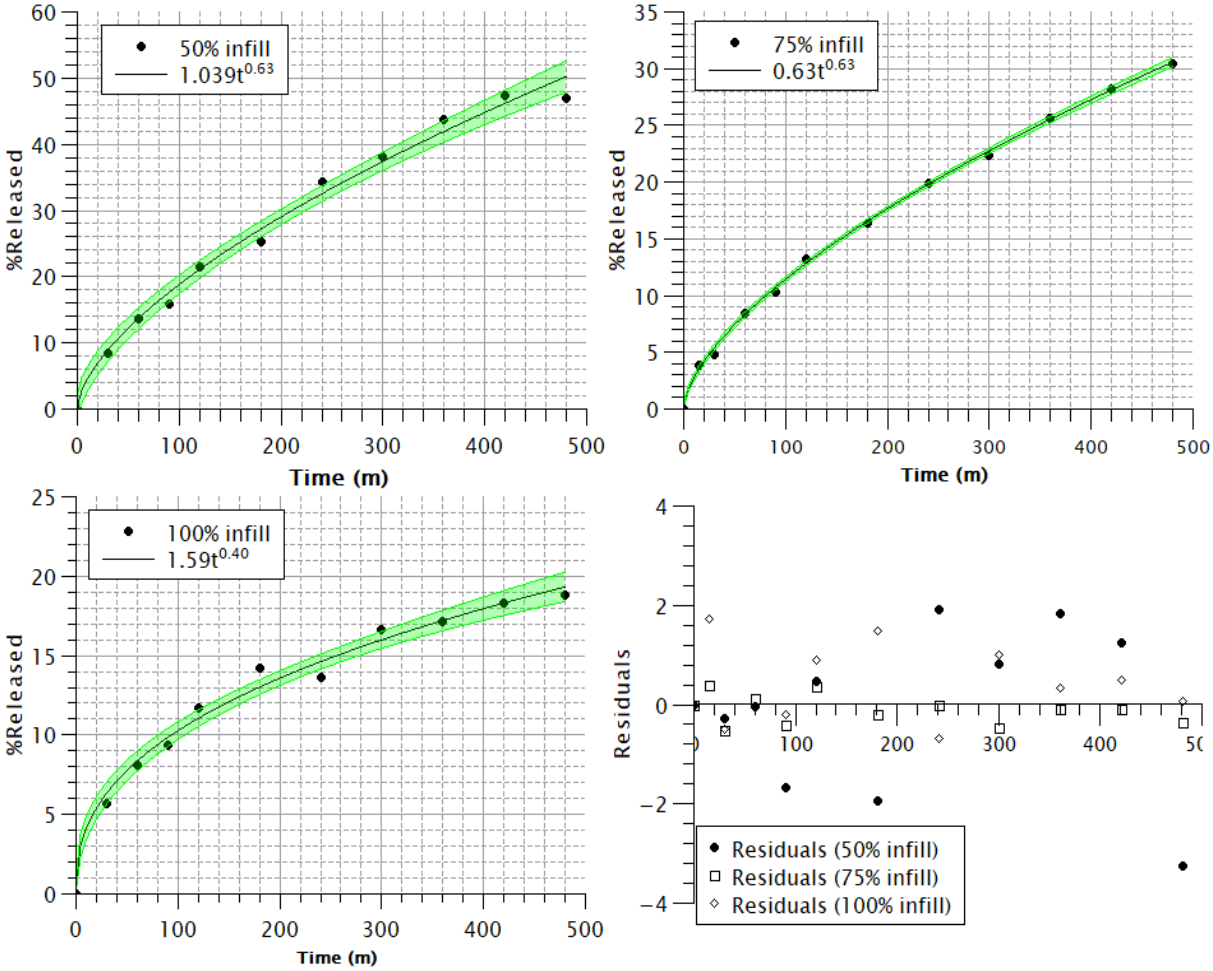

Figure 5-16: fitting the release rates (at pH 1.2) of the 3D printed formulations to the Korsmeyer-Peppas model. 95% confidence interval marked.

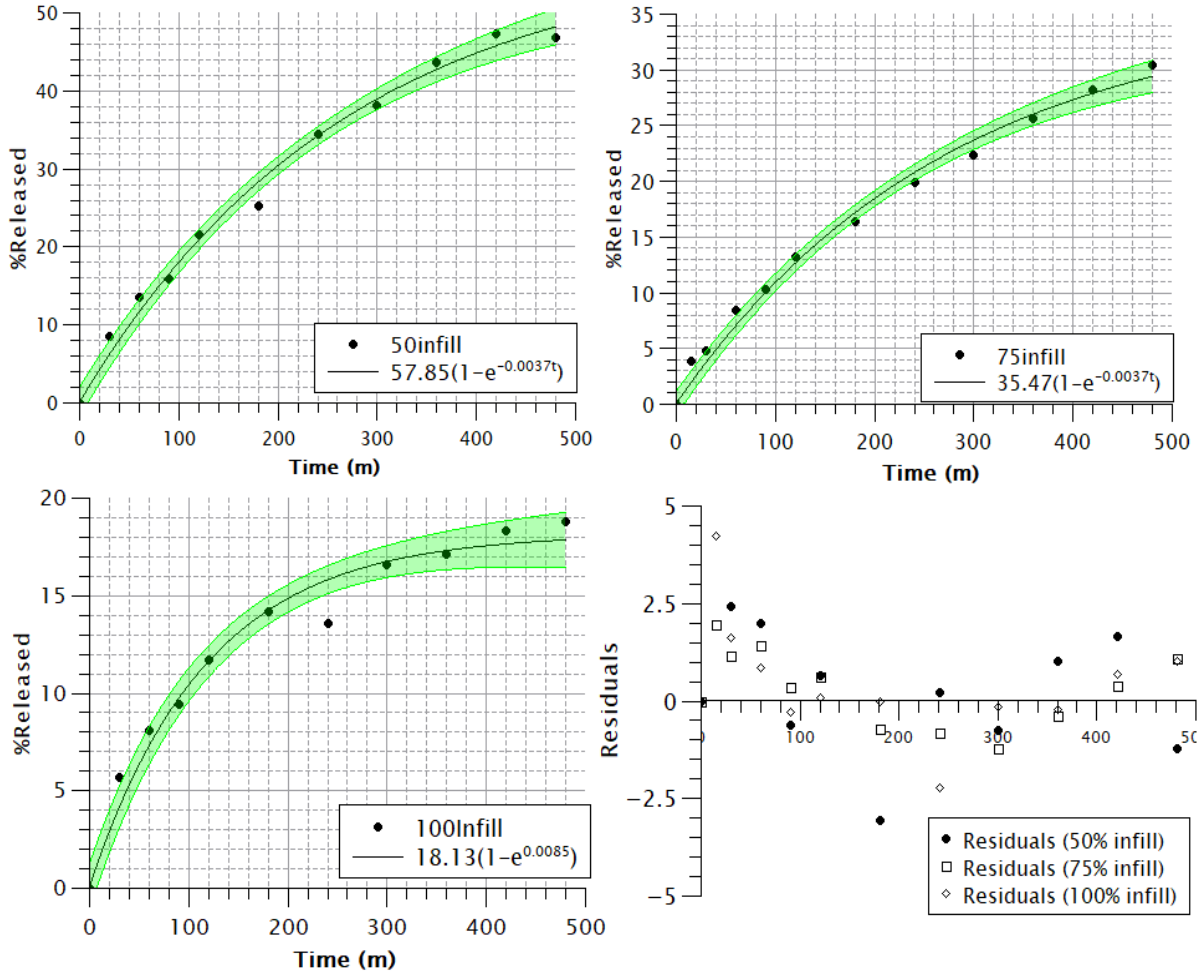

Figure 5-17: fitting the release rates (at pH 1.2) of the 3D printed formulations to the first-order model. 95% confidence interval marked.

Figure 5-18 shows the fitting of the 120 minutes of the buffer change release experiments to the Korsmeyer – Peppas, and the first-order model. The obtained fits did not differ significantly from the fits obtained from the experiments conducted in pH 1.2 for 8 hours presented above, particularly the first 120 minutes of it. Similar to all the other observed cases herein, the *n*-value corresponding to the Peppas coefficient fell in the range of $0.45 < n < 0.89$, indicating anomalous transport.

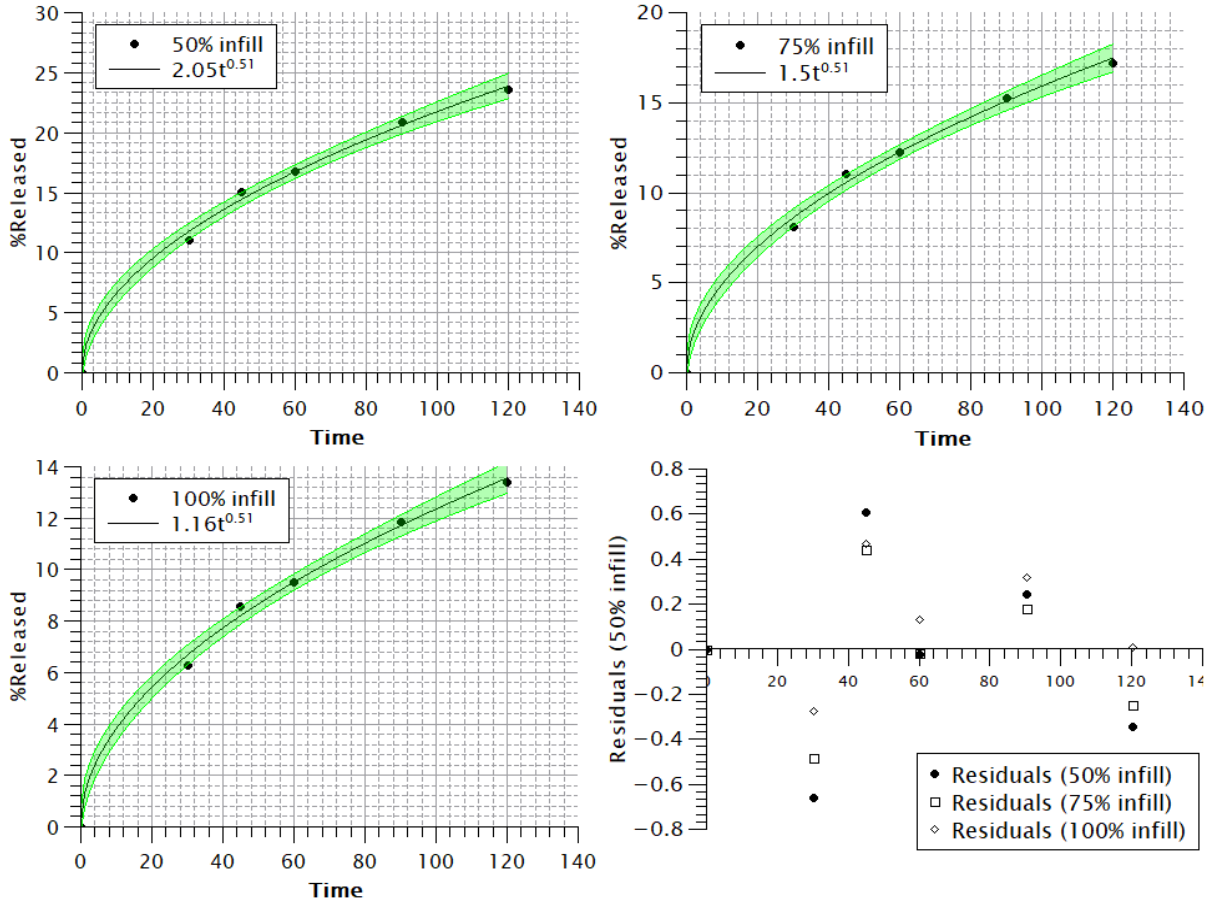

Figure 5-18: fitting the first 120 minutes (buffer change conditions) of the release rates of the 3D printed formulations to the Korsmeyer-Peppas model. 95% confidence interval marked.

Figure 5-19 shows the curve fits of the first 120 minutes of the buffer change drug release experiment to the first-order release model. For the portion of the curve following the buffer change, fitting due to the Korsmeyer – Peppas model was not possible due to the aforementioned restriction of 60% upper bound for model validity. Fitting to the first-order model was conducted, the results are shown below in Table 5-7.

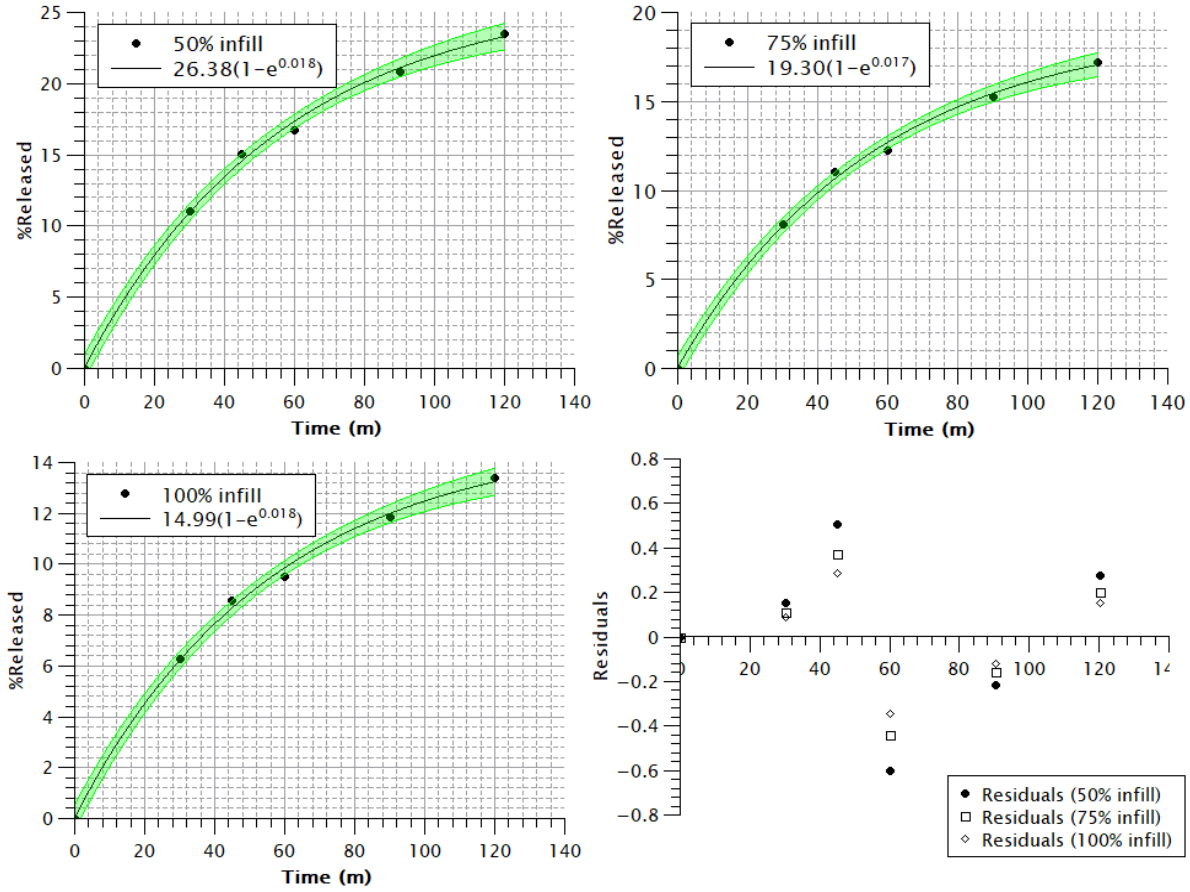

Figure 5-19: fitting the first 120 minutes (buffer change conditions) of the release rates of the 3D printed formulations to the first-order model. 95% confidence interval marked.

Figure 5-20 shows the drug release curves of the drug release experiments conducted using the buffer change method, following the buffer change, fit to the first-order release model.

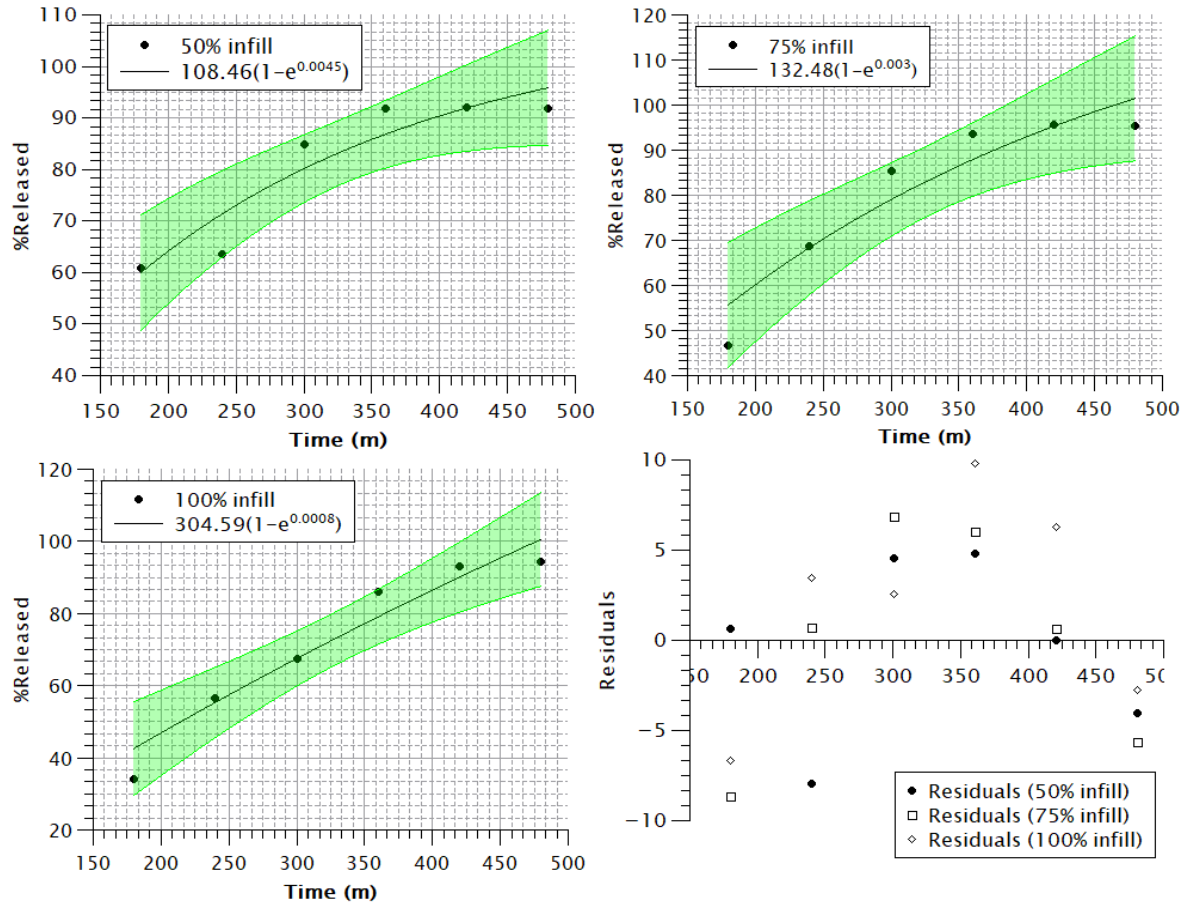

Figure 5-20: fitting the release rates of the buffer change release experiments (following buffer change) to the first-order release model

All three of the curves had an R^2 value < 0.95. Furthermore, as can be seen in Figure 5-20, there is a notable overall positive skew in the residuals, suggesting that the first-order model does not adequately describe the release mechanism in this particular case.

5.3.3. Swelling and drug release from the 3D printed meshes:

Figure 5-21 shows the decrease in pore area and the drug release rate of the 3D printed meshes.

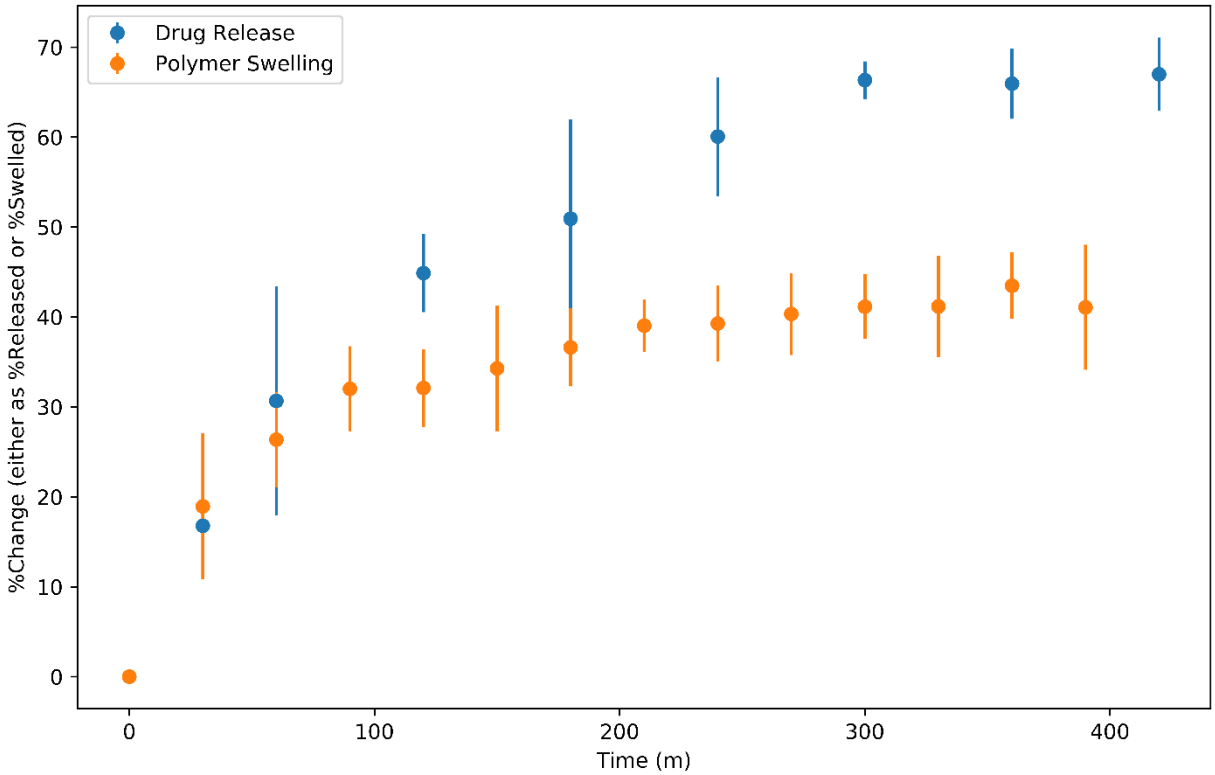

Figure 5-21: Drug release rate vs. polymer swelling rate.

Drug release rate from the meshes reached a plateau at ~70% release (300 minutes). Maximum polymer swelling was reached after ~200 minutes, the pore size having decreased by ~40%. The onset of the plateau of drug release appears to have occurred concurrently with the polymer reaching maximum swelling. Furthermore, much like their tablet counterparts, the grids remained intact throughout the entirety of the experiment, with no polymer erosion observed. Unsurprising, since HPMCAS, the primary matrix former of this formulation is an enteric polymer and is well-documented to have little-to-no solubility under pH 5 (98,112,138).

5.4. Discussion

5.4.1. Characterisation of the melt-extruded filaments:

As previously discussed in section 3.3.1., the results obtained from DSC, ATR-FTIR, and PXRD strongly suggest that PAC is molecularly dispersed in the HPMCAS-PEO carrier matrix. This, coupled with the uniformity of drug content along the lengths of the melt-extruded filaments strongly indicate that any observable differences in release rates are going to be solely due to the impact of the print geometry as opposed to the solid state of the drug.

The yellow-to-brown discolouration observed in the filaments and printed tablets (Figure 5-2) can be attributed to either the natural discolouration HPMCAS is susceptible to when undergoing thermal processing (163). However, it is possible that the observed degradation is due to the oxidation of paracetamol. Oxidation of paracetamol is documented to yield a red-orange discolouration due to the release of ammonium ions (196). The assay of drug content in the filament (Figure 5-4) suggests that somewhere between 4.6% to 9.4% of paracetamol was lost during processing. While some of the lost drug is probably due to paracetamol powder being lost during transfer, one cannot rule out the possibility of the thermal oxidation of paracetamol during thermal processing.

5.4.2. *In vitro* drug release studies:

5.4.2.1. Drug release in pH 6.8

When the drug release profiles were acquired using the paddle apparatus, the drug release rates were proportional to the infill density, with the 50% infill formulation being the fastest releasing, followed by the 75% infill, then the 100% infill formulation. On replicating the experiment using the basket apparatus. The release rates of both the 50% infill and the 75% infill were found to decrease significantly from the paddle counterparts. However, the 50% infill formulation was found to have a significantly faster release rate than the 100% infill formulation under those conditions.

The significant difference seen between the basket and the paddle is likely due to the differences in flow dynamics between the two apparatus, with the latter exerting greater shear on the tablets, and (as evidenced by the absence of any significant differences between the two 100% infill counterparts) greater solvent shear *through* the tablets.

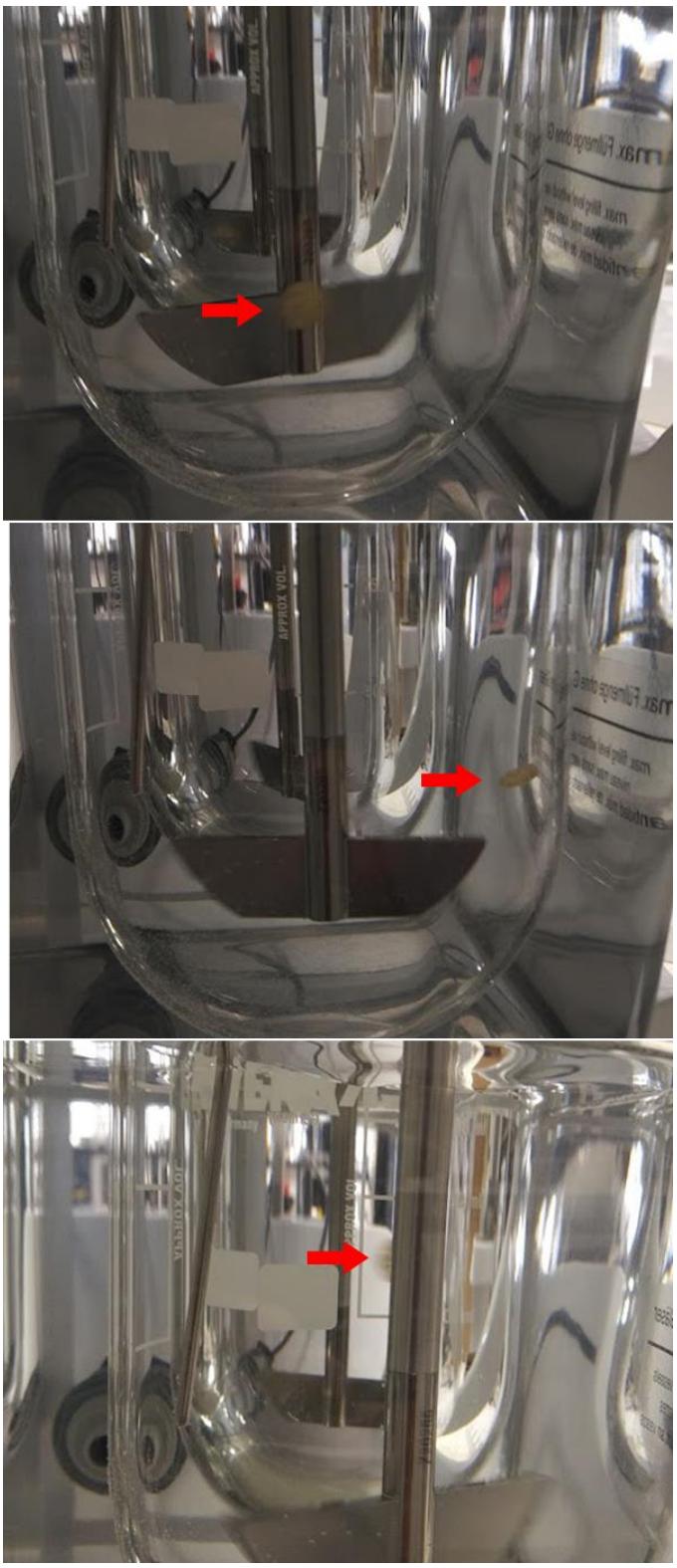

Figure 5-22: tablets in the dissolution bath during the release experiment conducted at pH 6.8 using the paddle apparatus. The tablet (marked) is shown swimming around the bath due to the shear applied by the paddle on the dissolution media

Photographs of the tablets during the release experiments with the paddle apparatus show the tablets being moved around the dissolution bath by the action of the paddle rotation (Figure 5-22). The basket apparatus, on the other hand, differs from the paddle in two

ways, the first being the fact that the basket confines the tablet within it, restricting the motion of the tablet during the dissolution experiment, and secondly, the basket apparatus is a thin cylinder that sits directly in the centre of the dissolution bath, and thus has much lower capacity to move the dissolution media than the much longer paddles. Therefore, the torque of rotation is much higher with the paddle apparatus than with the basket apparatus (Figure 5-23), due to the effective distance of the paddle apparatus being much longer than that of the basket.

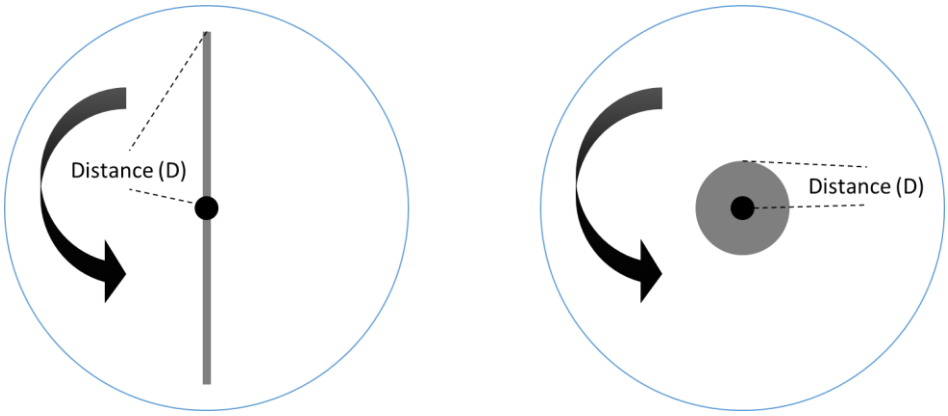

Figure 5-23: Graphical representation of the dissolution apparatus (cross-section) showing the effective distance available to shear the dissolution media by both the paddle (left) and the basket apparatus (right)

In the paddle apparatus, where the tablets are allowed to flow freely through the bath, the solvent movement around and through the open cavities of the lesser infill tablets yielded greater polymer-media interactions, resulting in the significantly faster drug release rates compared to when the tablets were confined to the basket apparatus. The 100% infill tablets, having no open internal structures, exhibited no significant difference between the paddle apparatus and the basket apparatus, since solvent motion is restricted only to the external surface of the tablet. This suggests that the drug release rate from open 3D printed systems is highly dependent on the hydrodynamics of the environment in which the dissolution is taking place (197,198).

5.4.2.2. Drug release in pH 1.2 and the impact of swelling:

The drug release rate of the three infill variants (50% infill, 75% infill, and 100% infill) followed a trend that was proportional to their infill density, with the 50% infill formulation being the fastest-releasing, followed by the 75% infill formulation, with the 100% infill formulation being the slowest of the three. This is likely due to the differences

in the surface areas of the three formulations, with the 50% and 75% infill tablets having greater surface areas to allow for drug diffusion.

One observation that was of interest is the fact that the roads comprising the tablets were observed to swell significantly throughout the 8 hours over which the release experiment was conducted (Figure 5-6). This swelling rate was approximated semi-quantitatively using the microscopic method outlined prior in section 5.2.2.6. The observed swelling rate of the grid structures cannot be readily extrapolated to the tablets, due to the significant differences in geometry, and the hydrodynamic environment of the dissolution media. However, if one were to consider the observed swelling in the context of drug release rate from the grids, it may provide some context to the swelling rates of the 3D printed tablets if viewed in light of their observed release rates. An estimation that is not too far-fetched, as the grids and the tablets are fabricated from the same formulation.

Of the 3D printed grids, the most notable observation is that the drug release required roughly the same time to reach a release plateau as the time required for maximum swelling to be achieved (~200 minutes). This suggests that there may be a correlation between the polymer swelling rate and drug release rate.

Observing the drug release rates from the 3D printed tablets shows that all three infills appear to be tending towards a drug release plateau (~300 minutes in the 50% infill, and ~180 minutes in the 75% infill formulation), with the exception of the 100% infill formulation which is maintaining a steady plateau of drug release from the onset of the experiment. Examining this observation in the context of the release-swelling correlation observed with the 3D printed grids (Figure 5-21) suggests that this tendency towards a plateau may be related to the swelling of the polymer in pH 1.2. This swelling-release correlation can be explained by either of two hypotheses, both of which are discussed in the subsequent paragraphs.

The first hypothesis as to why drug release is hindered by swelling is due to the effect swelling has on the surface area available for drug diffusion; the filled internal microstructure of the 100% infill tablet allows very little room for the swelling of the roads of the tablet. Similarly, the 75% formulation has a lower spatial allowance to accommodate swelling than the 50% infill formulation, therefore, it arrived at its "maximum" swelling faster than the 50% infill formulation. Both the tablets and more

noticeably the grids were observed to curl up significantly during the experiment, which indicates that the swelling is anisotropic. The fact that the formulation exhibits anisotropic swelling dictates that swelling will decrease the surface area of the pores within the tablets, as opposed to altering the aspect ratio of the tablets as a whole. The anisotropy of the 3D printed formulations is discussed further in section 5.4.2.4.

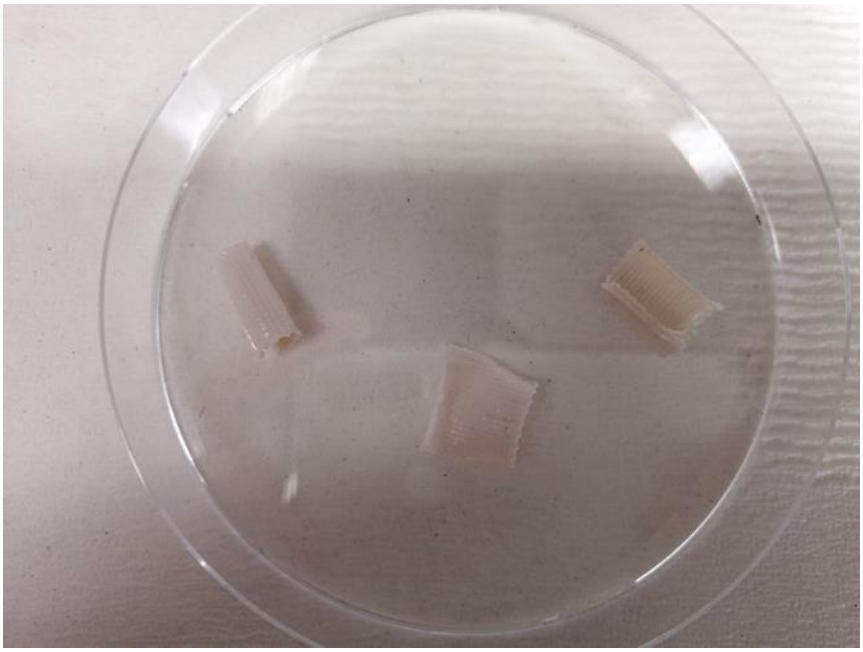

Figure 5-24: 3D printed grids post-dissolution, showing contortion due to anisotropic swelling

The second hypothesis explaining why drug release is hindered by swelling relates to the rate of drug liberation from the polymeric matrix. It is evident from the absence of dose dumping in the release rates of the three formulations (particularly the 100% infill formulation) that drug release from the polymer matrix is rate limited by the rate of polymer hydration. In such situations, the distance the dissolution media must travel to liberate a drug molecule increases as more drug is released. Polymer swelling during dissolution indicates solvent entrapment within the polymer matrix, which introduces a gradient through which the liberated drug molecules must first diffuse to be released from the tablets.

Verifying that the 50% and 75% infill formulations actually tend to steady plateau of drug release requires conducting the release experiments to completion. However, extrapolating from the behaviour of the 100% infill formulation, and the 3D printed grid may provide empirical evidence on the behaviour of the two lesser infill tablets.

In the drug release studies conducted under buffer change conditions, in which the tablets were allowed to swell in pH 1.2 media for 2 hours, then transferred to pH 6.8 PBS were then conducted to determine whether this swelling effect would have a significant impact on the release rate in situations similar to the pH changes expected an in-vivo scenario in which the formulation will likely travel from gastric pH to intestinal pH.

5.4.2.3. Drug release under buffer change conditions

As discussed in the previous section, drug release under buffer change conditions was conducted to determine whether the swelling of the polymer roads in acidic conditions was significant enough to negate the impact of the greater surface area of the lesser infill, open tablets. Microscopic images of the tablets after 2 hours in pH 1.2 media (Figure 5-10) showed some swelling over the 2-hour period. This experiment was performed to determine whether that swelling had an impact on the drug release rates of the 3D printed tablets.

A significant decrease in drug release was observed in the buffer change release studies compared their pH 6.8 PBS counterparts (Figure 5-25) for all the three infill formulations. The overall decrease in the release rates of the formulations in the buffer change experiments is most likely due to the low, diffusion-controlled release of HPMCAS in pH 1.2 media causing a “lag phase” in the drug release, one which is not seen in curves obtained in pH 6.8, resulting in the perceived overall decrease in drug release rate.

Similar to what was observed in other cases, the 50% infill formulation consistently had a significantly higher drug release rate than the 100% infill formulation.

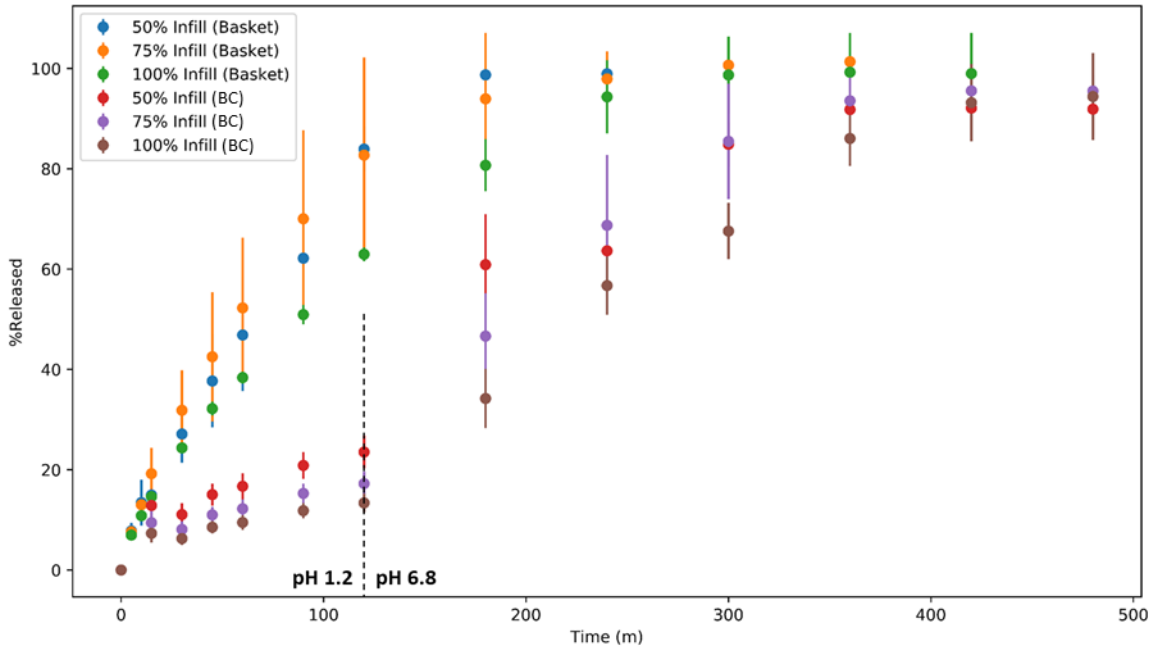

Figure 5-25: drug release profiles of the three infill formulations in pH 6.8 (basket apparatus) vs. their release profiles in buffer change (BC) conditions.

5.4.2.4. Reproducibility of drug release from the 100% infill formulation

Of all the release experiments conducted, the release curves obtained for the 100% infill formulation in pH 6.8 PBS using the paddle apparatus (Figure 5-7) notably exhibited a much wider standard deviation than any of its counterparts, showing an average standard deviation of ±11.79%, and a maximum standard deviation of ±19.78%.

The observed deviation is far greater than is to be expected of sampling error. The standard deviation at the last time point (480 minutes; the point at which the tablet has completely dissolved) is ±3.41%, at which point the possible causes of deviation are due to human and machine error as the tablets have dissolved completely and there is no more discrepancy to be observed due to drug release rate differences between the three replicates. This indicates that the relatively wide deviation between the 100% infill replicates at those conditions are due to genuine sample-to-sample differences.

Plotting the separate drug release curves of the three replicates of the 100% infill formulation separately shows three distinct curves, each with a different release rate (Figure 5-26). This was not observed when separating the replicates of the 50% infill formulation and the 75% infill formulation (Figure 5-27).

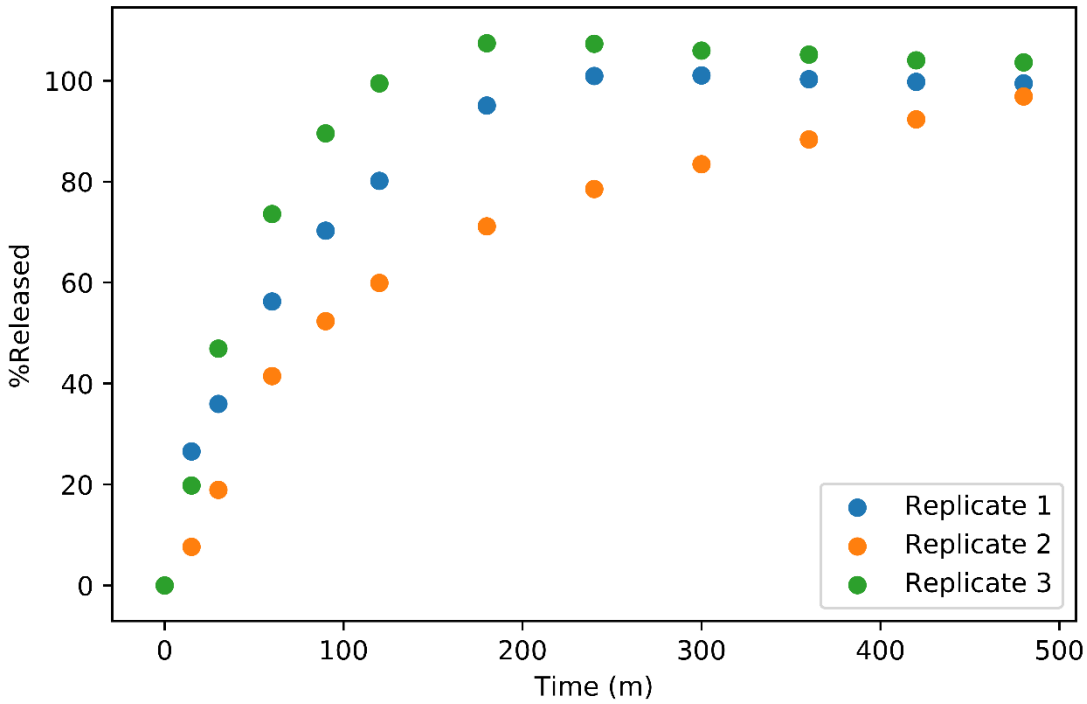

Figure 5-26: Release curves of the 100% infill formulation at pH 6.8 using the paddle apparatus, with the three replicates plotted separately

In the 50% infill formulation (Figure 5-27A), the observed discrepancies between the three replicates are two notable drops in drug release at t=30 minutes (Replicate 3) and t=60 (Replicate 2), which cannot be real observations as the amount of drug released cannot decrease. The observed drops in amounts of drug release may be due to accidental over-dilution on replenishing the dissolution media.

In the 75% infill formulation (Figure 5-27B), the plots of the three replicates appear to be largely similar, except for Replicate 3 possessing a slower release rate.

Estimates the release half-life (T_{50}) of the three different infill formulations based on the graphs of the separate replicates are shown in Table 5-4.

Table 5-4: T_{50} of each replicate of the three infills formulations at pH 6.8 using the paddle apparatus

Formulation	Replicate 1	Replicate 2	Replicate 3
100% infill	30 minutes	50 minutes	60 minutes
75% infill	40 minutes	30 minutes	30 minutes
50% infill	7 minutes	12 minutes	12 minutes

The difference in T_{50} between the three replicates of the 100% infill formulation is much larger than its lower infill counterparts. Furthermore, each replicate forms a smooth curve with no random scattering of sampling points, suggesting that 100% infill formulation has indeed exhibited three different drug release behaviours under those conditions.

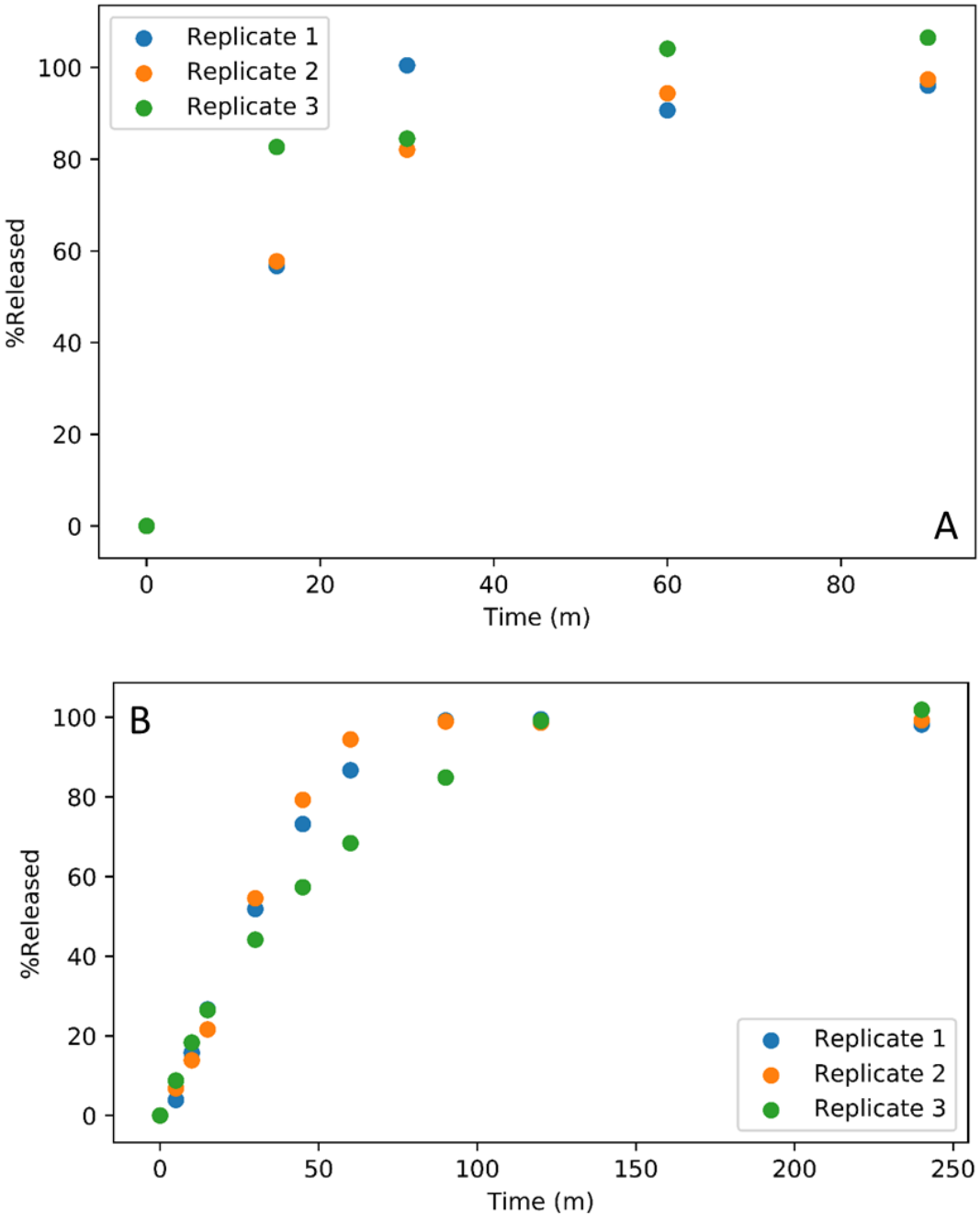

Figure 5-27: Release curves of the 50% infill formulation (A) and the 75% infill formulation (B) at pH 6.8 using the paddle apparatus, with the three replicates plotted separately

A possible explanation for this phenomenon may be due to the build-up and dissipation of thermal potential energy in the tablet during printing. The pre-processing for 3D printing is HME, which is well documented to align the polymer chains parallel to the direction of motion within the extruder (163,199). In printing, the polymer is first passed through the heated nozzle at the constant rate of the printing speed, with the direction of motion being parallel to that during extrusion. The aligned polymer chains are then deposited onto the build plate and must instantaneously be deflected at a 90° angle so that the road rests on the build plate (200). Once a road is deposited, it rapidly cools down with heat being transferred to the surrounding environment by convection (201). Concurrently, a new road is being deposited, forming a contact point with the prior, and similarly begins cooling down by transferring heat to the environment and exchanging heat with the neighbouring road (153,202).

For the tablets described herein, the 50% and 75% infill tablets have every single road exposed to air, making the surface area available for cooling much larger than that of the 100% infill tablets (Figure 5-28). Due to the aforementioned stressing and alignment during printing, this rapid cooling is hypothesised to cause anisotropic alignment of the polymer chains as they cool down too rapidly to relax and re-entangle post-printing.

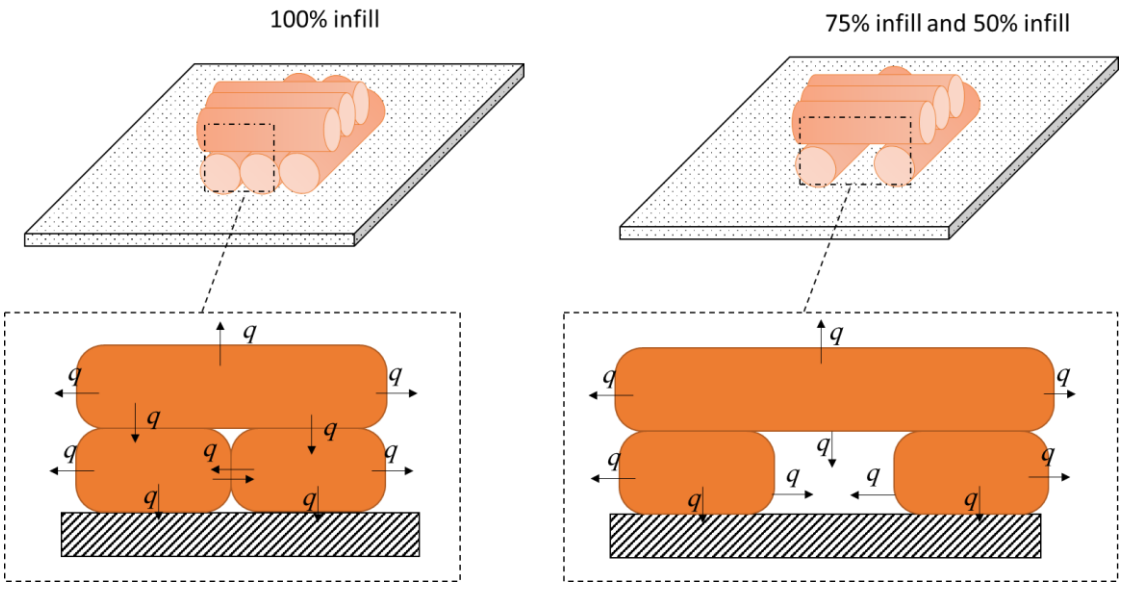

Figure 5-28: a sketch representing heat flow(q) while the tablets are cooling during, and post-printing

In 100%, roads which happen to be deposited in the inner sections of the object are restricted to exchanging heat with the neighbouring roads as they are isolated from the

external environment. This dictates that the 100% infill tablets will cool down at a slower rate than their lesser infill counterparts. Furthermore, the stresses forced on the melt, as well as the thermal gradient arising from the variability of heat transfer due to the majority of the roads being isolated from the air will dictate that roads in different regions of the tablet will cool down at different rates from one another, and thusly will possess different degrees of entanglement between the polymer chains as no two roads have been allowed to relax under similar conditions. This results in the build-up of thermal stress in the tablet. Residual thermal stress in 3D printed objects fabricated by FDM is a well-documented phenomenon (153,200–204).

When observed under polarised light, the 50% and 75% infill tablets exhibited light scattering diffraction (Figure 5-29). Seeing as DSC, PXRD, and FTIR data showed no evidence of crystallinity within the formulations and factoring in that the tablets were placed whole (2 mm thickness) on the microscope stage, it is unlikely that the observed light scattering is due to the presence of crystals within the formulation, which suggests that the observed light diffraction is due to the anisotropic alignment of polymer chains within the matrix of the tablets (205,206). This anisotropy was not observed in the 100% infill batch.

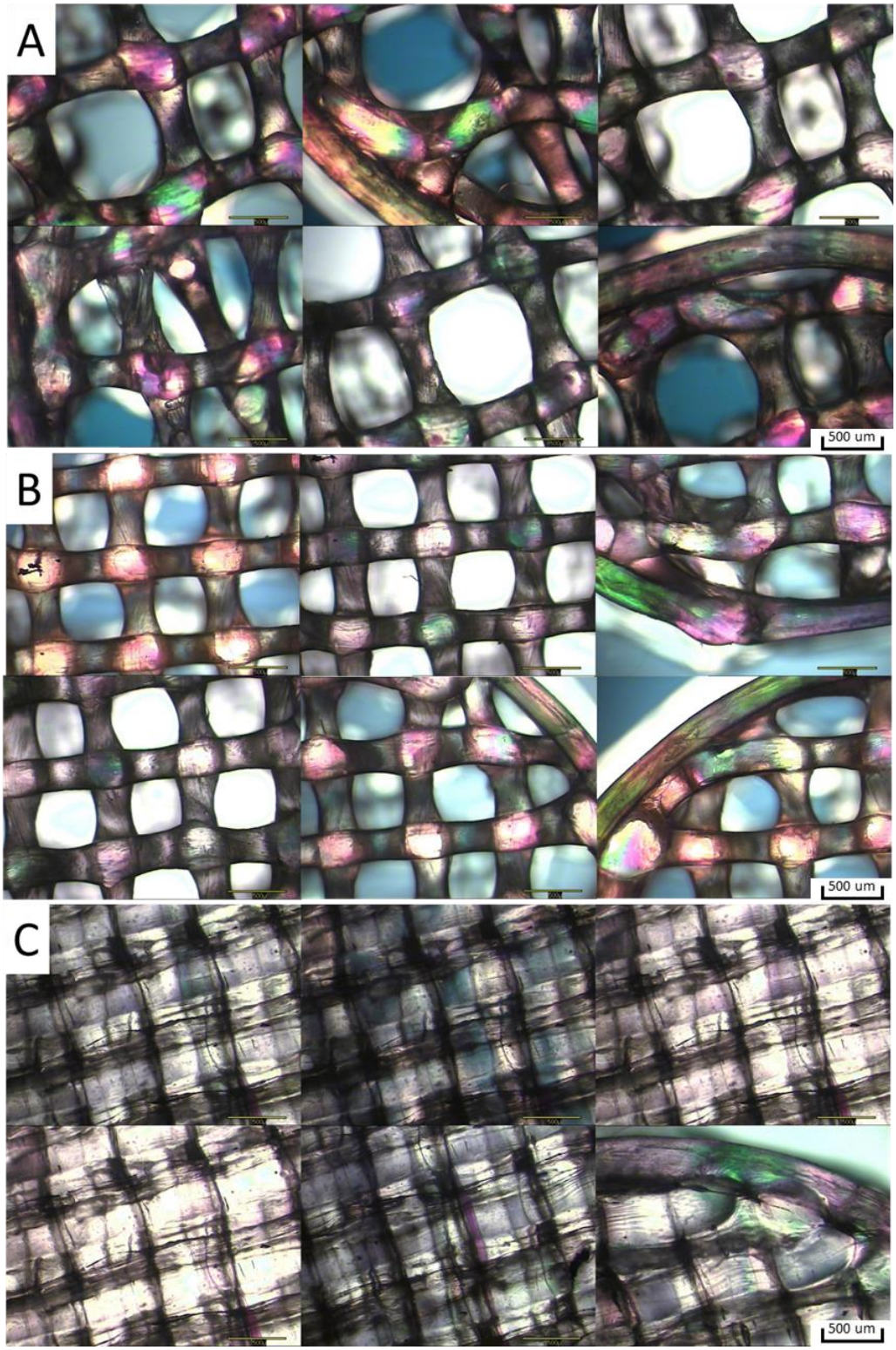

Figure 5-29: Polarized light microscopy images of the (A) 50% infill, (B) 75% infill, and (C) the 100% infill formulations.

Keeping the two lesser infill tablets isothermal at 100 ºC for 10 minutes caused the birefringent light scattering patterns to disappear (Figure 5-30). This observation strongly supports the argument presented prior relating to forced polymer chain entanglement and relaxation during printing; the anisotropy observed in the lesser infill batches may be

attributed to the system cooling rapidly, preventing the polymer chains from relaxing after the forced extrusion/printing alignment, while the hypothesised lower thermal gradients in the 100% infill tablets would allow some degree of polymer relaxation before the system drops to below its glass transition, forming a largely isotropic matrix.

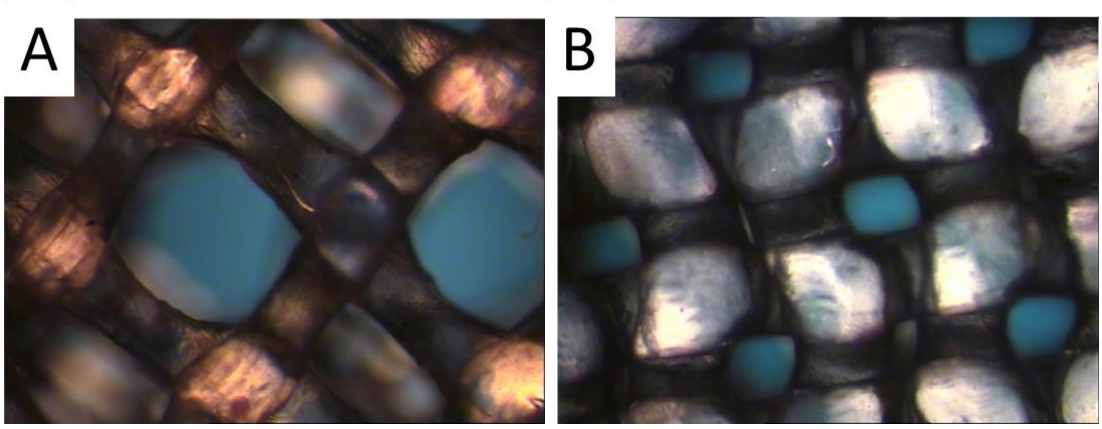

Figure 5-30: the 50% infill (A) and 75% infill (B) tablets after being heated at 100 ºC for 10 minutes

The argument presented prior shows that the 100% infill formulation is cooling at a slower rate and unevenly, compared to the 50% infill and 75% infill formulations. It is possible that the uneven cooling causes microscopic fractures to develop within the matrix of the 100% infill formulation. Such fractures are exaggerated when subjected to the high shear conditions of the paddle apparatus (as discussed in section 5.4.2.1.), causing pieces of the tablet to break off, thus causing the observed differences.

While one cannot dismiss the possibility that the observed discrepancy in the release profiles of the 100% infill tablets is due to the heterogeneity of the PEO content within the tablets causing varying hydrophilicity inside the tablet matrix, the thermal-history dependant anisotropy strongly supports the chain entanglement hypothesis. Furthermore, release rate discrepancies of this magnitude are commonly reported with FDM printed dosage forms, even in cases where the filament had been prepared via the soaking method (18,26,55,110,124), which decreases the likelihood of this phenomenon is due to content heterogeneity.

5.4.3. Dissolution kinetics model fitting:

The use of the coefficient of determination (R^2) to determine the goodness of fit when fitting dissolution data to a mathematical model is a commonly practised method in the literature (18,24,36,194,195,207). By that metric, good fits were achieved for all the release curves ($R^2 > 0.99$) to both the Korsmeyer – Peppas model and the first-order release model, with the exception of the fitting the latter 6 hours of the simulated in-vivo release studies (Table 5-8), for which $R^2 < 0.95$ for all three formulations.

The Korsmeyer – Peppas model is a popular method for categorising drug release profiles (24,36,70,194,195). It does, however, have known limitations. The model, as originally described by Ritger and Peppas, was intended to be only applied to describe diffusion-mediated (whether Fickian or non-Fickian) drug release of non-swellable systems (190). It is, nonetheless, often used to investigate the drug release kinetics of systems which are known to swell. Another limitation is that the model is only valid to describe drug release up to 60% of the dosage form content, leaving the latter 40% of the release profile completely unaccounted for, which is a significant portion to discard. Furthermore, while the Peppas coefficient (n) can clearly describe Fickian diffusion ($n = 0.5$ (sheets) or $n = 0.45$ (cylinders)), and zero-order ($n = 1$), the mechanism which Ritger and Peppas dubbed "anomalous transport" seemingly has little correlation with any actual physical phenomenon, as the anomalous transport mechanism is seemingly suitable to describe both non-Fickian diffusion, and erosion-controlled release.

Sunil et al. used the Korsmeyer – Peppas model, among others, to describe the release of indomethacin from a sucrose-fatty acid ester carrier matrix (194), achieving good fits ($R^2 \geqslant 0.98$) to all of nine formulations reported. Sunil et al. did note observing swelling with some of the reported formulations (attributed to their pregelatinsed starch content). The formulations. Paradoxically, the formulations reported by Sunil et al. achieved equally good fits to the Hixson-Crowell model, the Higuchi model, the zero-order release model, and the first-order release model. The Peppas coefficients (n-values) reported were attributed by Sunil to be indicative of anomalous transport.

.

Table 5-5: kinetic model fitting of formulations T1 through T9 as reported by Sunil et al. Table recreated from Sunil et al., (194)

Model	Zero Order		First-order		Higuchi	Hixson-Crowell	Pepas	
Batch	R^2	K_0	R^2	K	R^2	R^2	R^2	n
T_1	0.990	1.56	0.998	0.028	0.979	0.928	0.995	0.771
T_2	0.991	1.587	0.958	0.024	0.931	0.915	0.979	0.858
T_3	0.982	1.687	0.944	0.023	0.893	0.888	0.986	0.881
T_4	0.977	1.66	0.984	0.049	0.990	0.985	0.997	0.719
T_5	0.979	2.10	0.983	0.051	0.992	0.968	0.996	0.610
T_6	0.938	2.13	0.976	0.087	0.993	0.997	0.991	0.552
T_7	0.937	2.07	0.982	0.072	0.994	0.993	0.984	0.532
T_8	0.935	2.97	0.992	0.083	0.998	0.973	0.999	0.560
T_9	0.934	3.05	0.999	0.099	0.998	0.990	0.995	0.573

Maswadeh et al. (195) and Sagar et al. (70) reported results not unlike those reported by Sunil. Maswadeh reported on a formulation of ciprofloxacin microspheres whose release rates achieved good fits to the first-order release mode, the zero-order release model, Higuchi model, Hixson-Crowell, and the Korsmeyer-Peppas model. The *n*-values reported by Maswadeh were indicative of Fickian diffusion. Sagar, on the other hand, reported achieving good fits to the zero-order model, the Higuchi model, and the Korsmeyer – Peppas model when modelling the release rates of voriconazole-loaded Soluplus formulations. Sagar notably did not report the values acquired from the Peppas coefficient, and presented the Korsmeyer – Peppas model fit as a function of log(cumulative drug release %) vs. log(time), so there may be merit to approaching those reported results with some scepticism, despite the findings aligning with what is commonly reported in the literature.

Khaled et al. similarly used the Korsmeyer – Peppas power law to fit the release profiles of 3D printed formulations of HPMC-loaded guaifenesin (24). Khaled et al., similarly reported achieving good fits (R^2 = 0.99) with the Korsmeyer – Peppas model. Despite reporting observing swelling during the formulation, the *n*-value reported by Khaled was 0.44, which their work attributed to Fickian diffusion, as per the Peppas coefficient values outlined in Table 5-2. Khaled et al. also reported achieving similarly good fits to the first-order release model.

For the formulations presented herein, the release mechanism for release profiles acquired in pH 1.2 presumed to be non-Fickian diffusion; diffusion since the tablets remained perfectly intact during the experiment, and is presumed to be non-Fickain due to the swelling-release correlation discussed prior; Fickian diffusion is diffusion that occurs when the rate of polymer relaxation is much larger than the rate of solvent diffusion time. While non-Fickian diffusion occurs when polymer relaxation time happens at a similar rate to solvent diffusion time (208). According to the Peppas coefficient, the dominant release mechanism of the 50% infill and 75% infill tablets in pH 1.2 is anomalous transport. The 100% infill formulation had an *n*-value of 0.404 ± 0.024. Cases in which n < 0.45 were not accounted for in the works of Ritger and Peppas (190) and subsequent expansions (191,209). One may take this *n*-value to mean Fickian diffusion due to its proximity to 0.45. However, the same data set achieved good fits with the first-order model (Figure 5-16). Furthermore, the 100% infill tablets arise from the formulation as the 50% infill and 75% infill tablets, therefore, a change in the release mechanism is not expected. This leads to the conclusion that the observed value of 0.404 ± 0.024 is serving to highlight an issue with the Korsmeyer – Peppas model. It is probable that the true Peppas coefficient of this sample set is > 0.45, which was not observed due to the fitting being conducted on the mean release rate of three 100% infill replicates, without accounting for the standard deviations between the three replicates.

In the pH 6.8 drug release experiments, the tablets were visually seen to erode to completion when drug release was conducted at that pH. Polymer erosion is documented to be a time-dependent, first-order process (210). Fitting to the first-order release model achieved good fits, indicating that the drug release from the tablets at pH 6.8 follows first-order kinetics. Fitting to the Peppas coefficient similarly achieved good fits, and yielded values of n in the range of $0.45 < n < 0.89$, which, in the case of cylindrical geometries (190,192), are commonly associated with anomalous transport. However, as previously discussed, the first-order model has the advantage of allowing one to use the entirety of the release curve, while the Korsmeyer – Peppas equation omits the latter 40% of the release curve. Furthermore, little is known about what physical mechanism the term "anomalous transport" represents, and in the results reported herein, the term can be used to describe two physically different drug release mechanism (the diffusion-based release observed at pH 1.2, and the erosion-based release observed at pH 6.8).

For the buffer change release studies, the first 120 minutes (conducted at pH 1.2) were unremarkable, showing little difference from their counterparts acquired at that pH over 8 hours. The region of the curve acquired at pH 6.8 was remarkably different from its counterparts acquired solely in buffer media. The curve did not appear to follow a first-order release model. Therefore, it is possible that the swelling of the polymer matrix over the earlier 2 hours influenced the release mechanism. Looking closely at Figure 5-9, if one were to account for the error bars, it is entirely possible to fit a straight line through the buffer portion of the curve. Considering the underlying physical phenomena; that portion of the curve describes drug release from polymeric materials whose polymer chains were allowed to expand by the action of the solvent uptake and swelling in the earlier region of the curve. This spreading of the polymer chains grants greater solvent access through the polymer chains than what would have been achieved otherwise if the tablets were not allowed to swell prior (i.e. the case of drug release profiles acquired at pH 6.8 exclusively). This increase in the solvent access through the polymer will result in a change in the drug release mechanism, and although polymer erosion was observed, it is likely happening independently of the drug release in this particular case. However, due to the few available sampling points, the release mechanism for this curve only be described with certainty as ambiguous.

5.5. Conclusion

This study investigated the effect of varying the infill density on the drug release rates and kinetics of 3D printed oral solid dosage forms. For tablets printed at 50% and 75% infill, enhancement in dissolution rate proportional to the infill density was seen when drug release was conducted in the paddle apparatus, but was not seen when the experiment was reproduced using the basket apparatus. This was attributed to be due to the differences in fluid dynamics between the low-shear basket apparatus, and the comparatively high-shear paddle apparatus. This observation suggests that for such open systems, one needs to carefully consider the in-vivo environment in which they are expected to perform. For oral dosage forms, the hydrodynamic environment inside the gastrointestinal tract is not realistically mirrored by the "tablets rotating in a bowl" paradigm imposed by the pharmacopoeial dissolution bath (197). Therefore, it is easy to see situations in which the in-vivo performance of a 3D printed dosage form may be overestimated due to the difference in hydrodynamics between the in-vivo environment, and the in-vitro environment used as a reference during dissolution development.

Swelling of the polymer was observed to have an effect on drug release rate; the rate of drug release was found to be proportional to the rate of swelling, up to the point at which the tablets reached the maximum possible swelling, at which point drug release stagnated, likely due to the tablets reaching steady-state diffusion. It is worth noting that the "maximum possible swelling" observed was different for each infill variant, despite all infill variants coming from the same formulation. This was attributed to the fact that the lower the infill of a tablet, the more room is available for the roads to swell. Tablets with a higher infill density had less room to accommodate road swelling and thus reached their maximum possible swelling faster than the lower infill counterparts.

The results outlined prior indicate the importance of careful considerations of the geometry of the 3D printed tablet. Different geometries of the same formulation do not perform equivalently. The a priori equation of infill density to the surface area, while true, does not account for the observed effects of hydrodynamic flow, and polymer swelling. 3D printed dosage forms require not only careful formulation design, but also careful geometric design, one which accounts for properties of the polymer, and the environment in which the tablet is expected to perform.

Chapter 6
Conclusion and Future Work

6.1. Conclusions

The presented work was an exploration of the critical process parameters of FDM, investigated from a pharmaceutical perspective to determine the feasibility of FDM as a method to fabricate pharmaceutical solid dosage forms. As was discussed in Chapter 1, 3D printing process parameters can be generally grouped as being either machine parameters, process parameters, or material parameters. Said parameters were observed to have complex interactions that affect the final properties of the 3D printed dosage form.

6.1.1. Impact of material properties on the properties of 3D printed objects:

The primary limiting parameter to be overcome was observed to be the mechanical properties of the material comprising the filament (Chapter 3). Regardless of how suitable the thermal properties of a polymer are for 3D printing, FDM printers dictate that any material used must fall within a very narrow margin of suitable mechanical properties. If said properties are not met, the filament will block the feeding motors and stop the printing process, without the material ever even arriving at the melting zone to begin the polymer deposition process.

The effect of polymer melt flow was investigated and was found to have only a secondary effect on the properties of the 3D printed object. As discussed in Chapter 4, properties of 3D printed objects were not found to vary as significantly on changing printing temperature (and by extension, the random melt flow of the polymer), than on changes with printing speed. Polymer melt flow was, however, observed to strongly correlate with a printing distortion phenomenon we have dubbed the First Layer Effect (FLE). This effect was found to have an influence on the thickness of 3D printed objects.

As shown with the design geometries presented in Chapter 5, 3DP allows for the creation of porous solid dosage forms by varying a process parameter known as infill density. This porous design allows for an increase in surface area that can modulate drug release. However, as was observed with the formulation present, polymer swelling during dissolution may negate the effect of pore inclusion in the design, hindering the drug release rate. Under acidic conditions, the formulation reported in Chapter 5 had a diffusion-based drug release mechanism that is rate-limited by the polymer swelling rate. The reported study investigated the same formulations at three similar geometries (three infill variants). The three formulations ranged from no space between the printed roads (at 100% infill) to > 900 μm of space between every two parallel roads. The observed

trend in drug release was that the lesser the distance between the roads of the 3D printed tablet, the faster it reaches steady-state diffusion, which was attributed to the polymer having greater room available for swelling in the more open tablets, leading to the conclusion that polymer swelling can influence drug release rate from 3D printed tablets, subject to the geometry of the object.

Section 6.2.1. discusses possible methods for overcoming material limitations which were observed in this work. However, if one were to apply the use of FDM in its current form, material (both polymer and API) properties must be carefully selected to meet the requirements of the current iteration of FDM. The primary limitation to be addressed is the issue of the mechanical flexibility of the polymer; careful tuning of the mechanical properties of the filament via plasticisers must be conducted to ensure the filament would not fracture or coil during printing. Another important factor to consider is the thermal stability of the API. As was observed in Chapter 5, there is a strong possibility that paracetamol may have underwent thermal oxidation during processing, causing the brownish discolouration observed in the filament. Formulation of filaments for FDM dictates that the drug/polymer blend is thermally processed twice (once during HME, and a second during printing) to produce the final dosage form. Drugs and polymers which are thermolabile make poor candidates for FDM, and any drugs to be formulated for FDM must be thoroughly investigated for thermal stability (via TGA, both via heat cycling amd being held isothermal at the processing temperature) to ensure that the drug remains stable during processing. The third factor to consider when formulating filaments for FDM is the melt rheology of the polymer. Melt flow, however, as discussed previously and in Chapter 4, is a secondary factor, and does not impact printing as significantly as other process parameters.

6.1.2. Impact of machine parameters on the properties of 3D printed objects

For the make of the printer used herein, machine parameters such as nozzle diameter, filament diameter, and motor step size are hardware pre-sets and could not be varied without significant modifications of the printer.

Platform levelling, while not a “true” machine parameter, it is a user-manipulated calibration process. As was discussed in Chapter 4, the subjectivity of the platform levelling process was found to cause significant deviations when the same operator attempts to replicate an experiment on different days.

6.1.3. Impact of process parameters on the properties of 3D printed objects

Chapter 4 was an in-depth exploring of the impact of processing parameters on the properties of the 3D printed dosage forms. A complex interaction relating printing speed, dimensions, mass, and object road width was discovered. A notable inverse correlation between printing temperature and object mass was observed, suggesting that for larger scale operations, there may be a compromise between dosing accuracy and throughput.

A design limitation of the 3D printer, relating to the nature of operation of the stepper motors utilised in the printer, dictated a "lower limit" on the suitable printing temperature. For higher printing speeds, printing at lower temperatures is not possible due to the inverse correlation between the rotation speed and the output torque of the utilised motors.

6.1.5. General conclusion

Perhaps the greatest shortcoming of the currently available versions of FDM lies in the feeding mechanism. As discussed in Chapter 3, the filament-based mechanism currently employed by 3D printers restricts the library of materials available for pharmaceutical use to only those which possess adequate mechanical properties. Formulating filaments that possess the suitable mechanical properties requires extensive use of plasticisers which raises the cost and complexity of the formulation, and raises stability concerns as excessive plasticisation of the formulation can decrease the kinetic stability of an amorphous solid dispersion (158). Furthermore, the use of stepper motors to drive the feeding rollers was also shown to cause an issue relating to dosing accuracy. Thermal processing of pharmaceutical materials carries a great risk of inducing thermal degradation and keeping the operating temperature the barest minimum is often desired when thermally processing pharmaceutical formulations. If this strategy were to be employed in P3P, it would restrict the printing to only the lowest speeds, yielding a compromise between thermal stability and throughput.

3DP carries with it great prospects for the pharmaceutical industry, the previously highlighted freedom it allows for may usher in the next generation of pharmacotherapy; patient-tailored medicaments with precisely engineered drug release characteristics. However, the aforementioned limitations in mechanical properties (and by extension, formulation choices), and the stability-throughput compromise leads one to conclude that

for serious pharmaceutical applications, 3DP can only be properly investigated with a printer that is fit for purpose.

6.2. Future Outlooks

6.2.1. Overcoming materials limitations:

As previously discussed, the current biggest limitation against pharmaceutical adaptation of FDM is the restriction of the feeding mechanism. The formulation of a filament suitable for FDM is a complex process. This complexity may be the reason why the soaking method for filament drug loading continues to see use despite its inadequate drug loading capacity (128,178,211). The restriction imposed by the feeding mechanism led to the conclusion that, as it stands, filament-based FDM is not fit for pharmaceutical applications. Attempts at re-engineering the feeding mechanism have been conducted, the most notable of which is the Arburg® Freeformer Droplet Extrusion 3D printer (212). This 3D printer is similar to FDM in that it is a polymer melt deposition process. However, it is notable for having a unique feeding mechanism that is adapted from injection moulding. The feedstock of the 3D printer utilises pellets, which are propelled through the melting zone by single screw melt extruder. The polymer melt is then deposited in the nozzle cavity and then injected droplet-wise on the build plate. (Figure 6-1)

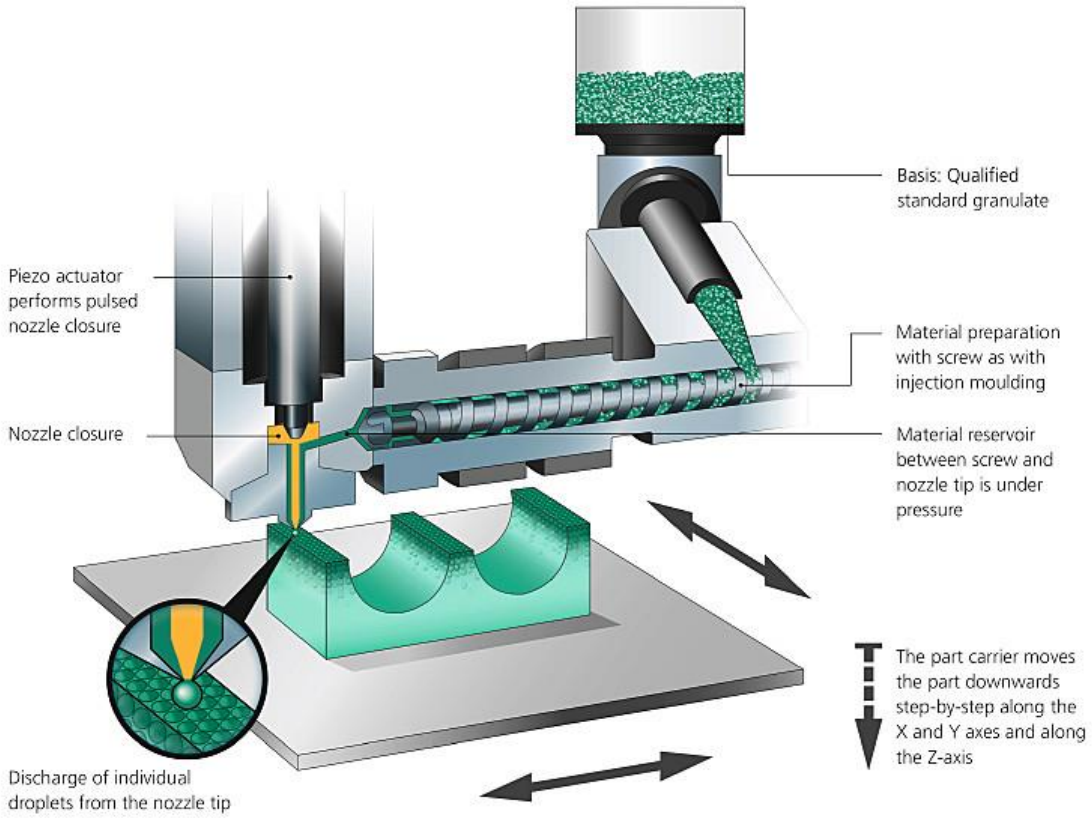

Figure 6-1: Anatomy of an Arburg Freeformer 3D printer. Figure retrieved from Arburg GmbH. (212)

To date, this printer has not been used in a pharmaceutical context. A comparative study similar to what was presented in Chapter 4, comparing a conventional FDM printer with the Arburg® Freeformer is perhaps a logical next step. It is clear from the filament-free design that this printer can accommodate a wider library of materials due to the absence of mechanical restrictions. But an investigation of its precision is needed before considering it for serious pharmaceutical applications.

6.2.2. Overcoming machine limitations:

As previously discussed, the Makerbot® Replicator 2 FDM 3D printer has been treated as a the de facto "standard" 3D printer for pharmaceutical use. It is obvious that the printer is not fit for purpose. The issue with build plate levelling discussed in Section 4.4.2. and more thoroughly investigated by Melocchi et al. (54) can potentially introduce significant variability in the printed dosage forms.

The need to manually level the build plate arises from the design of the Makerbot® Replicator 2 3D printer, namely the fact that during printer operation, the build plate does not remain stationary, but rather moves in the Z-axis to accommodate the subsequent layer once the former has been printed. This design of FDM printers is what is known as a Cartesian FDM Printer (213), named so for possessing three motors, each of which moves along one axis of the 3-dimensional Cartesian coordinate plane; two motors that move the print head in the X and Y axes, and a third that moves the build plate in the Z-axis.

An alternative design of FDM 3D printers called the delta design exists (213). Delta 3D printers opt for using a stationary build plate. Delta FDM printers still utilise three motors, but in this case all three motors are restricted to moving in the Y-axis exclusively (Figure 6-. The motors are all connected to the printer head, and offset between the location of the three motors at any given time is what moves the print head in 3D space.

All currently available Delta FDM 3D printers still utilise a filament feeding mechanism, but they possess the advantage of eliminating the need for levelling the build plate, greatly reducing variability that may arise in the 3D printed object due to the subjectivity of levelling the build plate.

Figure 6-2: a Delta FDM 3D printer. Image obtained from all3DP.com (213)

A second machine limitation that is critical to overcome is the inability to access the inside of the print head for cleaning. Appendix 1 reports an experiment in which calcium carbonate salt was incorporated into melt-extruded filaments of HPC. While the filament was successfully printed. Repeated use of the filament caused the building up of salt deposits inside the nozzle which led to the print head being completely blocked. All attempts to clean the nozzle through purging with other polymers or rinsing with solvents were unsuccessful, and the entire print head assembly had to be replaced entirely. This raises great concerns about the Good Manufacturing Practices (GMP) compliance of FDM. It is imperative that any equipment intended to be used for pharmaceutical manufacturing be easy to clean. Simply purging the printer nozzle with material prior to a print is not sufficient to demonstrate that the innards of the nozzle are thoroughly clean and do not contain any contaminants from a previous print. The only way to overcome this cleaning limitation is for a print head design in which the innards of the print head, including the nozzle, may be accessed for washing and scrubbing.

6.2.3. Generating a deeper understanding of FDM process parameters:

Process parameters, unlike machine and material parameters, are those which allow for the greatest degree of freedom. As such, it would be false to assume the existence of "process limitations". Rather, there is still a need for a deeper understanding of FDM process parameters, and how changing process parameters can influence the properties of 3D printed solid dosage forms.

Infill density, as an FDM process parameter, offers unprecedented control over the shape and morphology of oral solid dosage forms. Those 'open systems' which can be produced by printing at low infill density display a more complex drug release behaviour than what has been previously observed with traditional dosage forms.

The impact of the fluid dynamics on the release rate from 3D printed tablets observed in Chapter 5 is one of interest. As previously mentioned, the dissolution bath apparatus does not necessarily reflect physiological conditions. The novel capabilities offered by FDM (such as open tablets) make it yet even more challenging to extrapolate meaningful expectations of in-vivo performance based on what was seen in-vitro. A study comparing the in-vitro-in-vivo correlation (IVIVC) of an FDM printed dosage form vs. a traditionally manufactured dosage form is perhaps necessary to gain an understanding of the magnitude of this effect. The two standard apparatuses for investigating drug release rates in a dissolution bath are the paddle and basket apparatuses. Neither apparatus accurately mimics the hydrodynamic environment inside the stomach as the peristaltic movement has a different effect on fluid movement than a motor rotating a paddle or a basket. Open tablet geometries, such as those presented in Chapter 5, have exposed internal structures (roads), such open systems permit solvent flow through the tablet, rather than restricting it to the surface of the tablet as is the cases with traditional solid dosage forms. Obviously, the rate drug release will be significantly altered by the rate of solvent flow through the tablet, leading to significantly different drug release rates when the same formulation is investigated under different environments, as was observed in Chapter 5. The complex nature of drug release due to this solvent wash-through effect makes it exceedingly difficult to confidently extrapolate information about the in-vivo performance of open 3D printed tablets based on their in-vitro drug release. Drug release from open 3D printed dosage forms is a complex multivariate issue, that is influenced by several different variables like the BCS class of the drug, polymer swelling and/or erosion, the geometry of the 3D printed tablet, and the hydrodynamic environment in which dissolution is taking place. And although drug release kinetics model fitting may provide some useful metrics relating to drug release rate, more advanced modelling techniques (like computational fluid dynamics modelling) should be explored as means to attempt to predict the behaviour of those complex drug delivery systems.

6.2.4. Future prospects of pharmaceutical FDM 3D printing:

As it stands, the current greatest hurdle standing against real clinical applications of FDM as a pharmaceutical manufacturing tool is an engineering issue, rather than a pharmaceutical one. Many an example of proof-of-concept formulations has been reported and discussed throughout this work. However, until a fit for purpose FDM printer is available, we do not foresee FDM being used in a clinical setting, regardless of the abundance of literature demonstrating viable proof-of-concept formulations.

Sections 6.2.1. and 6.2.2. discussed currently available engineering solutions, each of which individually solves one of the issues bottlenecking actual commercial applications of FDM, namely the feeding issue, and the build plate levelling issue. A pharmaceutical FDM printer must incorporate design cues from both to be a fit-for-purpose printer. A third consideration for such a fit-for-purpose printer is ease of cleaning. It is beyond the scope of this writing (and beyond the capacity of the author) to design and propose a print head system whose innards can be accessed for cleaning. It is, however, paramount that any future research into pharmaceutical applications of FDM start by designing such a print head, which can be then incorporated into a Delta axes system, whose feeding mechanism is more friendly towards pharmaceutically-relevant materials.

With the availability of a printer that is functionally (and regulatory) suitable for the production of pharmaceutical solid dosage forms. Extensive work should be conducted into understanding how the complex geometries which can be produced by FDM affect the clinical performance of the produced dosage forms. As discussed in Chapter 5 and in Section 6.1.3., the complex geometries which can be produced by FDM mark an uncharted territory in pharmaceutical dosage forms. Extensive research into the dissolution and bioavailability of the geometrically complex 3D printed dosage forms will be necessary to understand how to best leverage the advantages of FDM and translate that into clinical benefits.

Referecnes

1. Williams HD, Trevaskis NL, Charman S a, Shanker RM, Charman WN, Pouton CW, et al. Strategies to address low drug solubility in discovery and development. Pharmacol Rev. 2013;65(1):315–499.
2. Liu H, Taylor LS, Edgar KJ. The role of polymers in oral bioavailability enhancement; A review. Polym (United Kingdom). 2015;77:399–415.
3. Wu CY, Benet LZ. Predicting drug disposition via application of BCS: Transport/absorption/ elimination interplay and development of a biopharmaceutics drug disposition classification system. Pharm Res. 2005;22(1):11–23.
4. Wening K, Breitkreutz J. Oral drug delivery in personalized medicine: Unmet needs and novel approaches. Int J Pharm. 2011;404(1–2):1–9.
5. Norman J, Madurawe RD, Moore CMV, Khan MA, Khairuzzaman A. A new chapter in pharmaceutical manufacturing: 3D-printed drug products. Adv Drug Deliv Rev. 2017;108:39–50.
6. Murray MD, Kroenke K. Polypharmacy and medication adherence: small steps on a long road. J Gen Intern Med. 2001 Feb;16(2):137–9.
7. Dwyer LL, Han B, Woodwell DA, Rechtsteiner EA. Polypharmacy in nursing home residents in the United States: Results of the 2004 National Nursing Home Survey. Am J Geriatr Pharmacother. 2010 Feb;8(1):63–72.
8. Maher RL, Hanlon J, Hajjar ER, Hajjar ER. Clinical consequences of polypharmacy in elderly. Expert Opin Drug Saf. 2014 Jan;13(1):57–65.
9. Hajjar ER, Cafiero AC, Hanlon JT. Polypharmacy in Elderly Patients. Am J Geriatr Pharmacother.
10. Brown D, Ford JL, Nunn AJ, Rowe PH. An assessment of dose-uniformity of samples delivered from paediatric oral droppers. J Clin Pharm Ther. 2004 Dec 1;29(6):521–9.
11. Bangalore S, Kamalakkannan G, Parkar S, Messerli FH. Fixed-Dose Combinations Improve Medication Compliance: A Meta-Analysis. Am J Med. 2007;120(8):713–9.
12. Goldberger JJ, Buxton AE. Personalized medicine vs guideline-based medicine. J Am Med Assoc. 2013;309(24):2559–60.
13. Alhnan MA, Okwuosa TC, Sadia M, Wan KW, Ahmed W, Arafat B. Emergence of 3D Printed Dosage Forms: Opportunities and Challenges. Pharm Res. 2016;33(8):1817–32.
14. Rocha CR, Torrado Perez AR, Roberson DA, Shemelya CM, MacDonald E,

Wicker RB. Novel ABS-based binary and ternary polymer blends for material extrusion 3D printing. J Mater Res. 2014;29(17):1859–66.

15. Sun Y, Soh S. Printing Tablets with Fully Customizable Release Profiles for Personalized Medicine. Adv Mater. 2015;27(47):7847–53.
16. Goyanes A, Buanz ABM, Basit AW, Gaisford S. Fused-filament 3D printing (3DP) for fabrication of tablets. Int J Pharm. 2014;476(1):88–92.
17. Ventola CL. Medical Applications for 3D Printing: Current and Projected Uses. P T. 2014 Oct;39(10):704–11.
18. Skowyra J, Pietrzak K, Alhnan MA. Fabrication of extended-release patient-tailored prednisolone tablets via fused deposition modelling (FDM) 3D printing. Eur J Pharm Sci. 2015;68:11–7.
19. Raijada D, Genina N, Fors D, Wisaeus E, Peltonen J, Rantanen J, et al. a Step Toward Development of Printable Dosage Forms for Poorly Soluble Drugs. J Pharm Sci. 2013;102(10):3694–704.
20. Markarian J. FDA and the Emerging Technology of 3D Printing.
21. Brooks M. FDA Clears First 3D-Printed Drug (Spritam [Levitracetam]) [Internet]. Medscape.com. 2015 [cited 2017 Apr 19]. Available from: http://www.medscape.com/viewarticle/848971
22. Bose S, Vahabzadeh S, Bandyopadhyay A. Bone tissue engineering using 3D printing. Mater Today. 2013 Dec 1;16(12):496–504.
23. Melchels FPW, Feijen J, Grijpma DW. A review on stereolithography and its applications in biomedical engineering. Biomaterials. 2010;31(24):6121–30.
24. Khaled SA, Burley JC, Alexander MR, Roberts CJ. Desktop 3D printing of controlled release pharmaceutical bilayer tablets. Int J Pharm. 2014;461:105–11.
25. Williams JM, Adewunmi A, Schek RM, Flanagan CL, Krebsbach PH, Feinberg SE, et al. Bone tissue engineering using polycaprolactone scaffolds fabricated via selective laser sintering. Biomaterials. 2005;26:4817–27.
26. Goyanes A, Buanz ABMM, Hatton GB, Gaisford S, Basit AW. 3D printing of modified-release aminosalicylate (4-ASA and 5-ASA) tablets. Eur J Pharm Biopharm. 2015;89:157–62.
27. Katstra W. E, Rowe C. W, Palazzolo R. D, Giritlioglu B, Teung P, Cima M. J, et al. Oral dosage forms fabricated by Three Dimensional Printing. J Control Release. 2000;66(1):11–7.
28. Yu D-G, Branford-White C, Yang Y-C, Zhu L-M, Welbeck EW, Yang X-L. A novel fast disintegrating tablet fabricated by three-dimensional printing. Drug Dev Ind

Pharm. 2009 Dec 20;35(12):1530–6.

29. Pryce-Lewis W, Cima M, Rowe C, Materna P. System and method for uniaxial compression of an article, such as a three dimensionally printed dosage form. US 8758658 B2, 2010.
30. Aprecia Pharmaceuticals. ZipDose® Technology [Internet]. [cited 2017 Apr 19]. Available from: https://www.aprecia.com/zipdose-platform/zipdose-technology.php
31. Markarian J. Using 3D Printing for Solid-Dosage Drugs. Pharm Technol. 2016;40(8):34–6.
32. Dalziel G, Nauka E, Zhang F, Kothari S, Xie M. Assessment of granulation technologies for an API with poor physical properties. Drug Dev Ind Pharm. 2012;9045(December 2011):1–11.
33. Robles-Martinez P, Xu X, Trenfield SJ, Awad A, Goyanes A, Telford R, et al. 3D printing of a multi-layered polypill containing six drugs using a novel stereolithographic method. Pharmaceutics. 2019;11(6).
34. Healy A V., Fuenmayor E, Doran P, Geever LM, Higginbotham CL, Lyons JG. Additive manufacturing of personalized pharmaceutical dosage forms via stereolithography. Pharmaceutics. 2019;11(12):13–5.
35. Khaled SA, Burley JC, Alexander MR, Yang J, Roberts CJ. 3D printing of five-in-one dose combination polypill with defined immediate and sustained release profiles. J Control Release. 2015;217:308–14.
36. Kyobula M, Adedeji A, Alexander MR, Saleh E, Wildman R, Ashcroft I, et al. 3D inkjet printing of tablets exploiting bespoke complex geometries for controlled and tuneable drug release. J Control Release. 2017 Sep 10;261:207–15.
37. Clark EA, Alexander MR, Irvine DJ, Roberts CJ, Wallace MJ, Yoo J, et al. Making Tablets for Delivery of Poorly Soluble Drugs Using Photoinitiated 3D Inkjet Printing. Int J Pharm. 2019;
38. Yu L. Amorphous pharmaceutical solids: Preparation, characterization and stabilization. Adv Drug Deliv Rev. 2001;48(1):27–42.
39. Makerbot LLC. User Manual | Replicator® 2X Dual Extrusion Experimental 3D Printer [Internet]. [cited 2017 Oct 4]. Available from: http://downloads.makerbot.com/replicator2x/MakerBot_Replicator_2X_User_Manual.pdf
40. Bakar NSA, Alkahari MR, Boejang H. Analysis on Fused Deposition Modelling Performance. J Zhejiang Univ Sci A. 2010;11(12):972–7.

41. Mohamed OA, Masood SH, Bhowmik JL. Optimization of fused deposition modeling process parameters: a review of current research and future prospects. Adv Manuf. 2015;3(1):42–53.
42. Jin YA, Li H, He Y, Fu JZ. Quantitative analysis of surface profile in fused deposition modelling. Addit Manuf. 2015;8(December):142–8.
43. Alhijjaj M, Belton P, Qi S. An investigation into the use of polymer blends to improve the printability of and regulate drug release from pharmaceutical solid dispersions prepared via fused deposition modeling (FDM) 3D printing. Eur J Pharm Biopharm. 2016;108:111–25.
44. Pietrzak K, Isreb A, Alhnan MA. A flexible-dose dispenser for immediate and extended release 3D printed tablets. Eur J Pharm Biopharm. 2015 Oct;96:380–7.
45. Charoo NA, Ali AA. Quality risk management in pharmaceutical development. Drug Dev Ind Pharm. 2013;39(7):947–60.
46. Teng Y, Qiu Z, Wen H. Systematical approach of formulation and process development using roller compaction. Eur J Pharm Biopharm. 2009;73(2):219–29.
47. Huang T, Wang S, He K. Quality control for fused deposition modeling based additive manufacturing: Current research and future trends. 2015 First Int Conf Reliab Syst Eng. 2015;56:1–6.
48. Lu L, Chen B, Sharf A, Zhao H, Wei Y, Fan Q, et al. Build-to-last: Strength to Weight 3D Printed Objects. ACM Trans Graph. 2014 Jul 27;33(4):1–10.
49. Gokstorp D. Prototyping a Custom 3D Printing Slicer Implementation of a Prototype Modular Infill, Tool Path and Gcode Generator in Houdini. Bournemouth University;
50. Peng A, Xiao X, Yue R. Process parameter optimization for fused deposition modeling using response surface methodology combined with fuzzy inference system. Int J Adv Manuf Technol. 2014;73(1–4):87–100.
51. Ziemian S, Okwara M, Ziemian CW. Tensile and fatigue behavior of layered acrylonitrile butadiene styrene. Rapid Prototyp J. 2015 Apr 20;21(3):270–8.
52. Weeren R van, Agarwala M, Jamalabad VR, Bandyophadyay A, Vaidyanathan R, Langrana N, et al. Quality of Parts Processed by Fused Deposition. In: Solid Freeform Fabrication. 1995. p. 314–21.
53. Bharath Vasudevarao B, Dharma Prakash Natarajan DP., Henderson MM, Vasudevarao B, Natarajan DP, Henderson MM. Sensitivitiy of RP Surface Finish to Process Parameter Variation. Solid Free Fabr Proc. 2000;251–8.
54. Melocchi A, Parietti F, Maroni A, Foppoli A, Gazzaniga A, Zema L. Hot-melt

extruded filaments based on pharmaceutical grade polymers for 3D printing by fused deposition modeling. Int J Pharm. 2016;509(1–2):255–63.

55. Goyanes A, Robles Martinez P, Buanz A, Basit AW, Gaisford S. Effect of geometry on drug release from 3D printed tablets. Int J Pharm. 2015 Oct;494(2):657–63.
56. Hsiao W-K, Lorber B, Reitsamer H, Khinast J. 3D printing of oral drugs: a new reality or hype? Expert Opin Drug Deliv. 2017;15:1–4.
57. Lim SH, Kathuria H, Tan JJY, Kang L. 3D printed drug delivery and testing systems — a passing fad or the future? Adv Drug Deliv Rev. 2018;
58. Qi S, Avalle P, Saklatvala R, Craig DQM. An investigation into the effects of thermal history on the crystallisation behaviour of amorphous paracetamol. 2007;
59. Jermain S V., Brough C, Williams RO. Amorphous solid dispersions and nanocrystal technologies for poorly water-soluble drug delivery – An update. Int J Pharm. 2018 Jan 15;535(1–2):379–92.
60. Jani R, Patel D. Hot melt extrusion: An industrially feasible approach for casting orodispersible film. Asian J Pharm Sci. 2015;10(4):292–305.
61. Maniruzzaman M. Co-extrusion as a Novel Approach in Continuous Manufacturing Compliance. :53–62.
62. Reguieg F, Ricci L, Bouyacoub N, Belbachir M, Bertoldo M. Thermal characterization by DSC and TGA analyses of PVA hydrogels with organic and sodium MMT. Polym Bull. 2020;77(2):929–48.
63. Alhijjaj M. Fabrication of Solid Dispersion Based Patches Using Hot Melt Injection Moulding and Fused Deposition Modelling 3D Printing. University of East Anglia; 2017.
64. Akande SO, Dalgarno K, Munguia J. Process control testing for fused filament fabrication. Rapid Prototyp J. 2017;23(2):246–56.
65. 3D Hubs. Local 3D printing services [Internet]. [cited 2018 Jun 27]. Available from: https://www.3dhubs.com/3d-printing
66. Huh KM, Kang HC, Lee YJ, Bae YH. pH-sensitive polymers for drug delivery. Macromol Res. 2012;20(3):224–33.
67. Mcilroy C, Olmsted PD. Deformation of an amorphous polymer during the fused-filament-fabrication method for additive manufacturing. Cit J Rheol. 2017;61:379.
68. Korte C, Quodbach J. Formulation development and process analysis of drug-loaded filaments manufactured via hot-melt extrusion for 3D-printing of medicines. Pharm Dev Technol. 2018 Feb 9;1–11.
69. Pawar J, Suryawanshi D, Moravkar K, Aware R, Shetty V, Maniruzzaman M, et al.

Study the influence of formulation process parameters on solubility and dissolution enhancement of efavirenz solid solutions prepared by hot-melt extrusion: a QbD methodology. Drug Deliv Transl Res. 2018;8(6):1644–57.

70. Kanase J, Burade B, Khandekar M, Sawant R, Repal R. Solubility and Dissolution Rate Enhancement of Antifungal Voriconazole By Hot Melt Extrusion and Development of Sustained Release Tablets. World J Pharm Res. 2014;3(4):1827–53.
71. Andrews GP, Abudiak OA, Jones DS. Physicochemical characterization of hot melt extruded bicalutamide- polyvinylpyrrolidone solid dispersions. J Pharm Sci. 2010;99(3):1322–35.
72. Djuris J, Nikolakakis I, Ibric S, Djuric Z, Kachrimanis K. Preparation of carbamazepine–Soluplus solid dispersions by hot-melt extrusion, and prediction of drug–polymer miscibility by thermodynamic model fittin. Eur J Pharm Biopharm. 2013;84(1):228–37.
73. Varshosaz J, Faghihian H, Rastgoo K. Preparation and characterization of metoprolol controlled-release solid dispersions. Drug Deliv. 2006;13(4):295–302.
74. Kolter K, Karl M, Gryczke A. Introduction to Solid Dispersions. Hot-Melt Extrusion with BASF Pharma Polymers. 2012. 9–18 p.
75. Siew A. Solving Poor Solubility with Amorphous Solid Dispersions. Pharm Technol. 2014;38(10).
76. Vehring R. Pharmaceutical particle engineering via spray drying. Pharm Res. 2008;25(5):999–1022.
77. Repka MA, Bandari S, Kallakunta VR, Vo AQ, McFall H, Pimparade MB, et al. Melt extrusion with poorly soluble drugs – An integrated review. Int J Pharm. 2018;535(1–2):68–85.
78. Marsac PJ, Shamblin SL, Taylor LS. Theoretical and practical approaches for prediction of drug-polymer miscibility and solubility. Pharm Res. 2006;23(10):2417–26.
79. Wu C, McGinity JW. Influence of methylparaben as a solid-state plasticizer on the physicochemical properties of Eudragit® RS PO hot-melt extrudates. Eur J Pharm Biopharm. 2003;56(1):95–100.
80. Savjani KT, Gajjar AK, Savjani JK. Drug solubility: importance and enhancement techniques. ISRN Pharm. 2012;2012(100 mL):195727.
81. Tian Y, Caron V, Jones DS, Healy A, Andrews GP. Using Flory – Huggins phase diagrams as a pre-formulation tool for the production of amorphous solid

dispersions : a comparison between hot-melt extrusion and spray drying. 2013;256–74.

82. Newman A. Making Amorphous API. In: Pharmaceutical Powder X-ray Diffraction Symposium. 2012.
83. Vippagunta SR, Brittain HG, Grant DJW. Crystalline solids. Adv Drug Deliv Rev. 2001;48(1):3–26.
84. Bashpa P, Bijudas K, Tom AM, Archana PK, Murshida KP, Banu KN, et al. Polymorphism of paracetamol : A comparative study on commercial paracetamol samples . Int J Chem Stud. 2014;1(6):25–9.
85. Grzesiak AL, Lang M, Kim K, Matzger AJ. Comparison of the Four Anhydrous Polymorphs of Carbamazepine and the Crystal Structure of Form I. J Pharm Sci. 2003;92(11):2260–71.
86. Hadžović E, Betz G, Hadžidedić Š, El-Arini SK, Leuenberger H, Hadzovic E, et al. Roller compaction of different pseudopolymorphic forms of Theophylline: Effect on compressibility and tablet properties. Int J Pharm. 2010;396(1–2):53–62.
87. Cahn RW. Melting from within. Vol. 413, Nature. Nature Publishing Group; 2001. p. 582–3.
88. Sri Syamala U. Calculation of MTDSC signals, factors effecting the signals and applications in drug development. 2018;
89. Kolesov BA, Mikhailenko MA, Boldyreva E V. Dynamics of the intermolecular hydrogen bonds in the polymorphs of paracetamol in relation to crystal packing and conformational transitions: A variable-temperature polarized Raman spectroscopy study. Phys Chem Chem Phys. 2011;13(31):14243–53.
90. Uzunović A, Vranić E, Hadžidedić Š. Impairment of the in vitro release of carbamazepine from tablets. Bosn J Basic Med Sci. 2010;10(3):234–8.
91. Friesen DT, Shanker R, Crew M, Smithey DT, Curatolo WJ, Nightingale JAS. Spray-Dried Dispersions : An Overview. 2008;5(6):1003–19.
92. Huang Y, Dai W-G. Fundamental aspects of solid dispersion technology for poorly soluble drugs. Acta Pharm Sin B. 2014;4(1):18–25.
93. Qi S, Gryczke A, Belton P, Craig DQM. Characterisation of solid dispersions of paracetamol and EUDRAGIT ® E prepared by hot-melt extrusion using thermal , microthermal and spectroscopic analysis. 2008;354:158–67.
94. Lloyd GR, Craig DQM, Smith A. An Investigation into the Melting Behavior of Binary Mixes and Solid Dispersions of Paracetamol and PEG 4000. 1997.
95. Djuris J, Nikolakakis I, Ibric S, Djuric Z, Kachrimanis K. Preparation of

carbamazepine-Soluplus® solid dispersions by hot-melt extrusion, and prediction of drug-polymer miscibility by thermodynamic model fitting. Eur J Pharm Biopharm. 2013;84(1):228–37.

96. Karandikar H. Suitability of Cellulose ester derivatives in Hot Melt Extrusion. University of Bradford; 2015.
97. Lehmkemper K, Kyerematen SO, Heinzerling O, Degenhardt M, Sadowski G. Impact of Polymer Type and Relative Humidity on the Long-Term Physical Stability of Amorphous Solid Dispersions. Mol Pharm. 2017;14(12):4374–86.
98. Sarode AL, Obara S, Tanno FK, Sandhu H, Iyer R, Shah N. Stability assessment of hypromellose acetate succinate (HPMCAS) NF for application in hot melt extrusion (HME). Carbohydr Polym. 2014;101(1):146–53.
99. Tian Y, Booth J, Meehan E, Jones DS, Li S, Andrews GP. Construction of drug-polymer thermodynamic phase diagrams using flory-huggins interaction theory: Identifying the relevance of temperature and drug weight fraction to phase separation within solid dispersions. Mol Pharm. 2013;10(1):236–48.
100. Knopp MM, Olesen NE, Huang Y, Holm R, Rades T. Statistical Analysis of a Method to Predict Drug-Polymer Miscibility. J Pharm Sci. 2016;105(1):362–7.
101. Abhay N. Padalkar 1*, Sadhana R. Shahi 1, Abhijit G. Kale 2, Mahesh Thube 1 VA. P 1. Formulation and Characterization of Novel Solid Dispersions of Hydrochlorothiazide by Solvent Evaporation Technique. Asian J Pharm Sci. 2012;1(2):1–8.
102. Mcphillips H, Craig DQM, Royall PG, Hill VL. Characterisation of the glass transition of HPMC using modulated temperature differential scanning calorimetry. Vol. 180, International Journal of Pharmaceutics. 1999.
103. Maniruzzaman M, Boateng JS, Snowden MJ, Douroumis D. A review of hot-melt extrusion: process technology to pharmaceutical products. ISRN Pharm. 2012;2012(2):436763–9.
104. International Union of Pure and Applied Chemistry. Gibbs energy (function), G. In: IUPAC Compendium of Chemical Terminology. Research Triagle Park, NC: IUPAC;
105. Sinko PJ. Martin's Physical Pharmacy and Pharmaceutical Sciences. Martin's Physical Pharmacy and Pharmaceutical Sciences. Lippincott Williams & Wilkins; 2011.
106. Hot Melt Extrusion. Particle Sciences. 2011;3.
107. Rate D, Of E, Voriconazole A, Hot BY, Extrusion M, Of D, et al. Antifungal

Voriconazole By Hot Melt Extrusion and. 2014;3(4):1827–53.
108. Hot melt extrusion for the production of controlled drug delivery systems. 2011;
109. Douroumis D. Hot Melt Extrusion processing: A rising star for dissolution enhancement of water insoluble drugs.
110. Ehtezazi T, Algellay M, Islam Y, Roberts M, Dempster NM, Sarker SD. The Application of 3D Printing in the Formulation of Multilayered Fast Dissolving Oral Films. J Pharm Sci. 2018 Apr 1;107(4):1076–85.
111. Zhao M, Barker SA, Belton PS, McGregor C, Craig DQM. Development of fully amorphous dispersions of a low Tg drug via co-spray drying with hydrophilic polymers. Eur J Pharm Biopharm. 2012;82(3):572–9.
112. Sarode AL, Sandhu H, Shah N, Malick W, Zia H. Hot melt extrusion (HME) for amorphous solid dispersions: Predictive tools for processing and impact of drug-polymer interactions on supersaturation. Eur J Pharm Sci. 2013;48(3):371–84.
113. Clas S-D, Dalton CR, Hancock BC. Differential scanning calorimetry: applications in drug development. Pharm Sci Technolo Today. 1999 Aug 1;2(8):311–20.
114. Abbott S. Solubility Science: Principles and Practice (Some additions on HSP). 2017.
115. Nugent P. Rotational Molding. Appl Plast Eng Handb. 2011 Jan 1;311–32.
116. Do Nald AM, Krame EJ. Plastic deformation mechanisms in poly(acrylonitrile-butadiene styrene) [ABS]. Vol. 17, JOURNAL OF MATERIALS SCIENCE. 1982.
117. McKeen LW, McKeen LW. Styrenic Plastics. Eff Creep Other Time Relat Factors Plast Elastomers. 2009 Jan 1;33–81.
118. Allen G (Geoffrey). Comprehensive polymer science and supplements. [Elsevier]; 1996.
119. Ultimate Materials Guide - Tips for 3D Printing with HIPS [Internet]. [cited 2019 Sep 30]. Available from: https://www.simplify3d.com/support/materials-guide/hips/
120. Okada T, Faudree MC, Tsuchikura N, Nishi Y. Improvement of low-temperature impact value of sandwich-structural (CFRP/ABS/CFRP) laminate plies by Homogeneous Low-Energy Electron Beam Irradiation (HLEBI). Mater Trans. 2016;57(3):305–11.
121. Polymer Science Learning Center. Polystyrene [Internet]. Polymer Science Learning Center; [cited 2019 Jan 30]. Available from: https://www.pslc.ws/macrog/styrene.htm
122. DeMerlis C., Schoneker D. Review of the oral toxicity of polyvinyl alcohol (PVA).

Food Chem Toxicol. 2003 Mar 1;41(3):319–26.

123. Rowe R, Sheskey P, Quinn M. Handbook of Pharmaceutical Excipients. Sixth. London: Pharmaceutical Press; 2009.

124. Pereira BC, Isreb A, Forbes RT, Dores F, Habashy R, Petit JB, et al. 'Temporary Plasticiser': A novel solution to fabricate 3D printed patient-centred cardiovascular 'Polypill' architectures. Eur J Pharm Biopharm. 2019 Feb;135:94–103.

125. Joo Y, Shin I, Ham G, Abuzar SM, Hyun S-M, Hwang S-J. The advent of a novel manufacturing technology in pharmaceutics: superiority of fused deposition modeling 3D printer. J Pharm Investig. 2019;

126. Melocchi A, Parietti F, Loreti G, Maroni A, Gazzaniga A, Zema L. 3D printing by fused deposition modeling (FDM) of a swellable/erodible capsular device for oral pulsatile release of drugs. J Drug Deliv Sci Technol. 2015 Dec;30:360–7.

127. Tidau M, Kwade A, Finke JH, Tidau M, Kwade A, Finke JH. Influence of High, Disperse API Load on Properties along the Fused-Layer Modeling Process Chain of Solid Dosage Forms. Pharmaceutics. 2019 Apr 22;11(4):194.

128. Ibrahim M, Barnes M, McMillin R, Cook DW, Smith S, Halquist M, et al. 3D Printing of Metformin HCl PVA Tablets by Fused Deposition Modeling: Drug Loading, Tablet Design, and Dissolution Studies. AAPS PharmSciTech. 2019 Jul 1;20(5).

129. Rahman S, Belton P, Qi S. The development of computer aided tools for the formulation design of FDM 3D printed polypills. In: 2nd International Conference on 3D Printing Technology and Innovations. London: International Journal of Advancements in Technology; 2018.

130. Saad B, Suter UW. Biodegradable Polymeric Materials. Encycl Mater Sci Technol. 2001 Jan 1;551–5.

131. Abdo HS, Elzatahry AA, Alharbi HF, Khalil KA. Electrical Conductivity Behavior of Biopolymer Composites. Biopolym Compos Electron. 2017 Jan 1;13–25.

132. PCL Low Temperature Filament - Natural - 1.75mm | Filaments.ca [Internet]. [cited 2019 Sep 30]. Available from: https://filaments.ca/products/pcl-low-temperature-filament-natural-1-75mm

133. Deshmukh K, Basheer Ahamed M, Deshmukh RR, Khadheer Pasha SK, Bhagat PR, Chidambaram K. Biopolymer Composites with High Dielectric Performance: Interface Engineering. In: Biopolymer Composites in Electronics. Elsevier Inc.; 2017. p. 27–128.

134. Kahovec J, Fox RB, Hatada K. Nomenclature of regular single-strand organic

polymers (IUPAC Recommendations 2002). Pure Appl Chem. 2002 Jan 1;74(10):1921–56.

135. Sigma Aldrich. Poly(ethylene glycol) and Poly(ethylene oxide) - Polymers | Sigma-Aldrich [Internet]. [cited 2019 Sep 30]. Available from: https://www.sigmaaldrich.com/materials-science/material-science-products.html?TablePage=20204110
136. Müller-Lissner S. Pharmacokinetic and pharmacodynamic considerations for the current chronic constipation treatments. Expert Opin Drug Metab Toxicol. 2013 Apr 21;9(4):391–401.
137. Prasad E, Islam MT, Goodwin DJ, Megarry AJ, Halbert GW, Florence AJ, et al. Development of a hot-melt extrusion (HME) process to produce drug loaded Affinisol^{TM} 15LV filaments for fused filament fabrication (FFF) 3D printing. Addit Manuf. 2019 Oct 1;29:100776.
138. Shin Etsu Co. AQoat product specifications sheet. Shin Etsu Co.;
139. Evonik Industries. Eudragit Product Specification Sheet.
140. Arafat B, Qinna N, Cieszynska M, Forbes RT, Alhnan MA. Tailored on demand anti-coagulant dosing: An in vitro and in vivo evaluation of 3D printed purpose-designed oral dosage forms. Eur J Pharm Biopharm. 2018 Jul;128(April):282–9.
141. BASF. Soluplus® Technical Information. 2010;(July):1–8.
142. Paradkar A, Kelly A, Coates P, York P. Shear and extensional rheology of hydroxypropyl cellulose melt using capillary rheometry. J Pharm Biomed Anal. 2009;49(2):304–10.
143. Ennis ZN, Dideriksen D, Vaegter HB, Handberg G, Pottegård A. Acetaminophen for Chronic Pain: A Systematic Review on Efficacy. Basic Clin Pharmacol Toxicol. 2016 Mar;118(3):184–9.
144. Boldyreva E V, Drebushchak VA, Paukov IE, Kovalevskaya YA, Drebushchak TN. DSC and adiabatic calorimetry study of the polymorphs of paracetamol. J Therm Anal Calorim. 2004;77(2):607–23.
145. Naumov DY, Vasilchenko MA, Howard JAK. The Monoclinic Form of Acetaminophen at 150K. Acta Crystallogr Sect C Cryst Struct Commun. 1998 May 15;54(5):653–5.
146. Ivanova BB. Monoclinic and orthorhombic polymorphs of paracetamol - Solid state linear dichroic infrared spectral analysis. J Mol Struct. 2005;738(1–3):233–8.
147. Ornelas A, Zacharias-Millward N, Menter DG, Davis JS, Lichtenberger L, Hawke D, et al. Beyond COX-1: the effects of aspirin on platelet biology and potential

mechanisms of chemoprevention. Cancer Metastasis Rev. 2017 Jun;36(2):289–303.
148. Flower R. What are all the things that aspirin does? BMJ. 2003 Sep 13;327(7415):572–3.
149. Varughese S, Kiran MSRN, Solanko KA, Bond AD, Ramamurty U, Desiraju GR. Interaction anisotropy and shear instability of aspirin polymorphs established by nanoindentation. Chem Sci. 2011 Oct 11;2(11):2236.
150. Brewer KJ. The Merck Index: An Encyclopedia of Chemicals, Drugs, and Biologicals, 14th ed. Edited by Maryadele J. O'Neil (Editor), Patricia E. Heckelman (Senior Associate Editor), Cherie B. Koch (Associate Editor), and Kristin J. Roman (Assistant Editor). Merck and Co., Inc.: Whitehouse Station, NJ. 2006. 2564 pp. $125.00. ISBN 0-911910-00-X. J Am Chem Soc. 2007 Jan 6;129(7):2197–2197.
151. Breitenbach J. Melt extrusion: from process to drug delivery technology. Eur J Pharm Biopharm. 2002;54(2):107–17.
152. Warimwe_probationary report.
153. Kousiatza C, Karalekas D. In-situ monitoring of strain and temperature distributions during fused deposition modeling process. Mater Des. 2016 May 5;97:400–6.
154. Craig DQM, Reading M, Reading M. Thermal Analysis of Pharmaceuticals. Craig DQM, Reading M, editors. CRC Press; 2006.
155. Otun SO, Meehan E, Qi S, Craig DQM. The use of quasi-isothermal modulated temperature differential scanning calorimetry for the characterization of slow crystallization processes in lipid-based solid self-emulsifying systems. Pharm Res. 2015;32(4):1316–24.
156. Katlafsky B, Keller RE. Attenuated Total Reflectance Infrared Analysis of Aqueous Solutions. Anal Chem. 1963 Oct;35(11):1665–70.
157. Fahrenfort J. Attenuated total reflection: A new principle for the production of useful infra-red reflection spectra of organic compounds. Spectrochim Acta. 1961 Jan 1;17(7):698–709.
158. Lee LC, Liong C-Y, Jemain AA. A contemporary review on Data Preprocessing (DP) practice strategy in ATR-FTIR spectrum. Chemom Intell Lab Syst. 2017 Apr;163:64–75.
159. Nidhi K, Indrajeet S, Khushboo M, Gauri K, Sen DJ. Hydrotropy: A promising tool for solubility enhancement: A review. Int J Drug Dev Res. 2011;3(2):26–33.
160. Al-akayleh F, Al-mishlab M, Shubair M, Alkhatib HS. Development and

evaluation of a novel , multifunctional , co- processed excipient via roller compaction of α-Lactose Monohydrate and Magnesium Silicate . 2013;4(June):27–37.

161. Bunaciu AA, Udriştioiu E gabriela, Aboul-Enein HY. X-Ray Diffraction: Instrumentation and Applications. Crit Rev Anal Chem. 2015 Oct 2;45(4):289–99.
162. Meyers HP. Introductory Solid State Physics. Taylor & Francis; 1990.
163. Lu J, Obara S, Ioannidis N, Suwardie J, Gogos C, Kikuchi S, et al. Understanding the Processing Window of Hypromellose Acetate Succinate for Hot-Melt Extrusion, Part I: Polymer Characterization and Hot-Melt Extrusion. Adv Polym Technol. 2016;00(0):1–13.
164. Varlashkin P. Approaches to Quantification of Amorphous Content in Crystalline Drug Substance by Powder X-ray Diffraction [Internet]. American Pharmaceutical Reviews. 2011 [cited 2020 Oct 2]. Available from: https://www.americanpharmaceuticalreview.com/Featured-Articles/36758-Approaches-to-Quantification-of-Amorphous-Content-in-Crystalline-Drug-Substance-by-Powder-X-ray-Diffraction/
165. Stable Micro Systems. Texture Analysis - A Beginner's Guide [Internet]. [cited 2019 Oct 4]. Available from: https://www.stablemicrosystems.com/BeginnersGuideToTextureAnalysis.html
166. Stable Micro Systems. Pasta and Rice Product Testing [Internet]. [cited 2017 Oct 14]. Available from: https://www.stablemicrosystems.com/PastaAndRiceTesting.html
167. Singh H, Rockall A, Martin CR, Chung OK, Lookhart GL. The analysis of stress relaxation data of some viscoelastic foods using a texture analyzer. J Texture Stud. 2006 Aug 1;37(4):383–92.
168. Grausgruber H, Hatzenbichler E, Ruckenbauer P. Analysis of repeated stickiness measures of wheat dough using a texture analyzer. J Texture Stud. 2003 Apr 1;34(1):69–82.
169. Mei X, Etzler FM, Wang Z. Use of texture analysis to study hydrophilic solvent effects on the mechanical properties of hard gelatin capsules. Int J Pharm. 2006 Nov 6;324(2):128–35.
170. Roggo Y, Chalus P, Maurer L, Lema-Martinez C, Edmond A, Jent N. A review of near infrared spectroscopy and chemometrics in pharmaceutical technologies. J Pharm Biomed Anal. 2007 Jul;44(3):683–700.
171. Abdi H, Williams LJ. Principal component analysis. Vol. 2, Wiley Interdisciplinary

Reviews: Computational Statistics. 2010. p. 433–59.
172. Ringnér M. What is principal component analysis? Nat Biotechnol. 2008;26(3).
173. Alhijjaj M, Nasereddin J, Belton P, Qi S. Impact of processing parameters on the quality of pharmaceutical solid dosage forms produced by fused deposition modeling (FDM). Pharmaceutics. 2019 Nov 27;11(12):633.
174. Dong L, Sun X, Chao Z, Zhang S, Zheng J, Gurung R, et al. Evaluation of FTIR spectroscopy as diagnostic tool for colorectal cancer using spectral analysis. 2014 Mar 25;122:288–94.
175. Stokes M. 3D printing for architects with MakerBot : build state-of-the-art architecture design projects with MakerBot replicator 1, 2, or 2X. Packt Pub; 2013.
176. Zhang J, Feng X, Patil H, Tiwari R V., Repka MA. Coupling 3D printing with hot-melt extrusion to produce controlled-release tablets. Int J Pharm. 2017;519(1–2):186–97.
177. Ponsar H, Wiedey R, Quodbach J. Hot-Melt Extrusion Process Fluctuations and Their Impact on Critical Quality Attributes of Filaments and 3D-Printed Dosage Forms. Pharmaceutics. 2020 Jun 3;12(6):511.
178. Wei C, Solanki NG, Vasoya JM, Shah A V., Serajuddin ATM. Development of 3D Printed Tablets by Fused Deposition Modeling Using Polyvinyl Alcohol as Polymeric Matrix for Rapid Drug Release. J Pharm Sci. 2020;109(4):1558–72.
179. Homaee Borujeni S, Mirdamadian SZ, Varshosaz J, Taheri A. Three-dimensional (3D) printed tablets using ethyl cellulose and hydroxypropyl cellulose to achieve zero order sustained release profile. Cellulose. 2020;27(3):1573–89.
180. Nasereddin JM, Wellner N, Alhijjaj M, Belton P, Qi S. Development of a Simple Mechanical Screening Method for Predicting the Feedability of a Pharmaceutical FDM 3D Printing Filament. Pharm Res. 2018 Aug 31;35(8):151.
181. Gültekin HE, Tort S, Acartürk F. An Effective Technology for the Development of Immediate Release Solid Dosage Forms Containing Low-Dose Drug: Fused Deposition Modeling 3D Printing. Pharm Res. 2019 Sep 1;36(9).
182. Iyer RM, Hegde S, DiNunzio J, Singhal D, Malick W. The impact of roller compaction and tablet compression on physicomechanical properties of pharmaceutical excipients. Pharm Dev Technol. 2014;19(Mcc):583–92.
183. Dawson PC. Flow Properties of Molten Polymers. In Springer, Dordrecht; 1999. p. 88–95.
184. International Organization for Standardization. ISO 1133-1:2011 - Plastics -- Determination of the melt mass-flow rate (MFR) and melt volume-flow rate

(MVR) of thermoplastics -- Part 1: Standard method [Internet]. 2011 [cited 2018 Jul 21]. Available from: https://www.iso.org/standard/44273.html

185. Sadia M, Isreb A, Abbadi I, Isreb M, Aziz D, Selo A, et al. From 'fixed dose combinations' to 'a dynamic dose combiner': 3D printed bi-layer antihypertensive tablets. Eur J Pharm Sci. 2018 Oct;123:484–94.
186. Lipták BG. Instrument engineers' handbook. Vol. 1, Process measurement and analysis. CRC Press; 2003.
187. Moons Electric Co. Ltd. MS17HD4P6038 - NEMA 17 Standard Hybrid Stepper Motors [Internet]. [cited 2018 Jun 28]. Available from: https://www.moonsindustries.com/p/nema-17-standard-hybrid-stepper-motors/ms17hd4p6038-000004611110008909
188. Lamichhane S, Park JB, Sohn DH, Lee S. Customized novel design of 3D printed pregabalin tablets for intra-gastric floating and controlled release using fused deposition modeling. Pharmaceutics. 2019 Oct 30;11(11):564.
189. The United States Pharmacopeial Convention. Notice of Adoption of Harmonized Standard | Dissolution [Internet]. Rockville, MD.; 2011 [cited 2020 Feb 25]. Available from: https://www.usp.org/harmonization-standards/pdg/general-methods/dissolution
190. Ritger PL, Peppas NA. A simple equation for description of solute release I. Fickian and non-fickian release from non-swellable devices in the form of slabs, spheres, cylinders or discs. J Control Release. 1987 Jun 1;5(1):23–36.
191. Bruschi ML, editor. Mathematical models of drug release. In: Strategies to Modify the Drug Release from Pharmaceutical Systems. Elsevier; 2015. p. 63–86.
192. Korsmeyer RW, Gurny R, Doelker E, Buri P, Peppas NA. Mechanisms of solute release from porous hydrophilic polymers. Int J Pharm. 1983;15(1):25–35.
193. Quinten T, Beer T De, Vervaet C, Remon JP. Evaluation of injection moulding as a pharmaceutical technology to produce matrix tablets. Eur J Pharm Biopharm. 2009;71(1):145–54.
194. Sunil SA, Srikanth MV, Rao NS, Raju V, Murthy KVR. Investigation on in vitro dissolution rate enhancement of indomethacin by using a novel carrier sucrose fatty acid ester. DARU, J Pharm Sci. 2012 Dec 19;20(1):4.
195. Maswadeh HM, Elsharif F, Saleh KI, Zayed G, Amin MA. Ciprofloxacin hydrochloride microspheres: Preparation, characterization and evaluation of dissolution kinetics and antibacterial activity. J Bionanoscience. 2015;9(3):231–8.
196. Tabassum S. Kinetics and mechanism of oxidation of organic compounds.

University. Aligarh; 2008.

197. Hribar M, Trontelj J, Klančar U, Markun B, Čeligoj Dujc T, Legen I. A Novel Intestine Model Apparatus for Drug Dissolution Capable of Simulating the Peristaltic Action. AAPS PharmSciTech. 2017 Jul 1;18(5):1646–56.
198. Miller RW. Roller compaction technology. In: Handbook of Pharmaceutical Granulation. New Brunswick, New Jersey; 1997. p. 159–90.
199. Mackley MR. Polymer Processing: the physics of stretching chains Recent developments In the physical understanding and the achievement of high chain extension in polymeric material could lead to significant advances In existing and new areas of polymer processing technology. Vol. 9, Phys. Technol. 1978.
200. McIlroy C, Olmsted PD. Disentanglement effects on welding behaviour of polymer melts during the fused-filament-fabrication method for additive manufacturing. Polymer (Guildf). 2017;123:376–91.
201. Ferreira RTL, Quelho de Macedo R. Residual thermal stress in fused deposition modelling. In Associacao Brasileira de Engenharia e Ciencias Mecanicas - ABCM; 2018.
202. Sun Q, Rizvi GMM, Bellehumeur CTT, Gu P. Effect of processing conditions on the bonding quality of FDM polymer filaments. Rapid Prototyp J. 2008 Mar 28;14(2):72–80.
203. Peterson AM. Review of acrylonitrile butadiene styrene in fused filament fabrication: A plastics engineering-focused perspective. Addit Manuf. 2019 May;27:363–71.
204. Cole DP, Riddick JC, Iftekhar Jaim HM, Strawhecker KE, Zander NE. Interfacial mechanical behavior of 3D printed ABS. J Appl Polym Sci. 2016;133(30):1–12.
205. Weber MF, Stover CA, Gilbert LR, Nevitt TJ, Ouderkirk AJ. Giant Birefringent Optics in Multilayer Polymer Mirrors Downloaded from.
206. Tagaya A. Birefringence of Polymer.
207. Benedetti C, Abatzoglou N, Simard J-S, McDermott L, Léonard G, Cartilier L. Cohesive, multicomponent, dense powder flow characterization by NIR. Int J Pharm. 2007 May 24;336(2):292–301.
208. Fu Y, Kao WJ. Drug release kinetics and transport mechanisms of non-degradable and degradable polymeric delivery systems. Vol. 7, Expert Opinion on Drug Delivery. 2010. p. 429–44.
209. Mircioiu C, Voicu V, Anuta V, Tudose A, Celia C, Paolino D, et al. Mathematical modeling of release kinetics from supramolecular drug delivery systems.

Pharmaceutics. 2019;11(3).

210. Göpferich A. Mechanisms of polymer degradation and erosion. Biomaterials. 1996;17(2):103–14.

211. Cerda JR, Arifi T, Ayyoubi S, Knief P, Paloma Ballesteros M, Keeble W, et al. Personalised 3d printed medicines: Optimising material properties for successful passive diffusion loading of filaments for fused deposition modelling of solid dosage forms. Pharmaceutics. 2020;12(4).

212. Arburg GmbH. Freeformer System [Internet]. 2014 [cited 2020 Feb 28]. Available from: https://www.arburg.com/en/gb/products-and-services/additive-manufacturing/freeformer-system/

213. Yusuf B. 3D Printers Explained: Delta, Cartesian, Polar, Scara | All3DP [Internet]. 2015 [cited 2020 Jul 24]. Available from: https://all3dp.com/know-your-fdm-3d-printers-cartesian-delta-polar-and-scara/

214. Wang Y, Xu PP, Li XX, Nie K, Tuo MF, Kong B, et al. Monitoring the hydrolyzation of aspirin during the dissolution testing for aspirin delayed-release tablets with a fiber-optic dissolution system. J Pharm Anal. 2012;2(5):386–9.

Appendix 1: Incorporation of insoluble salts in the filament and its impact on printability

A1.1. Introduction

The rising interest in P3P is mainly due to the prospects it offers in addressing the dosing personalisation challenge currently faced by the pharmaceutical industry (4). However, the two largest patient demographics who require robust dosing personalisation are incidentally the two demographics often regarded as being the least capable of handling oral solid dosage forms: paediatric patients and geriatric patients.

The purpose of this experiment was to develop a 3D printable formulation that can rapidly disintegrate either ex-vivo (by reconstitution prior to administration), or in the mouth. The rationale behind this design is to target patient groups who may have difficulty swallowing solid dosage forms, paediatric and geriatric patients. To this end, sodium bicarbonate ($NaHCO_3$) was chosen as a disintegration enhancing material. The hypothesised mechanism in which $NaHCO_3$ would induce the disintegration of a 3D printed dosage form is by compromising the structural integrity of the roads comprising the printed object, causing the collapse of the 3D structure upon hydration. Hydroxypropyl cellulose (HPC) was chosen as the main matrix-forming polymer because the polymer has been reported to yield mechanically suitable filaments without the need for further plasticisation (54).

A1.2. Materials and methods

A1.2.1.Materials:

HPC was used as the main matrix former. $NaHCO_3$ was used as the disintegration enhancer.

A1.2.1.Methods:

A1.2.1.1. Preparation of filament:

The HPC-$NaHCO_3$ filament was prepared by HME using an extrusion temperature of 130 °C. The formulation was prepared at two ratios: 95%:5% (HPC:$NaHCO_3$).

Prior to extrusion, the $NaHCO_3$ was milled using a ball mill at 30 oscillations per second for 5 minutes, to ensure that the particle size was smaller than the 400 μm printer nozzle.

A1.2.1.2. 3D printing

3D printing was attempted at 130 °C, 135 °C, and was successful at 140 °C. The STL file used for printing this formulation was the 10 mm diameter x 2 mm thickness cylinder described in section 5.2.3. Layer thickness was set to 0.2 mm.

A1.2.1.3. Scanning Electron Microscopy

SEM, coupled with elemental analysis, was conducted to determine the homogeneity of distribution of $NaHCO_3$ particles in the filament.

A1.2.1.4. Laser Diffraction

Laser diffraction was conducted to determine the particle size of $NaHCO_3$ both as purchased and post-milling.

A1.2.1.5. Texture Analysis

Texture analysis of both pure HPC filament, and the HPC + $NaHCO_3$ filament were conducted as per the method outlined in Chapter 3. The flexibility profiles of ABS, Mowiflex, and formulation HP10 were used as positive controls. The flexibility profiles of Soluplus, Eudragit EPO, and Copovidone were used as negative controls.

A1.3. Results and discussion

A1.3.1. Filament feedability testing:

Figure A-1 shows the Loadings Plot of the filament feedability testing. Both the pure HPC filament and the filament loaded with 5% $NaHCO_3$ clustered with the Mowiflex filament, indicating that both filaments possess suitable mechanical properties to be deemed feedable.

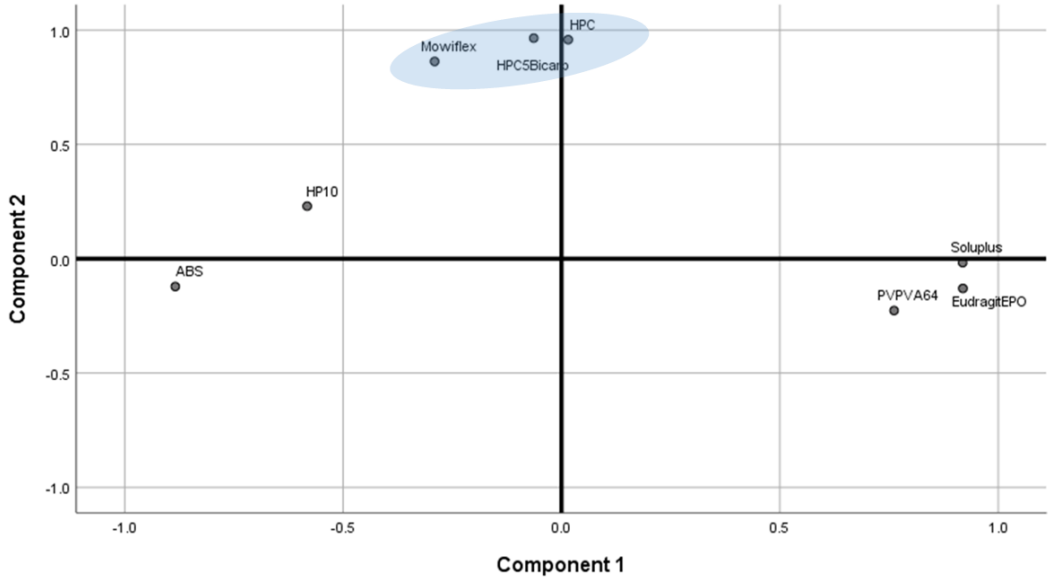

Figure A1-1: PCA loadings plot showing the feedability of the HPC-based filament. HPC5Bicarb: filament loaded with 5% $NaHCO_3$.

Table A1-1 shows the rounded correlation scores for the HPC-based filaments with all the control filaments. Similar to the results extracted from the loadings plot. The flexibility profiles of both HPC-based filaments were found to correlate with those of feedable filaments (ABS, Mowiflex, and HP10), and not correlate with the non-feedable, brittle filaments.

Table A1-1: Rounded correlation scores of the tested filaments

Tested filament	***ABS***	***Eudragit EPO***	***Mowiflex***	***Soluplus***	***Copovidone***	***HP10***
HPC + $NaHCO_3$	1	0	1	0	0	1
HPC	1	0	1	0	0	1

A1.3.2. Particle size analysis of the sodium bicarbonate:

Figure A1-2 shows the laser diffraction pattern of the $NaHCO_3$ as purchased. The smallest 10% of particles possessed a particle size $\leqslant$ 21.58 µm, the median particle size was $\leqslant$ 80.63 µm. At the 90th quartile was $\leqslant$ 810.79 µm. Notably, the diffractometer issued a warning that the presence of coarse particles exceeding the quantification limit of the diffractometer was detected. Suggesting that the true average particle size distribution of the $NaHCO_3$ powder is much larger than what was possible to quantify.

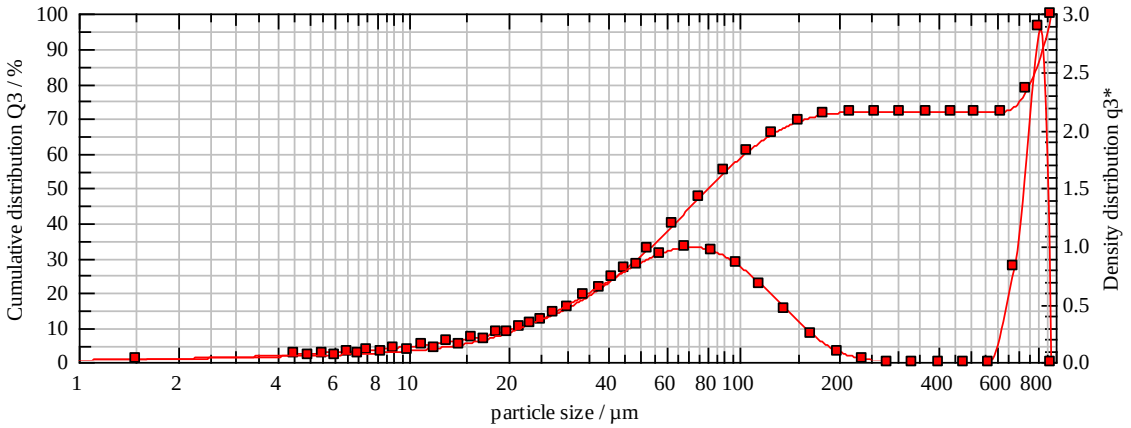

Figure A1-2: particle size distribution of unprocessed $NaHCO_3$ powder.

The presence of coarse particles exceeding the nozzle diameter of the printer is not desired as it will lead to blockages of the printer nozzle. Furthermore, $NaHCO_3$ is to be suspended as is in the matrix of the HPC, therefore, a finer particle size distribution is desired to allow for homogeneous dispersion of the salt particles within the matrix. Therefore, the $NaHCO_3$ powder was milled using a ball mill at a frequency of 30 oscillations per second, for 5 minutes. Figure A1-3 below shows the particle size distribution of the milled powder.

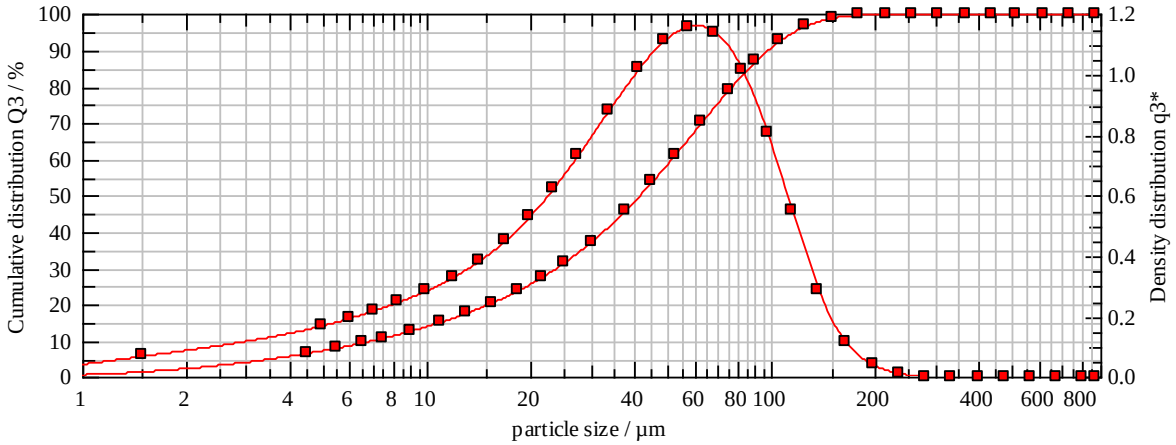

Figure A10-3: particle size distribution of milled $NaHCO_3$ powder.

As can be seen in Figure A1-3, the 10th quartile of particle size distribution was ⩽ 7.01 µm. The median particle size was ⩽ 41.48 µm, and the 90th quartile was ⩽ 98.43 µm. With 100% of the particles possessing a particle size smaller than 200 µm. This was deemed appropriate for the purpose of this experiment, as 100% of the particles were smaller than the nozzle diameter (400 µm).

A1.3.3.Scanning Electron Microscopy:

Figure A1-4 shows the SEM images of the pure HPC polymer. Both the surface and the cross-section of the pure HPC filament. The morphology of the filament was largely unremarkable, with the exception of some visible cracking in the cross-section of the polymer, which is assumed to be a scar caused by the razor blade used to expose the cross-section.

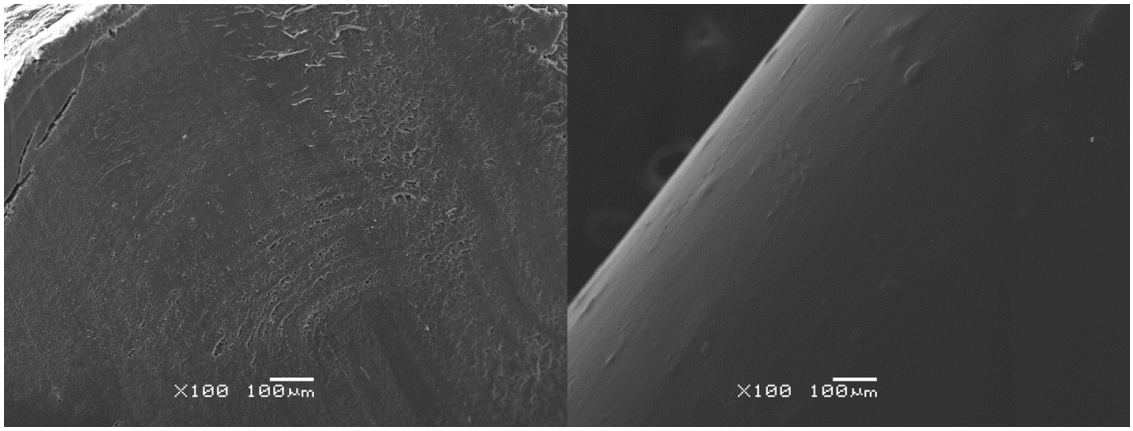

Figure A1-4: Surface (right) and cross-section (left) SEM images of pure HPC filament.

Figure A1-5 shows the surface and cross-section SEM images of the $NaHCO_3$-loaded HPC filament. There is a notable increase in surface roughness compared to the pure HPC filament shown in Figure A1-4. Deposits of what appears to be a crystalline material are also visible on the surface of the polymer and in the cross-section. Furthermore, cavities that are clearly different from the razor scarring mentioned prior are clearly visible in the cross-section of the polymer. Those cavities were likely formed during HME due to expelled moisture from the polymer reacting with a fraction of the $NaHCO_3$, expelling CO_2 gas and forming air pockets.

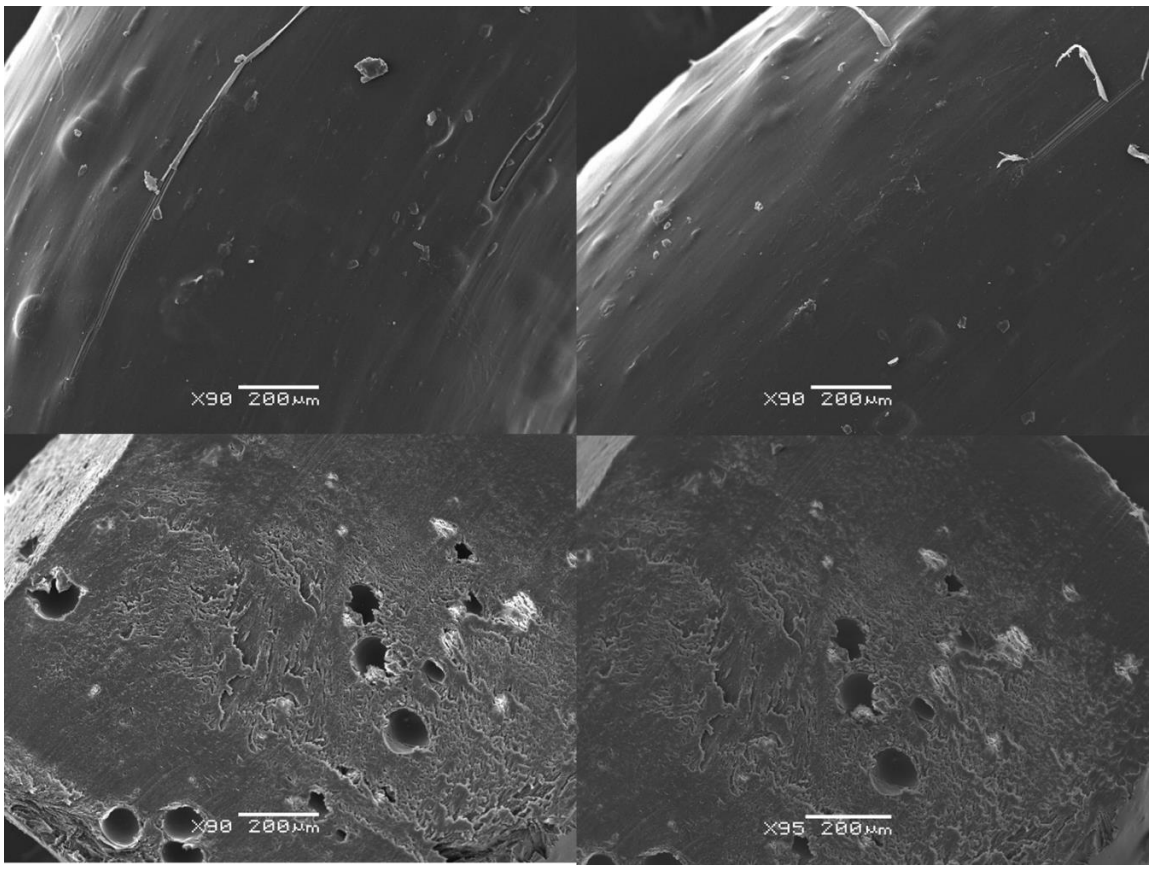

Figure A1-5: Surface (top) and cross-section (bottom) SEM images of HPC filament in which 5% $NaHCO_3$ has been incorporated.

To clearly visualise the uniformity of distribution of the $NaHCO_3$ within the matrix, elemental mapping for carbon and sodium was conducted. The surface mapping images can be seen below in Figure A1-6. The locations of the crystalline deposits previously mentioned correspond to the locations in which sodium was detected, indicating that the majority of said crystalline deposits are $NaHCO_3$ salt crystals. Furthermore, some sodium was detected on the outline of the aforementioned cavities in the matrix. This supports the previous hypothesis that the pockets were brought about by the reaction between $NaHCO_3$ and water present due to residual moisture. The presence of sodium in the vicinity of the air pockets indicates that that is a location in which the water-bicarbonate reaction has taken place, and sodium detected is actually sodium carbonate (Na_2CO_3), one of the products of the water-$NaHCO_3$ reaction, the other being CO_2, explaining the cavities.

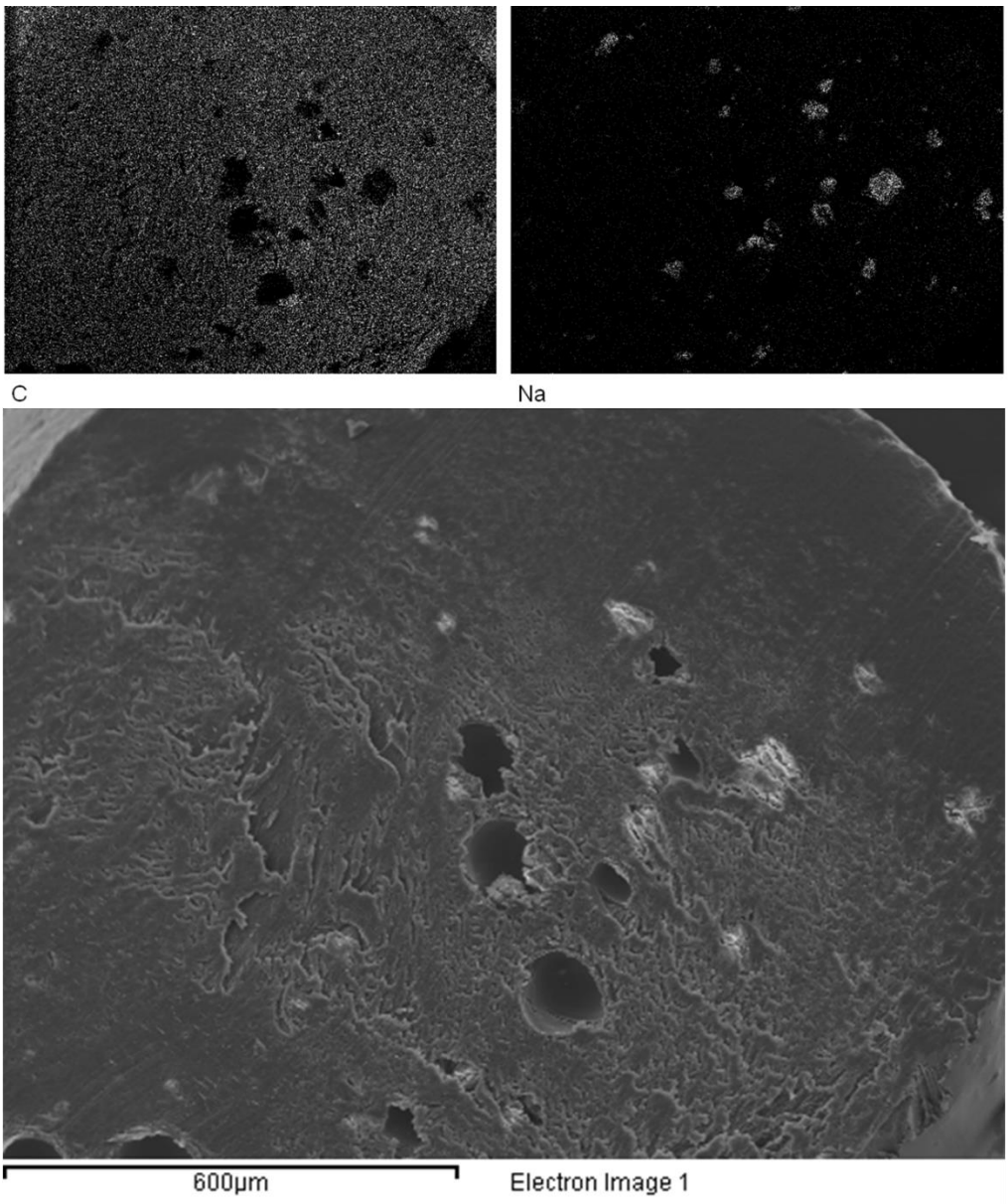

Figure A1-6: Elemental analysis mapping for carbon (left) and sodium (right) within the matrix of the filament (bottom)

A1.3.4.Disintegration time testing:

Figure A1-7 shows a picture of the tablet printed using the 5% $NaHCO_3$ filament. To test the disintegration ability of the tablet, the tablet was placed in a 10 ml syringe, distilled water was then drawn into the syringe and shaken gently until the tablet had visibly disintegrated.

Figure A1-7: 3D printed HPC-$NaHCO_3$ tablet.

This method of testing was used to mimic a real-life situation in which the tablet would be used by a patient, as the purpose of the formulation is to have the tablet be disintegrated ex-vivo prior to administration. The tablet was indeed found to disintegrate, taking approximately 9 minutes until it disintegrated sufficiently to be injected from the syringe into a glass vial (Figure A1-8).

Figure A1-8: HPC-$NaHCO_3$ tablet post-disintegration

On attempting to replicate the results of this experiment, printing a pair of two more tablets for replication was planned. However, upon attempting to print a set of tablets to replicate the experiment, the printer nozzle was found to be severely clogged. Attempts to unblock the nozzle using sufficiently thin needles, flushing with ABS, and even rinsing with water were attempted with no success. The nozzle had been so severely blocked that it had to be replaced. Unfortunately, this replacement required swapping the entire print head assembly. This severe blockage is assumed to be due to deposits of $NaHCO_3$ building up inside the nozzle, causing a severe blockage.

A1.4. Conclusion

The disintegration time for the trialled tablet was just over 9 minutes, which much longer than what is expected of a rapidly disintegrating formulation to achieve in order to be convenient for the patient. However, while anecdotal evidence of the sole trialled tablet suggests that with optimisation of the formulation, a rapidly disintegrating FDM-printed tablet may be achievable, replication of the results achieved was not possible, it, therefore, remains unclear whether the formulation trialled can reproducibly perform as reported.

The presence of the insoluble $NaHCO_3$ salt in the formulation led to a nozzle block that could not be resolved without undergoing an expensive replacement of the print head. This leads to either of two hypotheses: the first is that the particle size (100% of particles < 200 µm) was still much larger than what can be realistically processed through a 400 µm nozzle. The second is that printing of filled polymers is simply not possible due to particle build up in the nozzle. There is clearly a need to investigate this further, as the incorporation of insoluble inorganic solids like salts or clays is a commonly used pharmaceutical formulation tactic for enhancing the performance of some dosage forms. However, further investigation of this phenomenon was not possible. Repairing the blocked nozzle required purchasing a new print head assembly (£350), and the delivery time for the new print head was two months. Investigating the blocking phenomenon was deemed too severe a fiscal gamble should such experiments lead to yet another blocked nozzle. The observations presented herein are intended to advise against printing using filled polymers until this build up and blockage phenomenon has been thoroughly investigated and mitigated against.

Appendix 2:
Drug release rates from the acetylsalicylic acid-loaded polycaprolactone grids

A2.1. Introduction

Chapter 4 presented an investigation into the quality parameters and limitations of FDM as a tool for the manufacture of pharmaceutical dosage forms. The polymer used for that investigation was PCL. As part of that investigation, PCL was loaded with either 5%, 10%, or 15% ASA, to investigate the impact of drug loading on the FLE. On publishing that experiment (173), the addition of an investigation of the drug release rate from the 3D printed grids was recommended by the reviewers. While it is in the views of the author that the drug release studies have no experimental context in the scope of the aims of what was presented in Chapter 4, they were nonetheless conducted but were excluded from the main manuscript of the chapter. The results are therefore presented herein.

A2.2. Materials and methods

A2.2. In-vitro drug release studies:

ASA release studies from the 5%, 10%, and 15% loaded 3D printed grid films were conducted using the United States Pharmacopoeia (USP) apparatus II (paddle) using a revolution rate of 50 RPM. The grids were placed in 750 mL of pH 1.2 simulated gastric fluid for 2 hours, then transferred to 900 mL of pH 6.8 phosphate buffer saline. Determination of amount of ASA released was conducted using a Perkin Elmer Lambda 35 UV/Vis spectrophotometer (PerkinElmer, Inc., Waltham, MA, United States) at a wavelength of 265 nm (214).

A2.3. Results and Discussion:

Figure A2-1 shows the in vitro drug release rates for the 5%, 10%, and 15% ASA-loaded formulations in PCL. A significant difference in the release rate of the 5% formulation compared to its higher loading counterparts was observed. Both the 10% and 15% formulation achieved ~100% release in under 300 min. The 5% drug-loaded formulation, however, had released only ~30% of the drug after 8 h. As previously discussed, the 5% drug-loaded formulation was the only formulation in which the ASA was molecularly dispersed within the matrix of PCL, while both 10% and 15% drug-loaded contained phase-separated crystalline ASA. This is further evidenced by the aforementioned differences in release rate. PCL is a biodegradable polymer that is commonly used for implantable, long-term release formulations (123). It is insoluble in aqueous media and only degrades over time via hydrolysis of its ester linkages in physiological conditions. In the 5% drug-loaded formulation, the ASA is molecularly dispersed within the polymer, thus the drug release relies on the slow diffusion of ASA molecules from the PCL matrices and the polymer degradation. On the other hand, the 10% and 15% drug-loaded formulations contain phase-separated crystalline ASA which can dissolve much faster. No visible disintegration of the FDM printed films was observed over the 8 h dissolution tests.

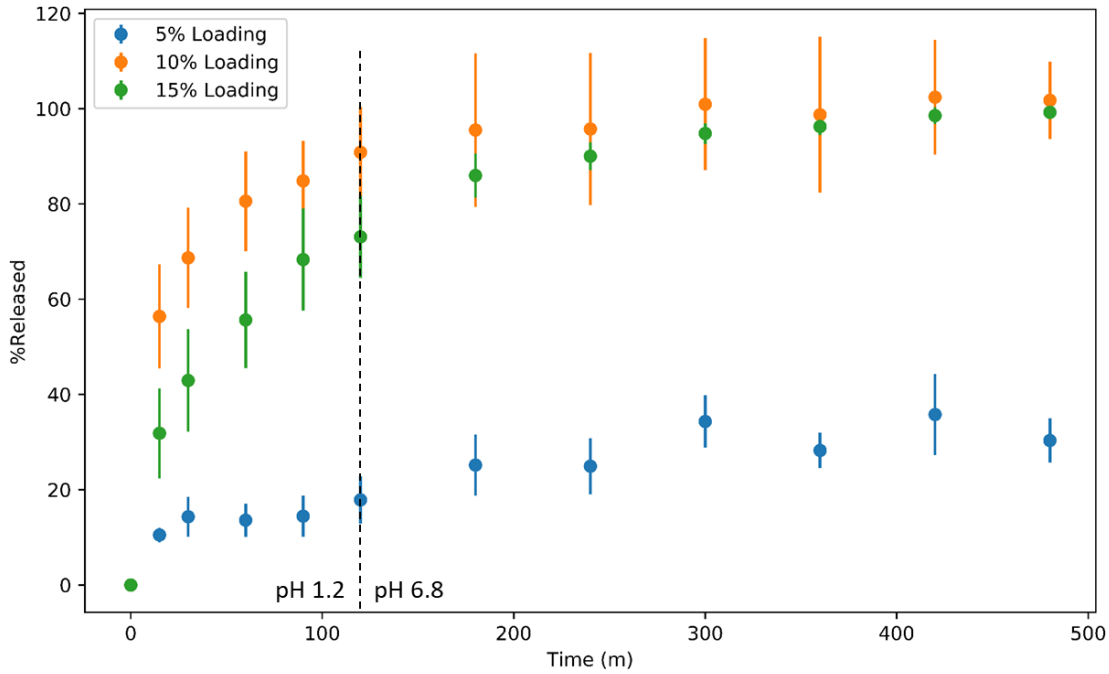

Figure A2-1: In vitro drug release profiles of FDM printed PCL films containing 5%, 10%, and 15% ASA.